HRS Cells and Tumor-Associated Macrophages as Dual Mediators of PD-1/PD-L1–Dependent $CD8^+$ T Cell Suppression in Classical Hodgkin Lymphoma

Dissertation

zur

Erlangung des Doktorgrades

der Naturwissenschaften (Dr. rer. nat.)

vorgelegt beim

Fachbereich 08 – Biologie und Chemie

der Justus-Liebig-Universität Gießen

vorgelegt von

Hasmik Yegoryan

aus Bazmaghbyur, Armenien

Gießen, 2025

1. Gutachterin: Prof. Dr. rer. nat. Undraga Schagdarsurengin
   Andrologisch-Urologischen Forschungslabor
   Fachbereich 08 – Biologie und Chemie
   Justus-Liebig-Universität Gießen

2. Gutachter: Prof. Dr. rer. nat. Roland Schmitz
   Institut für Pathologie
   Fachbereich 11 – Medizin
   Justus-Liebig-Universität Gießen

Tag der Disputation: 19.03.2026

Abstract

Classical Hodgkin lymphoma (cHL) features rare Hodgkin/Reed–Sternberg (HRS) cells within an immune-dense microenvironment, yet refractory disease persists in a subset of patients. This thesis interrogates how PD-1/PD-L1 signaling suppresses $CD8^+$ T-cell cytotoxic immunity by integrating tumor-intrinsic and microenvironmental mechanisms. We combined mechanistic co-cultures, PLA coupled to multiplex immunofluorescence (PLA/mIF) on FFPE tissues, and RNA-seq of tumor-educated macrophages to link cellular mechanism to tissue context. Using mechanistic co-cultures of antigen-specific $CD8^+$ T cells with HRS cells, we show that MHC-I–intact HRS cells directly restrain $CD8^+$ effector function through PD-1/PD-L1 engagement; both PD-1 blockade and HRS PD-L1 knockout enhanced $CD8^+$ activation and killing. In complementary systems incorporating tumor-associated macrophages (TAMs), PD-$L1^+$ macrophages suppressed $CD8^+$ T-cell activity via PD-1, and this inhibition was partially reversed by PD-1 blockade. Proximity ligation assay combined with multiplex immunofluorescence on FFPE sections confirmed in situ PD-1/PD-L1 engagement at two interfaces: $CD8^+$ - HRS, and $CD8^+$-TAMs contacts. Notably, EBV-positive tumors exhibited higher interaction rates across both interfaces, consistent with preserved MHC-I and enriched myeloid niches. PLA/IF further demonstrated that in tumors with limited CD8–HRS contact, $CD8^+$ T cells continued to form PD-1/PD-L1 interactions with macrophages, indicating that TAMs can function as alternative checkpoint partners when direct tumor engagement is reduced. Together, these data support a multilayered model in which HRS cells initiate checkpoint-mediated suppression that TAMs amplify and stabilize. Long-term co-cultures of HRS cells with PD-1–expressing cells revealed no sustained proliferative or survival advantage from PD-L1 ligation under nutrient-replete conditions, suggesting context dependence of PD-L1 reverse signaling. Finally, RNA-seq of macrophages exposed to HRS-conditioned media showed M2-like polarization with increased mediators such as VSIG4, MMP9, and PDGF ligands, reinforcing checkpoint-mediated suppression and impairing T-cell function. Together, these data support a layered model of immune evasion in cHL: HRS cells can initiate PD-1/PD-L1–dependent inhibition where MHC-I is intact, while M2-like TAMs act as compensatory/alternative partners that sustain suppression when direct CD8–HRS engagement is limited. This framework explains the variable efficacy of PD-1 blockade and supports macrophage-targeted therapies for more durable responses.

Zusammenfassung

Das klassische Hodgkin-Lymphom (cHL) enthält nur wenige Hodgkin/Reed–Sternberg-(HRS)-Zellen in einer immunzellreichen Mikroumgebung, doch ein Teil der Patienten bleibt refraktär. Diese Arbeit untersucht, wie die PD-1/PD-L1-Signalübertragung die zytotoxische $CD8^+$-T-Zell-Immunität durch tumorintrinsische und mikroenvironmentale Mechanismen unterdrückt. Wir kombinierten mechanistische Kokulturen, PLA/mIF an FFPE-Geweben und RNA-Seq von tumorerzogenen Makrophagen, um zelluläre Mechanismen mit dem Gewebekontext zu verbinden. In Kokulturen antigen-spezifischer $CD8^+$-T-Zellen mit HRS-Zellen zeigte sich, dass MHC-I-intakte HRS-Zellen die $CD8^+$-Effektorfunktion direkt über PD-1/PD-L1 hemmen; PD-1-Blockade oder PD-L1-Knockout steigerten Aktivierung und Zytotoxizität. In Systemen mit tumorassoziierten Makrophagen (TAMs) unterdrückten $PD\text{-}L1^+$-Makrophagen die $CD8^+$-Aktivität über PD-1, was durch PD-1-Blockade teilweise aufgehoben wurde. PLA/mIF bestätigte **in situ** PD-1/PD-L1-Interaktionen an zwei Schnittstellen: $CD8^+$–HRS und $CD8^+$–TAM. EBV-positive Tumoren zeigten an beiden Schnittstellen erhöhte Interaktionsraten, im Einklang mit erhaltenem MHC-I und einer myeloid-reichen Umgebung. Zudem interagierten $CD8^+$-T-Zellen bei eingeschränktem CD8–HRS-Kontakt weiterhin mit $PD\text{-}L1^+$-Makrophagen, was TAMs als alternative Checkpoint-Partner ausweist. Diese Befunde stützen ein Modell, in dem HRS-Zellen die Suppression einleiten und TAMs sie verstärken. Langzeit-Kokulturen zeigten keinen proliferativen oder überlebensbezogenen Vorteil durch PD-L1-Ligierung, was eine Kontextabhängigkeit des Reverse-Signalings nahelegt. RNA-Seq von Makrophagen, die HRS-konditioniertem Medium ausgesetzt waren, zeigte eine M2-ähnliche Polarisierung mit erhöhten Mediatoren wie VSIG4, MMP9 und PDGF-Liganden, die die Checkpoint-Suppression verstärken und die T-Zell-Funktion beeinträchtigen. Insgesamt ergibt sich ein Modell der Immunflucht, in dem HRS-Zellen eine PD-1/PD-L1-abhängige Hemmung einleiten, während M2-ähnliche TAMs die Suppression bei reduzierter CD8–HRS-Interaktion aufrechterhalten. Dies erklärt die variable Wirksamkeit der PD-1-Blockade und unterstützt makrophagenorientierte Therapiestrategien für dauerhaftere Antworten.

Table of Contents

List of Abbreviations

Abbreviation	Full Term
ABVD	Doxorubicin [Adriamycin], bleomycin, vinblastine, dacarbazine
AIM-V	Adult immunodeficiency medium-V
AVD	Doxorubicin, Vinblastine, Dacarbazine
BCR	B-cell receptor
BEACOPP	Bleomycin, etoposide, doxorubicin [Adriamycin], cyclophosphamide, vincristine [Oncovin], procarbazine, prednisone
BFP2	Blue fluorescent protein 2
β2M	β2-microglobulin
°C	Degree Celsius
CD30	Cluster of Differentiation 30
cHL	Classical Hodgkin Lymphoma
CM	Conditioned medium
CO2	Carbon dioxide
DAPI	4′,6-diamidino-2-phenylindole
DEGs	Differentially expressed genes
DGE	Differential gene expression
DMEM	Dulbecco's modified eagle medium
DMSO	Dimethyl sulfoxide
DNA	Deoxyribonucleic acid
dsRed	Discosoma red
EBV	Epstein–Barr virus
EDTA	Ethylenediamine tetraacetic acid
Endogenous TCR $CD8^+$ T cells	T cells expressing only endogenous TCR
FACS	Fluorescence activated cell sorting
FBS	Fetal bovine serum
FFPE	Formalin-fixed paraffin-embedded
FFS	Forward scatter

Fix/Perm	Fixation and permeabilization
GaLV	Gibbon ape leukemia virus
GFP	Green fluorescent protein
GM-CSF	Granulocyte-macrophage colony-stimulating factor
H	Hours
HIAR	Heat-induced antigen retrieval
HL	Hodgkin Lymphoma
HLA	Human leukocyte antigens
HRP	Horseradish peroxidase
HRS	Hodgkin Reed-Sternberg cells
IFN-γ	Interferon-gamma
IgV	Immunoglobulin variable
IHC	Immunohistochemistry
ILs	Interleukins (e.g. IL-2, IL-4)
IU/ml	International units per milliliter
JAK	Janus kinases
JLU	Justus-Liebig-University
KO	Knockout
LFC	Log_2 fold change
|LFC|	Absolute log_2 fold change
LMP1	Latent membrane protein 1
LMP2A	Latent membrane protein 2A
LP	Lymphocyte predominant
LPS	Lipopolysaccharide
M1 macrophages	Macrophages polarized with LPS/IFNγ towards type 1 (Th1) immunity (also called classically activated macrophages)
M2 macrophages	Macrophages polarized with IL-4/IL-13 towards type 2 (Th2) immunity (also called alternatively activated macrophages)
MACS	Magnetic activated cell sorting
M-CSF	Macrophage colony-stimulating factor
MEM	Minimal essential medium
MHC	Major histocompatibility complex
mIF	Multiplex immunofluorescent staining

min	minutes
MOPP	Mechlorethamine, vincristine [Oncovin], procarbazine, and prednisone
NF- κB	Nuclear factor-κB
NLPHL	Nodular lymphocyte predominant Hodgkin lymphoma
NY-ESO-1^{+} L1236	L1236 cell line, which express HLA-A2 and was transduced to express the NY-ESO-1 antigen
NY-ESO-1 TCR CD8^{+} T cells	CD8^{+} T cells transduced with a recombinant TCR recognizing the HLA-A*02–restricted melanoma antigen NY-ESO-1
Opti MEM	Optimized minimum essential medium
PBMCs	Peripheral blood mononuclear cells
PBS	Phosphate-buffered saline
PBST	Phosphate-buffered saline with Tween 20
PCA	Principal component analysis
PCR	Polymerase chain reaction
PD-1	Programmed cell death protein 1
PD-L1	Programmed cell death ligand 1
PD-L2	Programmed cell death ligand 2
PET/CT	Positron Emission Tomography combined with Computed Tomography
PLA	Proximity ligation assay
REP	Rapid expansion protocol
RetroNectinTM	Recombinant human fibronectin fragment
RNA	Ribonucleic acid
RNA-seq	RNA sequencing
RPMI	Roswell Park Memorial Institute medium
RT	Room temperature
sgRNA	Single-guide RNA
Slides	Mounted paraffin tissue sections
SSC	Side scatter
STAT	Signal transducers and activators of transcription
TAM	Tumor-associated macrophages

TCR	T cell receptor
TME	Tumor microenvironment
TNFR	Tumor necrosis factor receptor
TSA	Tyramide signal amplification
UKGM	Universitätsklinikum Gießen und Marburg
VISTA	V-domain immunoglobulin suppressor of T cell activation

1 Introduction

More than 180 years ago, Thomas Hodgkin described several cases of a disease later named Hodgkin disease [1]. Once recognized as a lymphoid malignancy, the disease was renamed Hodgkin lymphoma (HL) [2]. It is a rare malignancy, with approximately 83,000 new cases diagnosed globally each year and an age-standardized incidence rate of 0.98 per 100,000 [3]. Although it is rare overall, HL shows a characteristic bimodal age distribution. It occurs in older individuals as well as in young adults—among whom it is one of the most common cancers [4,5].

Over time, HL has transformed from a fatal disease into one of the most curable malignancies, with modern combined chemotherapy and radiotherapy achieving cure rates of approximately 80–90% [6].

1.1 Hodgkin lymphoma therapy: Milestones and emerging strategies

The introduction of radiotherapy in the early 1900s marked the first effective treatment, particularly for localized disease [7–9]. The 1960s marked a major milestone with the development of combination chemotherapy, particularly the MOPP regimen (mechlorethamine, vincristine [Oncovin], procarbazine, and prednisone), which achieved high rates of treatment response [10,11]. However, MOPP was eventually replaced by the ABVD regimen (doxorubicin [Adriamycin], bleomycin, vinblastine, dacarbazine) in the 1970s, as the cure rates were higher with ABVD and the long-term side effects were fewer [10,12–14]. ABVD remains a cornerstone of HL treatment to this day. In the following decades, efforts shifted toward optimizing therapy by balancing efficacy with long-term toxicity. Combined modality therapy, chemotherapy followed by involved-site radiotherapy, became standard for early-stage disease [14]. For advanced-stage and high-risk patients, intensified regimens such as BEACOPP (bleomycin, etoposide, doxorubicin [Adriamycin], cyclophosphamide, vincristine [Oncovin], procarbazine, and prednisone), introduced in the mid-1990s, offered improved disease control at the cost of increased toxicity [14,15].

More recently, response-adapted strategies using interim positron emission tomography combined with computed tomography (PET/CT) imaging have enabled personalization of treatment, allowing for escalation or de-escalation based on early response [7,16]. However, despite these advances and high long-term survival rates, the

majority of HL survivors face a significantly increased risk of serious late treatment-related complications. These include second cancers, cardiovascular and pulmonary diseases, thyroid problems, among others [17]. In response to long-term treatment-related complications, novel therapeutic agents have emerged over the past decade. Brentuximab vedotin, an antibody–drug conjugate targeting the cell surface marker CD30 expressed on malignant lymphocytes in HL, was initially approved for relapsed or refractory patients [18]. However, based on promising clinical outcomes in combination with AVD (ABVD without bleomycin, due to concerns over pulmonary toxicity), it is now increasingly incorporated into frontline treatment regimens [18,19].

Immune checkpoint inhibitors such as nivolumab and pembrolizumab, which target the programmed death-1 (PD-1) receptor to restore anti-tumor immune responses, have demonstrated durable efficacy in heavily pretreated patients with relapsed or refractory Hodgkin lymphoma [20,21]. Nivolumab is a fully human IgG4 monoclonal antibody that binds to PD-1 on activated T cells, preventing its interaction with programmed cell death ligand-1 (PD-L1) and programmed cell death ligand-2 (PD-L2). By interrupting the inhibitory PD-1/PD-L1 interaction, nivolumab restores T-cell effector functions, including proliferation, cytokine secretion, and cytotoxic activity against HRS cells. In an expanded phase 2 trial involving patients with relapsed or refractory disease following brentuximab vedotin treatment and stem cell transplant, nivolumab achieved an objective response rate of 66.3%, with 76.9% of patients remaining progression-free at 6 months; some experienced long-lasting responses [22]. Comparable clinical outcomes were observed with pembrolizumab, another PD-1–targeting antibody [23]. Initially approved for patients who had failed prior therapies, nivolumab and pembrolizumab are now increasingly integrated into earlier lines of treatment, reflecting a shift toward immunotherapy-based strategies in HL management. These promising outcomes offer the potential not only to improve cure rates but also to reduce the side effects and long-term toxicities associated with conventional chemotherapy. The mechanism of action of nivolumab in the context of cHL will be discussed in detail in a later section.

1.2 Classification of Hodgkin lymphoma

Hodgkin lymphoma is subdivided into two main subtypes, classical Hodgkin lymphoma (cHL) and nodular lymphocyte predominant Hodgkin lymphoma (NLPHL), based on

differences in the morphology and phenotype of the lymphoma cells, as well as the composition of the background cellular infiltrate [24]. NLPHL is a relatively rare subtype, accounting for approximately 5–10% of all HL cases and is characterized by the presence of neoplastic lymphocyte predominant (LP) cells.

The cHL is further subdivided into four histological subtypes: nodular sclerosis, mixed cellularity, lymphocyte-rich classic, and lymphocyte-depleted [25,26]. All cHL subtypes are characterized by neoplastic mononuclear Hodgkin cells and bi- or multinucleated Reed–Sternberg (HRS) cells. Nodular sclerosis, which accounts for about 70% of classical Hodgkin lymphoma cases, is characterized by collagen bands (sclerosing fibrosis) that separate nodules composed of inflammatory cells and a specific variant of HRS cells known as lacunar cells, which appear to sit in clear spaces ("lacunae") due to fixation artifacts. In contrast, mixed cellularity Hodgkin lymphoma lacks such bands, and HRS cells are scattered within a mixed inflammatory infiltrate, accounting for approximately 20-25% of cases. Lymphocyte-rich cHL, accounting for about 5% of cases, is a less common subtype characterized by a predominance of reactive lymphocytes in the background with scattered HRS cells. This subtype generally has fewer inflammatory cells compared to mixed cellularity and lacks the sclerosing fibrosis that is characteristic of nodular sclerosis. Additionally, it typically lacks neutrophils and eosinophils in the cellular infiltrate. Lymphocyte-depleted cHL is the rarest subtype, accounting for less than 1% of cases, and is characterized by a diffuse infiltration of HRS cells with minimal or absent reactive inflammatory cells in the background.

1.3 Cellular origin and phenotypic complexity of HRS cells

A defining feature of cHL is the presence of neoplastic mononuclear Hodgkin cells and bi- or multinucleated Reed–Sternberg cells (HRS) within a reactive, mixed inflammatory background (see Figure 1). Due to their rarity and atypical immunophenotype, the cellular origin of HRS cells remained uncertain for nearly a century, despite their initial description in the early 20th century.

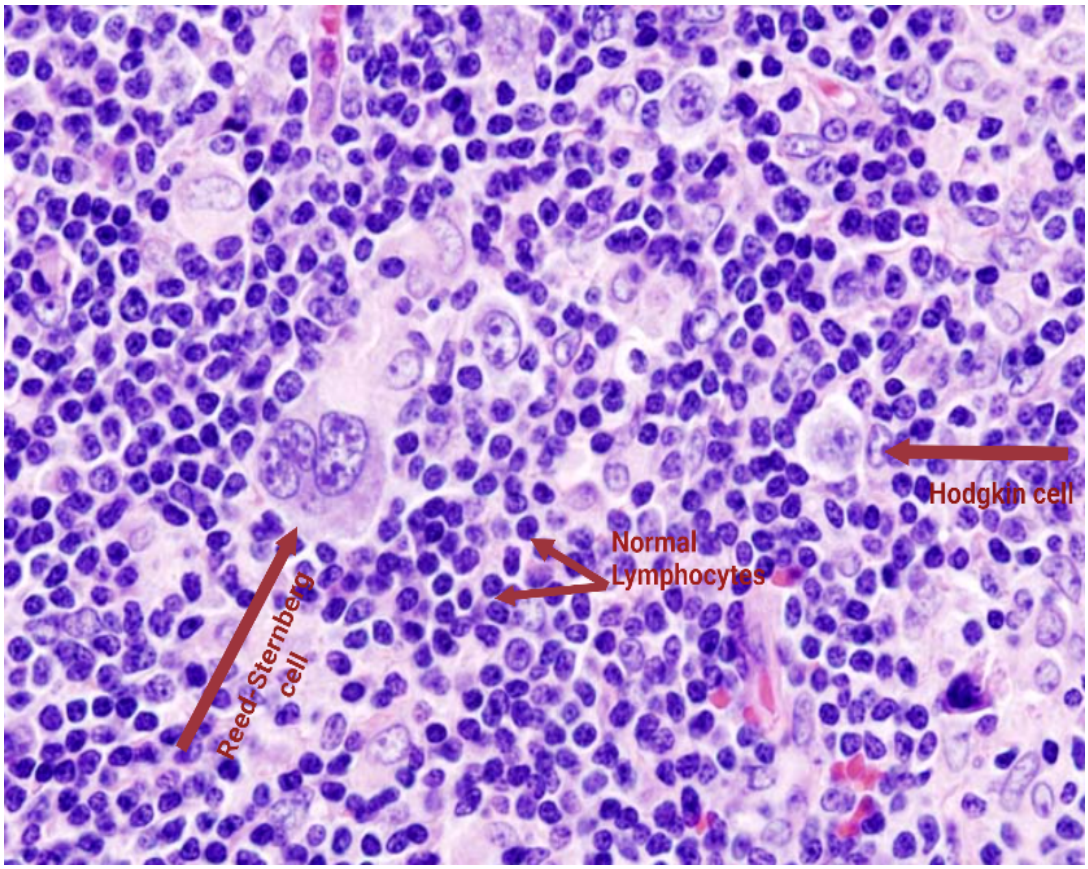

Figure 1. Cellular composition of classical Hodgkin lymphoma (cHL). Hematoxylin & eosin (H&E)–stained tissue shows malignant Reed–Sternberg cells with characteristic "owl-eye" bi- or multinucleated nuclei and mononuclear Hodgkin cells (HRS), highlighted separately from the surrounding normal lymphocytes. The tumor microenvironment also contains plasma cells, eosinophils, and macrophages, which collectively form a supportive niche that promotes HRS cell survival and immune evasion. (Image adapted from MDC Berlin, 2021).

The immunophenotypic profile of HRS cells does not resemble any normal immune cell subset, making it difficult to determine their lineage. Their phenotype is heterogeneous, showing co-expression of markers typically associated with multiple hematopoietic lineages, including dendritic cells, B cells, T cells, macrophages, and granulocytes [27,28]. The absence of B-cell receptor (BCR) expression and other characteristic B-cell markers further complicated their identification as B cells; however, the expression of the B-cell specific transcription factor PAX5 suggested a B-cell origin [28,29]. Despite this apparent contradiction, subsequent molecular studies have provided further insight into the true origin of HRS cells. Multiple lines of evidence support the view that HRS cells originate from pre-apoptotic germinal center (GC) B cells [29,30]. One of the key indicators of B-cell lineage is the presence of immunoglobulin variable (IgV) region gene rearrangements in HRS cells, a feature exclusive to B cells. The identification of somatic mutations within the IgV genes further supports a GC B-cell

origin, as somatic hypermutation is a process that occurs exclusively in germinal centers. Additionally, the detection of immunoglobulin class switching in HRS cells reinforces their derivation from GC B cells. Evidence for a pre-apoptotic origin comes from the observation that HRS cells often harbor deleterious somatic mutations, such as nonsense mutations in the IgV genes, which would normally lead to apoptosis in functional GC B cells. Collectively, these findings indicate that HRS cells are derived from crippled, pre-apoptotic GC B cells.

Although molecular evidence strongly supports a B-cell origin for HRS cells, their atypical phenotype can include expression of T-cell–associated markers such as granzyme B [31], CD3, and CD4 among others [27,32]. This unusual expression pattern has led to speculation that, in rare instances, the HRS cells may arise from T lymphocytes. Indeed, some studies of cHL cases expressing T-cell markers have revealed T-cell receptor (TCR) gene rearrangements in the absence of immunoglobulin (Ig) gene rearrangements, suggesting a true T-cell origin in a small subset of cases [33,34]. However, in the majority of cHL cases with T-cell marker expression, the HRS cells are still derived from B cells and simply display abnormal expression of T-cell–associated proteins [33–35]. Their expression of T-cell markers reflects abnormal expression rather than true lineage, further emphasizing the phenotypic complexity of these cells. Further investigation is needed to clarify the rare instances in which HRS cells may originate from T lymphocytes, as it remains uncertain whether these represent true T cell–derived Hodgkin lymphomas or rather some T-cell lymphomas that morphologically and immunophenotypically mimic classical Hodgkin lymphoma or cases in which T cells have acquired an HRS cell–like gene expression program [30].

A hallmark morphological feature of classical cHL is the distinctive owl-eye appearance of Reed-Sternberg cells, resulting from their bi- or multinucleated structure (see Figure 1). Time-lapse microscopy studies of HL cell lines revealed that mononuclear Hodgkin cells frequently fail to complete cytokinesis, leading to the formation of Reed-Sternberg cells through the re-fusion of sister cells that remain connected by microtubule bridges [36]. This suggests that mononuclear Hodgkin cells of GC B-cell origin give rise to Reed-Sternberg cells due to a defective cytokinesis process.

1.4 Dysregulation of JAK/STAT and NF-κB Signaling in cHL

Two major signaling pathways, JAK/STAT and NF-κB, are frequently altered in cHL, and their constitutive activation provides essential survival advantages to HRS cells while promoting profound immune evasion. Among these, the JAK/STAT pathway serves as a central mediator of cytokine signaling [30,37,38]. The JAK/STAT cascade is composed of transmembrane cytokine receptors, Janus kinases (JAKs), and the signal transducers and activators of transcription (STATs). Through this coordinated signaling module, the pathway governs diverse cellular processes, including differentiation, metabolic reprogramming, and immune regulation [38,39].

Upon binding of cytokines or growth factors to their specific transmembrane receptors, associated JAKs become activated and phosphorylate tyrosine residues in the receptor's intracellular domains, generating docking sites for STAT proteins. Once recruited, STATs are phosphorylated by JAKs to form pSTATs, which subsequently dissociate from the receptor complex and dimerize. These activated dimers then translocate into the nucleus, where they bind promoter regions of target genes and regulate transcription. Tight control of this signaling axis is maintained by several negative regulators, including SOCS proteins, PIAS family members, and protein tyrosine phosphatases (PTPs), which collectively prevent excessive or prolonged JAK/STAT activation [38,39].

In cHL, dysregulation of the JAK/STAT pathway is common and is driven by frequent genetic lesions affecting key components of this signaling system. Mutations in STAT6, STAT3, STAT5B, JAK1, and JAK2 cause these proteins constitutively active, thereby promoting the survival and proliferation of HRS cells. In addition, inactivating mutations in the negative regulators PTPN1 and SOCS1—among the most frequent mutations in cHL—further enhance pathway activity by abolishing essential inhibitory checkpoints [30,37,38,40]. Beyond these somatic mutations, constitutive JAK/STAT signaling in HRS cells is amplified by extensive autocrine and paracrine cytokine networks. HRS cells produce multiple interleukins and simultaneously express their corresponding receptors, enabling sustained autocrine stimulation. In parallel, immune cells within the cHL microenvironment supply additional cytokines that act in a paracrine manner, reinforcing JAK/STAT activation in HRS cells and contributing to the characteristic inflammatory milieu of the disease [30,37,38,41].

In addition to dysregulated JAK/STAT signaling, multiple other genes in cHL can be mutated or dysregulated, often altering pathways that support cell survival and immune evasion. Among these, mutations that drive constitutive nuclear factor-κB (NF-κB) activation represent a major hallmark of cHL and play a central role in its pathogenesis. Genomic gains and amplifications of *REL* are frequently detected and are associated with increased c-Rel protein expression, thereby enhancing NF-κB transcriptional activity [30,37,42]. Furthermore, inactivating mutations in negative regulators of NF-κB provide another mechanism driving persistent pathway activation [30,37]. Beyond these intrinsic alterations, NF-κB signaling is also activated by external cues such as cytokines, chemokines, and ligands associated with interleukins and tumor necrosis factor receptors (TNFRs) within the tumor microenvironment. Several TNFR family members, including CD30 and CD40, deliver potent pro-survival, anti-apoptotic, and pro-proliferative signals through NF-κB, as their ligands are abundantly provided by cells within the cHL microenvironment [30,37,43].

1.5 Tumor microenvironment in cHL

In cHL, HRS cells are scattered throughout a highly reactive tumor microenvironment (TME). This microenvironment is predominantly composed of non-tumor cells and accounts for the majority of the tumor mass, whereas HRS cells themselves make up only about 1–5% of it. This unique cellular composition represents another defining feature of cHL, distinguishing it from most other malignancies.

The TME consists of a diverse mixture of immune and non-immune cells, including T and B lymphocytes, neutrophils, eosinophils, macrophages, plasma cells, mast cells, fibroblasts, and a rich vascular network [44]. Owing to these variations in cellular composition each of the four histological subtypes of cHL (nodular sclerosis, mixed cellularity, lymphocyte-rich, and lymphocyte-depleted) exhibits characteristic patterns that reflect their distinct microenvironmental profiles [30,45–49].

HRS cells actively shape their tumor microenvironment by secreting a broad spectrum of cytokines, chemokines, and growth factors, thereby spatially remodeling the surrounding cellular landscape. They recruit various immune cells from the peripheral circulation and promote the local expansion of these populations, a process further

reinforced by reactive macrophages and mast cells. Specifically, HRS cells produce factors such as IL-5, IL-7, IL-8, IL-9, CCL5, CCL17, CCL20, and CCL22, which facilitate the recruitment of lymphocytes, granulocytes, macrophages, and mast cells [45,49,50]. Among these, chemokines such as CCL5, CCL17, CCL20, and CCL22 specifically attract Th2 and Treg subsets. Th2 cells support tumor growth by promoting angiogenesis and suppressing cell-mediated immunity, reducing the efficacy of tumor cell killing. Treg cells inhibit cytotoxic activity through multiple mechanisms, including IL-10 secretion and CTLA-4 or LAG3-mediated downregulation of CD3 signaling, specifically suppressing Th1 effector cells [45,48,49,51,52].

HRS cells are typically in close contact with, and surrounded by, $CD4^+$ T cells—predominantly Th2 and Treg subsets—forming characteristic 'rosettes'. These rosettes act as a protective wall around HRS cells, shielding them from cytotoxic attacks and exemplifying how HRS cells spatially organize their microenvironment to reinforce survival and immune evasion [45,49,52]. They also deliver pro-survival signals via CD40–CD40L interaction, leading to NF-κB activation. Interestingly, in HIV-associated cHL, these T-cell rosettes are often replaced by spindle-shaped $CD163^+$ macrophages, highlighting a distinct microenvironmental adaptation [53,54].

Importantly, HRS cells do not only shape their microenvironment by attracting immune cells but also modulate their functional state and differentiation through the secretion of critical factors. Although HRS cells themselves have limited proliferative capacity, they strategically manipulate surrounding normal cells to create a supportive microenvironment. For example, they can reprogram tumor-infiltrating T cells by skewing $CD4^+$ differentiation toward Th2 and Treg phenotypes, both of which favor immune suppression and tumor progression [45,49,52].

This reprogramming illustrates that the interactions between HRS cells and the surrounding microenvironment are not unidirectional. In fact, the dynamic interplay between HRS cells and the TME is bidirectional: while HRS cells actively recruit and shape immune populations, the recruited cells, in turn, secrete factors that further promote HRS survival and proliferation. This bidirectional crosstalk extends beyond immune cells to stromal components as well. For example, extracellular vesicles released by HRS cells can reprogram fibroblasts into cancer-associated fibroblasts with tumor-supportive functions. Although HRS cells do not produce eotaxin themselves, they secrete IL-13 and TNF-α, which stimulate fibroblasts to release eotaxin, thereby promoting the recruitment of eosinophils and T cells into the TME [48,49].

This bidirectional crosstalk illustrates how HRS cells not only shape their microenvironment but also exploit the recruited cells to reinforce their own survival and proliferation. In doing so, HRS cells employ multiple complementary strategies to establish and maintain a supportive tumor microenvironment. First, they actively recruit immune cells through the secretion of cytokines and chemokines. Second, they modulate the phenotype of recruited immune cells, reprogramming T cells, macrophages, and other components toward tumor-promoting functions. Third, HRS cells promote the local expansion of Th2 and Treg cells, fibroblasts, endothelial cells, and monocytes, reinforcing the structural and functional network of the TME. Finally, they can exert direct inhibitory effects on cytotoxic T and NK cells, limiting effective anti-tumor immunity [30,45–49,55].

The cumulative outcome of these strategies is a tumor microenvironment capable of suppressing immune responses, sustaining HRS survival and proliferation, and contributing to therapy resistance. This coordinated remodeling underscores the complexity of cHL's TME and highlights why disrupting these interactions is a critical focus for therapeutic development [30,45–49,55].

1.6 Epstein–Barr Virus–Associated cHL

Epstein–Barr virus (EBV) infection represents an additional layer of immune modulation in a substantial subset of classical Hodgkin lymphoma cases. Approximately 40% of patients harbor EBV-positive HRS cells [56], and the virus is thought to contribute to lymphomagenesis through the expression of latent genes that provide survival and immune-evasive advantages [57]. In EBV-positive cHL, the viral proteins latent membrane protein 1 (LMP1) and latent membrane protein 2A (LMP2A) are consistently expressed. LMP1 functions as a constitutive mimic of CD40 signaling, while LMP2A imitates BCR signaling—both of which are critical for the survival of germinal center–derived B cells [57]. In addition to promoting HRS cell persistence, LMP1 has been shown to induce PD-L1 expression, further reinforcing local immunosuppression [58]. Clinically, EBV-positive cHL is often associated with a poorer prognosis, and circulating EBV DNA has been identified as an independent predictor of treatment failure [59]. In addition to promoting HRS cell survival, EBV-driven immune modulation—particularly increased PD-L1 expression and alterations of the surrounding microenvironment—facilitates immune escape in EBV-positive cHL.

1.7 Tumor-associated macrophages in cHL

Tumor-associated macrophages (TAMs) are among the most abundant and functionally diverse immune cells in the tumor microenvironment. They actively shape the local milieu, influencing tumor growth, progression, and response to therapy [60,61]. In classical Hodgkin lymphoma (cHL), TAMs play a particularly important role in remodeling the immune and stromal landscape, where they contribute to immune evasion mechanisms that protect HRS cells. Their remarkable plasticity allows them to adopt different functional states, ranging from pro-inflammatory to immunosuppressive, depending on environmental stimuli.

Macrophages represent one of the most adaptable immune cell types, capable of switching their roles depending on the signals they receive. They may stimulate or suppress immune activity, drive inflammation or resolve it, and within tumors they can either limit or promote disease progression [60,62,63]. To simplify this diversity, the concept of macrophage polarization has been proposed, categorizing them into two functional states M1 and M2, each shaped by distinct cytokine environments [62,63]. These heterogeneous cells originate from circulating monocyte precursors and differentiate under the influence of cytokines and growth factors within the tissues they infiltrate, acquiring distinct functional phenotypes.

Classically activated M1 macrophages typically develop in response to IFN-γ or bacterial components. They secrete pro-inflammatory cytokines that enhance adaptive immune responses and can induce apoptosis in malignant cells. Alternatively activated M2 macrophages arise in cytokine-rich environments, particularly in the presence of Interleukins 4 and 13 (IL-4 and IL-13). They release anti-inflammatory cytokines, growth factors, and immunosuppressive mediators that support tissue repair and promote apoptosis resistance in malignant cells. In sharp contrast to the tumor-suppressive potential of M1 macrophages, M2 macrophages are generally associated with immunosuppression and tumor progression [45,60,62,63]. Although macrophage polarization is often described as two opposing subsets, many markers overlap across populations and are expressed at varying levels. For example, M2 macrophages may still express certain M1 markers, albeit at lower levels, and vice versa [64]. Thus, the M1/M2 distinction should be understood as a spectrum rather than two fixed categories. Macrophages display substantial plasticity and can shift their phenotype in response to microenvironmental conditions [62,64]. In cancer, however, M2-like states are often

predominant and strongly associated with tumor-promoting function [46,65,66]. These macrophages secrete cytokines such as IL-6 and growth factors that drive tissue remodeling, angiogenesis, and immune suppression, ultimately facilitating tumor growth [46]. Additionally, these macrophages contribute to tumor progression by suppressing cytotoxic T cell activity and recruiting regulatory T cells, thereby promoting immune evasion. Recent studies have shown that HRS cells recruit peripheral monocytes into the tumor microenvironment but secrete cytokines such as IL-10, TGF-β, GM-CSF, IL-13, and CCL5, collectively driving macrophages toward an M2-like phenotype [46]. This polarization is often reflected by the expression of CD163, a marker proposed to identify immunosuppressive TAMs [66,67]. Increased macrophage expression has been consistently linked to poorer outcomes in cHL patients [60,66]. Notably, TAMs are more abundant in EBV-positive cHL than in EBV-negative cases, and in EBV-positive tumors, they are strongly associated with CD163 expression, indicating a predominance of the M2-like phenotype. In contrast, CD68 is more broadly expressed on monocytes and macrophages, as well as on subsets of dendritic cells, neutrophils, basophils, and mast cells, highlighting the more restricted specificity of CD163 for M2-like macrophages [68,69]. Notably, M2-like TAMs often express immune checkpoint molecules such as PD-L1, contributing to an immunosuppressive microenvironment that facilitates tumor immune evasion in cHL. This aspect, including PD-L1 expression, will be explored in the next section.

1.8 Immune evasion mechanisms of HRS cells in cHL

Through this dynamic crosstalk, HRS cells not only remodel their surroundings but also progressively disable effective anti-tumor immunity, ensuring that infiltrating immune cells are recruited to support, rather than attack, the malignant HRS cells. Numerous strategies of immune evasion have been described in cHL. These include the recruitment and expansion of immunosuppressive cell populations such as regulatory T cells and TAMs, the secretion of cytokines and chemokines that skew immune responses toward tumor-promoting phenotypes, genetic alterations or infrequent expression of major histocompatibility complex (MHC) molecules to impair antigen presentation, and the upregulation of inhibitory immune checkpoint pathways, including PD-1/PD-L1 and CTLA-4. Collectively, these mechanisms enable HRS cells to escape immune response and maintain a supportive tumor microenvironment.

1.8.1 MHC class I–antigen presentation mediated immune evasion in cHL

T cells use their surface receptor, the T cell receptor (TCR), to recognize peptides presented on major histocompatibility complex (MHC) molecules. These peptides can be derived from normal host proteins (self-peptides), invading pathogens such as viruses and bacteria, or from tumor-associated proteins. A key feature of immune surveillance is the ability of T cells to distinguish between self and non-self (including modified self) peptides.

MHC molecules, also known as human leukocyte antigens (HLA) in humans, are extremely polymorphic, which allows them to present a broad and diverse range of peptides to T cells. They are divided into two main classes: Class I MHC molecules, expressed on all nucleated cells, present endogenous peptides to $CD8^+$ cytotoxic T cells, whereas class II MHC molecules, restricted to professional antigen-presenting cells, present exogenous peptides to $CD4^+$ helper T cells. T cell activation occurs only when the TCR specifically recognizes and binds to an MHC molecule displaying a foreign or altered peptide (see Figure 2). This recognition step is tightly regulated, ensuring that immune responses are directed against potentially harmful pathogens or tumor cells, rather than healthy tissues [70–74]. Thus, TCR–MHC–peptide recognition forms the cornerstone of adaptive immunity, guiding precise activation of T cells against specific antigens. Although inactivating alterations of the MHC class II transactivator, CIITA, have been described in cHL, highlighting potential suppression of $CD4^+$ T cell–mediated immunity [75,76], the focus of this thesis is on $CD8^+$ T cell–mediated immune surveillance. This distinction allows us to concentrate on mechanisms of MHC class I disruption and *B2M* alterations, which are central to HRS cell evasion of cytotoxic T cell responses.

Given the central role of MHC molecules in initiating T cell–mediated immunity, disruptions in their expression or function provide tumor cells with an efficient means of immune evasion. In cHL, disruptions of MHC class I expression on HRS cells, most notably through genetic alterations in β2-microglobulin (*B2M*), play a central role in evading $CD8^+$ T cell–mediated immune surveillance. *B2M* encodes an essential structural subunit of MHC class I molecules, required for their stability and surface expression. Inactivating mutations or copy number loss of *B2M* in HRS cells prevent proper assembly of MHC class I complexes, leading to absent or reduced MHC class I expression on the cell surface [77–79]. As a result, these cells are unable to present antigenic peptides

effectively to $CD8^+$ cytotoxic T cells, impairing one of the most critical mechanisms of anti-tumor immunity.

HRS cell expression of *β2M*, MHC class I, and MHC class II has been evaluated in patients with relapsed/refractory cHL treated with nivolumab. In this study, HRS cell membrane expression of *β2M* was negative in 71% of tumors, decreased in 22%, and positive in 7%. Similarly, MHC class I expression was negative in 64% of patients, decreased in 29%, and positive in 7% [80]. Thus, loss of β2M is a key driver of impaired MHC class I expression in cHL. Overall, 93% of evaluable patients had absent or decreased expression of β2M and MHC class I, underscoring the high prevalence of disrupted antigen presentation in cHL [80]. These findings provide quantitative evidence of the frequent loss or reduction of MHC class I–related antigen presentation in HRS cells, supporting the role of *B2M* alterations in impairing $CD8^+$ T cell–mediated immune surveillance [79–81].

However, more recent studies reported lower frequencies of *B2M* and MHC class I loss in cHL cases, ranging from ~22–39% [82–88], suggesting that suppression of $CD8^+$ T cell–mediated immunity may also be driven by PD-1/PD-L1 interactions rather than MHC class I deficiency alone, emphasizing that *B2M* loss is only one mechanism of immune evasion, and other pathways, including checkpoint-mediated suppression, are also important. These observations also highlight cohort variability and set the stage for a closer examination of these findings.

In this context, noninvasive cfDNA profiling has recently emerged as a powerful approach to overcome the scarcity of HRS cells in tissue, enabling comprehensive characterization of the genetic heterogeneity of cHL. This approach enabled genomic characterization of the largest cHL cohort to date and revealed two distinct genetic subtypes, H1 and H2. H1 tumors, characterized by a cytokine-driven phenotype and crosstalk signaling within the cHL TME, are frequently paired with MHC class I loss, serving as a mechanism of immune evasion. By contrast, H2 tumors, in which *B2M* mutations are infrequent, show higher $CD8^+$ T cell infiltration and PD-L1 amplifications that drive T cell exhaustion, indicating that immune escape in this subgroup relies less on MHC class I disruption and more on PD-1/PD-L1–mediated suppression [86].

Building on these genomic insights, a complementary study applied spatially resolved multiplexed protein imaging with transcriptomic sequencing, profiling over 23 million cells from EBV-positive and EBV-negative cHL tumors. This high-resolution approach enabled detailed characterization of HRS cell states and their

microenvironmental interactions. Strikingly, HRS cells in EBV-positive cHL show nearly universal membranous positivity for B2M and MHC-I, whereas fewer than 25% of EBV-negative cases express these molecules. This observation has also been corroborated by other studies reporting that EBV-associated cHL retains or even overexpresses MHC class I [77,89]. Furthermore, EBV-positive HRS cells frequently exhibit increased triple-positive expression of $B2M^+$/$MHC\text{-}I^+$/$MHC\text{-}II^+$, underscoring coordinated upregulation of antigen-presenting machinery. Notably, MHC-I–positive HRS cells were also identified in EBV-negative cHLs, and their associated neighborhoods closely resembled those of EBV-positive cases. This suggests that MHC-I–positive HRS cells foster an immune-enriched tumor microenvironment even in the absence of EBV positivity, with neighborhoods characterized by enriched infiltration of $CD8^+$ T cells, activated $PD\text{-}1^+$ and V-domain immunoglobulin suppressor of T cell activation ($VISTA^+$) T and B cells, and $PD\text{-}L1^+$ macrophages, reinforcing the notion that immune escape in cHL involves multiple complementary mechanisms, including but not limited to MHC class I loss [82].

1.8.2 PD-1/PD-L1 pathway mediated immune evasion in cHL

Following recognition of peptide–MHC complexes, T cells require additional signals to become fully activated and initiate an effective immune response. An effective T-cell response to a target antigen requires two distinct signals. Signal 1 is delivered through the TCR upon binding of antigenic peptides presented on MHC molecules. However, TCR engagement alone is insufficient to induce cytokine production or sustain T-cell proliferation and instead leads to anergy (i.e., functional unresponsiveness to subsequent stimulation with the same antigen or to IL-2) [90–94].

To achieve full activation, T cells require a second, co-stimulatory signal that amplifies TCR-derived signaling and enables clonal expansion and differentiation. This co-stimulatory signal is provided by antigen-presenting cells through engagement of co-stimulatory receptors on the T-cell surface [90–93]. A subset of co-stimulatory receptors, such as CD28, is expressed constitutively on resting and activated T cells, whereas others are induced only after T-cell activation [90–92,95,96]. Among the inducible receptors, 4-1BB (CD137) is upregulated following antigen-dependent activation and serves as a hallmark of antigen-experienced T cells. Signaling through 4-1BB promotes T-cell proliferation, survival, and sustained effector function, particularly

within the $CD8^+$ T-cell compartment. Because its expression is tightly linked to antigen-driven activation, 4-1BB is widely recognized as a sensitive marker of activated T cells [93,95–98].

Once activated, $CD8^+$ T cells initiate effector functions, but their activity must be tightly controlled to maintain immune homeostasis. Following this engagement, T cells, particularly $CD8^+$ cytotoxic T cells, become activated and induce effector responses. However, to prevent excessive tissue damage and autoimmunity, these responses are tightly regulated through inhibitory immune checkpoint pathways, which act as physiological brakes that restrain T cell proliferation, cytokine production, and cytotoxic activity once an immune response is underway [99–102].

In the tumor microenvironment, these inhibitory pathways become especially important. Tumor cells, including HRS cells in cHL, take advantage of these inhibitory pathways to suppress $CD8^+$ cell function despite adequate antigen presentation, complementing evasion strategies such as MHC class I downregulation (see Figure 2).

PD-1 is an inhibitory receptor expressed on the surface of activated T cells, after antigen recognition. Its ligands, PD-L1 and PD-L2, are expressed on antigen-presenting cells, including dendritic cells, macrophages, and some B cells, as well as by tumor cells. Both ligands deliver inhibitory signals upon binding PD-1, initiating intracellular cascades that attenuate TCR signaling, reduce cytokine secretion, and limit T cell proliferation and cytotoxicity. In physiological conditions, the PD-1/PD-L1 checkpoint functions as a critical regulatory “brake” on T cell activity, maintaining self-tolerance, preventing autoimmunity, and minimizing tissue damage, thereby ensuring that immune responses remain proportional, appropriately targeted, and well-controlled [99–103] (see Figure 2).

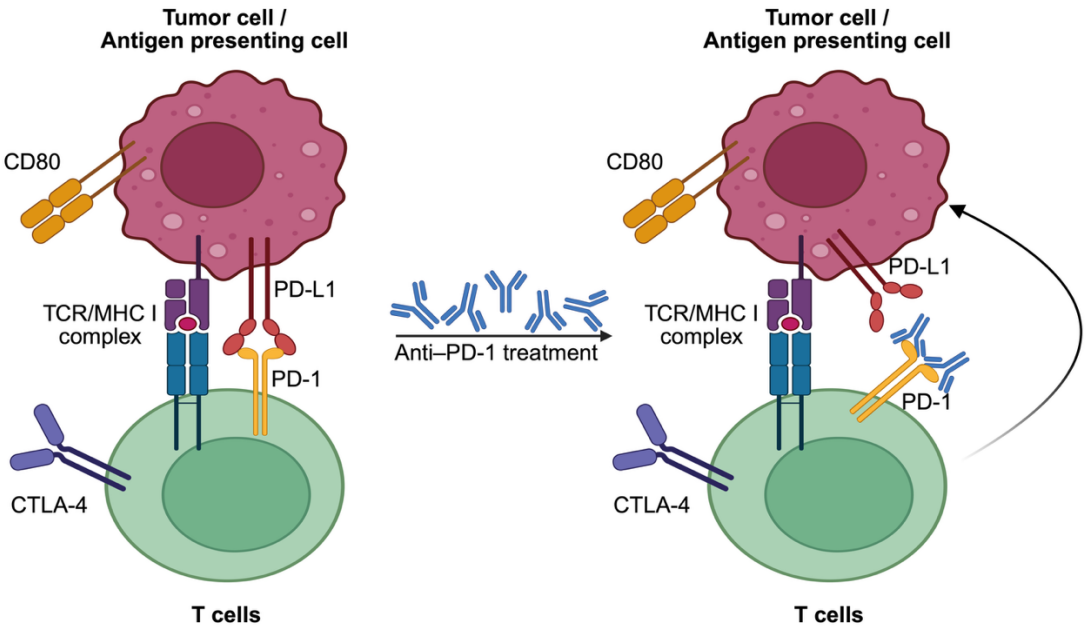

Figure 2. The PD-1/PD-L1 immune checkpoint pathway and its therapeutic blockade. $CD8^+$ T cells require recognition of antigenic peptides presented on MHC class I molecules via their T cell receptor (TCR), together with co-stimulatory signals, to become activated. Upon activation, they proliferate and exert cytotoxic effects on target cells. Engagement of PD-1 on T cells by its ligands PD-L1 or PD-L2, expressed on antigen-presenting cells or tumor cells, transmits inhibitory signals that attenuate TCR signaling, reduce cytokine production, and limit T cell proliferation and cytotoxicity. HRS cells take advantage of this pathway by upregulating PD-L1, thereby suppressing anti-tumor $CD8^+$ T cell responses even in the presence of adequate antigen presentation. Therapeutic immune checkpoint inhibitors, such as anti–PD-1 antibodies, restore T cell function by disrupting PD-1/PD-L1 interactions, effectively "releasing the brake" on cytotoxic T cells and enabling restored immune responses against tumor cells. (Created using BioRender).

While essential for preserving peripheral tolerance, PD-1-mediated inhibition can be hijacked in pathological contexts such as cancer and chronic infections. Sustained PD-1 engagement contributes to T cell exhaustion, a dysfunctional state marked by reduced cytokine production (IL-2, IFN-γ, TNF), impaired proliferation, and diminished cytotoxic activity. Exhausted T cells also display persistent expression of inhibitory receptors such as PD-1, TIM-3, and LAG-3, reflecting ongoing negative regulatory signaling and limited capacity to generate durable memory responses [99,100,102,104–107].

PD-1/PD-L1 interactions also influence $CD4^+$ T cells and NK cells by inducing exhaustion of these cells within the tumor microenvironment [80,107–109].

In cHL, inhibitory immune checkpoints represent a particularly important mechanism of immune evasion. Among these, the PD-1/PD-L1 axis is most significant. HRS cells commonly overexpress PD-L1 and PD-L2 as a result of genetic alterations in

the 9p24.1 locus. This region contains the PD-L1 and PD-L2 genes, which are directly amplified, as well as the JAK2 gene, whose enhanced activity further promotes PD-L1/PD-L2 expression via the JAK–STAT signaling pathway. These 9p24.1 alterations are among the most characteristic genetic lesions in cHL, occurring in approximately 75% of cases [110,111]. EBV infection can also contribute to PD-L1 upregulation in HRS cells [58]. PD-L1 and PD-L2 overexpression by HRS cells provides a major immunosuppressive mechanism, as binding to PD-1 inhibits the activity of cytotoxic T cells and other PD-1–expressing immune cells [104].

Notably, PD-L1 is expressed not only by HRS cells but also by TAMs, which constitute a major component of the tumor microenvironment [107,112]. PD-L1–positive TAMs are spatially organized in defined niches surrounding HRS cells, where their close proximity is likely to reinforce local immunosuppression and facilitate tumor immune evasion [113].

Interestingly, a recent study demonstrated that a fraction of PD-L1 expressed by TAMs may in fact be acquired from HRS cells through trogocytosis, a process involving the intercellular transfer of membrane fragments from HRS cells to monocytes in cHL. This phenomenon was not observed in monocytes co-cultured with PD-L1/PD-L2–deficient HRS cells [114]. Since trogocytosis requires direct cell–cell contact, this mechanism could explain the enrichment of PD-L1^{+}/PD-L2^{+} TAMs in close proximity to HRS cells and may further contribute to immune evasion [113]. The expression of PD-L1 can also be upregulated by cytokines such as IFN-γ and GM-CSF, secreted by HRS cells and other components of the tumor microenvironment, further amplifying local immunosuppression [112]. CD8^{+} T cells, including the PD-1^{+} subset, are more frequently found near PD-L1^{+} TAMs than PD-L1^{-} TAMs, suggesting that these TAMs may either enhance antitumor immunity through antigen presentation or mediate immunosuppression via engagement of PD-1 [82,113]. Other inhibitory receptors also contribute to T-cell regulation in cHL, including CTLA-4, LAG-3, TIM-3, and TIGIT [75,115–117].

Together, the spatial distribution of PD-L1–positive HRS cells, PD-L1–expressing TAMs, and PD-1–expressing lymphocytes, including cytotoxic CD8^{+} T cells, highlights the central role of the PD-1/PD-L1 pathway in cHL [82,113]. This organization is thought to create a synergistic immunosuppressive niche that further facilitates tumor immune evasion.

This spatially organized, PD-1/PD-L1–driven immunosuppression provides the rationale for therapeutic PD-1 blockade in cHL. Nivolumab disrupts PD-1–mediated inhibitory signaling and thereby restores T-cell function, enhancing TCR signaling, cytokine production, and the cytotoxic activity of $CD8^+$ T cells within the tumor microenvironment.

1.9 Motivation and Objectives

Although modern therapies, including combination chemotherapy and immune checkpoint inhibitors, have markedly improved outcomes in cHL, a subset of patients continue to experience refractory disease. This persistence highlights the unique immune-privileged niche of HRS cells. Understanding the specific mechanisms that suppress cytotoxic immunity in this disease therefore remains a critical unresolved question**.**

Loss of MHC class I through genetic alterations (e.g., *B2M* inactivation) is a well-characterized escape mechanism [30]. Yet a substantial fraction of HRS cells retain MHC class I, and $CD8^+$ T cells are often present in their vicinity, implying that additional checkpoint-mediated pathways constrain cytotoxic function even when antigen presentation is preserved [82,86]. The PD-1/PD-L1 axis has emerged as a central immune checkpoint in this context. Although PD-1 blockade (e.g., nivolumab) shows high clinical efficacy in cHL, the precise contribution of PD-1/PD-L1 interactions to $CD8^+$ T cell inhibition in MHC class I–intact HRS cells remains incompletely understood.

Beyond tumor-intrinsic mechanisms, the cHL microenvironment is enriched with $PD\text{-}L1^+$ tumor-associated macrophages (TAMs) [82,113] that are spatially organized near $CD8^+$ T cells, suggesting that macrophages may serve as checkpoint partners sustaining local immune suppression. However, direct evidence that TAMs functionally inhibit antigen-specific $CD8^+$ T cell activity via PD-1/PD-L1 interactions in situ remains limited, and the extent to which PD-1 blockade can reverse this macrophage-mediated inhibition has not been systematically defined. In parallel, whether long-term effects of sustained PD-L1 signaling provide autonomous survival cues to HRS cells remains unclear.

TAMs in cHL frequently display M2-like phenotype, and yet the mechanisms driving their polarization—and how such macrophages, in turn, regulate $CD8^+$ T-cell effector function—remain not fully elucidated. Emerging evidence suggests that PD-1/PD-L1 signaling functions across distinct immune cell populations in cHL, involving

both MHC-I–intact HRS cells and PD-L1$^+$ macrophages. However, the relative contributions of these populations to CD8$^+$ T-cell suppression, and the extent to which PD-1 blockade can reverse these effects, are not fully defined.

This thesis aims to define how the PD-1/PD-L1 axis regulates CD8$^+$ T-cell suppression, macrophage-mediated regulation, and its effects on HRS cell survival in cHL. To achieve this, a controlled experimental model is required to dissect the individual contributions of HRS cells, macrophages, and CD8$^+$ T cells to immune evasion.

Specifically, it will:

1. Establish an engineered antigen-specific co-culture model incorporating HRS cells, macrophages, and CD8$^+$ T cells. While some components of such systems have been used previously, this integrated configuration has not been applied to interrogate PD-1/PD-L1–dependent suppression in cHL and will provide a controlled framework to dissect the individual contributions of each cell type.
2. Determine whether MHC-I–intact HRS cells suppress CD8$^+$ T cells via PD-1/PD-L1 and test the reversibility of this suppression with nivolumab.
3. Investigate how TAMs suppress CD8$^+$ T cell activity through PD-1/PD-L1 interactions and evaluate the extent to which PD-1 blockade can reverse this inhibition.
4. Evaluate whether sustained PD-1/PD-L1 engagement delivers reverse signals to HRS cells that affect survival/proliferation.
5. Establish how HRS-derived soluble factors influence TAM polarization and contribute to the development of an immunoregulatory phenotype that constrains CD8$^+$ T cell function.

By dissecting tumor-intrinsic (HRS/CD8) and microenvironmental (TAM/CD8) checkpoint interactions, establishing an integrated experimental model, and testing their pharmacologic reversibility, this work seeks to clarify why PD-1 blockade succeeds in cHL and to identify complementary targets (e.g., macrophage markers) that could enhance CD8$^+$ T-cell immunity. To achieve these aims, the thesis combines mechanistic co-cultures, proximity ligation assays (PLA) integrated with multiplex immunofluorescence (mIF) for spatial validation in formalinfixed, paraffin-embedded (FFPE) cHL tissue, and transcriptomic profiling of tumor-educated macrophages, thereby linking cellular mechanisms to tissue context.

2 Materials and Methods

This chapter describes the materials and experimental approaches used to investigate the interactions between engineered human primary $CD8^+$ T cells, NY-ESO-1-expressing HRS cells, and macrophages. The generation and expansion of T cells expressing an HLA-A*02-restricted anti-NY-ESO-1 TCR are detailed, along with the generation of NY-ESO-1-expressing HRS cells and gene-edited variants. Methods for differentiating and polarizing macrophages to express NY-ESO-1 are also outlined, enabling functional studies. RNA-seq–based transcriptional profiling of macrophages polarized with HRS cells conditioned media is also included. A series of co-culture assays were performed to assess T cell cytotoxicity, activation, and degranulation, both with and without immune checkpoint inhibition. Finally, proximity ligation assays (PLA) combined with multiplex immunofluorescence (mIF) were conducted on cHL tissue sections to visualize PD-1/PD-L1 interactions and identify the involved cell populations using confocal microscopy.

The materials section that follows lists all reagents, biological samples, equipment and other key components used throughout this study.

2.1 Experimental Materials and Resources

Table 1. Commercial reagents used in this study

Reagent	Supplier	Catalog Number
7-AAD Viability Staining Solution	BioLegend	420404
AIM-V Medium	Gibco	A3830801
Alexa Fluor 488 tyramide reagent	Invitrogen	B40953
Alexa Fluor 568 tyramide reagent	Invitrogen	B40956
Alexa Fluor 647 tyramide reagent	Invitrogen	B40958
Antibody Diluent with Background Reducing Components	DAKO	S3022
Blasticidin	InvivoGen	Ant-bI-05
Brilliant Violet 421 Annexin V	BioLegend	640924
BSA (Bovine Serum Albumin)	Sigma-Aldrich	7906-100G
CellTracker Deep Red Dye	Invitrogen	C34565
Cytofix/Cytoperm™ Fixation and Permeabilization Solution	BD Biosciences	554722

CytoFLEX Daily QC Fluorospheres	Beckman Coulter	B53230
DMEM	Capricorn	DMEM-HA
DNase I, Bovine Pancreas	Sigma-Aldrich	260913-10MU
Doxycycline Hydrochloride	Sigma-Aldrich	D3447-500MG
DPBS	Gibco	14190144
FBS	Gibco	10270106
FcR Blocking Reagent, human	Miltenyi Biotec	130-059-901
GolgiStop	BD Biosciences	554724
L-Glutamine (200 mM)	Thermo Fisher Scientific	25030081
Lenti -X Concentrator	Takara	631232
Lipopolysaccharides from Escherichia coli O55:B5	Sigma-Aldrich	L4005-100MG
Lymphoprep	STEMCELL Technologies	07811
Lymphoprep	Axis-shield	1114544
Lysing Buffer	BD Biosciences	555899
Macrophage-SFM (1X)	Gibco	12065074
NaCl	Carl Roth	3957.1
Opti-MEM™ I	Gibco	11058021
Penicillin- Streptomycin- Glutamine (100x)	Gibco	10378016
Penicillin/Streptomycin (100x)	Cegrogen	P0100-790
Perm/Wash buffer	BD Biosciences	554723
Prolong Diamond Antifade Mountant	Invitrogen	P36961
Puromycin	Sigma-Aldrich	P7255-25MG
Recombinant Human GM-CSF Protein	ImmunoTools	11343125
Recombinant Human IFN-gamma Protein	R&D systems	285-IF-100
Recombinant Human Inerleukin-2 (IL-2)	ImmunoTools	11340027
Recombinant Human Interleukin-4 (rh IL-4)	ImmunoTools	11340045
Recombinant Human M-CSF, research grade	ImmunoTools	11343115
Recovery™ Cell Culture Freezing Medium	Gibco	12648010
RetroNectin® Recombinant Human Fibronectin Fragment	Takara	T100A
RotI®Histofix, 10L	Carl Roth	2213.1
RPMI 1640	Capricorn	RPMI-A
Spectral DAPI	Akoya Biosciences	FP1490
SuperBoost Goat anti-Mouse Poly HRP	Invitrogen	B40961
SuperBoost Goat anti-Rabbit Poly HRP	invitrogen	B40962
Tag-it Violet Proliferation and Cell Tracking Dye	BioLegend	425101
TransIT-293	Mirus	MIR 2706

Tris base	Carl Roth	4855.2
Tris-HCL	Carl Roth	9090.3
Trypan Blue Stain (0.4%)	Gibco	15250061
TrypLE Express Enzyme (1X)	Thermo Fisher Scientific	12604013
Trypsin EDTA (0.05%) in DPBS (1x)	Cegrogen	N0100-720
Tween® 20	Carl Roth	9127.2
ULTRA Cell Conditioning Solution (ULTRA CC2)	Ventana-Roche	950-223
UltraPure 0.5M EDTA	Invitrogen	15575038

Table 2. Commercial kits and assay systems used in this study

Kits and Assay systems	**Supplier**	**Catalog Number**
ALEXA Fluor 488 Tyramide Super Boost Kit goat anti-mouse IgG	Invitrogen	B40912
ALEXA Fluor 488 Tyramide Super Boost Kit goat anti-rabbit IgG	Invitrogen	B40922
Amax Human Macrophage Nucleofector Kit	Lonza	VPA-1008
BOND™ Polymer Refine Detection Kit	Leica Biosystems	DS9800
CD14 MicroBeads, human	Miltenyi Biotec	130-050-201
CD56 MicroBeads, human	Miltenyi Biotec	130-050-401
CD8 MicroBeads REALease, human	Miltenyi Biotec	130-117-036
Duolink In Situ Detection Reagents Red	Sigma-Aldrich	DUO92008-100RXN
Duolink In Situ PLA Probe Anti- Mouse Minus	Sigma-Aldrich	DUO92004-100RXN
Duolink In Situ PLA Probe Anti- Mouse Plus	Sigma-Aldrich	DUO92001-100RXN
Duolink In Situ PLA Probe Anti-Rabbit Minus	Sigma-Aldrich	DUO92005-100RXN
Duolink In Situ PLA Probe Anti-Rabbit Plus	Sigma-Aldrich	DUO92002-100RXN
LNGFR MicroBeads, MACSelect	Miltenyi Biotec	130-091-330
PD-1/PD-L1 Blockade Bioassay	Promega	J1250
QuantSeq 3'mRNA-seq Library Pre Kit FWD with UDI12 nt Set A1	Lexogen	191.96
RNeasy Plus Mini Kit	QIAGEN	74136
VenorGem Advance	MB minera biolabs	11-7024

Table 3. Cell culture media and buffers used in this study

Description	Composition
D10 medium	DMEM, 10% FBS, 2 mM, L-glutamine, 1% penicillin-streptomycin
Complete RPMI	RPMI, 20% FBS, 2 mM L-glutamine, 1% penicillin-streptomycin
AIM-V Medium	AIM-V, 10% FBS, 2 mM L-glutamine 1% penicillin-streptomycin
FACS staining buffer	DPBS, 2% FBS, 5 mM EDTA
PFA	4% paraformaldehyde (PFA)
MACS buffer (version 1)	PBS, 0.5% BSA, 2 mM EDTA, pH 7.2
MACS buffer (version 2)	PBS, 0.5% BSA, 5 mM EDTA, pH 7.2
Macrophage differentiation medium	RPMI, 10% FBS, 50 ng/ml M-CSF (or GM-CSF for M1), 2 mM L-glutamine, 100 U/ml penicillin, 100 µg/ml streptomycin
M1 macrophage polarization medium (complete)	RPMI, 10% FBS, 2 mM L-glutamine, 100 U/ml penicillin, 100 µg/ml streptomycin, 50 ng/ml GM-CSF, 100 ng/ml LPS, 25 ng/ml IFN-γ
M2 macrophage polarization medium (complete)	RPMI, 10% FBS, 2 mM L-glutamine, 100 U/ml penicillin, 100 µg/ml streptomycin, 50 ng/ml M-CSF, 20 ng/ml IL-4
Macrophage culture medium	Macrophage-SFM, 10% FBS, 2 mM glutamine
Cell culture freezing medium	RPMI, 20% FBS, 10% DMSO

Table 4. Buffers used in PLA in this study

Description	Composition
Duolink PLA In Situ Wash Buffer A	0.01 M Tris, 0.15 M NaCl, 0.05% Tween 20, pH 7.4
Duolink PLA In Situ Wash Buffer B	0.2 M Tris, 0.1 M NaCl, pH 7.5
0.01x Wash Buffer B	Wash buffer B diluted 1:100 in Millipore H2O

Table 5. Fluorochrome-conjugated antibodies used for flow cytometry and cell sorting

Antibodies*	Supplier	Catalog Number	Clone	Working Dilution
CD3-FITC	BioLegend	344804	SK7	1:500
CD4-PE	BioLegend	344605	SK3	1:500
CD8a-APC	BioLegend	301049	RPA-T8	1:250
CD8-PerCP	BioLegend	344707	SK1	1:500

CD56-PE	BioLegend	318305	HCD56	1:500
CD271 (NGFR)-APC	BioLegend	345108	ME20.4	1:500
CD271 (NGFR)-PE	BioLegend	345106	ME20.4	1:250
CD279 (PD-1)-PE	Invitrogen	12-2799-42	J105	1:100
CD137-PE	BD Pharmingen	555956	4B4-1	1:10
CD14-PE	Biolegend	367104	63D3	1:500
Active Caspase 3-PE	BD Pharmingen	570183	C92-605.rMAb	1:25
CD107a (LAMP-1)-APC	BioLegend	328608	H4A3	1:20
CD80-APC	BioLegend	305220	2D10	1:500
CD86-APC	BioLegend	374207	BU63	1:500
CD274 (PD-L1)- Alexa Fluor 647	Cell Signaling	41726S	D8TAX	1:500
HLA-A2-APC	BD Pharmingen	561341	BB7.2	1:20
NY-ESO-1-PE	Cell Signaling	65699S	D1Q2U	1:50
CD163-PerCP	BioLegend	333625	GHI/61	1:500
CD197-PE	BioLegend	353203	G043H7	1:500
CD206-APC	BioLegend	321109	15-2	1:500
HLA-DR, DP, DQ-APC	BioLegend	361713	Tü39	1:500
HLA-A, B, C -APC	BioLegend	311410	W6/32	1:20

*All antibodies listed here are anti-human

Table 6. Isotype control antibodies used in flow cytometry and magnetic activated cell sorting (MACS)

Isotype Control Antibody	Supplier	Catalog Number	Clone
Mouse IgG1, κ isotype - FITC	BioLegend	400107	MOPC-21
Mouse IgG1, κ isotype - APC	BioLegend	400122	MOPC-21
Mouse IgG1, κ isotype - PE	BioLegend	400112	MOPC-21
Mouse IgG1, κ isotype - PerCP	BioLegend	400148	MOPC-21
Mouse IgG1, κ isotype - PE	BD Pharmingen	555749	MOPC-21
Mouse IgG2b, κ isotype - APC	BD Bioscience	555745	27-35
Rabbit IgG, isotype - Alexa 647	Cell Signaling	2985S	DA1E
Rabbit IgG, isotype - PE	Cell Signaling	5742S	DA1E
Human IgG4 Isotype	BioLegend	403702	QA16A15
Human IgG1 Isotype	BioLegend	403502	QA16A12
MACSelect Control Antibody-FITC	Milteny Biotec	130-090-326	Polyclonal

Table 7. Antibodies used for cell culture in this study

Antibodies	Supplier	Catalog Number	Clone
Anti-PD-1 antibody (Nivolumab)	Selleckchem	A2002	N/A
Anti-PD-L1 antibody (Avelumab)	Selleckchem	A2015	N/A
Anti-human CD3 mouse antibody (Purifed NA/LE)	BD Bioscience	566685	OKT3

Table 8. Antibodies used for IHC, PLA and mIF in this study

Antibodies	Supplier	Catalog Number	Clone	Dilution	Applied
PD-1	Cell Signaling	43248S	EH33	1:50	PLA
PD-L1	Cell Signaling	15165S	E1J2J	1:100	PLA
CD8	Agilent DAKO	M7103	CD8/144B	1:100	IF, IHC
CD68	Agilent DAKO	M0876	PG-M1	1:250	IF, IHC
CD3	Agilent DAKO	M7254	F7.2.38	1:250	IF, IHC
CD30	Agilent DAKO	M075101-2	Ber-H2	1:100-PLA+IF 1:250-IHC	IF, IHC
CD30	Leica Bioscience	NCL-L-CD30-591	JCM182	1:100-IHC	IF, IHC
CD163	Leica Bioscience	NCL-L-CD163	10D6	1:100-PLA+IF 1:50-IHC	IF, IHC
CD4	Abcam	ab133616	EPR6855	1:200	IF, IHC

Table 9. Commercial cell lines used in this study

Cell Lines	Supplier	Catalog Number
HEK293FT	Thermo Fisher Scientific	R70007
L1236	DAMZ	ACC530
PG13	ATCC	CRL-10686
Phoenix Eco cell	ATCC	CRL-3214

Table 10. Other cell lines and biological samples used in this study

Cell lines and tissue	Source	Description / Notes

Primary human T cells	PBMCs* from healthy donors	Provided by Blood Donation Center, UKGM
Primary human macrophages	PBMCs* from healthy donors	Provided by Blood Donation Center, UKGM
FFPE** tissue of cHL	Institute of Pathology JLU Gießen (clinical)	cHL (Classical Hodgkin Lymphoma) tissue

* PBMCs – peripheral blood mononuclear cells; ** FFPE - Formalin-Fixed, Paraffin-Embedded

Table 11. Plasmids used in this study

Plasmid Name	**Supplier/source**	**Catalog Number/ reference**
TCR-alpha-p2a-TCR-beta-ihres-NGFR-MSCV-BCL6-t-2A-BCL2	GeneScript	SC0001
pcDNA3.1-NY-ESO-1-p2a-eGFP	GeneScript	SC0001
PDCD1-Ptwist-Lenti SFFV Puro WPRE	TWIST Bioscience	107452
pLenti-guide-BFP2	Addgene	99374
pLenti-guide-dsRed	Addgene	128055
pLenti-guide-GFP	Schmitz lab (generated in house)	N/A
pLenti-guide-Hygro-mTagBFP2	Addgene	99374
pLVX-TRE3G	Clontech Laboratories	N/A
pLVX-Tre3G-NY-ESO-1-BSR	Constructed in-house	See Section 3.2.1
pmaxGFP	Lonza	N/A
pMD2.G	Addgene	12259
psPax2	Addgene	12260

Table 13. sgRNA sequences, target genes, and corresponding vectors used in this study

sgRNA ID	**Target Gene**	**Target Sequence (5′→3′)**	**Vector Used**
AAVS1	PPP1R12C	GGGGCCACTAGGGACAGGAT	pLenti-Guide-DsRed

sgB2M-44711569	Beta-2-Microglobulin	GAGTAGCGCGAGCACAGCTA	pLenti-Guide-GFP
sgCD274-5462888	CD274 (PD-L1)	ACATGTCAGTTCATGTTCAG	pLenti-Guide DsRed
sgCD274-5462933	CD274 (PD-L1)	ACTGCTTGTCCAGATGACTT	pLenti-Guide-DsRed

Table 14. Plastic ware and consumables used in this study

Item	Supplier	Catalog Number
15ml conical centrifuge tubes	Falcon	352096
50ml conical centrifuge tube	Greiner Bio-One	227261
96 Well Round (U) Bottom Plate, TC Surface	Thermo Fisher Scientific	163320
CellTrics 30µm sterile	Sysmex Partec	04-004-2326
Cover glasses	Marienfeld superior	102192
CryoPure tubes, 2 ml, QuickSeal screw cap	Sarstedt	72.380.992
Disposal bags	Carl Roth	E706.1
Filter tip PP, premium surface 0-100µl rack pack	Nerb Plus	06-642-5300
Filter tip PP, premium surface 0-200µl rack pack	Nerb Plus	06-662-5300
Filter tip PP, premium surface 100-1000µl rack pack	Nerb Plus	06-695-5300
LS Colums	Miltenyi Biotec	130-042-401
Millex-HV Syringe Filter Unit, 0.45 µm, PVDF, 33 mm, gamma sterilized	Merckmillipore	SLHV033RS
Millipore® Stericup® Quick Release Vacuum Filtration System	Merck	S2HVU05RE
Non-tissue culture-treated 24- well plates	Falcon	351147
Non-tissue culture-treated 6- well plates	Thermo Scientific	150239
Omnifix® Luer Solo, Single-use 3-piece syringe	B. Braun	4616103V
Parafilm® M Sealing Film	Merck	HS234526C
S-Monovette® Lithium heparin, 7.5 ml tube	Sarstedt	01-1604
SafeSeal SurPhob Spitzen	Biozym	VT0200
Sterile Plastic Pasteur Pipettes	Cole-Parmer	439511
SuperFrost Plus adhesion Microscope slides	Epredia	J1800AMNZ
Tissue culture dish, 100x20mm surface	Sarstedt	3.3902.300
Tissue culture flask, T-175, surface	Greiner Bio-One	660175
Tissue culture flask, T-25, surface	Sarstedt	83.3910.002

Tissue culture flask, T-75, surface	Sarstedt	83.3911.002
Tissue culture treated 12 well plate	CytoOne	CC7682-7512
Tissue culture treated 24 well plate	CytoOne	CC7682-7524
Tissue culture treated 6 well plate	CytoOne	CC7682-7506
Transfer pipette, 3.5 ml	Sarstedt	86.1172
Tube, 5 ml, (LxØ): 75 x 12 mm, PP	Sarstedt	55.1578
Tube, 5 ml, (LxØ): 75 x 12 mm, PS	Sarstedt	55.1579.002

Table 15. Laboratory equipment and devices used in this study

Devices	**Supplier**
12-channel microlitre pipette (Eppendorf Research® plus, 30–300 µl)	Eppendorf, Hamburg, Germany
CytoFLEX S Flow Cytometer	Backman Coulter, Brea, USA
FACSMelody Cell Sorter	Becton Dickinson, Franklin Lakes, USA
Heidolph Unimax 1010 DT Platform Shaker	Heidolph, Schwabach, Germany
Heracell™ 150i CO_2 incubator	Thermo Fisher Scientific, Dreieich, Germany
Heraeus Megafuge 16 Centrifuge	Thermo Fisher Scientific, Dreieich, Germany
Heraeus Multifuge X3 FR	Thermo Fisher Scientific, Dreieich, Germany
HERAfreeze™ HFU T Series ultra-low temperature freezer	Thermo Fisher Scientific, Waltham, USA
Leica THUNDER Imager DM i8	Leica Microsystems, Wetzlar, Germany
LS4800 Series Liquid Nitrogen Refrigerator	Worthington Industries, Columbus, USA
LSM 800 Confocal Laser Scanning Microscope	Carl Zeiss, Oberkochen, Germany
MEMMERT WNE 7 water bath, 7L	Memmert, Scwabach, Germany
MSC-Advantage™ Class II Biological Safety Cabinets	Thermo Fisher Scientific, Waltham, USE
NextSeq 500/550 Sequencing System	Illumina, San Diego, USA
Nikon Eclipse TS2-FL inverted microscope	Nikon Corporation, Tokyo, Japan
Nucleofector 2b device	Lonza, Basel, Switzerland
Pannoramic SCAN II slide scanner	3DHistech, Budapest, Hungary
Siemens iQ500 Freestanding Fridge KS36VAXEP	Siemens AG, Munich, Germany
Single-channel microlitre pipette (Eppendorf Research® plus,100-1000 µl: 20-200 µl: 10-100 µl: 2-20µl: 0.5-10 µL:)	Eppendorf, Hamburg, Germany
Test Tube shaker; Vortex mixer uniTEXER1	LLG Labware, Chicago, USA

Test tube shakers Genie® Vortex Mixer Model	Scientific Industries, Bohemia, USA
Vacusafe	INTEGRA Bioscience, Zizers, Switzerland
Water bath WBT 1 series round bath opening	Carl Roth, Karlsruhe, Germany
Zeiss Primovert microscope	Carl Zeiss, Oberkochen, Germany

Table 16. Software and digital tools used in this study

Software Name	Version	Provider/Developer	Purpose
FlowJo	10.10	BD Biosciences	Flow cytometry data analysis
BioRender	Web-based	BioRender	Scientific illustration creation
GraphPad Prism	7.05	GraphPad software	Data visualization, statistical testing
ImageJ/Fiji	2.3.0/Fiji 1.53	NIH/Fiji Community	Image analysis
Pannoramic Viewer	2.2.0	3DHISTECH Ltd	Viewing and annotating scanned digital slides
SnapGene	6.0	Dotmatics	DAN seq analysis and cloning maps
ZEN (Blue Edition)	2.6	Carl Zeiss	Microscope image and analysis

Table 17. List of figures used in this study

Figure Number and Name
1- Cellular composition of classical Hodgkin lymphoma (cHL)
2- The PD-1/PD-L1 immune checkpoint pathway and its therapeutic blockade
3- Schematic workflow for generation of anti-NY-ESO-1 $CD8^+$ T cells
4 -Schematic representation of the generation of NY-ESO-1-expressing macrophages
5- Workflow of the PLA to detect PD-1/PD-L1 interactions
6- Schematic illustration of the TSA system
7- Generation of monoclonal PG13 retroviral producer clones
8- Validation of retroviral transduction and NGFR-based enrichment of NY-ESO-1-reactive TCR T cells
9- Validation of CD56 depletion and $CD8^+$ T-cell enrichment during generation of NY-ESO-1–reactive TCR T cells

10- Antigen-dependent induction of PD-1 expression in NY-ESO-1–reactive $CD8^+$ T cells following co-culture with NY-ESO-1^+ L1236 HRS cells

11- Validation of endogenous HLA A2 expression and generation of MHC I–deficient B2M knockout (KO) L1236 cells by flow cytometry Generation of monoclonal PG13 retroviral producer clones

12- Validation of NY-ESO-1 transduction in L1236 cells by flow cytometry

13- Validation of endogenous PD-L1expression and generation of PD-L1–knockout (KO) L1236 cells by flow cytometry

14-Validation of endogenous PD-1 expression and PD-1 transfection in HEK293FT cells by flow cytometry

15-Validation of M1 and M2 macrophage polarization by light microscopy

16-Validation of NY-ESO-1 expression in M2 macrophages by fluorescence microscopy

17-Validation of antibodies by IHC

18-Validation of PD-1 and PD-L1 antibodies for Brightfield PLA

19-Validation of PD-1/PD-L1 interaction by Fluorescent PLA

20-Validation of CD163 and CD8 antibodies in single and combined IF staining

21-Validation of CD68, CD3, and CD30 antibodies in single and combined IF staining

22- PD-1/PD-L1 blockade restores T-cell activation in an MHC-I–dependent manner in co-cultures with NY-ESO-1–expressing HRS cells

23- Representative flow-cytometry plots showing that PD-1 blockade enhances T-cell activation in MHC-I^+ co-cultures but not in MHC-I–deficient targets

24- PD-1/PD-L1 blockade enhances T-cell cytotoxicity and induces apoptosis of HRS cells in an MHC-I–dependent manner

25- PD-L1 knockout enhances T-cell activation in an MHC-I–dependent manner

26- L1236-conditioned medium enhance $CD8^+$ T cell activation in M2 macrophage co-cultures

27- PD-1 blockade tends to enhance $CD8^+$ T-cell activation in co-cultures with M2 macrophages and MHC-I–deficient HRS cells

28- PCA reveals that macrophages exposed to Hodgkin lymphoma–conditioned media cluster with M2-polarized cells, indicating a similar transcriptional profile

2.2 Generation of CD8$^+$ T cells expressing anti-NY-ESO-1 TCR

This section describes the generation of human primary CD8$^+$ T cells engineered to express T cell receptors (TCRs) recognizing the HLA-A*02-restricted melanoma antigen NY-ESO-1 [118] (see Figure 3). The TCR-modified T cells were produced to investigate their interaction with NY-ESO-1-expressing HRS cells or macrophages in downstream functional assays. First, the transfection of Phoenix-ECO cells [119] was performed (Section 2.2.1), followed by the production of retroviral supernatant using PG13 packaging cells [120–122] (Sections 2.2.2–2.2.4). Next, the isolation of PBMCs for T cell generation was performed (Appendix A1), followed by the transduction of primary human T cells to express the anti-NY-ESO-1 TCR, and their subsequent rapid expansion (Sections 2.2.5–2.2.7).

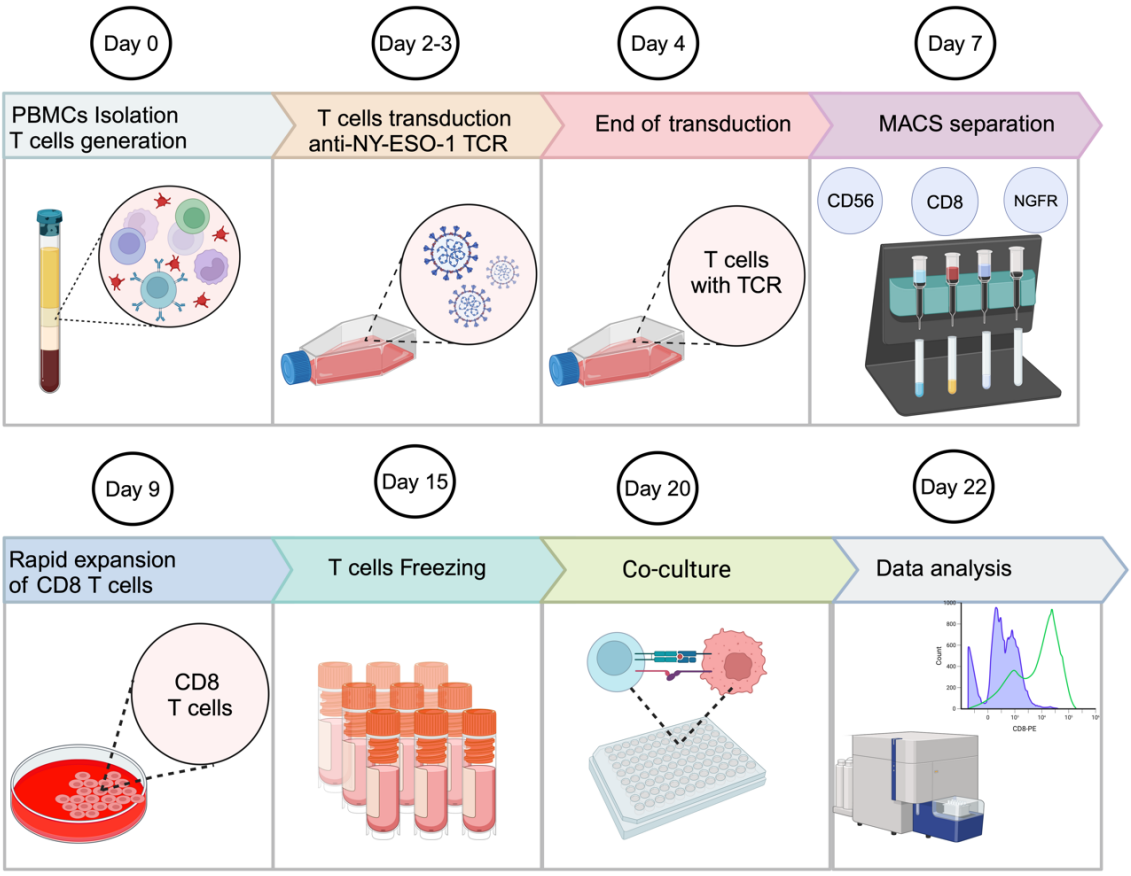

Figure 3. Schematic workflow for generation of anti-NY-ESO-1 CD8$^+$ T cells. PBMCs were first isolated and cultured. Subsequently, T cells were transduced using retroviral supernatant produced from PG13 cells. CD8$^+$ T cells expressing the anti-NY-ESO-1 TCR were then selected using MACS. Following rapid expansion, the cells were cryopreserved and later used for co-culture experiments. Data acquisition was performed using a flow cytometer, and data were analyzed with FlowJo software (Created using BioRender).

2.2.1 Transfection of Phoenix-ECO cells with a retroviral vector

Virus supernatant for retroviral transduction of T cells was produced using the human 293T-derived Phoenix-Eco and murine PG13 γ-retroviral packaging cell lines (ecotropic and gibbon ape leukemia virus (GaLV) envelopes, respectively) [119–122]. Phoenix Eco cells were first transfected with a retroviral vector encoding a TCR specific for the HLA-A*02-restricted melanoma antigen NY-ESO-1[118]. Viral supernatant collected from Phoenix Eco cells, was then used to transduce PG13 cells, generating stable retroviral producer cell clones for subsequent T cell transduction.

The following procedure was used to generate the virus-containing supernatant from Phoenix-Eco cells. Phoenix-ECO cells were cultured in D10 medium. One day before transfection, Phoenix-ECO cells were seeded in a 10 cm tissue culture dish at 60% confluency. Prior to transfection, supernatant was replaced with fresh D10 medium (8ml). Cells were transfected using TransIT-293 transfection reagent according to manufacturer's instructions [123]. For each dish, 20 µl serum-free Opti-MEM was mixed with 4µg MSCV-TCR-LNGFR plasmid. 18 µl TransIT-293 transfection reagent was diluted with 980µl Opti-MEM, incubated for 5 min at room temperature (RT), and combined with the mixture of Opti-MEM and plasmid. This transfection mixture (1ml) was incubated for 20 min at RT and then added dropwise to the cells. The tissue culture dish was gently rocked back and forth and from side to side to evenly distribute the transfection mixture. Then the plates were incubated at 37°C in a 5% CO_2 incubator. Virus-containing supernatant was collected into a new falcon tube 48h post-transfection. Cell debris was removed by centrifugation at 500xg for 10 min, followed by filtration of the supernatant through a 0.45µm low-protein binding membrane (Millipore Steriflip HV/PVDF). Phoenix-ECO cells were transfected freshly for each round of transduction of PG13 cells, ensuring the use of fresh virus-containing supernatant to achieve the highest retroviral titers through immediate infection of PG13 cells.

2.2.2 PG13 cell transduction for anti-NY-ESO-1 TCR vector production

A PG13 retroviral packaging cell clone was generated following the procedure previously described [124–126]. PG13 cells were cultured in T-75 tissue culture flask supplemented with D10 medium. The day before transduction, non-tissue culture-treated 6-well plates were coated with 20µg/ml recombinant human fibronectin fragment (RetroNectin™) by following to the manufacturer's instructions [127]. Before coating, RetroNectin™

solution (20 µg/ml) was prepared by diluting in sterile PBS. Then, 2 ml of that solution was transferred into each well of non-tissue culture-treated 6-well plates. The plates were covered with paraffin film and incubated at 4°C overnight. On the following day, before loading with retroviral supernatant, the RetroNectin™ solution was removed, and 2 ml of D10 medium was added. The plates were then incubated for 30 min at RT. 4ml filtered, fresh retroviral supernatant (generated in Section 2.1.1) was added to each well of RetroNectin™ coated plate and centrifuged (2000xg, 32°C, 3h). Simultaneously, PG13 cells were detached from the T-75 tissue culture flask by trypsinization and were counted using a hemocytometer. After centrifugation, the retroviral supernatant was removed and 5×10^5 PG13 cells were added to each well, followed by centrifugation (1000 × g, 10 min, 32°C). After centrifugation, plates were returned to the 37°C, 5% CO^2 incubator. After 20 h of incubation, the transduction was repeated. New non-tissue culture-treated 6-well plates were coated with RetroNectin™ in the same manner as in the first round of transduction. Freshly prepared retroviral supernatant from Phoenix-ECO cells (Section 2.2.1) was added to each well, and the plates were centrifuged identically as in the first round of transduction. The PG13 cells from the first round of transduction were detached from tissue culture dish by trypsinization (incubating with 1m trypsin for 2min). Then, cells were transferred into a new 15 ml Falcon tube containing D10 medium and centrifuged at 500 x g for 5 min. After centrifugation, the supernatant was removed, and the cell pellet was resuspended in 4 ml of D10 medium. From that solution 2ml was transferred into new 15ml falcon tube containing 2ml fresh D10 medium (dilution 1:2) and then transferred onto the new retrovirus-coated plates and the plates were centrifuged at 1000×g for 10 min at 32°C. 20h post-transduction, the retroviral supernatant was replaced with D10 medium (or if needed, PG13 cells were transferred into a T75 tissue culture flask) and incubated for 48 h. To assess transduction efficacy, the surface expression of the NGFR gene was measured by flow cytometer. The PG13 producer cell line was passaged every three days, aliquoted, and frozen at -80°C. PG13 producer cell clones were generated by limiting dilution cloning see Section 2.2.3.

2.2.3 Generation of monoclonal PG13 cells via limiting dilution cloning

Monoclonal PG13 retroviral producer cell lines were generated by using limiting dilution from the pool of anti-NY-ESO-1 TCR expressing PG13 cells. Transducing cells with retrovirus lead to a heterogeneous polyclonal population, characterized by varying

numbers of integration events and sites of pro-viral integration across cells. Over time, selective pressure on this heterogeneous cell pool may lead to reduced transgene expression, as lower-expressing clones gradually dominate in the polyclonal cell population. Using limiting dilution to generate a monoclonal cell line increases the likelihood of maintaining stable transgene expression within that cell populations. Pool of anti-NY-ESO1 TCR expressing PG13 cells were washed with PBS and then detached from tissue culture flask by trypsinization. Cells were washed and resuspended with fresh D10 medium any cell clumps were break up into individual cells by passing several times through a serological pipet. Relatively diluted cell solution ($<10^6$cells/ml) was prepared before cells were counted by hemocytometer. The homogenized cell solution underwent several serial dilutions, and cells were subsequently transferred to 10 ml of fresh D10 medium to achieve concentrations of 10,000 cells/ml, 1,000 cells/ml, and 100 cells/ml, respectively. A higher volume of homogenized cell solution was transferred in each step to ensure greater accuracy. Finally, a solution with a concentration of 1.5 cells/ml was prepared from the 100 cells/ml dilution by transferring the cells into fresh 43 ml of D10 medium. This 1.5 cells/ml solution was used to seed the 96-well plate. 200µl of 1.5 cells/ml solution was transferred into each well of a 96 well plate. By this process, the plate was seeded at an average density of 0.5 cells/well. Seeding an average of 0.5 cells/well ensures that some wells receive a single cell, while minimizing the likelihood that any well receives more than one cell. In order to facilitate microscope focusing during the subsequent scanning of the plate for individual cells, approximately 1000 cells were seeded into one of the corner wells of the 96-well plates. Incubate plates at 37°C incubator for 7-14 days. After approximately 7 days, the plates were examined under a microscope to assess cell growth (if no colonies were observed, the incubation was continued). The entire plate was examined under a microscope, and the wells where cell growth was observed, were marked. At that time, the cells appeared as colonies in the well. If there was more than single cell seeded in a well more than one colony was observed. Wells with more than a single colony were considered to not contain a monoclonal population and were therefore discarded. The cells were expanded, and before reaching over-confluency, they were trypsinized and carefully transferred into 24-well plates without any cross-contamination between independent monoclonal cell lines. After expanding the monoclonal PG13 cell lines, the surface expression of the targeted gene LNGFR was measured by flow cytometry. The monoclonal cell lines exhibiting the highest transgene

expression were selected for virus production as described in Section 2.2.4 with some of them being aliquoted and frozen at -80°C.

2.2.4 Production of retroviral supernatant from PG13 cells

Human primary T cells were transduced with anti-NY-ESO-1 HLA-A2-restricted TCR following the procedure previously described [124–126], with the following modifications. The day before isolating PBMCs for T cell generation, monoclonal PG13 retroviral producer cell lines (clone 4C3) were seeded in 6-well plates at a density of $4x10^4$ cells/cm^2 in D10 medium (3 ml per well) on day 0. After 48h of incubation, the medium was changed with fresh D10 medium, and the cells were incubated for another 24h for virus generation. Virus-containing supernatant was collected on the day of transduction. Cell debris was removed by centrifugation at 500xg for 10 min followed by filtration of the supernatant through a 0.45µm low-protein binding membrane (Millipore Steriflip HV/PVDF). Retroviral containing virus was generated freshly for each round of T cells transduction.

2.2.5 Transduction of T cells for anti-NY-ESO-1 TCR expression

Freshly isolated PBMCs (see Appendix A for the isolation protocol) were washed with RPMI 1640 without supplements, centrifuged and the cell pellet was resuspended at a concentration of $1x10^6$ cell/ml in T-cell medium containing IL-2 (300 IU/ml) and soluble anti-CD3 antibody OKT3 (50ng/ml) for T-cell stimulation on day 1. This stimulation activates T lymphocytes within the PBMC population and leads to their preferential expansion, resulting in a T-cell–enriched culture (see Supplementary Figure S4). Primary anti-NY-ESO-1 human T cells were generated as described [125,126,128,129]. 1.5 ml of this mixture were seeded in each well of 24-well plate and incubated for 48h. On day 2, non-tissue culture-treated 6-well plates were coated with 10 µg/ml RetroNectin™ (2 ml per well), covered with paraffin film, and stored overnight at 4°C (Section 2.2.2), following manufacturer's instructions [127]. On the following day, the RetroNectin™ solution was removed, and 2 ml of T cells medium was added. The plates were then incubated for 30 minutes at RT. Retroviral supernatant from the 4C3 producer cell clone as described in Section 2.2.4 was used for transduction. After incubation, the blocking solution was aspirated from RetroNectinTM coated plates, and 4ml of retroviral supernatant (diluted 1:1 with D10 medium) was added to each well. Then the plates were

centrifuged at 2000xg for 2h at 32°C. Simultaneously, peripheral blood T lymphocytes stimulated with IL-2 and OKT3 on day 1 were collected in a 50 ml Falcon tube and centrifuged at 500xg for 5 min. The cells were resuspended at a concentration of 0.5×10^6 cells/ml in T cells medium containing 300 IU/ml of IL-2. After centrifugation, half the volume of supernatant was removed from each well of the retrovirus-coated plates, and 4 ml T cells were added to each well. The final concentration of IL-2 in each well was 300 IU/ml. After T cells were added to each well, the plates were centrifuged for 10 min at 1000×g and then incubated at 37°C overnight.

On the following day transduction was repeated. New non-tissue culture-treated 6-well plates were coated with RetroNectin™ (on day 3) and blocked in the same fashion as in the first transduction. Retroviral supernatant was added to each well and the plates were centrifuged identically as in the first transduction. T cells from first transduction were collected into new 50ml falcon tube and centrifuged for 5 min at 500xg. The cell pellet was resuspended in T cells medium, and cells were then transferred onto the new retrovirus-coated plates in the same manner as during the first transduction. Subsequently, the plates were centrifuged at 1000xg for 10 min. After a 20 h incubation, the T cells were removed from the plates and suspended in fresh T cell medium with 300 IU/mL of IL-2 at a concentration of 0.5×10^6 cells/ml and cultured at 37° and 5% CO_2 for 72 h.

After incubation, the surface expression of the target gene (LNGFR) was measured by flow cytometer with anti-CD271 (NGFR) to determine transduction efficacy. The expression of CD3, CD4, CD8 and CD56 was measured by flow cytometer with the respective antibodies listed in the Table 5.

2.2.6 Selection of $CD8^+$ T cells expressing NY-ESO-1-reactive TCR

$CD8^+$ positive T cells were isolated using CD56, CD8, and LNGFR magnetic beads sequentially, following the manufacturer's instructions [130–132]. Briefly, cells were magnetically labeled first with CD56 MiroBeads. Then the cell suspension was loaded onto MS or LS positive selection column, which was placed in the magnetic field of a MACS Separator. The magnetically labeled $CD56^+$ cells were retained within the column. The unlabeled cells (mixture of $CD8^+$ and $CD4^+$ positive T cells) run through and were collected for the further selection. Positive selection of $CD56^+$ T cells enables the generation of beads-free populations of $CD8^+$ and $CD4^+$ T cells for next selection.

Before next selection, the number and percentage of $CD4^+$ and $CD8^+$ T cells population was measured by flow cytometer using antibodies listed in the Table 5. The CD56+ T cell content in the unlabeled cell fraction is typically 0%.

Then mixture of $CD8^+$ and $CD4^+$ positive T cells (unlabeled cell fraction, after $CD56^+$ MACS separation) underwent another selection by using REAlease® CD8 MicroBead Kit [131]. Recombinantly engineered antibody fragments to label specific cell surface marker (CD8) was used in this kit. The fragments had low affinity for epitopes when functioning as monomers. However, when fragments were multimerized as a REAlease Biotin Complex (CD8-Biotin) they bind to epitopes with high avidity. Multimer or monomer state of antibody fragments can be controlled by using the REAlease method. This enabled controlled label release, whereby monomerized antibody fragments detached from the cell surface, allowing the recovery of cells free of beads and labels. Briefly, mixture of $CD8^+$ and $CD4^+$ positive T cells were labeled with REAlease CD8-Biotin Complex. Afterward, REAlease Anti-Biotin MicroBeads were introduced into the mixture and incubated at RT for 5 min to enable the binding of Anti-Biotin MicroBeads to the REAlease Biotin Complex. Then, the cell suspension was loaded onto a MS or LS Column. The magnetically labeled cells were captured and held within the column ($CD8^+$ T cells). The unlabeled $CD4^+$ T cells run through. After several washing steps, the column was removed from the magnetic field, and the target $CD8^+$ T cells were eluted using REAlease Bead Release Reagent, which simultaneously detached the MicroBeads from the cells. Finally, during the subsequent incubation with the REAlease Release Reagent, the REAlease Biotin Complex underwent monomerization and dissociated from the cell surface, resulting in $CD8^+$ T cells which are free of all labels. After incubation, isolated CD8+ T cells were centrifuged at 300xg for 7 min, and the supernatant was completely removed. Cells aliquots were fluorescently stained with anti-CD8-PerCP antibody and cell number measured using flow cytometry. The $CD8^+$ T cell content of the isolated fraction was typically >95%.

Subsequently, the $CD8^+$ T cells underwent a second positive selection using MACSelect LNGFR Microbeads, following the manufacturer's instructions [132]. The cells were incubated for 15 min at 4°C with the appropriate amount of LNGFR MicroBeads, followed by magnetic separation with LS columns, resulting in a cell population of >95% LNGFR-positive ones. After three rounds of subsequent MACS selection, $CD8^+$, LNGFR+ T cells were seeded out in T cell medium with 300 IU/ml of IL-2 at a concentration of $0.5x10^6$ cells/ml (in a 24-well plate) and incubated for 48 h until

needed for rapid expansion protocol described in Section 2.2.7. As a control for some experiments, a fraction of T cells was intentionally left untransduced. These untransduced T cells underwent only CD56 and CD8 magnetic separation and were cultured in the same manner as described above.

In experiments where the total number of transduced T cells was sufficiently high, fluorescence-activated cell sorting (FACS) was used as an alternative to MACS to obtain maximally pure NY-ESO-1–reactive $CD8^+$ T cells.

To isolate CD8+NGFR+ T cells for co-culture assays with macrophages (Section 2.5.4), T cells were sorted aseptically using CD8 and LNGFR antibodies following transduction (Section 2.2.5) and used for co-culture one day after sorting by culturing in T cell medium containing 300 IU/ml IL-2 overnight.

2.2.7 Rapid expansion of anti-NY-ESO-1 $CD8^+$ T cells

To produce a large number of transduced CD8-positive T cells recognizing the NY-ESO-1 antigen, as well as untransduced $CD8^+$ T cells (wild-type controls: only with endogenous TCR), the cells were stimulated to proliferate using a rapid expansion protocol (REP) [126,133–136]. Before REP, T cells were first cultured with OKT3 and IL-2 (Section 2.2.5). The cells underwent two rounds of transduction or were left untransduced, then underwent MACS selection as described above in Section 2.2.6. The day before REP, freshly isolated PBMCs (see Appendix A for the details) were washed with RPMI 1640 without supplements, centrifuged and the cell pellet was resuspended with 10 ml complete RPMI medium. Then PBMCs were transferred into T75 cell culture flask containing 40ml complete RPMI medium. After overnight incubation, PBMCs were transferred into T25 cell culture flask and irradiated (5000 rad) (Department of Radiation Therapy, UKGM Giessen). After irradiation, PBMCs (feeder cells) were transferred into new 50ml Falcon tube and centrifuged for 5min, at 500xg, and then resuspended in T cells medium. Then cells were counted by using flow cytometer. Ten days after the start of the cultures, transduced and untransduced (wild type) T cells only with endogenous TCR were collected into 50ml falcon tubes, were counted using flow cytometer, and resuspended in T cell medium. From this suspension, 0.5×10^6 transduced and untransduced (wild type) T cells were transferred into new T75 flasks. 50×10^6 allogeneic, irradiated feeder cells were then added (ratio of feeder cells to responding transduced or untransduced T cells was 100:1). Next, 35 ml of T cell medium were added to the cell

mixture, along with 6000 IU/ml IL-2 and 50 ng/ml OKT3. When the number of transduced T cells was high, a T175 (with 150 ml T cell medium) culture flask was used along with scaled-up reagents. The cells were cultured at 37°C with 5% CO_2. After five days, the cells were counted, resuspended at a concentration of 10-20x10^6 cells/ml in freezing medium, and frozen at -80°C for 2 days, followed by transfer to liquid nitrogen until functional experiments (Section 2.5).

2.3 Generation of NY-ESO-1-Expressing HRS cells

This section describes the methods used to generate the NY-ESO-1-expressing HRS cells, specifically the L1236 cell line, for studying its interaction with T cells. The primary goal was to express the NY-ESO-1 antigen on these cells, enabling recognition by T cell receptors engineered to specifically target NY-ESO-1. L1236 cells were routinely tested for mycoplasma contamination using the Venor®GeM advance kit, according to the manufacturer's instructions, and were confirmed to be mycoplasma-free before use. First, the production and purification of lentiviral particles for efficient transduction were performed (Section 2.3.1 and 2.3.2), followed by the generation of NY-ESO-1-expressing L1236 cells via lentiviral transduction (Section 2.3.3). Next, single guide RNA (sgRNA)-mediated lentiviral transduction to create gene knockouts in the NY-ESO-1-expressing L1236 cells were conducted (Section 2.3.4), enabling to investigate how the absence of specific immune-associated molecules impacts the interaction between these cells and T cells.

2.3.1 Vector construction

pLVX-TRE3G-NY-ESO-1-BSR was created by removing the puromycin resistance gene from the pLVX-TRE3G vector using *BfuAI/KpnI* restriction enzymes and replacing it with a synthetic Blasticidin (BSR) resistance gene. NY-ESO-1 was isolated via PCR from the pcDNA3.1+ NY-ESO-1-P2A-eGFP construct and cloned into the pLVX-TRE3G-BSR vector (digested with *BamHI*) using Gibson cloning.

The sgRNA sequences targeting *B2M, CD274, CD80, CD86,* and the *AAVS1* control were cloned into pLenti guide GFP, pLenti guide dsRed, or pLenti guide BFP2 vectors using *BsmBI*. Detailed sequences of the sgRNAs and their corresponding vectors are provided in Table 13.

2.3.2 Lentivirus production and purification

Lentiviral particles were generated by transfecting HEK293FT cells using a standard second-generation packaging system. This procedure was used for producing lentiviruses for both NY-ESO-1 overexpression and CRISPR/Cas9-mediated gene knockout experiments (see Section 3.3.3 and 3.3.4). To generate lentivirus, HEK293FT cells were cultured in D10 medium. One day before transfection, HEK293FT cells were seeded in a 10 cm tissue culture dish at 60% confluency. Cells were transfected using TransIT-293 transfection reagent according to manufacturer's instructions [123]. For each dish, 50 µl (volume was adjusted to plasmids volume) serum-free Opti-MEM was mixed with 6µg of plasmid (either overexpression construct or sgRNA vector), 4.5 µg psPax2 and 1.5 µg pMD2.G. 27 µl TransIT-293 transfection reagent was diluted with 950µl Opti-MEM, incubated for 5 min at RT, and combined with the mixture of Opti-MEM and plasmid. This transfection mixture (1ml) was incubated for 30 min at RT and then added dropwise to the cells. The tissue culture dish was gently rocked back and forth and from side to side to evenly distribute the transfection mixture. Virus-containing supernatant was collected into a new falcon tube 72 h post-transfection. Cell debris was removed by centrifugation at 500×g for 10 min, followed by filtration of the supernatant through a 0.45µm low-protein binding membrane (Millipore Steriflip HV/PVDF). The virus-containing supernatant was concentrated using Lenti-X Concentrator by combining 1 volume of Lenti-X Concentrator with 3 volumes of clarified viral supernatant. The mixture was gently inverted to mix and incubated for at least 3h at 4°C. Then centrifuged at 1500×g, for 45 min, at 4°C. After centrifugation, the supernatant was carefully removed to avoid disturbing the off-white pellet, which became visible after the spin. Virus was concentrated 100x by resuspended the pellet in 100 µl of sterile PBS, aliquoted, and used freshly or frozen at -80°C.

2.3.3 Lentiviral transduction of L1236 cells for NY-ESO-1 expression

Doxycycline-inducible Cas9-expressing L1236 cell lines (L1236-Cas9 cells), generated in Prof. Schmitz's lab, were used in this study. Lentiviral particles encoding NY-ESO-1 (see Section 2.3.2) were used to transduce L1236-Cas9 cells, which do not express NY-ESO-1 endogenously. For transduction, 50,000 cells were seeded per well in 500 µl complete RPMI medium in a 24-well plate. After seeding, 3 µl of concentrated virus was

added, and the plate was gently rocked to ensure even distribution. Various cell numbers and virus volumes were tested until optimized (details are not included). After 24 h of incubation at 37°C in 5% CO_2, 500 µl of complete RPMI medium was added, and the plate was incubated for an additional 48 h. Three days post transduction with NY-ESO-1, transduction efficiency was assessed by taking an aliquot of the cells, treating them with doxycycline to induce NY-ESO-1 overexpression and performing intracellular staining for NY-ESO-1 (see Appendix B for the details). Following NY-ESO-1 transduction, the cells underwent selection. 50,000 cells were seeded per well in a 24-well plate with 500 µl of complete RPMI medium. Different blasticidin concentrations (0 µg/ml, 1 µg/ml, 5 µg/ml, 10 µg/ml) were added for 14 days, during which non-transduced control cells were killed. Cells were passaged every three days, with medium adjusted according to cell growth and the blasticidin concentration. Fresh medium with the appropriate blasticidin concentration was used at each passage. NY-ESO-1 expression was monitored by flow cytometry. After selection, cells treated with 5 µg/ml blasticidin, which supported healthy cell growth and > 95% NY-ESO-1 expression, were expanded, aliquoted, and used fresh or frozen until use.

2.3.4 sgRNA-mediated knockout in NY-ESO-1-expressing L1236 cells

To achieve knockout of the *B2M* gene, as well as *CD274,* a fraction of NY-ESO-1-expressing L1236 cells was transduced with lentiviral vectors encoding gene-specific sgRNAs targeting the respective genes of interest. Lentiviral particles carrying these sgRNAs were produced as described in Section 2.3.2. Transduction was carried out using the same procedure previously described for NY-ESO-1 (Section 2.3.3). Three days post-transduction, the expression of either dsRed or GFP, depending on the sgRNA vector used, was assessed using a flow cytometer to evaluate transduction efficiency. Cas9 expression was induced by adding 250 ng/ml doxycycline for 8–11 days. During this period, cells were passaged every three days with fresh doxycycline-containing medium, and the surface expression of the targeted genes (*CD274, HLA-A/B/C or HLA-A2*) was monitored by Flow Cytometry. Following doxycycline induction, transduced cells underwent two rounds of FACS sorting (see Appendix B for the details), after which they were expanded and used for further experiments.

2.4 Generation and polarization of NY-ESO-1-expressing macrophages

This section describes the methods used to differentiate and polarize macrophages, as well as generate NY-ESO-1-expressing macrophages, in order to study their polarization induced by conditioned medium (CM) or their interactions with T cells. Monocyte-derived macrophages were first differentiated and polarized into M1 and M2 subtypes (Section 2.4.1). To investigate the effect of Hodgkin cell supernatant on macrophage polarization, macrophages were treated with CM from Hodgkin cell lines (Section 2.4.1). Next, the NY-ESO-1 antigen was introduced into M2 macrophages via nucleofection (Section 2.4.2), enabling their recognition by T cell receptors specifically targeting NY-ESO-1. These preparatory steps allowed subsequent co-culture experiments with engineered T cells (see Figure 4).

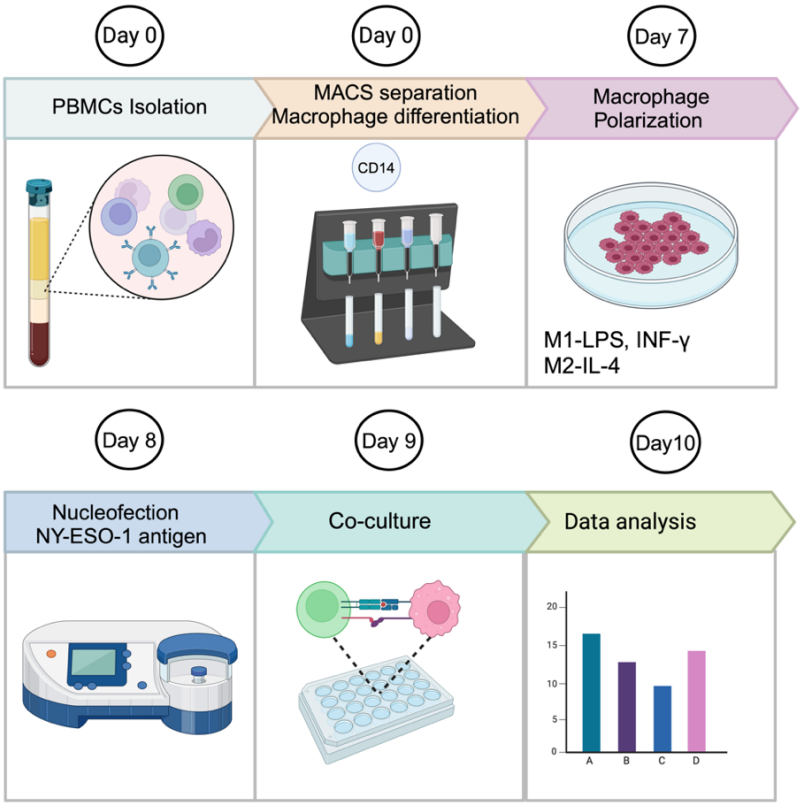

Figure 4. Schematic representation of the generation of NY-ESO-1-expressing macrophages. PBMCs were first isolated, and $CD14^+$ monocytes were enriched using MACS. These monocytes were cultured in differentiation medium and subsequently polarized into macrophages. The polarized macrophages were either harvested for RNA sequencing (RNA-seq) or transfected via nucleofection and used in co-culture experiments. For co-culture experiments, data acquisition was performed using a flow cytometer, and analysis was conducted with FlowJo software (Created using BioRender).

2.4.1 Macrophage differentiation, polarization and RNA-seq

Freshly isolated HLA-A2 positive PBMCs (see Appendix A) were washed with ice-cold PBS. After washing steps, PBMCs underwent magnetic separation by using CD14 Microbeads following the manufacturer's instructions [137]. Briefly, cells were magnetically labeled with CD14 MicroBeads by incubating 15 min at the 4°C. Then the cell suspension was loaded onto LS positive selection columns, which was placed in the magnetic field of a MACS Separator. The magnetically labeled $CD14^+$ cells were retained within the column, resulting in a cell population consisting of > 95% $CD14^+$ monocytes. To monitor the efficiency of MACS separation, the surface expression of CD14 was measured by flow cytometer using a CD14-PE antibody.
After MACS separation, $CD14^+$ monocytes were washed, centrifuged, and the cell pellet was resuspended in differentiation medium containing either 50 ng/ml M-CSF (Macrophage colony-stimulating factor) or 50 ng/ml GM-CSF (Granulocyte-macrophage colony-stimulating factor) to promote macrophage differentiation. The cells were seeded in a 24-well tissue culture plate at a density of 5×10^5 cells per well and cultured for 7 days. The medium was changed every third day, following vigorous washing with pre-warmed PBS to remove non-adherent cells. On day 8, macrophages were washed once with pre-warmed PBS, and fresh complete M1 or M2 macrophage polarization medium was added to induce polarization into the M1 or M2 subtypes. For M1 polarization, macrophages pre-treated with GM-CSF for 7 days were further cultured in complete medium containing 100 ng/ml Lipopolysaccharide (LPS) and 25 ng/ml IFN-γ. For M2 polarization, macrophages pre-treated with M-CSF for 7 days were further cultured in complete medium containing 20 ng/ml IL-4.

Induction of Macrophage Polarization via Conditioned Medium:

On day 8 of macrophage treatment, fresh CM was prepared by harvesting confluent L1236 cells. After centrifugation at 500×g for 5 min, the supernatant was collected, transferred to a new 50 ml Falcon tube, and diluted 1:1 with RPMI supplemented with 20% FBS. This CM was then added to the cultures to investigate macrophage polarization into the M1 and M2 subtypes under CM treatment. The plates were incubated at 37°C for 24 h. After incubation, the medium was removed, and fully differentiated macrophages were washed once with pre-warmed PBS. To detach the macrophages, 500

µl of TrypLE Express reagent was added per well, and the plates were incubated for 20-30 min at RT. During the incubation, the plates were gently rocked from time to time to facilitate the detachment of the macrophages from the plastic surface. After incubation, the macrophages were collected into a new 50 ml Falcon tube, and complete RPMI medium was added to the tube. The cells were then centrifuged at 300 × g for 7 min and subsequently processed using Nucleofection (see Sec 3.3.2) or prepared for RNA sequencing (RNA-seq).

For RNA-seq, total RNA was isolated from cells using the RNeasy Plus Mini Kit, libraries were prepared with the QuantSeq 3′ mRNA-Seq V2 Library Prep Kit FWD with unique dual indices (12 nt), and sequencing was performed on the NextSeq 500/550 system according to the manufacturer's instructions.

2.4.2 Nucleofection of macrophages for NY-ESO-1 expression

M2-polarized macrophages (Section 2.4.2) were transfected with the NY-ESO-1 antigen, following the manufacturer's instructions for the Amaxa Human Macrophage Nucleofector Kit. Briefly, before transfection, 1.5 ml of macrophage culture medium was added per well of a 24-well plate and pre-warmed by placing it in a 37°C, 5% CO_2 incubator. The entire supplement was added to the Nucleofector Solution. Simultaneously, the cells were centrifuged at 300 × g for 7 min and then resuspended in culture medium at a concentration of 5×10^5 cells/ml. The cells were then centrifuged again at 300 × g for 7 min, and the supernatant was discarded completely to ensure no residual medium covered the cell pellet. The cell pellet was resuspended in 100 µl of room-temperature Nucleofector Solution per sample.

The cell suspension was incubated for 15 min in Human Macrophage Nucleofector Solution. After incubation, 100 µl of the cell suspension was combined with 5 µg of DNA (pcDNA3.1-NY-ESO-1-p2a-eGFP) or 2 µg of pmaxGFP vector, which served as a control for transfection. The cell/DNA suspension was transferred into a certified cuvette using a 200 µl pipette, avoiding the generation of air bubbles, and the cuvette was closed with the cap. The Nucleofector program Y-010 was selected on the Nucleofector 2b device. The cuvette containing the cell/DNA suspension was inserted into the Nucleofector cuvette holder, and the selected program was applied. The cuvette was removed from the holder as soon as the program was finished. 500 µl of pre-warmed culture medium for macrophages was added to the cuvette, and then the sample was

carefully transferred into the 24-well plate (final volume of 1.5 ml of pre-warmed culture medium for macrophages) using a Pasteur pipette. The plates were immediately placed in a 37°C, 5% CO_2 incubator for 24 h. After incubation, transfection efficiency was checked by assessing GFP expression under inverted microscopy.

2.5 Functional assays with T cells, macrophages and HRS cells

This section describes a series of co-culture experiments designed to evaluate the functional responses of T cells and Hodgkin cells in various contexts. These assays include T cell and tumor cell co-cultures to assess baseline interactions (Section 2.5.1), cytotoxicity through caspase-3 activation (Section 2.5.2) and degranulation via CD107a expression (Section 2.5.3), with or without the addition of Nivolumab to modulate the PD-1/PD-L1 interaction. Additionally, T cell and macrophage co-culture assays were conducted to assess T cell activation and function (Section 2.5.4). Next, co-culture assays involving PD-1-transduced HEK293FT cells were performed to investigate tumor cell proliferation under conditions modulating the PD-1/PD-L1 interaction (Section 2.5.5).

2.5.1 Rationale for Nivolumab Concentration

For all co-culture experiments involving Nivolumab, a concentration of 15 µg/ml was used, based on prior in vitro studies demonstrating effective PD-1 blockade without cytotoxicity [138–140]. For some co-cultures, preliminary experiments testing different concentrations and incubation times were performed to determine optimal conditions; only the optimized concentration and conditions are reported in this manuscript.

2.5.2 T cell and HRS cell co-culture assays: 41BB activation

The anti-NY-ESO-1 TCR-transduced primary human CD8+ T cells (as described in Section 2.2.5) were thawed in T cell medium containing 3 U/ml DNase [128,141,142] and seeded at a density of $2x10^6$ cells/ml. Then, the cells were cultured in an incubator at 37°C and 5% CO_2 overnight. After incubation, cells were counted using flow cytometer to determine overnight recovery and viability. T cells were then centrifuged, and the cell pellet was resuspended at a concentration of $2×10^6$ cells/ml in T cell medium containing 300 IU/ml IL-2 for 24 h. Cells were passaged every three days with fresh medium containing 300 IU/ml IL-2. After 10 days of culture, the surface expression of the targeted

genes (CD56, LNGFR) was measured by flow cytometer, and cells underwent a second round of MACS separation (Section 2.2.6) if necessary.

One day before co-culture NY-ESO-1 expressing L1236 cells (target HRS cells) were treated with 250ng/ml doxycycline to induce the expression of NY-SO-1. Before co-culture, NY-ESO-1 expressing L1236 cells were typically labeled with Tag-it Violet dye according to the manufacturer's instructions. Briefly, 1 µl of 5mM Tag-it Violet™ stock solution was added to 1 ml of PBS to prepare a 5 µM working solution. Cells were incubated in 1 ml of the 5 µM working solution for 20 min at RT in the dark. After incubation, 5 ml of complete RPMI medium was added to quench the staining process. The cells were centrifuged for 5 min at 500xg, then resuspended in pre-warmed complete RPMI medium and incubated for 10 min at RT in the dark. Finally, Violet was measured using flow cytometer.

Before the co-culture experiment, Nivolumab functionality and different concentrations were tested using the PD-1/PD-L1 blockade bioassay, following the manufacturer's instructions.

Co-culture experiments were conducted in round-bottom 96-well plates with 1×10^5 anti-NY-ESO-1 TCR-transduced primary human CD8+ T cells and 1×10^5 NY-ESO-1 expressing L1236 cells in the presence or absence of 15µg/ml Nivolumab. Different concentrations of Nivolumab and varying time periods of incubation were tested until optimized (not detailed in this manuscript). After incubation, the cells were transferred into flat-bottom 96-well plates and centrifuged for 5 min at 500xg. The supernatant was then aspirated by flicking the plate. Cell pellets were resuspended in 50 µl of antibody solutions diluted in FACS staining buffer and incubated at 4°C for 30 min. Cells were washed and resuspended in 200 µl of FACS staining buffer prior to measurement by a flow cytometer. For cell identification, either NY-ESO-1 expressing L1236 cells were stained with Tag-it Violet™ dye before co-culture, as mentioned above, or T cells were stained with CD8a-APC antibody after co-culture. To detect T cell activation, cells were stained with the T cell activation marker 4-1BB (CD137) after co-culture.

2.5.3 T cell and HRS cell co-culture assay: Caspase 3 activation

A co-culture experiment was conducted to assess Caspase-3 activation in target cells. Prior to co-culture, NY-ESO-1 expressing L1236 cells (target cells) were stained with

Tag-it Violet dye (Section 2.5.1). The co-culture assay was conducted as described in Section 2.5.1. The detection of activated caspase-3 was carried out as described previously [143], with the following modifications. After incubation, the cells were transferred to flat-bottom 96-well plates and centrifuged for 5 min at 500 x g. The supernatant was discarded by gently flicking the plate. The cell pellets were resuspended in 200 µl of FACS wash buffer, centrifuged again for 5 min at 500 x g, and the supernatant was discarded. The cells were fixed and permeabilized by resuspending the pellet in 100 µl of fixation and permeabilization buffer (Fix/Perm), followed by incubation for 10 min at RT in the dark. The cells were then washed by adding 100 µl of perm/wash buffer (pre-diluted 1:10 in distilled H_2O), centrifuged 5 min 500xg and the supernatant was discarded by gently flicking the plate. Cell pellets were resuspended in 50 µl of anti-activated caspase-3 antibody, pre-diluted 1:25 in perm/wash buffer, and incubated for 20 min at RT in the dark. After incubation, the cells were washed with 150 µl of perm/wash buffer, centrifuged for 5 min at 500 x g, and the supernatant was discarded. Finally, the cell pellets were resuspended in 200 µl of FACS wash buffer, and the expression of activated caspase-3 was measured using a flow cytometer, following the gating strategy described in supplementary Figure S2.

2.5.4 T cell and HRS cell co-culture assay: CD107a degranulation

To evaluate the antitumor activity of anti-NY-ESO-1 TCR-transduced primary human CD8+ T cells, a degranulation assay was performed by monitoring CD107a expression during co-culture with target cells in the presence or absence of Nivolumab [141,144]. Cells were prepared as described in Section 2.5.1.

Briefly, co-culture experiments were set up in round-bottom 96-well plates, with 1×10^5 anti-NY-ESO-1 TCR-transduced primary human $CD8^+$ T cells and 1×10^5 unstained target cells per well. Each well contained 100 µL of each cell suspension, bringing the final volume to 200 µl. Cells were treated with 15 µg/ml of Nivolumab, while control wells were treated with 15 µg/ml of an IgG antibody or left untreated. The cells were incubated for 19 h at 37 °C in a 5% CO_2 incubator.

Following incubation, 10 µl of anti-human CD107a-PE antibody was added to each well and incubated for an additional hour. Meanwhile, a monensin solution was prepared by diluting 2 µl of GolgiStop in 75 µl of T cell medium. 5 µl of this solution

were added to each well, and the contents were mixed thoroughly by pipetting. The cells were then incubated for 4 h at 37 °C in a 5% CO_2 incubator.

After the incubation, the cells were centrifuged at 500×g for 5 min, and the supernatant was discarded by gently flicking the plate. The cell pellets were resuspended in 50 µl of anti-human CD8a-APC antibody, pre-diluted in FACS wash buffer, and incubated for 30 min at 4 °C. The cells were then washed by adding 150 µl of FACS wash buffer, centrifuged for 5 min at 500×g, and the supernatant was discarded. Finally, the cell pellets were resuspended in 200 µl of FACS wash buffer, and the expression of CD107a-PE was measured using a flow cytometer, following the gating strategy described in supplementary Figure S2.

2.5.5 T cell, M2 macrophage, and HRS cell co-culture assays

The generation of anti-NY-ESO-1 TCR-transduced primary human $CD8^+$ T cells (Section 3.2.5) and NY-ESO-1-expressing M2 macrophages (Section 3.4.2) was initiated on the same day to ensure the availability of fresh cells for co-culture. One day prior to co-culture, M2 macrophages were nucleofected and seeded into a 24-well plate at a density of 5×10^5 cells/ml per well (Section 3.4.2).

T cell–M2 macrophage co-culture assay in the presence of CM derived from HRS cells:

In the first experimental setup, co-culture experiments were conducted by carefully removing the medium from the NY-ESO-1-expressing M2 macrophages, ensuring the cell layer remained intact. Next, 1 ml of T cell medium containing either 5×10^5 $CD8^+$ T cells or anti-NY-ESO-1 TCR-transduced $CD8^+$ T cells was added to the NY-ESO-1-expressing M2 macrophage layer. The co-cultures were then treated with CM derived from L1236 cells, while control wells were left untreated (T cell medium added only).

T cell–M2 macrophage–HRS cell co-culture assay:

To further investigate the impact of tumor cells and immune checkpoint blockade on T cell activation, a second co-culture model was established with minor modifications. In this setup, following the same co-culture preparation steps, L1236 cells with B2M knockout were added onto the T cells and M2 macrophage co-cultures instead of CM. After seeding the tumor cells, wells were either treated with Nivolumab or left untreated (T cell medium added only).

The cells were then incubated for 24 h at 37°C in 5% CO_2. After incubation, the cells were transferred into 15ml falcon tube and centrifuged for 5 min at 500xg. Cell pellets were resuspended in 100 µl of FcR blocking reagent diluted in FACS staining buffer and incubated at 4°C for 30 min. Cells were washed and resuspended in 100 µl of antibody solution diluted in FACS staining buffer and incubated at 4°C for 30 min. Then the cells were washed and resuspended in 100 µl FACS staining buffer prior to measurement by a flow cytometer. For cell identification, either anti-NY-ESO-1 TCR-transduced $CD8^+$ T cells were stained with Tag-it Violet™ dye before co-culture, or M2 macrophages were GFP-positive due to nucleofection. To detect T cell activation, cells were stained with the T cell activation marker 4-1BB (CD137) after co-culture.

2.5.6 HEK293FT cell and HRS cell co-culture assays

HEK293FT cells, which do not express PD-1 endogenously, were transduced with the pTwist lentiviral construct to express PD-1 on their surface. The transduced HEK293FT cells, along with control HEK293FT cells (lacking PD-1 expression), were co-cultured with tumor cells (PD-L1 expressing L1236 cells), either with or without Nivolumab, to assess the impact of PD-1/PD-L1 interaction on tumor cell proliferation.

Transduction of HEK293FT cells:

The day before transduction, HEK293FT cells were seeded in a 6-well plate at a density of 1.5×10^5 cells per well. HEK293FT cells were transduced with pTwist lentivirus containing the PD-1 insert. Lentivirus was generated as described in Section 2.3.2. After resuspending the off-white pellet in 100 µl of sterile PBS, 15 µl of the virus suspension was added to each well. Following a 24 h incubation at 37°C in 5% CO_2, the medium was replaced with fresh D10 medium, and the plate was incubated for an additional 48 h. Surface expression of the targeted gene PD-1 was then measured by flow cytometer. Transduced cells underwent a selection process, where HEK293FT cells were split and puromycin was added at different concentrations (0.5 µg/ml, 1 µg/ml, 2 µg/ml), and resistant cells were grown out for 7 days. Cells were passaged every 3 days. After puromycin selection, cells treated with 1 µg/ml were chosen for further experiments, since this concentration supported optimal growth and resulted in over 95% PD-1 expression. These cells were expanded and co-cultured with PD-L1 expressing L1236 cell lines.

HEK293FT cell and tumor cell co-culture assays:

One day before co-culture, HEK293FT cells were harvested by trypsinization and the cells were washed with D10 medium, centrifuged and the cell pellet was resuspended with 10 ml D10 medium. Then HEK293FT cells were transferred into T25 cell culture flask and irradiated (3000 rad). After irradiation cells were transferred into new 50ml Falcon tube and centrifuged for 5 min, at 500×g then resuspended in D10 medium. Then cells were counted by using flow cytometer. Then seeded out in 12-well plate at a density 0.25×10^6 cells per well in 2 ml of D10 medium (0.15×10^6 and 0.35×10^6 cells per well also tested).

Before co-culture, L1236 cell lines were typically labeled with Tag-it Violet dye according to the manufacturer's instructions. Briefly, 1µl of 5mM Tag-it Violet™ stock solution was added to 1 ml of PBS to prepare a 5 µM working solution. Cells were incubated in 1 ml of the 5 µM working solution for 20 min at RT in the dark. After incubation, 5 ml of complete RPMI medium was added to quench the staining process. The cells were centrifuged for 5 min at 500×g, then resuspended in pre-warmed complete RPMI medium and incubated for 10 min at RT in the dark. Finally, to check the staining violet was measured using flow cytometer.

Co-culture experiments were conducted by carefully removing the medium from HEK293FT cells, taking care not to disrupt the cell layer. Subsequently, 2 ml of complete RPMI medium containing 0.1×10^6 L1236 cells was added onto the HEK293FT cell layer. Cells were treated with 15 µg/ml of Nivolumab, while control wells were left untreated. Then the cells were incubated 2-3 days at 37°C in 5% CO_2.

After incubation, L1236 cells were carefully removed using a 1000 µl pipette and transferred into 5 ml Eppendorf tube. An aliquot of the collected cells was taken to determine cell number and assess staining intensity. If the violet dye signal intensity had decreased due to cell proliferation, the cells were stained with Tag-it violet dye as described above. Subsequently, 0.1×10^6 L1236 cells (collected from the old culture after 2-3 days of incubation) were transferred onto a fresh, irradiated HEK293FT cell layer and incubated for another 2-3 days.

This procedure, involving the transfer of L1236 cells from the old culture after each incubation period onto a fresh, irradiated HEK293FT cell layer, was repeated for a total of 13-14 days. An aliquot of the collected L1236 cells was taken to assess activated Caspase 3 expression on L1236 as described in Section 2.5.2.

2.6 Proximity ligation and multiplex immunofluorescence on FFPE sections

This section describes the combined use of PLA and mIF on FFPE tissue sections from cHL samples. PLA was established to detect and visualize PD-1/PD-L1 interactions. To identify the specific cell types involved in these interactions, subsequent mIF staining was performed on the same tissue sections, and imaging was carried out using confocal microscopy. To optimize the PLA–mIF workflow, deparaffinization, dehydration (see Section 2.6.1), and heat-induced epitope retrieval (HIER) (see Section 2.6.2) steps were refined first, and antibody specificity and dilutions were subsequently optimized using immunohistochemistry staining (IHC) (see Section 2.6.3).

2.6.1 Deparaffinization and dehydration

All cases of cHL were provided by the Institute of Pathology, JLU Gießen. All samples were anonymized prior to analysis. All selected cases were reviewed and confirmed as classical cHL by an experienced pathologist before inclusion in the study. Ethical approval was obtained from the Ethik-Kommission des Fachbereichs Medizin der JLU Gießen (approval number: [AZ 97/25]).

FFPE tissue blocks were cut sequential 2-µm-thick sections from Hodgkin cases using microtomes. To improve adherence to the glass slides and decrease the chances of sections dissociating from the slides, paraffin tissue sections were mounted on tissue-adhesive-coated slides, which is especially important for sections undergoing HIER in future steps. The cutting and mounting of paraffin tissue sections onto slides were done manually at the Institute of Pathology. After being mounted onto slides, paraffin tissue sections were dried at 60°C in an oven overnight to increase the adhesion of the tissue sections to the surface of the glass slides. Then, the slides with mounted paraffin tissue sections (slides) underwent deparaffinization, rehydration, and HIER before being used for the IHC, PLA or IF staining to guarantee that the antibodies had full access to the tissue antigens. Deparaffinization, dehydration, and HIER of slides were processed as previously described [145,146] , with the following modifications. After drying slides overnight in oven, the slides were placed in a cuvette containing fresh, sufficient amount xylene to cover the tissue sections completely and incubate for 15 min with gentle shaking. Then the slides were transferred into new cuvette containing fresh xylene and incubate another 10 min. After incubation the slides were washed twice in 100% ethanol

(for 5 min each time). The slides were immersed in a new cuvette containing 96% ethanol for 5 min, repeated twice. Then, the slides were washed with 70% ethanol for 5 min, followed by washing in 4.5% formaldehyde (Histofix) for 20 min, and rinsed in distilled water for 3 min.

2.6.2 Heat induced epitope (antigen) retrieval

Formalin is an excellent fixative for preserving tissue morphology. However, it can lead to the formation of molecular cross-links in proteins. This can alter the native three-dimensional protein conformation, thereby changing the normal structure of the epitope (the specific region of the protein where the antibody binds), making it more difficult for the antibody to bind to its targets [145,146]. Heat-induced epitope retrieval (HIER), also known as 'antigen retrieval,' restores protein structure by returning the three-dimensional protein configuration to something close to its native state, which increases epitope availability for antibody binding [145,146].

After deparaffinization and dehydration (Section 2.6.1), the slides were placed in a cuvette containing prewarmed antigen retrieval solution [147,148] (CC2 buffer: to prewarm, the cuvette was loosely covered with a lid, and placed in the microwave for 45 seconds at full power) and incubated for 30 min in a 95°C water bath. After incubation, the cuvette was transferred onto ice for 10 min to cool down. Then, the slides were transferred to a new cuvette containing distilled water. The borders of the tissue were marked with a hydrophobic barrier pen to define the staining area and minimize reagent usage in subsequent steps.

2.6.3 Immunohistochemistry (IHC)

The antibodies intended for use in PLA and mIF on FFPE tissue of cHL were tested using IHC to evaluate their binding capacity to their respective antigens. The tested antibodies are listed in Table 8. Various antibody dilutions were assessed, and the optimal dilution was selected for further experiments. After deparaffinization and dehydration (Section 2.6.1), the slides underwent HIER as previously described in section 2.6.2. Following these steps, the slides were processed using the reagents from the BOND™ Polymer Refine Detection Kit, according to the manufacturer's instructions. After the staining Slides were permanently cover-slipped using permanent mounting medium to preserve

the slide. Then slides were digitized using the Pannoramic SCAN II slide scanner with the manufacturer's acquisition software suite.

2.6.4 Duolink-proximity ligation assay (PLA)

Duolink-PLA is an in-situ immunoassay that detects endogenous proteins and protein-protein interactions in fixed cells and tissues with high specificity and sensitivity. To detect in situ PD-1 and PD-L1 interactions in FFPE tissue sections of cHL, two primary antibodies (anti-PD-1 and anti-PD-L1) raised in different species were used to target the two distinct proteins, PD-1 and PD-L1 (see Figure 5). Species-specific secondary antibodies conjugated with unique short oligonucleotides (known as PLA PLUS and MINUS probes) bind specifically to the primary antibodies. Subsequently, two connector DNA oligonucleotides were introduced into the system. When the PLA probes are in close proximity (<40 nm), these connector DNA oligonucleotides bind with the PLA probes through enzymatic ligation, forming a circular DNA template. To amplify this reaction via rolling circle amplification, nucleotides, polymerase (specifically Phi29 DNA polymerase, known for its exceptional processivity and strand displacement ability [149,150]), and fluorescently-labeled complementary oligonucleotides were applied. One of the PLA probes acted as a primer for the polymerase, generating a repeating (some hundredfold), concatemeric product that remained tethered to the secondary antibody. The added fluorescently-labeled oligonucleotides then hybridized to the amplified DNA, highlighting the signal [149,151,152,152]. Each PLA signal consisted of approximately 1,000 bound fluorescent probes, that together appeared as a distinct dot that can be easily visualized under confocal microscopy. These PLA signals can be quantified and mapped to specific subcellular locations using microscopy images [149,151,153,154].

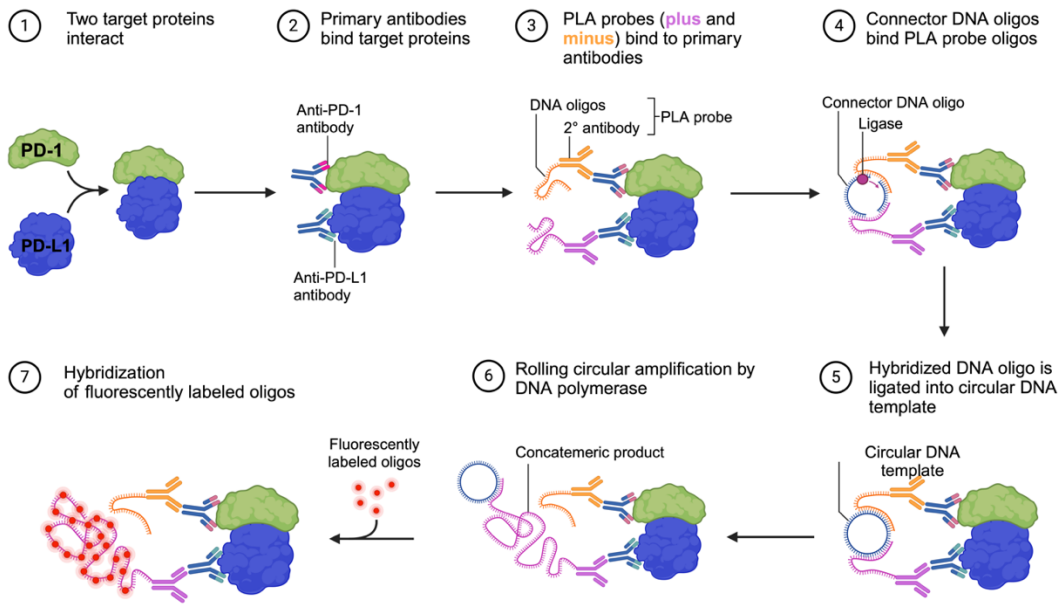

Figure 5. Workflow of the PLA to detect PD-1/PD-L1 interactions. Each step of the PLA protocol is described in the Figure. (Created using BioRender)

Duolink-PLA experiments were conducted using Duolink® PLA Fluorescent reagents according to the manufacturer's instructions [155], with the following modifications. To ensure the successful execution of a Duolink® PLA experiment, a sufficient amount of reagent (100-150 µl per slide, depending on the size of the tissue) was used, and the slides were not allowed to dry before adding reagents, which minimized background noise during imaging [155].

Blocking step: After deparaffinization, dehydration (Section 2.6.1) and subsequent antigen retrieval (Section 2.6.2), distilled water was tapped off, and 2-3 drops of Duolink® Blocking Solution were added to each slide to block endogenous Fc receptors and minimize non-specific antibody binding. Slides were then incubated in a pre-heated humidity chamber for 60 min at 37°C.

Primary antibodies: After incubation, the blocking solution was tapped off, and 100–150 µl of the primary antibody mixture (anti-PD-1 and anti-PD-L1) diluted in Duolink® Antibody Diluent, was applied to the tissue. Slides were incubated in a pre-heated humidity chamber for 60 min at RT or overnight at 4°C. After incubation, the antibody mixture was tapped off, and the slides were immediately placed in 1× Wash Buffer A, followed by three washes for 5 min each at RT with agitation.

Duolink® PLA Probe incubation: While the slides were washing, the Duolink® PLA probe solution was prepared by diluting the MINUS and PLUS probes 1:5 in Duolink® Antibody Diluent. After washing, excess wash buffer was tapped off, and 100 µl of the PLA probe solution was applied to each slide. Slides were incubated in a pre-heated humidity chamber for 60 min at 37°C. Following incubation, the PLA probe was tapped off, and slides were immediately placed in 1× Wash Buffer A, then washed twice for 5 min each at RT with agitation.

Ligation: During the wash, the ligation solution was prepared by diluting 5× Duolink® Ligation Buffer 1:5 in high-purity water, followed by adding ligase at a 1:40 dilution. After washing, excess wash buffer was tapped off, and the ligation solution was applied to the tissue. Slides were incubated in a pre-heated humidity chamber for 30 min at 37°C. Following incubation, the solution was tapped off, and slides were placed in 1× Wash Buffer A, then washed twice for 5 min each at RT with agitation.

Amplification: In parallel with washing, the amplification solution was prepared by diluting the 5x Amplification Buffer 1:5 in high-purity water. As the buffer is light-sensitive, slides and reagents were protected from light from this point onward. Polymerase was then added at a 1:80 dilution. After washing, excess buffer was tapped off, and the amplification solution was applied to the tissue. Slides were incubated in a pre-heated humidity chamber for 120 min at 37°C, after which the solution was tapped off.

Final washing steps: Then, the slides were washed with 1x Wash Buffer B three times for 5 min each at RT with agitation, followed by washing in 0.01x Wash Buffer B for 1 min at RT with agitation.

Counterstaining: After washing, excess buffer was removed, and nuclei were counterstained with 100–150 µl DAPI (1:10 in PBS). Slides were incubated for 5 min at RT, then washed once in 1× Wash Buffer B for 5 min and once in 0.01× Wash Buffer B for 1 min, both at RT with agitation.

Mounting: Excess wash buffer was tapped off, and slides were mounted with a minimal volume of ProLong Mounting Medium, avoiding air bubbles under 0.16–0.19 mm coverslips. Slides were stored at 4°C for 15 min to 2 days before analysis with Confocal Microscope.

For optimization of the fluorescent PLA workflow, brightfield PLA was additionally performed. After deparaffinization, dehydration (Section 2.6.1), and

subsequent antigen retrieval (Section 2.6.2), distilled water was tapped off, and the brightfield PLA was carried out according to the manufacturer's instructions.

2.6.5 Multiplex Immunofluorescent staining (mIF)

To identify the cells involved in the PD-1/PD-L1 interaction, a mIF detection method was applied to FFPE tissue sections of cHL following PLA. To amplify the signal and enhance sensitivity, an indirect mIF technique was used, involving antibodies from the same species. This approach was combined with tyramide signal amplification (TSA), enabling the simultaneous detection of multiple markers with increased specificity and sensitivity [147,156–158] (see Figure 6).

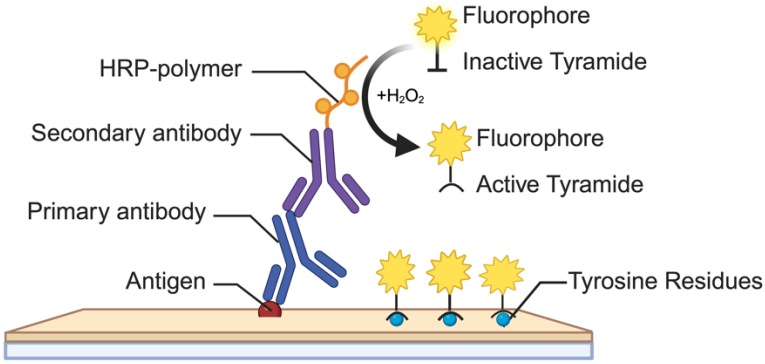

Figure 6. Schematic illustration of the TSA system. This schematic illustrates the TSA system, where primary antibodies bind target proteins, and HRP-conjugated secondary antibodies activate tyramide substrates. The activated tyramide molecules then covalently bind to nearby proteins, amplifying the signal for enhanced detection. (Created using BioRender)

In the mIF, primary antibodies were used (see Table 8) to target distinct proteins. Species-specific secondary antibodies conjugated with horseradish peroxidase (HRP) specifically bind to the primary antibodies. Subsequently, an inactive tyramide substrate conjugated with a fluorophore was introduced into the system. In the presence of H_2O_2, HRP catalyzes the activation of multiple tyramide molecules by converting the inactive tyramide substrate into a highly reactive form, which covalently binds to tyrosine residues on nearby proteins of interest. This results in the formation of a permanent attachment. Since many tyramide-fluorophore conjugates can be deposited around each HRP-labeled target, stable, high-density labeling is achieved [147,156–158]. Consequently, even low levels of target molecules can produce strong signals due to the dense accumulation of fluorophores. The bound primary antibody/secondary antibody complex was then eluted

with a citrate-based CC2 buffer. As a result, only the deposited tyramide remains covalently bound to the tissue near the first antigen of interest. This allows the use of a second primary antibody from the same species to detect the next antigen of interest. To overcome the difficulties in finding appropriate combinations of antibodies from different species, this method enables the repeated use of antibodies from the same species without cross-reactivity issues. The procedure can be repeated to detect additional targets [147,156–158].

After analyzing the PLA reaction using a confocal microscope, the slides were placed in a cuvette containing a PBS Tween 20 (PBST) and washed for 15-30 min at RT with agitation until the coverslip could be gently removed. Then the slides were transferred into a new cuvette containing fresh PBST and washed once for 5 min at RT with agitation. After washing, the excess wash buffer was tapped off the slides.

Antibody elution step (1): The slides were placed in a cuvette with prewarmed antigen retrieval solution (CC2 buffer) and incubated for 10 min at 95°C to remove the PLA reaction (primary and secondary antibodies). After cooling for 10 min on ice, the slides were transferred to a new cuvette with distilled water. The tissue borders were marked with a hydrophobic barrier pen to define the staining area and minimize reagent use in subsequent steps.

Blocking Step (2): After washing, distilled water was tapped off the slides and 0.3% H_2O_2 in methanol was added to block endogenous HRP activity. The slides were incubated for 15 min at RT. Following incubation, the blocking solution was tapped off, and the slides were placed into a cuvette with PBST. The slides were washed three times for 3 min each at RT with agitation.

Primary antibodies (3): were diluted in the antibody diluent (see Table 8). After washing, blocking solution was tapped of the slides and 100-150µl primary antibodies solution was added to each sample. The slides were incubated in a humidity chamber for 60 min at RT or overnight at 4°C. After incubation, the slides were washed with fresh PBST three times for 3 min each at RT with agitation. Then excess wash buffer was tapped of the slides.

Secondary antibodies (4): 2-3 drops of poly-HRP conjugated secondary antibody (ready to use - Goat anti-Mouse or Goat anti-Rabbit IgG) were applied. The slides were incubated in a humidity chamber for 60 min at RT or overnight at 4°C. Then the slides were washed three times for 5min each in PBST at RT with agitation.

Signal amplification (5): In parallel with washing, fresh tyramide working solution was prepared. For a 500 µl reaction, 5µl of 100×Tyramide stock solution (Alexa Fluor

tyramide reagent + 150 µl DMSO) and 5µl of 100×H_2O_2 solution (50µl 3% H_2O_2 + 1ml distilled H_2O) were added to 500 µl of 1× Reaction buffer (50µl 20×Reaction buffer + 1ml distilled H_2O). After washing, 100-150 µl freshly prepared tyramide working solution were added on each sample and incubated in a humidity chamber for 10 min at RT.

Reaction Stop (6): During incubation, the Reaction Stop reagent was prepared by diluting the stock solution 1:10 in PBS. After incubation, the tyramide solution was tapped off, and the Reaction Stop reagent was added to the tissue, followed by 5 min incubation at RT in a humidity chamber. The slides were then washed three times for 3 min each in PBST at RT with agitation.

Antibody elution step (7): The slides were placed in a cuvette with prewarmed antigen retrieval solution (CC2 buffer). The slides were incubated for 15 min in a 95°C water bath, then cooled on ice for 10 min. Next, the slides were transferred to a new cuvette with distilled water. The tissue borders were marked with a hydrophobic barrier pen. Finally, the slides were washed three times for 3 min each in PBST at RT with agitation.

Second primary antibodies (9): After washing, excess wash buffer was tapped of the slides and 100-150µl primary antibodies solution was added to each sample. The slides were incubated in a humidity chamber for 60 min at RT or overnight at 4°C. After incubation, the slides were washed with fresh PBST three times for 3 min each at RT with agitation. Step (4), (5), (6) and (7) was repeated.

Third primary antibodies (10): After washing, excess wash buffer was tapped of the slides and 100-150µl primary antibodies solution was added to each sample. The slides were incubated in a humidity chamber for 60 min at RT or overnight at 4°C. After incubation, the slides were washed with fresh PBST three times for 3 min each at RT with agitation. Step (4), (5), (6) and (7) was repeated.

Secondary species-specific antibody conjugated with a fluorophore of choice (11): After washing, excess wash buffer was tapped of and 100-150 µl secondary antibody conjugated to fluorophore was added to each sample. The slides were incubated in a humidity chamber for 30 min at RT. After incubation, the slides were washed with fresh PBST three times for 3 min each at RT with agitation. Then excess wash buffer was tapped of the slides. Steps (9) and (10) were applied when mIF staining was not combined with PLA. When combined with PLA, step (11) should follow step (8), skipping step (9) and (10).

Counterstaining (12): Nuclei were counterstained with 100-150 µl of DAPI, diluted 1:10 in PBS. The slides incubated in a humidity chamber for 7 min at RT. Then the slides were washed with fresh PBST three times for 5 min each at RT with agitation. Then excess wash buffer was tapped of.

Mounting (13): Slides were then mounted with anti-fade mounting medium. The slides were stored at 4°C for 15 min to up to 2 days before being analyzed Confocal microscope.

2.6.6 Confocal microscopy for PLA and IF analysis

The results of both the Duolink PLA and mIF staining were visualized using a Zeiss LSM 800 Confocal Laser Scanning Microscope. Confocal images were acquired with a Plan-Apochromat 40×/1.1 water objective, and image acquisition and analysis were performed using Zen 2.5 software. For optimal fluorescence settings, the automatic 'Smart Setup' function of the Zen 2.5 software was applied to each fluorophore. The laser voltage was set to 750 V for all analyses. The pinhole diameter was adjusted to 2.69 Airy units for DAPI, 1.79 Airy units for Texas Red, and for Alexa 488.

2.6.7 Quantification of PLA interactions

Image analysis and quantification were performed using FIJI/ImageJ with a custom script designed to align and merge the PLA and mIF images acquired from the same tissue regions. After alignment, the combined image displayed PLA puncta together with all mIF and DAPI channels. PLA puncta were then manually annotated by the user: individual puncta were assigned to specific cell types (e.g., $CD8^+$ T cells, HRS, macrophages) using designated function keys (e.g., F1, F2, F3). The script automatically recorded each annotation and compiled the resulting counts, enabling quantification of PD-1/PD-L1 interactions according to the neighboring cell phenotype.

The interaction rate represents the fraction of all partner cells ($CD163^+$ M2 macrophages or $CD30^+$ HRS cells) that are engaged in a PD-1/PD-L1 interaction with $CD8^+$ T cells. It is defined as: Interaction rate = I / (I + P + S),

I — Interacting ($CD8^+$ T cells is in contact with partner cell (CD30/ CD163) and PLA+ dots present (PD-1/PD-L1), P — Proximal (Non-Interacting) $CD8^+$ T cell is close to partner cell (CD30/CD163) and NO PLA dots, S — Single (Isolated) Partner cell (CD30/CD163) has no $CD8^+$ T cell nearby and no opportunity for interaction

This metric uses all partner cells (I + P + S) as the denominator to estimate how frequently each cell population (M2 or HRS) participates in PD-1/PD-L1 interactions with $CD8^+$ T cells. By including interacting, proximal, and isolated cells, this rate reflects the overall burden of PD-1/PD-L1 engagement within each cell compartment, making it suitable for comparing $CD8^+$ T-cell interactions with M2 macrophages vs HRS cells.

3 Results

3.1 Validation of effector and target cells for functional assays

For functional analyses of antigen-specific $CD8^+$ T cell responses, the generation of NY-ESO-1-reactive $CD8^+$ T cells was first validated. This included establishing stable retroviral producer clones, efficiently transducing primary human T cells, and subsequently enriching $CD8^+$ T cells expressing the NY-ESO-1-specific TCR, thereby generating a defined effector population for downstream assays.

In parallel, L1236 HRS cells were validated as target cells by confirming endogenous HLA-A*02 and MHC class I expression and modified via B2M knockout (KO) to produce MHC I-deficient variants. Both wild-type and B2M KO L1236 cells were then transduced to express NY-ESO-1, ensuring antigen presentation. Additionally, PD-L1 expression on L1236 cells was confirmed, and PD-L1 KO cells were generated to investigate the role of PD-L1–mediated immune regulation.

Similarly, macrophages were differentiated and polarized into M1 and M2 subtypes, with polarization validated by characteristic marker expression. To ensure suitability as antigen-presenting target cells, M2 macrophages were subsequently transfected to express the NY-ESO-1 antigen.

HEK293FT cells were transfected to express PD-1 and were generated to investigate PD-1–PD-L1 reverse signaling in HRS cells.

Together, these steps (details description in Chapters 3.1.1 to 3.1.5) established well-characterized effector and target cell systems suitable for subsequent functional assays.

3.1.1 Validation of the generated PG13 cell line for NY-ESO-1 TCR vector production

As a first step toward generating a stable retroviral producer line for T cell transduction, Phoenix Eco cells were transfected with a retroviral vector encoding a TCR specific for the HLA-A*02-restricted melanoma antigen NY-ESO-1[118] (see Section 2.2.1). NGFR was included in the construct as a selectable marker to monitor both transfection and subsequent transduction efficiency. Transfection efficiency in Phoenix Eco cells, assessed by the percentage of $NGFR^+$ cells, was considerably higher in transfected cells

than in untransfected wild-type controls (see Figure 7A), confirming successful transfection.

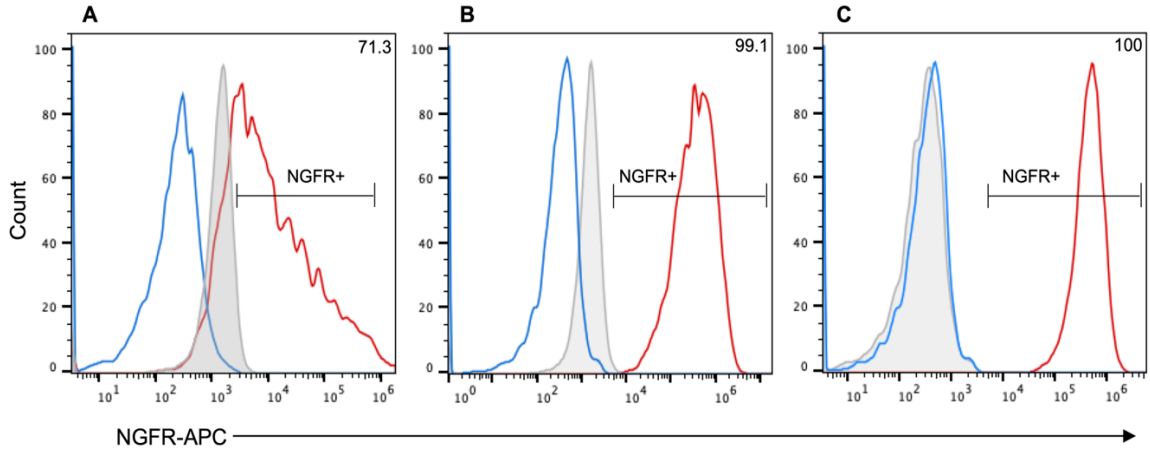

Figure 7. Generation of monoclonal PG13 retroviral producer clones. (A) Phoenix Eco cells were transfected with a retroviral vector encoding an NY-ESO-1–specific TCR. NGFR expression was analyzed by flow cytometry to assess transfection efficiency. Viral supernatant collected from transfected cells was then used to transduce PG13 cells. (B) PG13 cells were transduced using retroviral supernatant harvested from Phoenix Eco cells. NGFR expression was assessed by flow cytometry to determine transduction efficiency. Transduced PG13 cells were then used to generate monoclonal retroviral producer cell lines. **(**C) Monoclonal PG13 producer clones were generated by limiting-dilution cloning. Surface NGFR expression was measured by flow cytometry, and clones with the highest expression were selected for virus production. Untransduced/untransfected cells (wild-type controls) served as controls for all experiments. Overlaid histograms illustrate NGFR-expressing cells (red), representing transfected or transduced populations, compared to untransduced/untransfected NGFR-negative control cells (blue), with a filled gray histogram showing the respective isotype control. The percentage of $NGFR^+$ cells is indicated, and histograms were normalized to mode.

Viral supernatants harvested from transfected Phoenix-Eco cells were subsequently used to transduce PG13 cells (see Section 2.2.2). This two-step packaging strategy (ecotropic Phoenix-Eco →amphotropic PG13) enables generation of retroviral particles suitable for human T-cell transduction (see Section 2.2). Following transduction, PG13 cells were subjected to limiting-dilution cloning to isolate monoclonal producer lines (via NGFR expression) (see Section 2.2.3). In stable retroviral producer lines, NGFR expression can be used as a proxy for productive virus production when formal titer determination is not performed [159]. Flow-cytometry analysis demonstrated robust NGFR expression in transduced PG13 cells, whereas untransduced wild-type controls lacked detectable expression (see Figures 7B–C). Nearly all transduced cells expressed NGFR, indicating highly efficient retroviral transduction. Monoclonal PG13 lines were screened based on NGFR expression, and the clone exhibiting the highest marker expression was expanded. Although viral titer was not formally quantified, a small-scale

transduction confirmed functional infectivity (see Figure S6), and the selected clone efficiently transduced human T cells in subsequent experiments. The chosen clone maintained stable NGFR expression across subsequent passages, demonstrating consistent vector integration and production capability. These clones were then expanded and used for downstream retroviral T-cell transduction experiments.

3.1.2 Validation and generation of NY-ESO-1 reactive CD8$^+$ T cells

Following the establishment of monoclonal PG13 producer clones, PBMCs were isolated (see Appendix A1) as the initial step toward generating NY-ESO-1 reactive TCR CD8$^+$ T cells. Flow cytometry analysis confirmed the presence of lymphocytes, monocytes, and granulocytes within the PBMC population, reflecting successful isolation of the heterogeneous cell types typical of PBMCs (see Figure S1).

To generate NY-ESO-1 reactive TCR CD8$^+$ T cells, PBMCs were first activated with OKT3 and IL-2, resulting in a predominantly CD3$^+$ T-cell population (see Supplementary Figure S4). Activated CD3$^+$ T cells were then divided into two fractions: one fraction was transduced with retroviral vectors encoding the NY-ESO-1-specific TCR (see Section 2.2.5) using viral supernatant produced by the PG13 producer clones, whereas the second fraction was intentionally left untransduced. NGFR was included as a marker to monitor transduction efficiency. Flow cytometry analysis demonstrated a clear NGFR-positive population within the transduced fraction, whereas untransduced (wild-type) fraction lacked NGFR expression entirely (see Figure 8A-B, red histograms). The untransduced T-cell fraction, which retained only endogenous TCRs, was used as a matched negative control to assess NY-ESO-1-reactive TCR specificity in downstream co-culture assays.

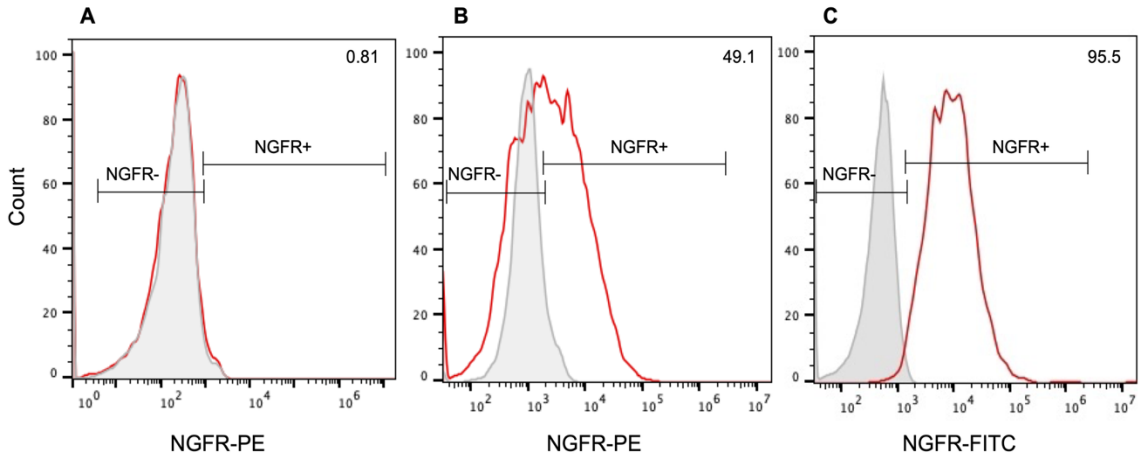

Figure 8. Validation of retroviral transduction and NGFR-based enrichment of NY-ESO-1–specific TCR T cells. (A) After IL-2/OKT3 activation, untransduced $CD3^+$ T cells showed no detectable NGFR expression, confirming an $NGFR^-$ baseline population and the specificity of NGFR staining. These untransduced T cells, expressing only endogenous TCRs, were used as negative controls in subsequent co-culture assays. Overlaid histograms compare NGFR signal (red) with the corresponding isotype control (filled gray). (B) Following retroviral transduction with an NY-ESO-1–specific TCR construct, a clear $NGFR^+$ subset emerged, indicating successful expression of the introduced TCR. Overlaid histograms show $NGFR^+$ transduced cells (red) relative to the isotype control (filled gray). (C) $NGFR^+$ cells were subsequently enriched (MACS or FACS) to isolate the successfully transduced T-cell fraction (after prior $CD8^+$ enrichment). Histograms illustrate the enriched $NGFR^+$ population (red) compared with the matched isotype control (filled gray). Together, these data confirm efficient retroviral transduction and successful isolation of $NGFR^+$ NY-ESO-1–reactive TCR-expressing T cells. Percent $NGFR^+$ cells are indicated. Histograms normalized to mode.

Following retroviral transduction, $CD3^+$ T cells underwent three consecutive rounds of MACS to enrich for the desired $CD8^+$ $NGFR^+$ population. The first step involved depletion of $CD56^+$ cells to remove residual natural killer (NK) cells and other CD56-expressing subsets. Although these $CD56^+$ cells represent only a small population, their removal is important to prevent their potential expansion in later passages. Flow cytometry analysis confirmed successful depletion, as CD56 expression was undetectable in the post-sorted population (see Figure 9A-B, red histograms). From the CD56-depleted fraction**,** positive selection for $CD8^+$ cells was then performed (see Figure 9C-D, red histograms), followed by selection of $NGFR^+$ cells (see Figure 8C, red histograms), to isolate transduced $CD8^+$ T cells expressing the NY-ESO-1-specific TCR. The untransduced T-cell fraction was processed in parallel and underwent the same CD56-depletion and CD8-enrichment steps (see Figure S5) to ensure identical activation and purification histories between experimental (NY-ESO-1-specific TCR $CD8^+$ T cells) and control T-cell populations (endogenous TCRs $CD8^+$ T cells).

Overlaid histograms showed a clear rightward shift in fluorescence intensity for CD8 and NGFR staining in the sorted cells relative to their respective isotype controls

(CD8: Figure 9D, red histogram; NGFR: Figure 8C, red histogram), confirming successful enrichment of $CD8^+$ and $NGFR^+$ T cells. This sequential selection strategy thus yielded a highly purified $CD8^+$ $NGFR^+$ T cell population, corresponding to $CD8^+$ T cells uniformly expressing the introduced NY-ESO-1–specific TCR, thereby completing the generation of antigen-specific effector T cells for subsequent experiments.

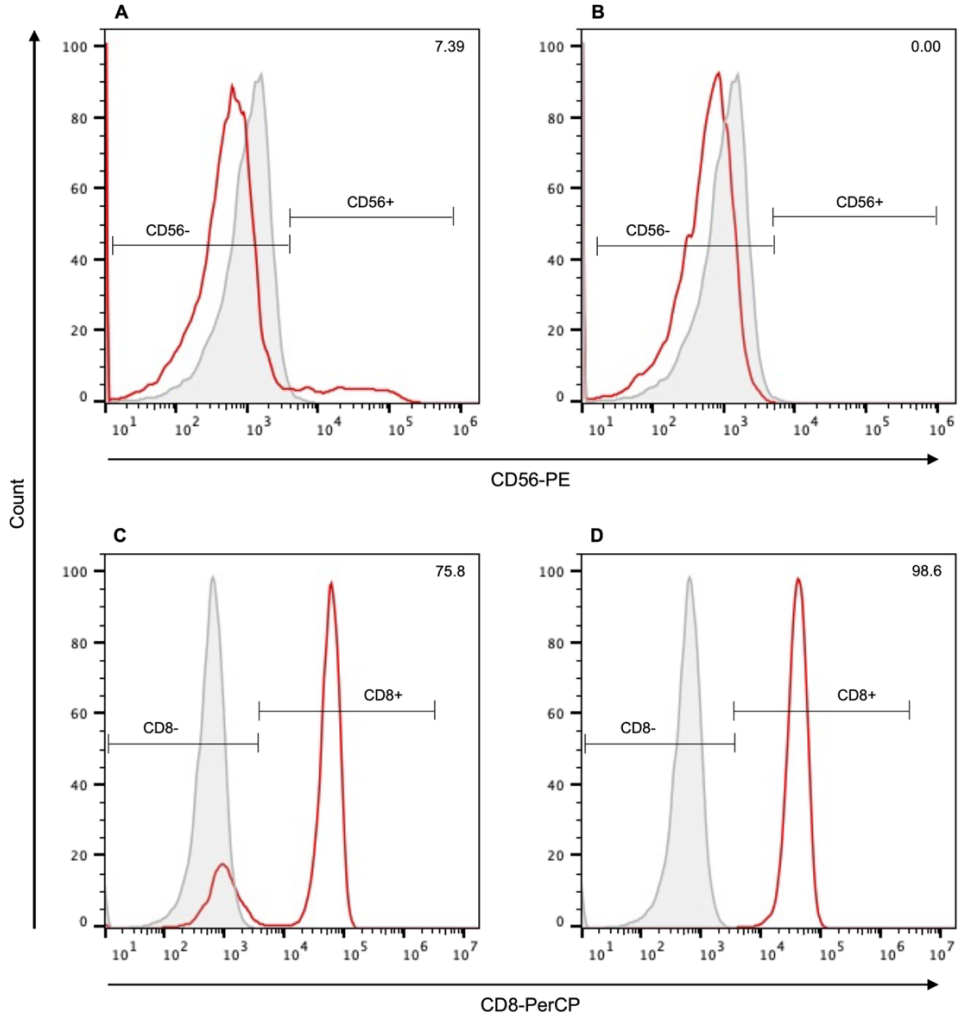

Figure 9. Validation of CD56 depletion and $CD8^+$ T-cell enrichment during generation of NY-ESO-1–reactive TCR T cells. (A–B) Following retroviral transduction with an NY-ESO-1–specific TCR construct, $CD56^+$ cells were depleted to remove NK cells and $CD56^+$ T-cell subsets**.** Panel A shows the population before CD56 MACS depletion, and Panel B shows the population after depletion**.** In panel B, overlaid histograms demonstrate complete loss of $CD56^+$ cells (red) compared with the isotype control (filled gray), confirming highly efficient depletion. (C–D) CD56-depleted T cells were subsequently subjected to $CD8^+$ MACS enrichment to obtain a purified $CD8^+$ T-cell fraction—an essential step for the downstream isolation of transduced $CD8^+$ $NGFR^+$ T cells. Panel C shows the population before CD8 MACS enrichment, and Panel D shows the population after enrichment. Overlaid histograms depict the $CD8^+$ population (red) relative to the isotype control (filled gray), demonstrating the successful generation of a highly pure $CD8^+$ T-cell subset. Percentages of marker-positive cells are indicated; histograms normalized to mode.

3.1.3 Validation of antigen-dependent PD-1 induction during co-culture with NY-ESO-1–expressing HRS cells

Following the generation of NY-ESO-1–reactive CD8⁺ T cells and endogenous TCR CD8⁺ T cells (see Sections 3.1.2), co-culture assays were performed to assess PD-1 expression in the context of NY-ESO-1 recognition. The HRS cell line L1236, which constitutively expresses PD-L1, was used as the target cell population. Because PD-1 is upregulated on CD8⁺ T cells following TCR-mediated recognition of cognate antigen presented on MHC class I, this system enabled evaluation of PD-1 induction specifically in response to NY-ESO-1/HLA-A*02 complexes on L1236 cells.

NY-ESO-1–reactive CD8⁺ T cells were co-cultured with NY-ESO-1–expressing L1236 cells, and PD-1 expression was analyzed by flow cytometry. A distinct PD-1⁺ population was detected within the NY-ESO-1–reactive CD8⁺ T-cell fraction following co-culture (see Figure 10, red), indicating successful recognition of NY-ESO-1 presented by L1236 cells and subsequent activation-induced PD-1 upregulation. In contrast, endogenous TCR CD8⁺ T cells, which lack the NY-ESO-1–specific TCR, did not express PD-1 when co-cultured under identical conditions (see Figure 10, blue). The absence of PD-1 expression in the endogenous TCR population demonstrates that PD-1 induction arose specifically from NY-ESO-1 recognition rather than nonspecific activation. These findings confirm that PD-1 expression in this system is strictly dependent on NY-ESO-1–specific TCR engagement.

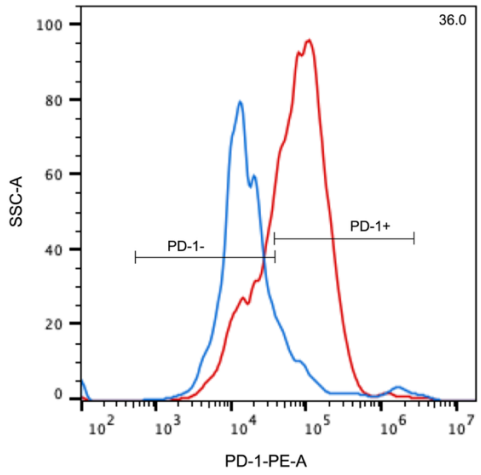

Figure 10. Antigen-dependent induction of PD-1 expression in NY-ESO-1–reactive CD8⁺ T cells following co-culture with NY-ESO-1⁺ L1236 HRS cells. Overlaid histograms compare PD-1 expression in endogenous TCR CD8⁺ T cells and NY-ESO-1–reactive CD8⁺ T cells after co-culture with the HRS cell line L1236, which endogenously expresses HLA-A*02 and was transduced to express NY-ESO-1 (NY-ESO-1⁺ L1236). Endogenous TCR CD8⁺ T cells (blue histogram) showed no induction of PD-1 following co-culture, consistent with the absence of NY-

ESO-1–specific TCR recognition. In contrast, NY-ESO-1–reactive CD8⁺ T cells (red histogram) upregulated PD-1 after co-culture, indicating activation through specific recognition of NY-ESO-1/HLA-A*02 complexes on L1236 cells. Percentages of PD-1⁺ cells are indicated; histograms are normalized to mode.

3.1.4 Validation of L1236 cells for antigen presentation and immunoregulation

To determine whether L1236 HRS cells can serve as appropriate target cells for CD8⁺ T cells engineered with a TCR recognizing the HLA-A*02-restricted melanoma antigen NY-ESO-1 [118] (NY-ESO-1 reactive TCR CD8⁺ T cells), endogenous HLA-A2 expression was first measured by flow cytometry. Since TCR recognition requires that both the engineered T cells and the target cells share the same HLA-A2 allele, confirming HLA-A2 expression on L1236 cells was essential. Staining for MHC class I molecules (HLA-A, -B, -C) showed high expression in the vast majority of L1236 cells, and subsequent staining specifically for HLA-A2 confirmed that these cells endogenously express the HLA-A2 allele (see figure 11A-B, red).

Flow cytometry thus confirmed robust expression of MHC class I and HLA-A2 on L1236 cells, supporting their suitability for presenting the NY-ESO-$1_{157–165}$ epitope in the context of HLA-A2.

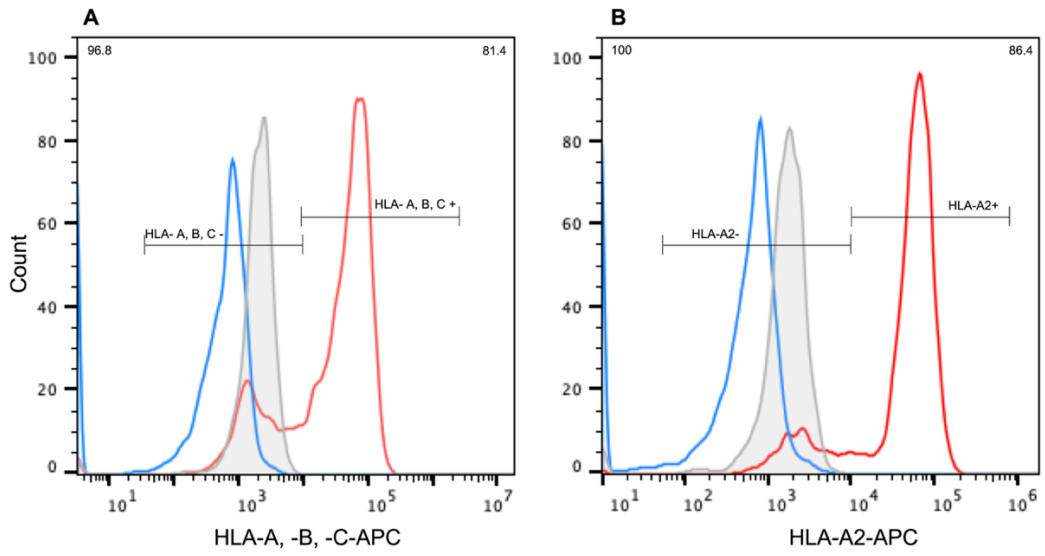

Figure 11. Validation of endogenous HLA-A2 expression and generation of MHC-I–deficient B2M knockout (KO) L1236 cells by flow cytometry. Overlaid histograms show staining for MHC class I (HLA-A, -B, -C) and HLA-A2 on wild-type L1236 cells (red) compared to B2M-KO L1236 cells (blue), with a filled gray histogram showing the respective isotype control. Wild-type L1236 cells displayed robust surface expression of MHC-I and HLA-A2, whereas L1236 B2M-KO cells lacked detectable expression, validating successful knockout and MHC-I deficiency.

To investigate the functional consequences of deficient antigen presentation, B2M KO L1236 cells were generated using sgRNA-mediated gene editing (section 2.3.4). Flow cytometry confirmed successful knockout by demonstrating complete loss of surface MHC class I molecules (HLA-A, -B, -C) and specific loss of HLA-A2 expression (see Figure 11A-B, blue). Compared to wild-type L1236 cells, B2M KO cells lacked detectable surface MHC I, generating an MHC I–deficient variant suitable for evaluating antigen-dependent T-cell responses.

Following validation of HLA-A2 expression on wild-type L1236 cells and confirmation of successful B2M knockout (resulting in HLA-A2–negative L1236 cells), the next step was to prepare the target cells for recognition by NY-ESO-1 reactive TCR $CD8^+$ T cells. Since the NY-ESO-1–specific TCR recognizes peptides derived from the NY-ESO-1 antigen presented by MHC class I molecules, both wild-type and B2M-KO L1236 cells were transduced with a retroviral vector encoding NY-ESO-1 to ensure target antigen expression (see Section 2.3.3). Transduction efficiency was assessed by flow cytometry using intracellular staining for NY-ESO-1 (see Appendix B). In the overlaid histograms (see Figure 12A, red), a clear rightward shift was observed in the red histogram compared to the isotype control (filled gray histogram), indicating that robust NY-ESO-1 expression was achieved in wild-type L1236 cells. Similarly high transduction efficiency was also observed in the B2M-KO L1236 cells (see Figure 12B, red).

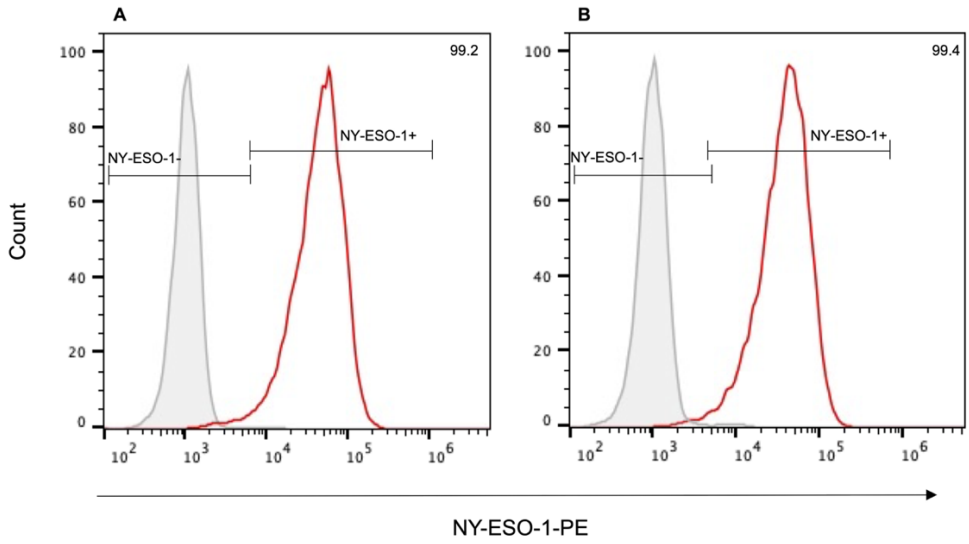

Figure 12. Validation of NY-ESO-1 transduction in L1236 cells by flow cytometry. (A), (B) Overlaid histograms show intracellular staining for NY-ESO-1 on wild-type L1236 cells (A, red) and B2M-KO L1236 cells (B, red) compared to matching isotype controls (filled gray). Both variants exhibited strong intracellular expression of NY-ESO-1, confirming successful transduction.

Following validation of HLA-A2 expression on wild-type L1236 cells and confirmation of transduction of the target antigen NY-ESO-1, the next step was to validate PD-L1 expression on the surface of L1236 cells to investigate the PD-1/PD-L1 pathway, which is relevant for the potential inhibition of T cell responses against HRS cells. To provide genetic evidence that PD-L1 expressed by L1236 cells contributed to the suppression of antigen-specific T-cell activation, PD-L1 was knocked out in L1236 cells (see Section 2.3.4).

PD-L1 expression was measured by flow cytometry in both wild-type L1236 cells and the B2M KO variant. In the overlaid histogram (see Figure 13A), the red histogram showed a clear rightward shift compared to the PD-L1 KO cells (blue histogram), indicating robust PD-L1 surface expression in wild-type L1236 cells, whereas the knockout cells showed no detectable PD-L1 expression. Similarly, B2M KO L1236 cells also exhibited high PD-L1 surface expression, and this was completely lost in the corresponding PD-L1 KO variant (see Figure 13B).

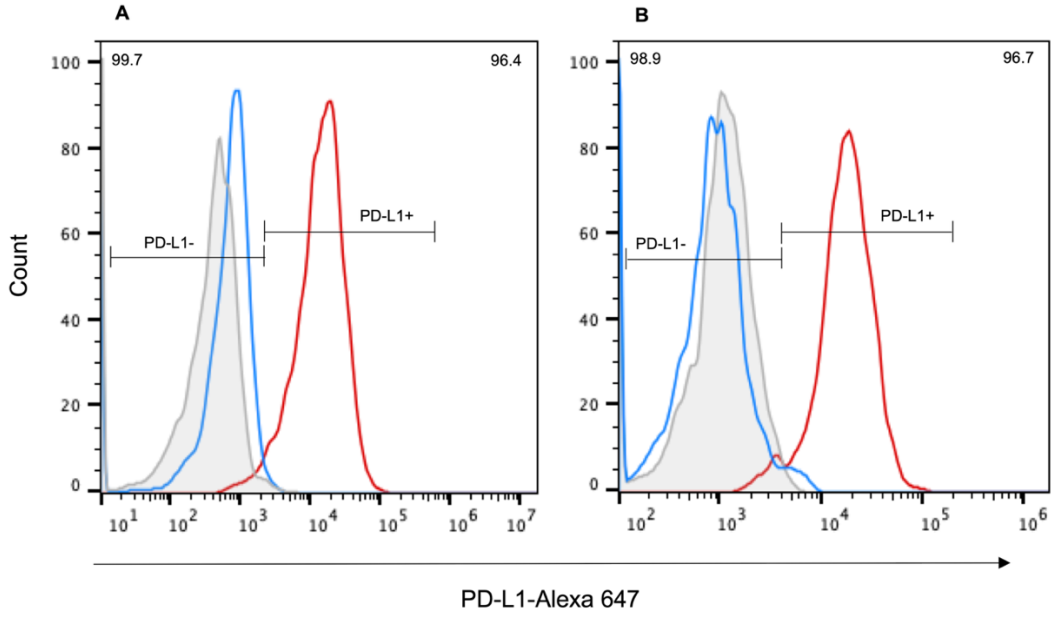

Figure 13. Validation of endogenous PD-L1expression and generation of PD-L1–knockout (KO) L1236 cells by flow cytometry. (A), (B) Overlaid histograms show PD-L1 staining on wild-type L1236 cells (A, red) and B2M-KO L1236 cells (B, red) compared to their respective PD-L1 KO counterparts (blue), with a filled gray histogram showing the respective isotype control. Both wild-type and B2M-KO variants exhibited robust PD-L1 expression, whereas PD-L1 KO cells lacked detectable expression, validating endogenous PD-L1 expression and successful knockout in each variant.

Both the PD-L1-deficient models and their wild-type counterparts were subsequently used to evaluate the functional impact of tumor cell PD-L1 expression on T-cell responses.

3.1.5 Validation of PD-1 expression in HEK293FT cells

To investigate the impact of PD-1/PD-L1 reverse signaling on HRS cell proliferation and survival, HEK293FT cells were engineered to express PD-1 via plasmid transfection as described in Section 2.5.5. Flow cytometry confirmed that wild-type HEK293FT cells did not endogenously express PD-1, as the red histogram overlapped with the isotype control (filled gray), indicating a PD-1$^-$ population (see Figure 14A).

In contrast, transfected HEK293FT cells displayed a clear rightward shift in the red histogram compared to the isotype control (filled gray), confirming successful surface expression of PD-1 (see Figure 14B). This generated an enriched PD-1$^+$ HEK293FT cell population suitable for co-culture with PD-L1$^+$ L1236 cells to assess the functional consequences of prolonged checkpoint engagement.

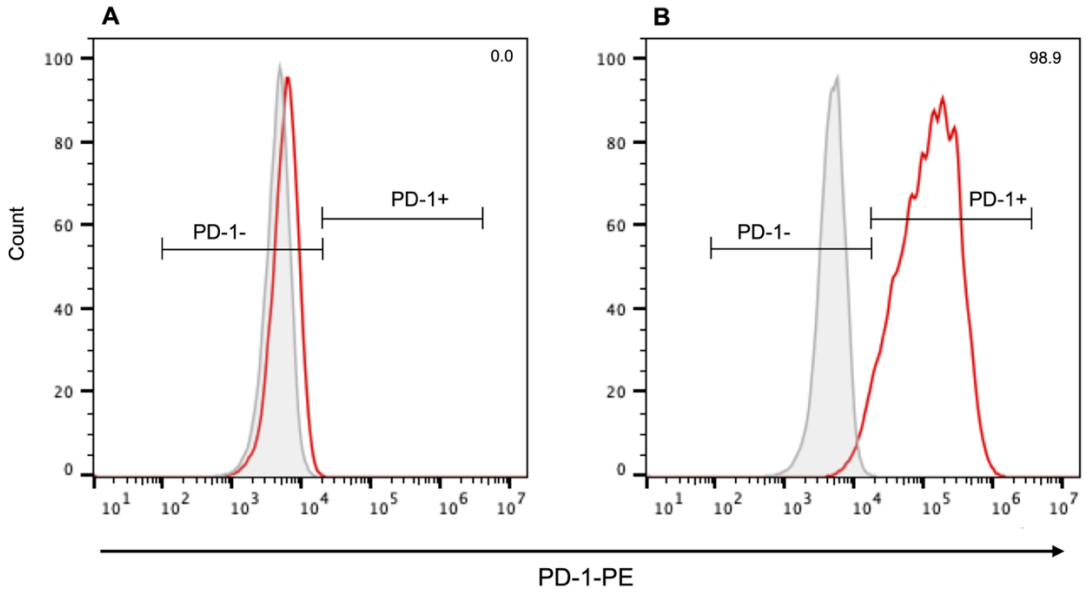

Figure 14. Validation of endogenous PD-1 expression and PD-1 transfection in HEK293FT cells by flow cytometry. (A), (B) Overlaid histograms show staining for PD-1 on wild-type HEK293FT cells (A, red) and transfected HEK293FT cells (B, red) compared to matching isotype controls (filled gray). (A) Wild-type HEK293FT cells showed no detectable PD-1 surface expression, resulting in a PD-1$^-$ population of ~100% purity. (B) In contrast, transfected HEK293FT cells showed robust PD-1 surface expression, resulting in a PD-1$^+$ population of ~100% purity.

3.1.6 Validation of M1/M2 Macrophage Polarization and NY-ESO-1 Expression

As a first step to determine whether Hodgkin cell CM can influence macrophage polarization, monocyte-derived macrophages were first differentiated and polarized into M1 and M2 subtypes to serve as defined reference populations (Section 2.4.1). M1 and

M2 subtypes were generated under standard conditions as baseline controls for comparison with CM-treated macrophages. Morphological validation was performed by light microscopy (see Figure 14A–B). M1 macrophages exhibited a rounded or pancake-like morphology, while M2 macrophages appeared more elongated and spindle-shaped. These distinct morphological features are consistent with previously published studies showing that M1 polarization (induced by IFN-γ and LPS) results in more circular cell shapes, whereas M2 polarization (stimulated by IL-4) produces more elongated macrophages [160,161]. This morphological confirmation validates the polarization protocol and provides a reference for studying the effects of Hodgkin cell–derived cytokines and chemokines on macrophage phenotype. It also enabled generation of M2 macrophages for co-culture with T cells (see Section 3.4).

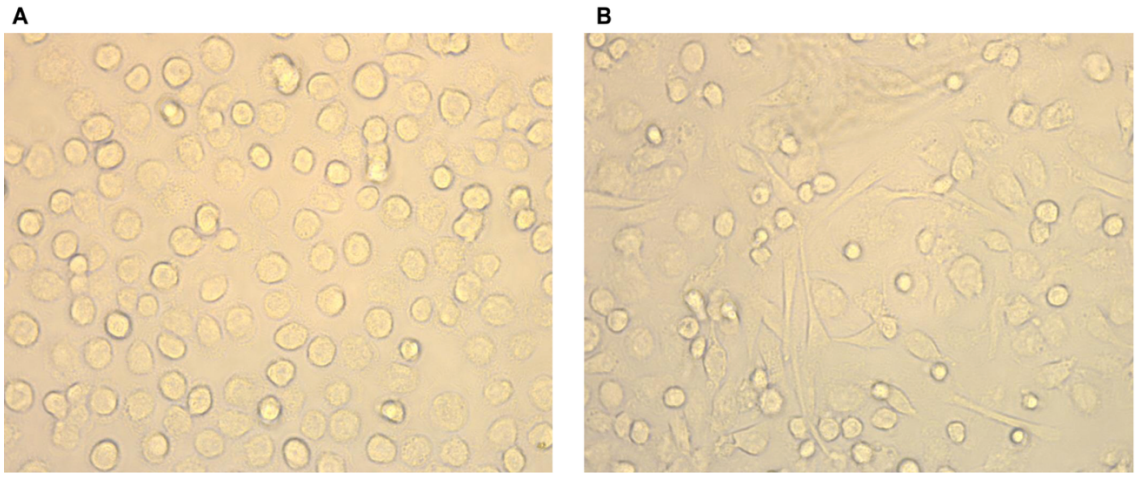

Figure 15. Validation of M1 and M2 macrophage polarization by light microscopy. (A) Light microscopy image of M1-polarized macrophages (stimulated with LPS and IFN-γ) showing a predominantly rounded morphology. (B) Light microscopy image of M2-polarized macrophages (stimulated with IL-4) displaying an elongated, spindle-like shape. These morphological characteristics confirm successful polarization. Images were acquired at 400× total magnification.

Validation of generation of NY-ESO-1 expressing M2

Following validation of M2 macrophage polarization, the next step was to prepare M2 macrophages for recognition by NY-ESO-1–reactive TCR $CD8^+$ T cells. As previously described, the NY-ESO-1–specific TCR recognizes peptides derived from the NY-ESO-1 antigen presented on MHC class I molecules. To ensure target antigen expression, M2 macrophages were transfected with a plasmid encoding NY-ESO-1 fused to GFP (see Section 2.4.2). Transfection efficiency was assessed by fluorescence microscopy based on GFP expression using the Leica THUNDER Imager DM i8

widefield microscope. GFP-positive cells were clearly visible (see Figure 16), confirming successful transfection of M2 macrophages.

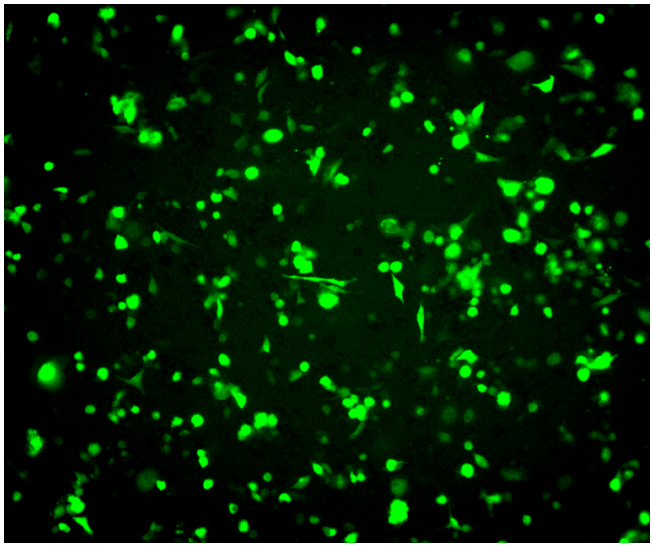

Figure 16. Validation of NY-ESO-1 expression in M2 macrophages by fluorescence microscopy. M2 macrophages were transfected with a plasmid encoding NY-ESO-1 fused to GFP to enable recognition by NY-ESO-1–specific TCR $CD8^+$ T cells. GFP-positive cells were clearly visible, confirming successful transfection. Images were acquired using the Leica THUNDER Imager DM i8 widefield microscope. 20× magnification. Scale bar = 50 µm.

3.2 Validation of PLA and mIF staining assays

To establish PLA and mIF as reliable readouts in this study, a stepwise validation was performed. Antibody specificity and staining performance were first confirmed by chromogenic IHC, and initial working concentrations were defined. IHC stainings were reviewed by a pathologist to confirm specificity. Based on these results, the selected antibody clones and dilutions were transferred to Brightfield PLA, where concentrations were further refined to balance signal specificity and background. After successful validation in Brightfield PLA, the workflow was adapted to Fluorescent PLA, which required additional optimization of antibody concentrations as well as adjustments to deparaffinization, dehydration, and HIER conditions to achieve a stable and reproducible PLA signal suitable for higher-resolution imaging.

In parallel, a corresponding validation pipeline was established for mIF. Antibody specificity was first confirmed by chromogenic IHC and then transferred to single-stain immunofluorescence to assess performance under fluorescent conditions. Based on these results, individual antibodies were incorporated into multiplex panels, with sequential

adjustments made to staining order, fluorophore selection, and antibody concentrations to minimize channel crosstalk and background. The cHL cases, representing the primary disease context of this study, were used throughout the optimization and validation process to ensure both technical feasibility and biological relevance.

Together, these steps (details description in Chapters 3.2.1 to 3.2.4) established specific and reproducible validated PLA and mIF staining pipelines, suitable for downstream analyses in cHL tissues.

3.2.1 Validation of antibodies by IHC

Each antibody included in PLA and mIF panels was first assessed by chromogenic IHC on cHL FFPE tissues (see Section 2.6.3). CD30, CD163, CD68, CD3, and CD8 demonstrated staining patterns consistent with their known cellular and subcellular localization in HRS cells, macrophages, and T-cell subsets (see Figure 17). PD-1 and PD-L1 exhibited staining patterns consistent with their established expression profiles, including PD-1 on T cells and PD-L1 on HRS cells and tumor-associated macrophages, confirming appropriate membranous localization (see Figure 18). Staining patterns were reproducible across multiple cHL cases, and non-specific background staining was minimal for all antibodies. Negative controls, including omission of primary antibody yielded no detectable staining. Clone comparison and titration experiments further identified the optimal antibody clone and an initial dilution based on signal intensity, accurate localization pattern, and overall signal-to-noise ratio (see Figures 17-18). These IHC validation steps established reliable baseline performance, with final antibody dilutions subsequently readjusted during optimization of PLA and IF assay conditions, confirming specificity and supporting downstream assay development.

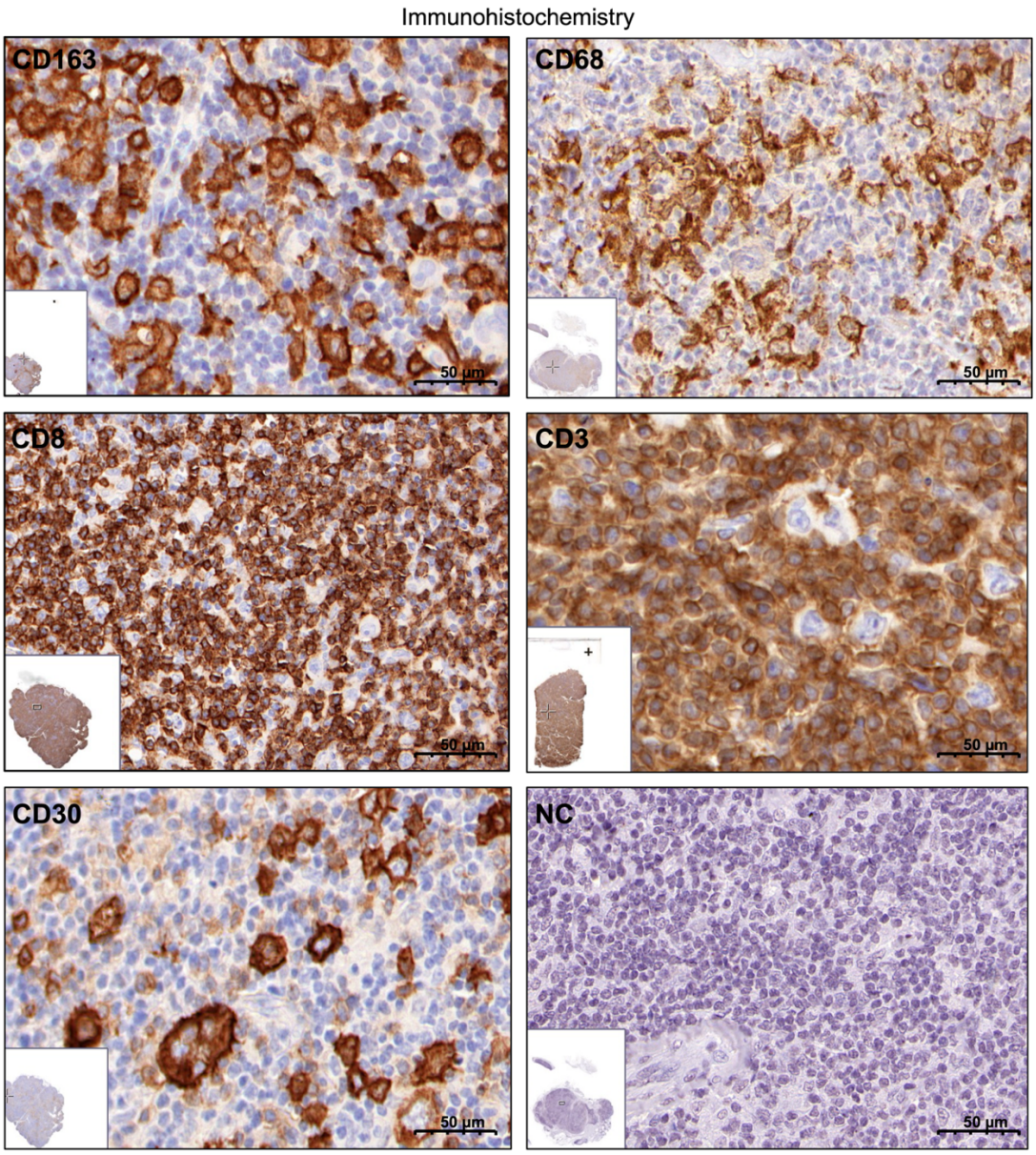

Figure 17. Validation of antibodies by IHC. Representative chromogenic IHC staining (40× magnification) of cHL tissues showing validation of antibodies used for downstream mIF analyses. CD30 staining highlights HRS cells with strong membranous/cytoplasmic expression. CD163 and CD68 mark macrophages with expected cytoplasmic localization, while CD3 and CD8 staining identify T cell populations with characteristic membranous expression. Negative control (NC), performed by omission of the primary antibody, demonstrates absence of non-specific background staining. These results confirm antibody specificity and suitability for subsequent PLA and mIF experiments. Slides were digitized using the Pannoramic SCAN II slide scanner. Scale bar = 50 µm.

3.2.2 Validation of Brightfield PLA

Following IHC validation, antibodies were applied to Brightfield PLA. Side-by-side comparison of chromogenic IHC and PLA (see Figure 18) demonstrated that PLA puncta formed precisely in regions showing PD-1 or PD-L1 expression. These patterns were consistent with their expected cellular distribution and provided direct confirmation that PLA signal corresponds to true antigen localization. This PLA validation was performed specifically for PD-1 and PD-L1 antibodies, and initial dilutions derived from IHC were used as a starting point for PLA-specific optimization to maximize puncta formation while minimizing non-specific background. PLA reactions yielded distinct puncta localized to the expected cellular compartments. Negative controls, in which one primary antibody was omitted, showed minimal puncta formation, thereby confirming assay specificity. This spatial correspondence between chromogenic IHC signal and PLA puncta demonstrates that PLA detects PD-1/PD-L1 interactions only in antigen-positive regions, supporting accurate proximity detection. Together, these results validate the suitability of PD-1 and PD-L1 antibodies for PLA–based proximity assays.

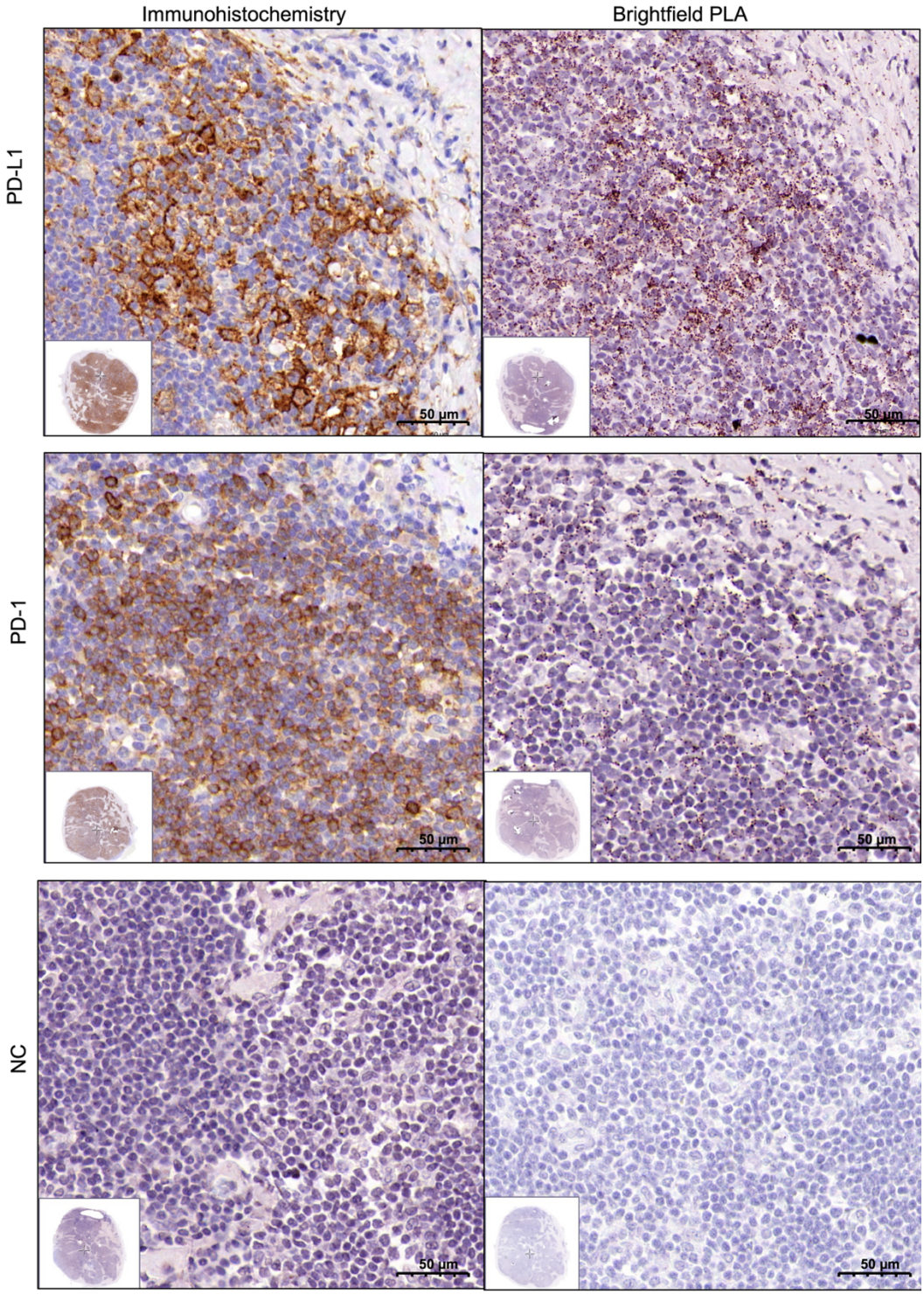

Figure 18. Validation of PD-1 and PD-L1 antibodies for Brightfield PLA. Side-by-side chromogenic IHC and Brightfield PLA images of PD-1 and PD-L1 staining in cHL tissue (40× magnification). Chromogenic IHC demonstrates specific expression of PD-1 and PD-L1 with expected cellular distribution. Corresponding Brightfield PLA confirms the suitability of both antibodies for proximity ligation, yielding distinct puncta localized to regions corresponding to IHC-positive staining. Negative controls (NC), performed by omission of one primary antibody, show absence of puncta, confirming assay specificity. These results validate PD-1 and PD-L1 antibodies for use in Brightfield and Fluorescence PLA assays. Slides were digitized using the Pannoramic SCAN II slide scanner. Scale bar = 50 µm.

3.2.3 Validation of Fluorescent PLA

Optimized antibody pairs for PD-1 and PD-L1 from Brightfield PLA were subsequently transferred to Fluorescent PLA (see Section 2.6.4). As the assay was transitioned to fluorescent PLA, antibody concentrations were further refined, and deparaffinization, dehydration, and HIER conditions were adjusted to ensure a stable and reproducible fluorescent PLA signal. The fluorescent readout enabled higher-resolution imaging, and PD-1/PD-L1 interactions were visualized as distinct puncta, consistent with the known expression patterns of PD-1 and PD-L1 in cHL. Omission of one primary antibody resulted in absence of puncta, confirming assay specificity (see Figure 19). These results validate the fluorescent PLA pipeline for detection of PD-1/PD-L1 interactions in cHL.

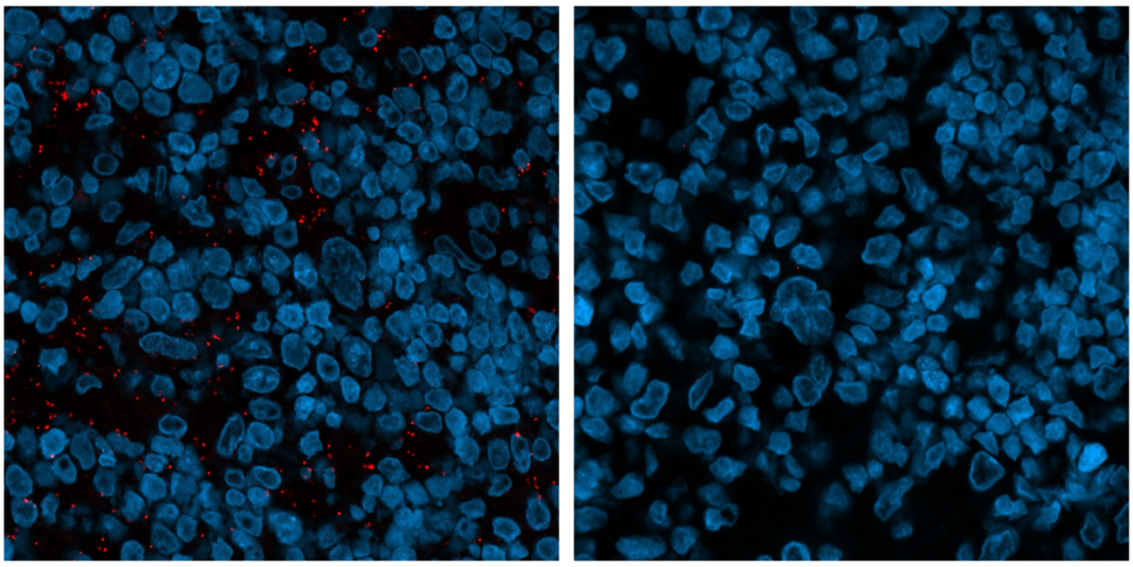

Figure 19. Validation of PD-1/PD-L1 interaction by Fluorescent PLA. Representative fluorescent PLA images (40× magnification) of classical Hodgkin lymphoma (cHL) tissue demonstrating PD-1/PD-L1 interactions. Distinct fluorescent puncta are visible in tumor-associated regions, consistent with the expected biological distribution of PD-1/PD-L1 proximity. Negative control (NC), performed by omission of one primary antibody, shows absence of puncta, confirming assay specificity. These results validate the fluorescent PLA assay for detecting PD-1/PD-L1 interactions in cHL. Images were acquired using a Zeiss LSM 800 Confocal Laser Scanning Microscope. Scale bar = 50 µm.

3.2.4 Validation of multiplex immunofluorescence (mIF)

In parallel to PLA, antibodies were validated for use in mIF. Each antibody was first transferred from IHC to single-plex IF to confirm performance under fluorescence conditions. Single-stain experiments confirmed expected localization patterns and demonstrated minimal autofluorescence or non-specific background in negative controls lacking the primary antibody. Once validated individually, antibodies were combined into

multiplex IF panels. Fluorophore selection, order of staining and antibody concentrations were optimized to avoid spectral overlap and preserve antigenicity across sequential staining and stripping steps. Comparisons of single-plex and multiplex conditions confirmed that staining intensity and localization were preserved consistently in the multiplex setting. All validation and optimization steps were performed directly on cHL tissue sections to ensure that staining performance and spatial marker distribution reflected the relevant disease context. Expected expression and spatial patterns of immune and tumor-associated markers were reproduced, confirming both technical feasibility and biological relevance of the mIF pipeline in cHL (see Figures 20-21).

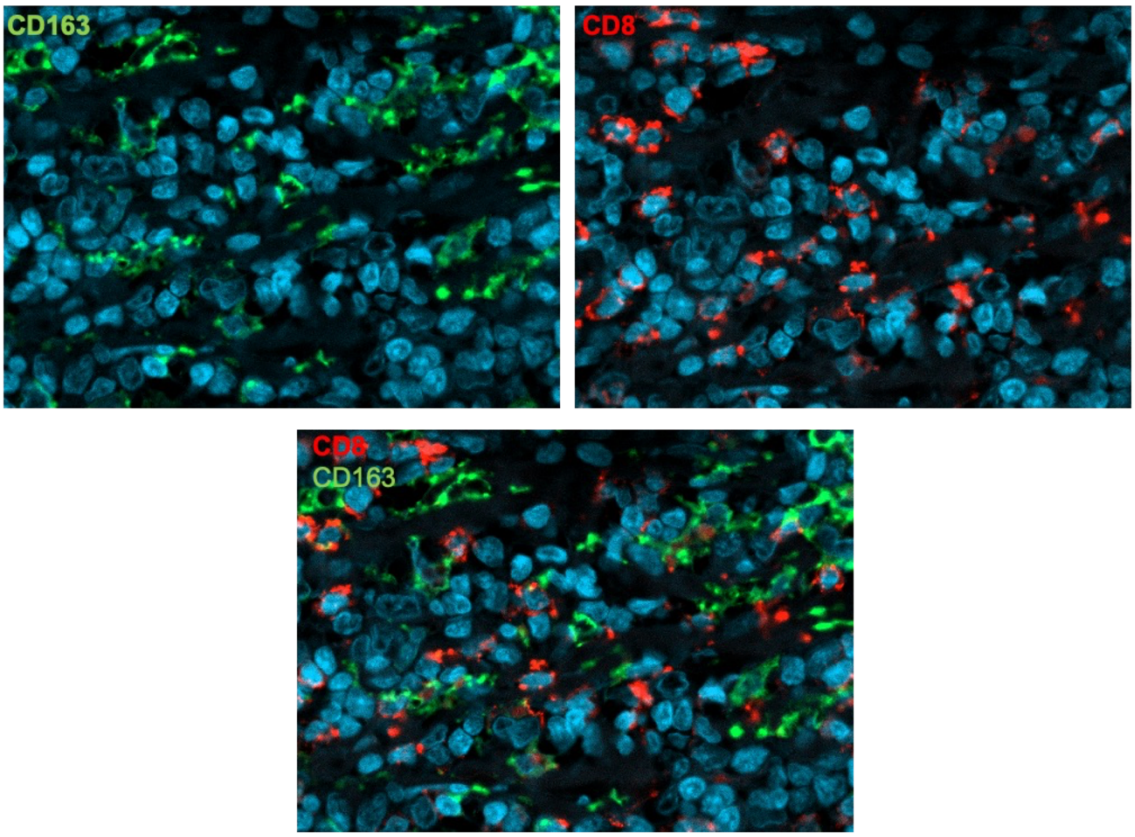

Figure 20. Validation of CD163 and CD8 antibodies in single and combined IF staining. Representative single-plex immunofluorescence staining (40× magnification) of cHL tissue showing CD163 and CD8 individually, followed by their combined staining in a multiplex format. CD163 demonstrates expected cytoplasmic localization in macrophages, while CD8 highlights cytotoxic T cells with characteristic membranous expression. In the combined panel, both markers retain their expected distribution and staining intensity, confirming compatibility and preservation of signal in the multiplex setting. CD163 was detected using Alexa Fluor 488 and CD8 with Alexa Fluor 563. Images were acquired using a Zeiss LSM 800 Confocal Laser Scanning Microscope. Scale bar = 50 µm.

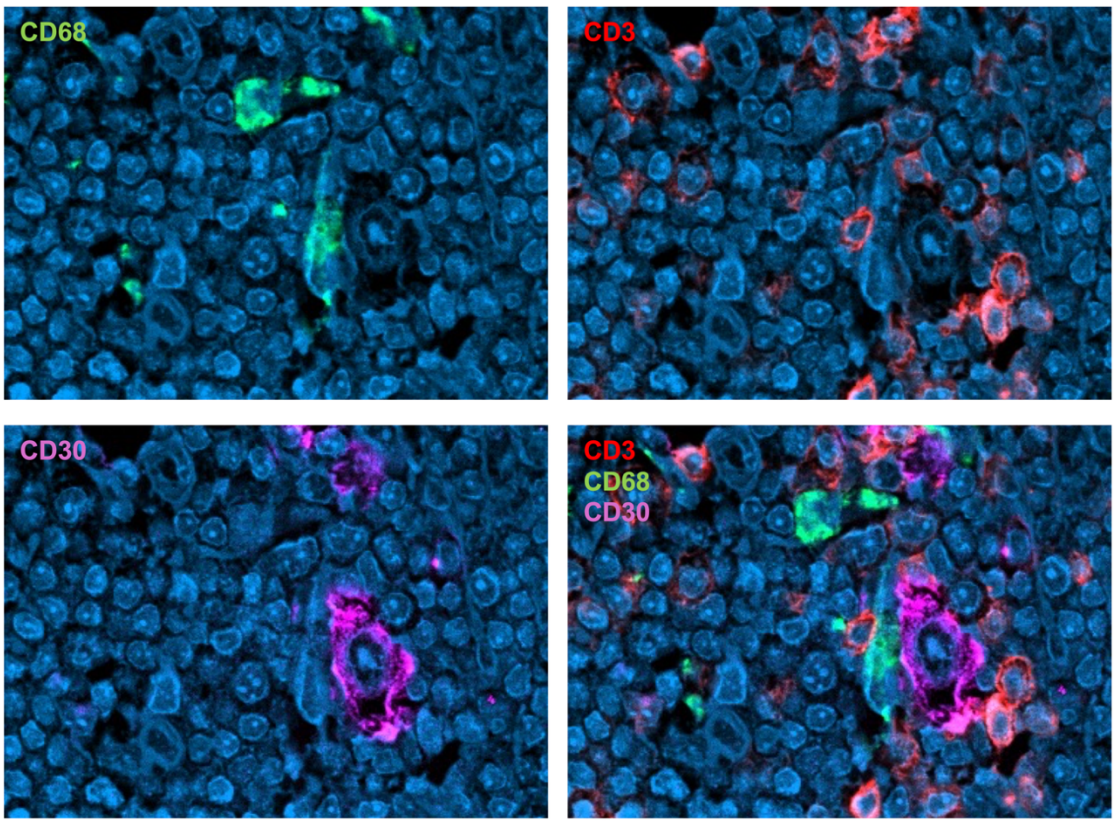

Figure 21. Validation of CD68, CD3, and CD30 antibodies in single and combined IF staining. Single-plex immunofluorescence staining of CD68, CD3, and CD30 in cHL tissue demonstrates expected expression patterns, with CD68 marking macrophages, CD3 identifying T cells, and CD30 staining Hodgkin Reed–Sternberg cells. The combined multiplex staining panel shows preservation of signal intensity, spatial localization, and antigen distribution across all three markers, confirming suitability of these antibodies for inclusion in mIF analyses. CD68 was visualized with Alexa Fluor 488, CD3 with Alexa Fluor 563, and CD30 with Alexa Fluor 647. Images were acquired using a Zeiss LSM 800 Confocal Laser Scanning Microscope. 40× magnification. Scale bar = 50 µm.

3.3 PD-L1 on HRS cells suppresses T cell activation, reversible by PD-1 blockade

To determine whether antigen-specific $CD8^+$ T cells can directly recognize and exert cytotoxicity against HRS cells, and whether PD-1 blockade enhances these responses, a co-culture assay was established. TCR recognition requires that both the engineered T cells and the target cells share the same HLA-A2 allele. Therefore, $CD8^+$ T cells transduced with a recombinant TCR specific for the HLA-A*02–restricted melanoma antigen NY-ESO-1 (epitope 157–165) [118] (NY-ESO-1 TCR $CD8^+$ T cells) were co-cultured with the HRS cell line L1236, which endogenously expresses HLA-A2 and was transduced to express NY-ESO-1 (hereafter NY-ESO-1^+ L1236).

To assess the role of antigen presentation via MHC-I in $CD8^+$ T cell activation, cytotoxicity, and induction of apoptosis in target cells, co-cultures were performed using either wild-type L1236 cells ($MHC\text{-}I^+$) or B2M-KO L1236 cells (MHC-I–deficient), both expressing NY-ESO-1. In parallel, untransduced T cells expressing only endogenous TCR (endogenous TCR $CD8^+$ T cells) were cultured with the indicated L1236 variants as controls (see Figure 22B, 23, 24, 25). To evaluate whether blocking PD-1/PD-L1 immune checkpoint interactions enhances T-cell responses, co-cultures were treated with 15 µg/ml Nivolumab, an anti-PD-1 antibody, or left untreated by culturing in T-cell medium alone (see Figure 22, 23, 24). T cell activation was assessed by 4-1BB expression, cytotoxic activity by CD107a surface expression as a marker of degranulation, and tumor cell apoptosis by caspase-3 activation in HRS cells. This experimental design enabled comparison of T cell activation, cytotoxicity and apoptosis in target HRS cells in the presence or absence of MHC-I expression and checkpoint inhibition.

T cell activation was influenced by both MHC-I expression on target cells and PD-1 blockade. When co-cultured with MHC-I–positive NY-ESO-1–expressing L1236 cells, $CD8^+$ T cells expressing the NY-ESO-1–specific TCR showed activation, indicated by increased 4-1BB expression (see Figure 22B; representative flow cytometry plots shown in Figure 23B and E), whereas activation was significantly reduced when MHC-I–deficient B2M-KO L1236 cells were used. This confirmed that antigen presentation via MHC-I is essential for TCR-mediated recognition.

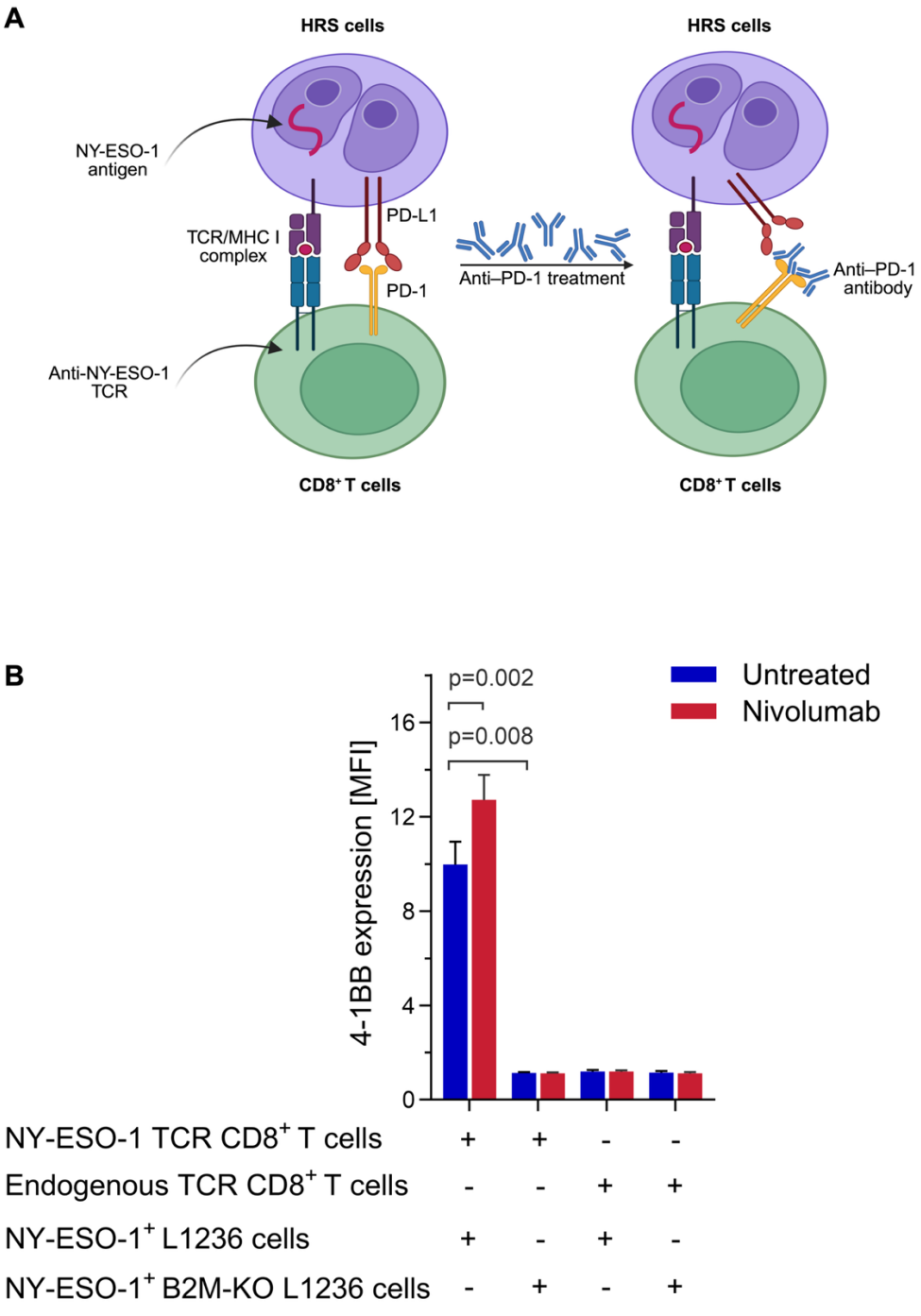

Figure 22. PD-1/PD-L1 blockade restores T-cell activation in an MHC-I–dependent manner in co-cultures with NY-ESO-1–expressing HRS cells. (A) Schematic of the T-cell co-culture assay used for the analysis of T-cell activation, cytotoxicity, and apoptosis of Hodgkin Reed–Sternberg cells (HRS). HLA-A2⁺ L1236 (HRS) cells transduced to express the NY-ESO-1 antigen (NY-ESO-1⁺ L1236) were co-cultured with CD8⁺ T cells engineered to express a TCR recognizing the HLA-A2–restricted NY-ESO-1$_{157–165}$ peptide (NY-ESO-1 TCR CD8⁺ T cells). Co-cultures included either wild-type L1236 cells (MHC-I⁺) or B2M-knockout (KO) L1236 cells (MHC-I–deficient), both expressing NY-ESO-1. Endogenous TCR CD8⁺ T cells were cultured in parallel with the same L1236 variants as antigen specificity controls. Cells were cultured in T-cell medium alone (untreated, blue) or treated with 15 µg/ml Nivolumab (red). (B) T-cell activation was assessed by surface expression of 4-1BB after 24 h of co-culture (n = 4). Data are presented as mean ± SEM. Statistical significance was determined using a paired two-tailed Student's t-test; *p*-values are shown on the figure.

Notably, within MHC-I–positive co-cultures, treatment with Nivolumab further enhanced T cell activation, as reflected by significantly increased 4-1BB expression (see Figure 22; representative flow cytometry plots shown in Figure 23B and C), compared to untreated control. This effect was specific to MHC-I–positive conditions, as no comparable enhancement was observed when B2M-KO (MHC-I–deficient) L1236 cells were used, highlighting the requirement for antigen presentation in PD-1 blockade–mediated restoration of T cell activation (see Figure 22; representative flow cytometry plots shown in Figure 23E and F).

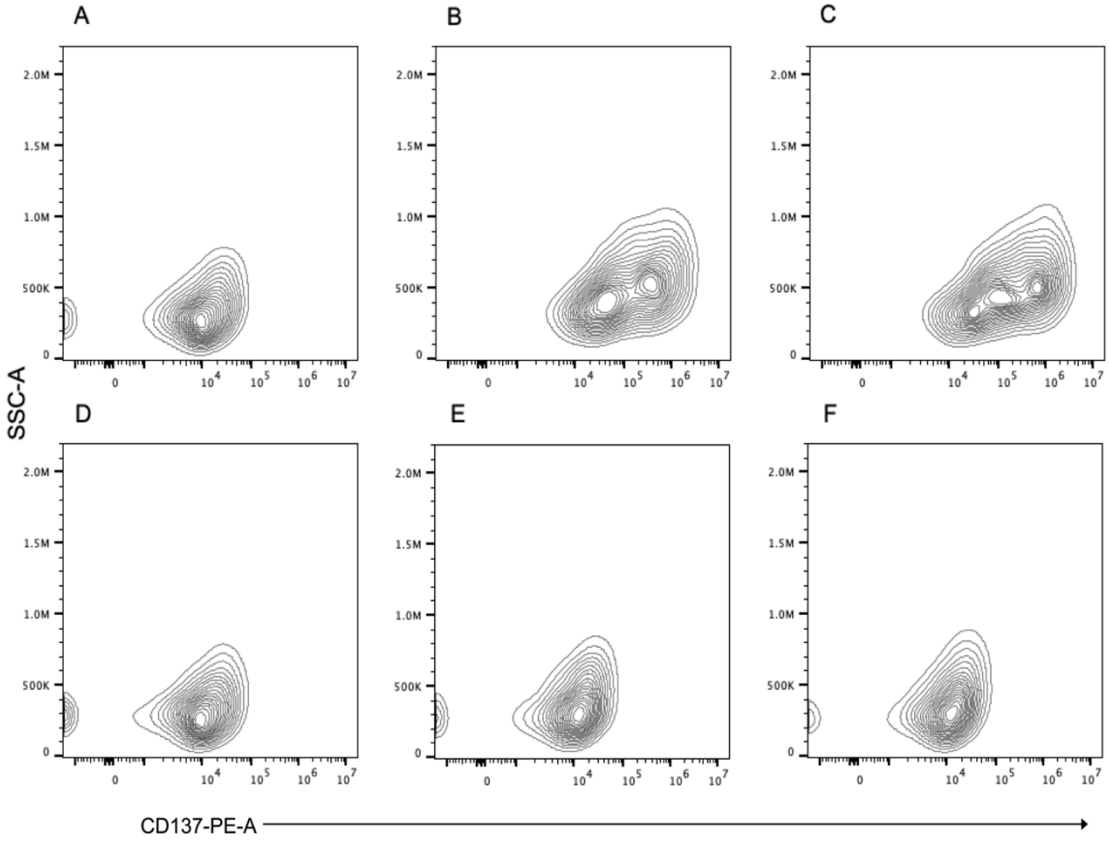

Figure 23. Representative flow-cytometry plots showing that PD-1 blockade enhances T-cell activation in MHC-I$^+$ co-cultures but not in MHC-I–deficient targets. (A–F) Primary human CD8$^+$ T cells transduced with a TCR specific for the NY-ESO-1 antigen (NY-ESO-1 TCR CD8$^+$ T cells) or untransduced (endogenous TCR) CD8$^+$ T cells were co-cultured for 24 h with NY-ESO-1$^+$ L1236 HRS cells. Co-cultures included either wild-type L1236 cells (MHC-I$^+$) or B2M-knockout (KO) L1236 cells (MHC-I–deficient). Within each condition, cultures were left untreated (control) or treated with 15 µg/ml Nivolumab. (A–C) Co-cultures with MHC-I$^+$ L1236 cells: (A) endogenous TCR CD8$^+$ T cells, (B) NY-ESO-1 TCR CD8$^+$ T cells – untreated, (C) NY-ESO-1 TCR CD8$^+$ T cells – treated with Nivolumab. (D–F) Co-cultures with MHC-I–deficient B2M-KO L1236 cells: (D) endogenous TCR CD8$^+$ T cells, (E) NY-ESO-1 TCR CD8$^+$ T cells – untreated, (F) NY-ESO-1 TCR CD8$^+$ T cells – treated with Nivolumab. CD8$^+$ T cells were gated and analyzed for 4-1BB (CD137) expression as a marker of activation. Representative plots show up-regulation of 4-1BB upon co-culture with MHC-I$^+$ targets and its reduction in MHC-I–deficient conditions, with further enhancement by Nivolumab specifically in MHC-I$^+$ co-cultures.

To determine whether the observed activation translated into effector function, T cell cytotoxicity was also assessed in the same experimental setup. When co-cultured with MHC-I–positive NY-ESO-1–expressing L1236 cells, $CD8^+$ T cells expressing the NY-ESO-1–specific TCR showed increased CD107a surface upregulation as a marker of degranulation (see Figure 24A), indicating effective cytotoxic activity. In contrast, CD107a expression was significantly reduced when MHC-I–deficient B2M-KO L1236 cells were used, demonstrating that antigen presentation via MHC-I is essential for TCR-mediated cytotoxicity. Moreover, within MHC-I–positive co-cultures, treatment with Nivolumab tended to enhance T-cell cytotoxicity, as reflected by a trend toward higher CD107a expression compared to untreated controls (see Figure 24A). While this difference did not reach statistical significance, a consistent trend was observed, suggesting that PD-1 blockade may contribute to enhanced cytotoxic potential. This trend was specific to MHC-I–positive conditions, as no comparable tendency was observed with MHC-I–deficient target cells, consistent with MHC-I–dependent, antigen-specific effects of PD-1 blockade.

To evaluate the impact of these interactions on target cell death, apoptosis of HRS cells was assessed by caspase-3 activation. When co-cultured with MHC-I–positive L1236 cells, NY-ESO-1 TCR $CD8^+$ T cells induced elevated caspase-3 activation in target cells, confirming efficient T-cell–mediated apoptosis (see Figure 24B), whereas caspase-3 activation was significantly lower when MHC-I–deficient L1236 cells were used, demonstrating that antigen presentation via MHC-I is essential for TCR-dependent killing. Furthermore, in MHC-I–positive co-cultures, Nivolumab treatment tended to increase caspase-3 activation in target cells, indicating enhanced tumor-cell apoptosis (see Figure 24B). Although this difference did not reach statistical significance due to the limited number of replicates (n=2, restricted by available cell numbers), the trend was consistent across experiments, suggesting that PD-1 blockade may promote T-cell–mediated killing of HRS cells. This tendency was not observed with MHC-I–deficient target cells, indicating that effective antigen presentation is required for PD-1 blockade to augment T-cell–mediated apoptosis.

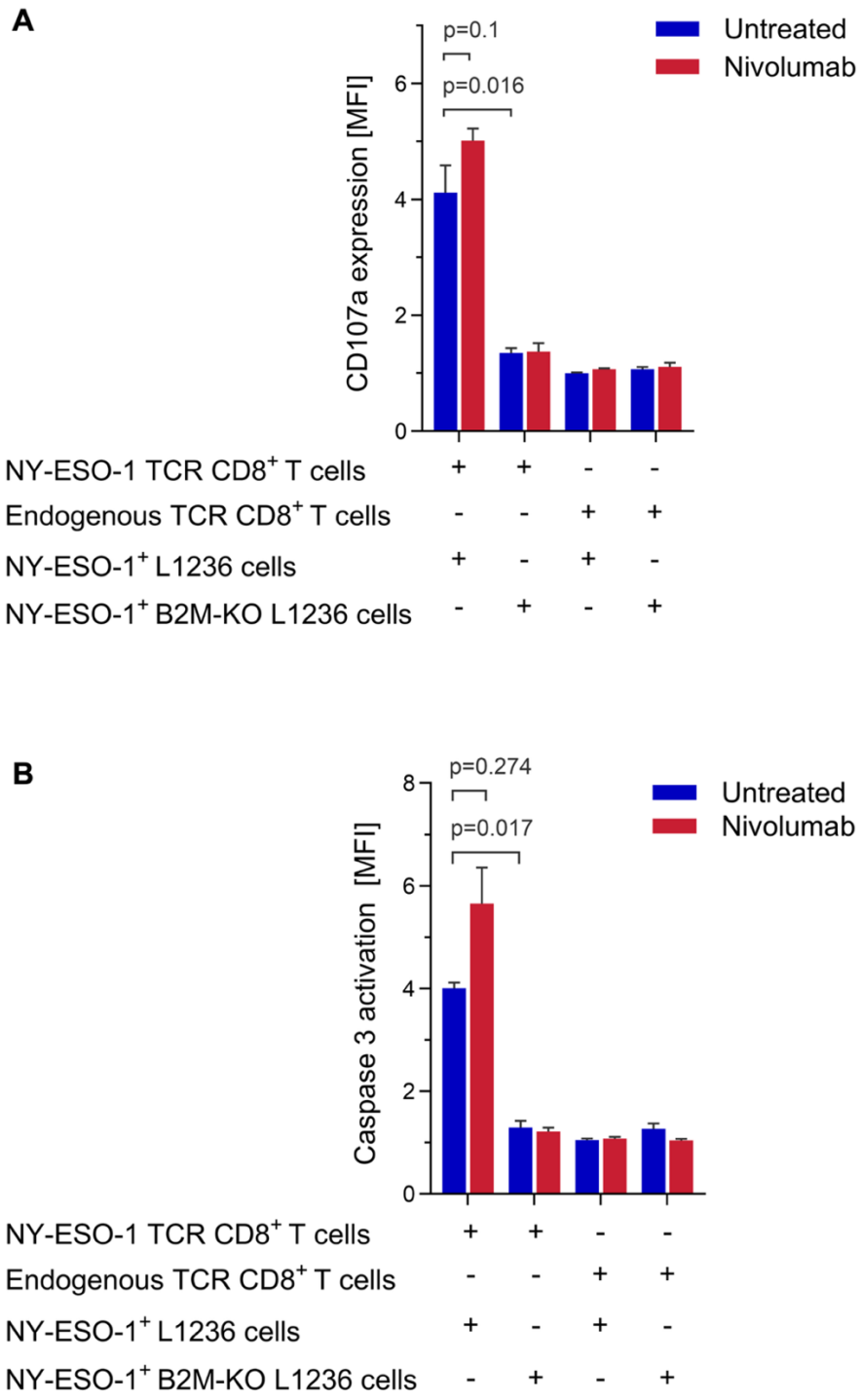

Figure 24. PD-1/PD-L1 blockade enhances T-cell cytotoxicity and induces apoptosis of HRS cells in an MHC-I–dependent manner. Co-cultures were established as described in Figure 20A. Primary human CD8+ T cells transduced with a TCR specific for the NY-ESO-1 antigen (NY-ESO-1 TCR CD8+ T cells) or endogenous TCR CD8+ T cells were co-cultured with NY-ESO-1+ L1236 HRS cells, either wild-type (MHC-I+) or B2M-KO (MHC-I–deficient). Cells were cultured in T-cell medium alone (untreated, blue) or treated with 15 µg/ml Nivolumab (red). (A) T-cell cytotoxicity was assessed by surface expression of CD107a as a marker of degranulation after 24 h of co-culture (n = 2). (B) Apoptosis of HRS cells was evaluated by caspase-3 activation after 6 h of co-culture (n = 2). Data are presented as mean ± SEM. Statistical significance was determined using a paired two-tailed Student's t-test; *p*-values are shown on the figure.

As expected, endogenous TCR CD8⁺ T cells did not exhibit significant activation, cytotoxicity, or induction of apoptosis across all co-culture conditions (MHC-I–positive and MHC-I–deficient L1236, ± Nivolumab), confirming the antigen specificity of the observed effects (see Figures 22, 23).

Genetic knockout of PD-L1 enhances antigen-specific T cell activation

To validate the role of PD-L1 in suppressing T cell responses, NY-ESO-1–expressing L1236 cells and NY-ESO-1 expressing B2M-KO L1236 were lentivirally transduced to generate PD-L1-KO variants (see Section 2.3.4 and Figure 13C-D).

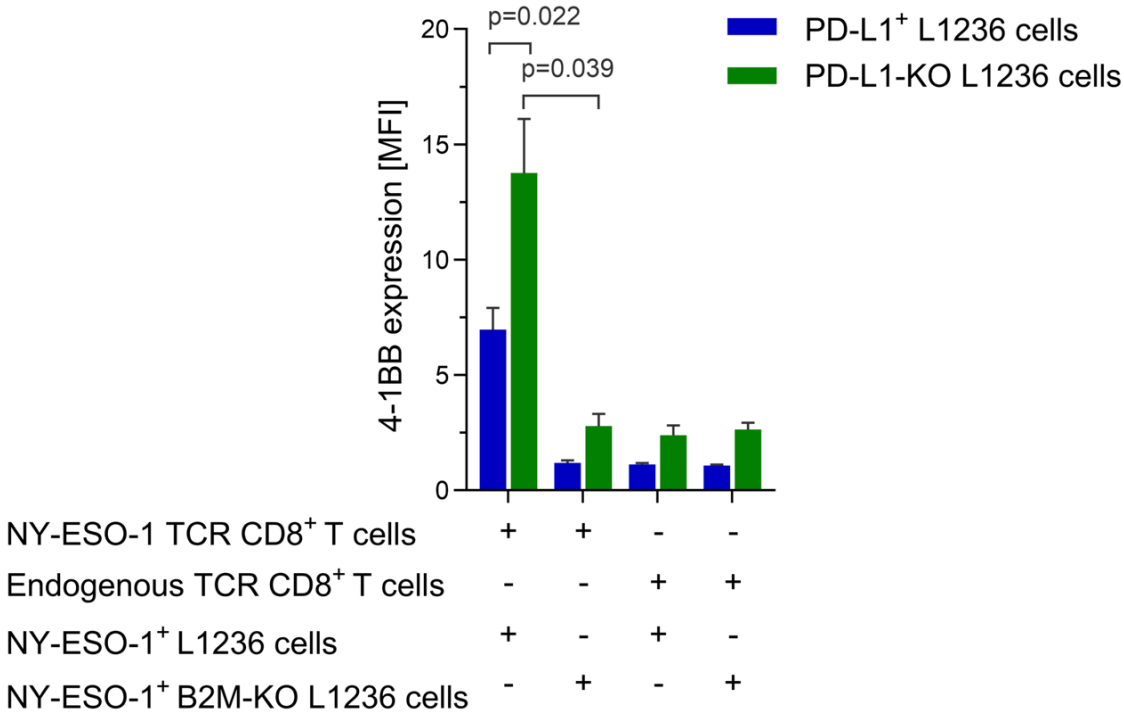

Figure 25. PD-L1 knockout enhances T-cell activation in an MHC-I–dependent manner. Primary human CD8⁺ T cells transduced with a TCR specific for the NY-ESO-1 antigen (NY-ESO-1 TCR CD8⁺ T cells) or CD8⁺ T cells with endogenous TCR were co-cultured for 18 h with NY-ESO-1–expressing L1236 Hodgkin Reed–Sternberg (HRS) cells. Co-cultures included wild-type L1236 cells (PD-L1⁺, blue bars), PD-L1–knockout (KO) L1236 cells (green bars), and their respective B2M-deficient counterparts (MHC-I–deficient). T-cell activation was assessed by surface expression of 4-1BB (CD137) after 18 h of co-culture (n = 3). Data are presented as mean ± SEM. Statistical significance was determined using a paired two-tailed Student's *t*-test; *p*-values are shown on the figure.

These PD-L1–deficient cells were then co-cultured with NY-ESO-1–specific TCR CD8⁺ T cells under the same conditions as before, but without Nivolumab treatment.

T cell activation, measured by 4-1BB expression after 18 h, was significantly enhanced in co-cultures with PD-L1-KO L1236 cells compared to wild-type controls (see Figure 25). In contrast, co-culture with PD-L1-KO B2M deficient L1236 cells resulted in significantly reduced T cell activation, consistent with the loss of antigen presentation through MHC-I. As these PD-L1–deficient cells lacked the PD-1/PD-L1 interaction, Nivolumab treatment was not applied. This provides genetic evidence that PD-L1 expression on L1236 cells contributes to the suppression of antigen-specific T cell activation.

Together with prior findings using Nivolumab, these data confirm that PD-1/PD-L1 signaling suppresses T cell function in this model and that disrupting this interaction—either pharmacologically or through genetic knockout of PD-L1—can restore T cell activity in an MHC-I dependent manner. Overall, this setup provided a systematic comparison of direct $CD8^+$ T cell–HRS interactions in the presence or absence of antigen presentation and checkpoint inhibition, providing a baseline for subsequent studies incorporating TAMs.

3.4 HRS cells and M2 macrophages modulate $CD8^+$ T cell activation

HRS cells and tumor-associated macrophages (TAMs) have been implicated in shaping an immunosuppressive tumor microenvironment in cHL [30,106]. M2-polarized macrophages, which frequently express PD-L1 and are enriched in proximity to $CD8^+$ T cells, are thought to restrict cytotoxic activity and dampen T cell activation [66]. Moreover, PD-1/PD-L1 signaling has been established as a central immune checkpoint limiting anti-tumor immunity [162].

Despite these observations, the specific mechanisms by which HRS cells modulate antigen-specific $CD8^+$ T cell activation in the presence of M2 macrophages remain poorly defined. Addressing this gap is particularly relevant given the spatial organization of PD-$L1^+$ HRS cells, PD-$L1^+$ TAMs and $CD8^+$ T cells in the cHL microenvironment, which suggests a coordinated suppression of effector responses [82,113].

To systematically dissect these interactions, functional co-culture assays were established to evaluate three complementary mechanisms: (i) the effect of soluble mediators derived from HRS cells, (ii) direct cell–cell interactions involving MHC-I–deficient HRS cells, and (iii) the contribution of immune checkpoint signaling through

PD-1/PD-L1 blockade. Inclusion of PD-1 blockade was critical, as this pathway represents a dominant immune evasion mechanism in cHL and allowed us to determine whether interference with PD-1/PD-L1 interactions could restore T cell activation.

This experimental framework employed antigen-specific NY-ESO-1 TCR–engineered $CD8^+$ T cells as a defined effector population, enabling precise assessment of T cell activation under controlled conditions. The co-cultures were designed to clarify how HRS cells and M2 macrophages influence antigen-specific T cell activation and whether functional responses can be restored under checkpoint inhibition. Experiments were performed in a stepwise manner, representing one of the first systematic attempts to dissect how HRS cells and TAMs jointly regulate antigen-specific T cell responses in a co-culture model.

3.4.1 L1236-derived soluble factors modulate interactions between M2 macrophages and $CD8^+$ T cells

To determine whether M2 macrophages impair antigen-specific $CD8^+$ T cell activation and whether HRS-derived soluble factors influence this effect, NY-ESO-1 TCR–engineered $CD8^+$ T cells were co-cultured with NY-ESO-1–expressing M2 macrophages. Co-cultures were treated either with conditioned medium (CM) from L1236 cells or with T cell medium as a control (see Figure 26A-B). To evaluate whether the effect of CM was dependent on the presence of M2 macrophages or could also influence T cells independently, NY-ESO-1 TCR $CD8^+$ T cells were additionally cultured alone in the presence of L1236 CM. $CD8^+$ T cells expressing only endogenous TCRs were co-cultured with the indicated M2 macrophages as specificity controls (see Figure 26B).

This approach allowed a systematic assessment of how M2 macrophages modulate T cell activation and whether soluble factors released by HRS cells alter these interactions, providing a controlled framework to dissect direct versus indirect mechanisms of immunosuppression.

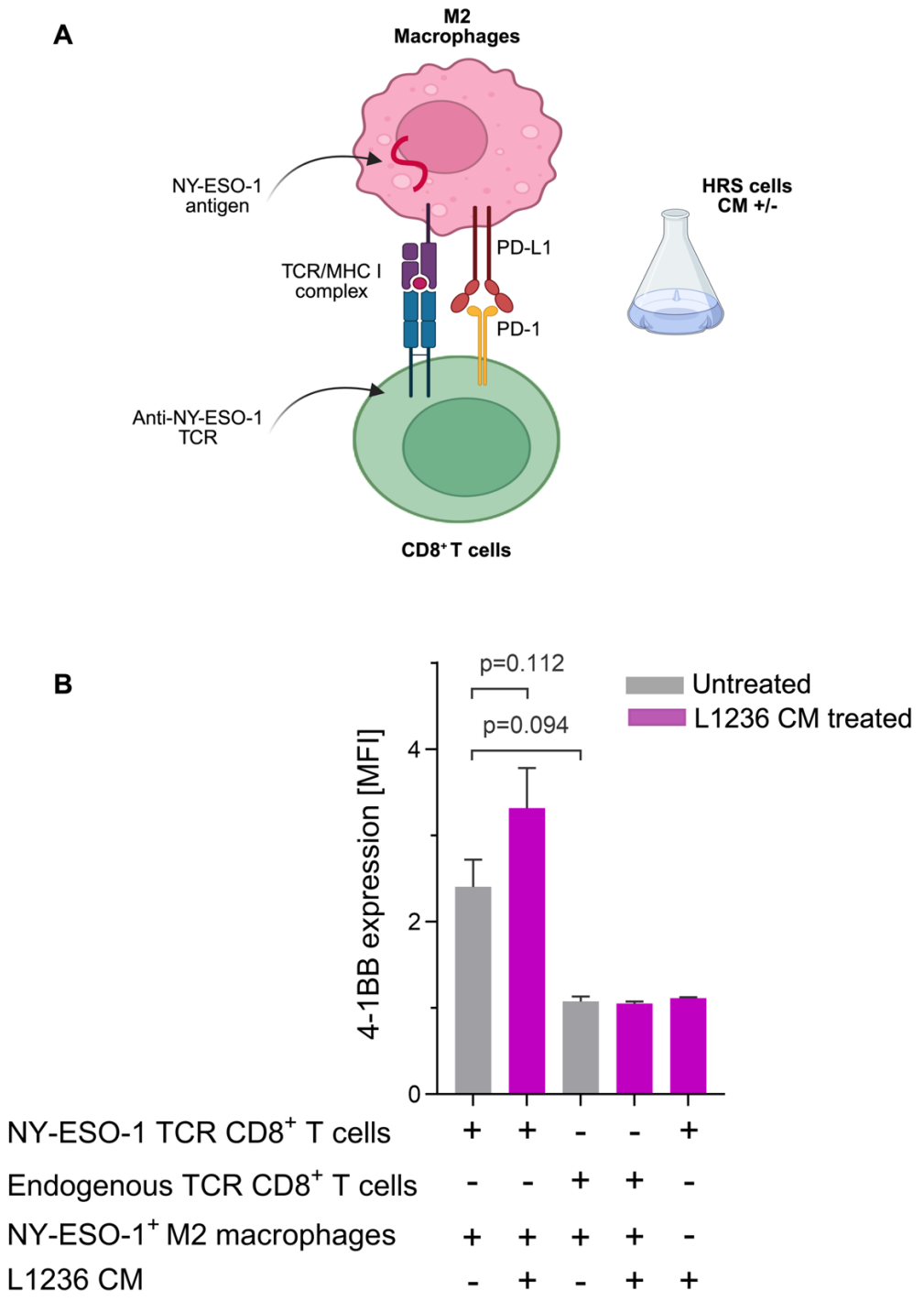

Figure 26. L1236-conditioned medium enhance CD8⁺ T cell activation in M2 macrophage co-cultures. (A) Schematic illustration of the T-cell–M2 macrophage co-culture assay. HLA-A2⁺ M2 macrophages transfected to express the NY-ESO-1 antigen (NY-ESO-1⁺ M2 macrophages) were co-cultured with NY-ESO-1 TCR CD8⁺ T cells, in the presence or absence of conditioned medium (CM) derived from the HL cell line L1236. **(B)** T-cell activation, measured by 4-1BB expression after 24 h of co-culture. NY-ESO-1 TCR CD8⁺ T cells were co-cultured with NY-ESO-1⁺ M2 macrophages with or without L1236 CM. As controls, NY-ESO-1 TCR T cells were cultured alone with L1236-CM, and endogenous TCR CD8⁺ T cells were co-cultured with M2 macrophages. Cultures were either untreated (gray bars) or treated with L1236 CM (pink bars), (n = 2). Data are presented as mean ± SEM. Statistical significance was determined using a paired two-tailed Student's *t*-test; *p*-values are shown on the figure.

When co-cultured with NY-ESO-1$^+$ M2 macrophages, CD8$^+$ T cells expressing the NY-ESO-1–specific TCR showed activation, as indicated by increased 4-1BB expression compared to endogenous TCR CD8$^+$ T cells (see Figure 26B, gray). Treatment with L1236- CM tended to further enhance T-cell responses against NY-ESO-1$^+$ M2 macrophages, as reflected by a consistent increase in 4-1BB expression compared to untreated control, although this difference did not reach statistical significance (see Figure 26B). In contrast, culture of T cells with L1236 CM alone, without M2 macrophages, resulted in reduced T cell activation. These findings suggest that effective TCR-mediated recognition requires antigen presentation via MHC-I, and that the cytokine-mediated effects of L1236 CM primarily influence the T cell–M2 macrophage interaction rather than T cells alone. As expected, CD8$^+$ T cells expressing only endogenous TCRs showed minimal activation under all conditions, confirming the antigen specificity of the observed responses and serving as a baseline for statistical comparison in Figure 26B. Collectively, these results indicate that soluble factors released by L1236 cells may promote a TAM-like phenotype in M2 macrophages, which is associated with stronger T cell activation compared to M2 macrophages cultured without L1236 CM.

3.4.2 PD-1 blockade restores CD8$^+$ T cell activation in HRS–M2 macrophage co-culture

To test whether the presence of MHC-I–deficient HRS cells alters T cell–M2 macrophage interactions, triple co-cultures were established by co-culturing CD8$^+$ T cells engineered to express a NY-ESO-1–specific TCR with NY-ESO-1–expressing M2 macrophages in the presence of MHC-I–deficient HRS cells (see Figure 27A-B).
In parallel, endogenous TCR CD8$^+$ T cells were co-cultured with the indicated combinations of M2 macrophages and MHC-I–deficient HRS cells as antigen specificity controls (see Figure 27B). To assess whether blocking the PD-1/PD-L1 immune checkpoint interactions enhances T-cell activation in this context, co-cultures were treated with 15 µg/ml Nivolumab or left untreated by culturing in T cell medium alone.
This experimental setup enabled the direct comparison of T cell responses in the presence of HRS cells and evaluation of the impact of PD-1 blockade on T cell activation within the T cell–M2 macrophage–HRS cell network.

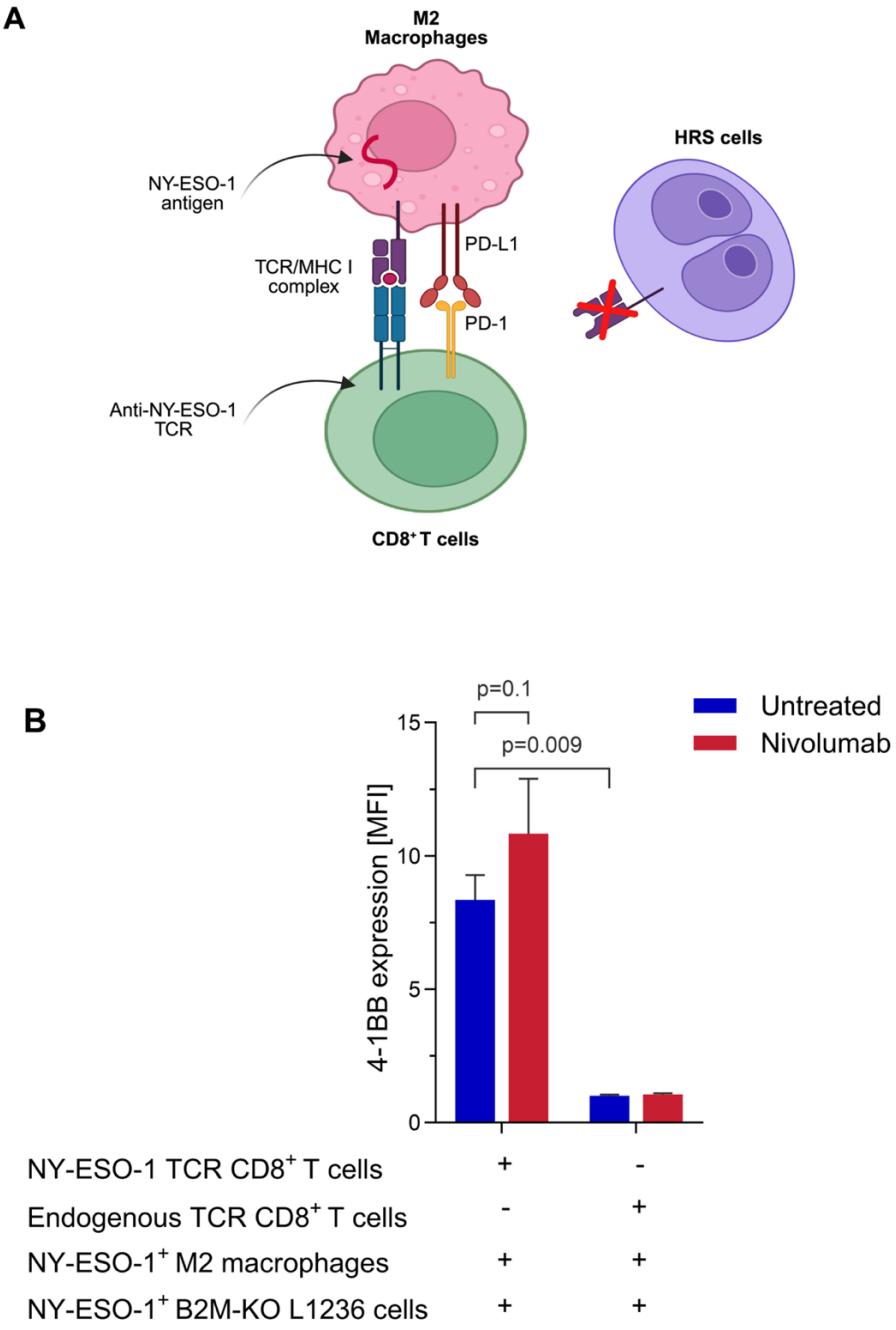

Figure 27. PD-1 blockade tends to enhance CD8⁺ T-cell activation in co-cultures with M2 macrophages and MHC-I–deficient HRS cells. (A) Schematic of the T cell–M2 macrophage and HRS cell co-culture assay. NY-ESO-1⁺ M2 macrophages and NY-ESO-1 TCR CD8⁺ T cells were co-cultured in the presence of NY-ESO-1⁺ B2M-KO L1236 HRS cells. CD8⁺ T cells expressing only endogenous TCRs were also cultured with the indicated cell combinations as antigen-specificity controls. (B) T-cell activation was assessed by surface 4-1BB expression after 24 hours of co-culture. Cultures were either untreated (blue bars) or treated with 15 µg/ml Nivolumab (red bars), (n = 2). Data are presented as mean ± SEM. Statistical significance was determined using a paired two-tailed Student's t-test; p-values are shown on the figure.

When co-cultured with NY-ESO-1$^+$ M2 macrophage and HRS cells, CD8$^+$ T cells expressing the NY-ESO-1–specific TCR showed activation, as indicated by increased 4-1BB expression (see Figure 27B, blue), whereas activation was significantly reduced when CD8$^+$ T cells expressing only endogenous TCRs were co-cultured. This confirmed that TCR-mediated recognition is essential for T-cell activation and suggests that T cells primarily interact with M2 macrophages rather than MHC-I–deficient HRS cells.

Notably, treatment with Nivolumab tended to enhance T-cell responses against M2 macrophages, as reflected by increased 4-1BB expression compared with untreated conditions (see Figure 27B).

As expected, endogenous TCR CD8$^+$ T cells remained unresponsive under all conditions, further supporting the antigen specificity of the observed responses. These findings suggest that PD-1/PD-L1 interactions between CD8$^+$ T cells and M2 macrophages contribute to the suppression of T-cell activation in the presence of HRS cells, and that blockade of this pathway with Nivolumab may partially restore antigen-specific T-cell responses.

3.5 HRS cells drive macrophage polarization toward an M2-like phenotype

HRS cells not only evade direct T cell recognition but also shape the tumor microenvironment through secretion of soluble mediators, a complex mixture of cytokines, chemokines, and growth factors implicated in promoting immune escape in Hodgkin lymphoma [30,45–47]. In cHL, TAMs with an M2-like phenotype are consistently associated with immune suppression and poor clinical outcome [61,67,163–165]. The specific influence of HRS-derived soluble factors on macrophage polarization, however, remains largely undefined. The specific influence of HRS-derived soluble factors on macrophage polarization has recently emerged as a focus of intense research interest [166–169]. Given the established role of TAMs in promoting immune suppression and tumor progression [166–169], HRS cell–derived soluble mediators are expected to drive macrophage polarization toward a TAM-like phenotype.

An in vitro macrophage differentiation system was established using primary monocytes isolated from healthy donors (see Section 2.4.1). Monocytes were either harvested on day 1 without stimulation to serve as a baseline control, or cultured under

one of four polarization conditions after in vitro differentiation and a subsequent 24-hour polarization step (see 2.4.1):
(1) classical M1 polarization induced by LPS and IFN-γ;
(2) alternative M2 polarization using IL-4;
(3) stimulation with CM derived from the Hodgkin lymphoma cell line L1236; or
(4) stimulation with CM derived from the Hodgkin lymphoma cell line HDLM2.
For clarity, the latter two groups are hereafter referred to as L1236-CM and HDLM2-CM conditions, respectively. Each condition was tested using biological replicates from independent donors.

To comprehensively assess the influence of HRS-derived soluble factors on macrophage polarization, transcriptional profiles were subsequently evaluated using principal component analysis (PCA), global differential gene expression, and targeted analysis of polarization and immunosuppressive markers.

3.5.1 HRS cell CM induces M2-like transcriptional programs in macrophages

Following polarization, transcriptomic profiling of macrophages was performed using RNA sequencing, and transcriptional variation across conditions was examined by principal component analysis (PCA). The first two principal components accounted for 33.97% (PC1) and 20.56% (PC2) of the total variance. In the PCA plot (see Figure 28), monocytes were clearly separated along the negative axis of PC1, whereas all macrophage populations, irrespective of polarization stimulus, shifted toward positive PC1 values, reflecting the major transcriptional transition associated with monocyte-to-macrophage differentiation.

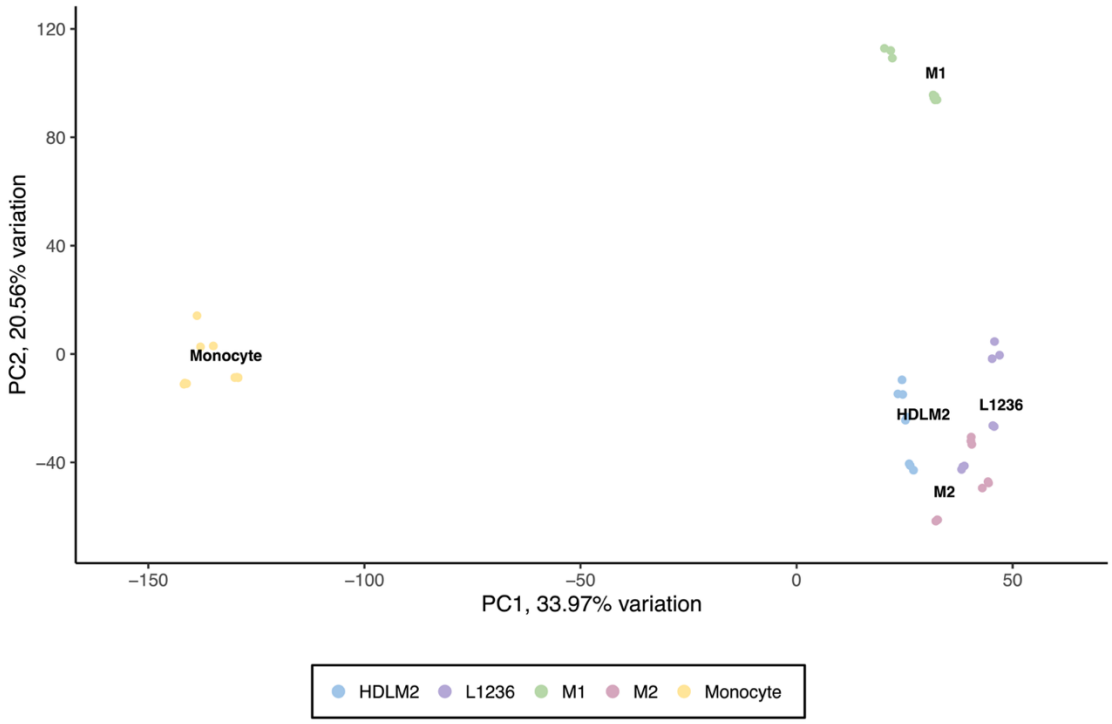

Figure 28. PCA reveals that macrophages exposed to Hodgkin lymphoma–conditioned media cluster with M2-polarized cells, indicating a similar transcriptional profile. Primary human monocytes were either left untreated (monocyte control) or differentiated in vitro under one of four conditions: classical M1 polarization (LPS + IFN-γ), alternative M2 polarization (IL-4), or stimulation with conditioned media (CM) from the Hodgkin lymphoma cell lines L1236 (L1236 CM) or HDLM2 (HDLM2 CM). Each condition was performed using three independent biological donors (n = 3). PCA was conducted on the full RNA-sequencing dataset. The first two principal components explained 33.97% (PC1) and 20.56% (PC2) of the total variance. Monocytes clustered along negative PC1 values, while all macrophage populations shifted toward positive PC1 values, reflecting transcriptional changes associated with monocyte-to-macrophage differentiation. Along PC2, M1-polarized macrophages were separated from M2-polarized and CM-treated macrophages, which clustered together in the lower right quadrant. Tight grouping of biological replicates confirmed the reproducibility of transcriptional responses across donors.

Along the PC2 axis, distinct clustering patterns were observed among the polarized macrophage groups. M1-polarized macrophages (LPS + IFN-γ) were separated from the other conditions and localized in the upper region of the plot, whereas M2-polarized macrophages (IL-4) and tumor-CM–stimulated macrophages (L1236-CM and HDLM2-CM) clustered closely in the lower right quadrant. This spatial relationship suggested that exposure to HRS cell–derived conditioned media induced transcriptional programs more closely aligned with M2-like polarization. Tight clustering of biological replicates within each condition further confirmed the reproducibility of the transcriptional responses and underscored the robustness of the observed polarization patterns.

These PCA-based results provided a foundation for subsequent analyses to identify gene-level differences among polarization conditions and to determine whether CM-stimulated macrophages exhibit distinct or shared features with established macrophage subtypes.

Differential Gene Expression Highlights M2 Profile

To further quantify the transcriptional shifts observed in PCA and identify M2-associated genes, global differential gene expression analysis was performed. To characterize transcriptional programs underlying macrophage polarization and assess how HRS-derived conditioned media (CM) influence these programs, differential gene expression (DGE) analysis was performed comparing M2- versus M1-polarized macrophages. This comparison aimed to identify genes that define the M2 phenotype and to assess how macrophages stimulated with tumor-derived CM align with this expression profile. Based on samples from three independent donors, this analysis identified 1,029 significantly differentially expressed genes (DEGs), using a threshold of absolute $\log_2$ fold change ($|LFC| \geq 2$ and adjusted p-value (padj) ≤ 0.01. Of these, 429 genes were upregulated in M2 macrophages, and 600 were downregulated (i.e., upregulated in M1 relative to M2). This DEG list served as the basis for subsequent comparative transcriptomic analysis. For each of the 1,029 DEGs, $\log_2$ fold change (LFC) values were calculated in four pairwise comparisons relative to unstimulated monocytes (M0): M1 vs. M0, M2 vs. M0, L1236 CM vs. M0, and HDLM2 CM vs. M0. Genes lacking valid LFC values in any of these comparisons—due to low or undetectable expression—were excluded to avoid missing data and ensure consistent clustering (see Figure 28). The final heatmap thus includes only DEGs with valid LFCs across all four comparisons. Each row in the heatmap represents a gene from the filtered DEG list, while each column corresponds to a polarization condition compared to M0. Color intensity reflects the magnitude and direction of gene regulation. The heatmap revealed distinct expression patterns that emphasize the close transcriptional resemblance between macrophages exposed to tumor-derived CM and M2 macrophages (see Figure 29). Genes that were upregulated in M2 macrophages relative to M1 also showed increased expression in macrophages treated with conditioned media from both L1236 and HDLM2 cells. Conversely, genes that were downregulated in M2 compared to M1 also showed reduced expression in the CM-treated macrophages. This similarity indicates that macrophages

exposed to HRS-derived soluble factors acquire a transcriptional program closely resembling the M2 phenotype. Hierarchical clustering further supported these findings by grouping L1236 CM and HDLM2 CM samples with M2 macrophages, distinctly separate from M1. A broader view of the heatmap highlights genes associated with classical (M1) and alternative (M2) activation, reinforcing the polarization differences and underscoring the alignment of CM-treated macrophages with the M2 subtype (see Figure 29). These results provide a comprehensive transcriptomic view supporting the ability of HRS cells to shape a tumor-supportive macrophage phenotype.

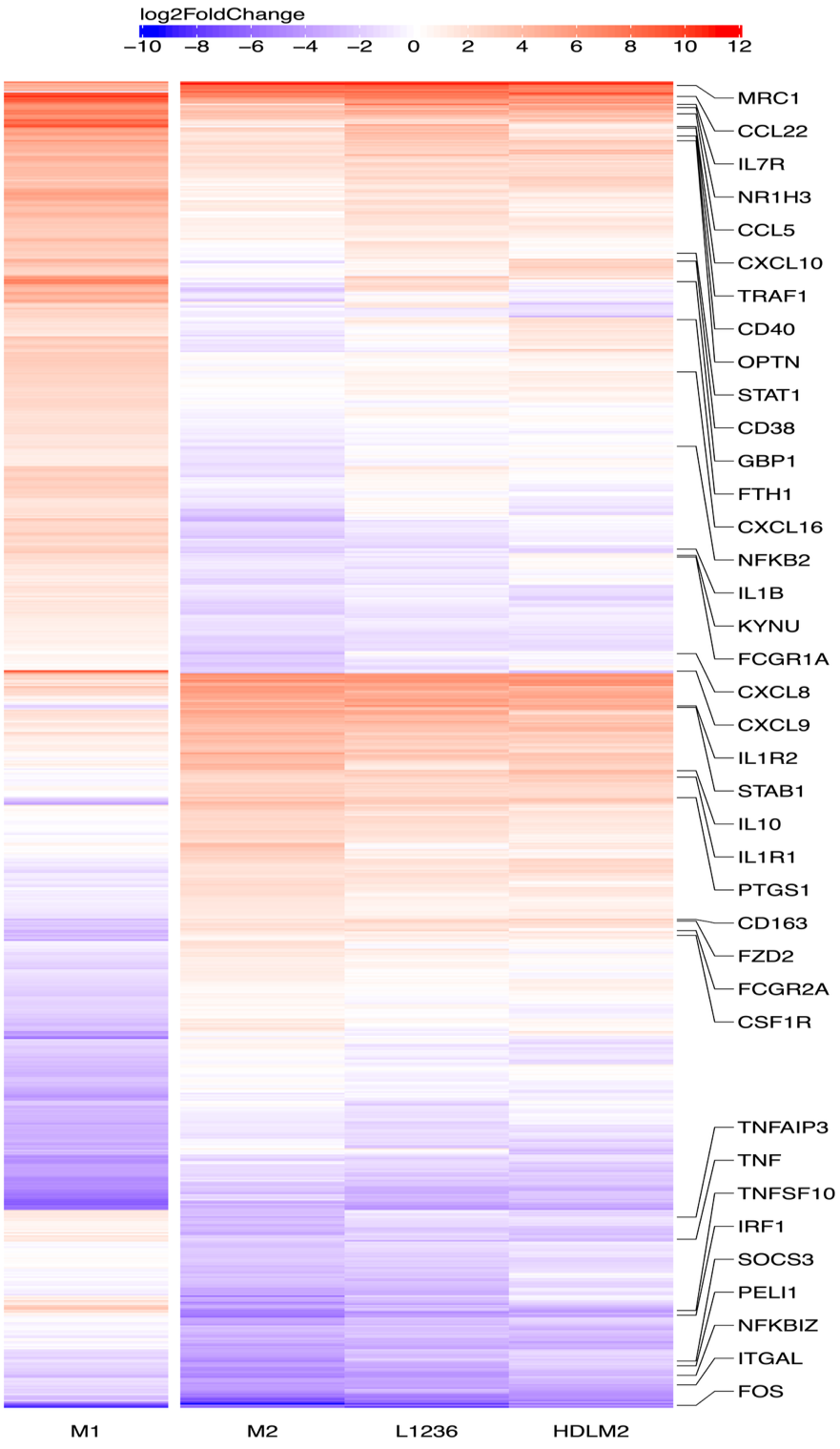

Figure 29. Differential gene expression analysis reveals that macrophages treated with Hodgkin lymphoma–conditioned media exhibit a gene expression profile closely matching M2-polarized macrophage. Primary human monocytes from three independent donors were differentiated under four conditions: classical M1 polarization (LPS and IFN-γ), alternative M2 polarization (IL-4), or stimulation with conditioned media (CM) from Hodgkin lymphoma cell lines L1236 or HDLM2. Unstimulated monocytes (M0) served as controls. Differential gene expression analysis comparing M2 and M1 macrophages identified 1,029 significant DEGs ($|\log_2$ fold change$| \geq 2$, adjusted $p \leq 0.01$), including 429 genes upregulated and 600 genes

downregulated in M2 relative to M1. This M2 gene signature was used to generate a heatmap displaying $\log_2$ fold changes across four pairwise comparisons relative to M0: M1 vs. M0, M2 vs. M0, L1236 CM vs. M0, and HDLM2 CM vs. M0. The heatmap illustrates distinct transcriptional profiles, with CM-treated macrophages clustering closely to M2-polarized cells. This pattern supports the similarity of tumor-conditioned macrophages to the M2 polarization state.

3.5.2 HRS cell CM induces classical M2 gene signatures

While global clustering highlighted the overall similarity between CM-stimulated and M2 macrophages, a targeted analysis of canonical polarization markers was conducted to validate these findings and improve interpretability. To enable a more focused comparison of macrophage polarization states, a targeted heatmap was generated using a curated subset of classic M1- and M2-associated genes well established in the literature and identified within the differentially expressed genes from the prior global analysis. This refined analysis highlights the expression patterns of canonical markers that distinguish classically activated (M1) from alternatively activated (M2) macrophages (see Figure 30). M1-polarized macrophages demonstrated strong upregulation of pro-inflammatory genes including CXCL9, IL1B, TNF, TNFAIP3, TNFSF10, and IRF1 [170–173]. In contrast, M2-polarized macrophages showed elevated expression of hallmark alternative activation markers such as CD163, IL10, IL1R2, and STAB1 [170,172,173]. Macrophages treated with conditioned media from Hodgkin lymphoma cell lines (L1236 and HDLM2) exhibited a gene expression profile closely resembling the M2 polarization state, with similar upregulation of these classic M2 markers (see Figure 30). These results support the conclusion that soluble factors secreted by HRS cells induce macrophage polarization toward an M2-like phenotype. This analysis was based on averaged fold-change data derived from three independent biological donors per condition, as represented in the previously generated global differential gene expression heatmap.

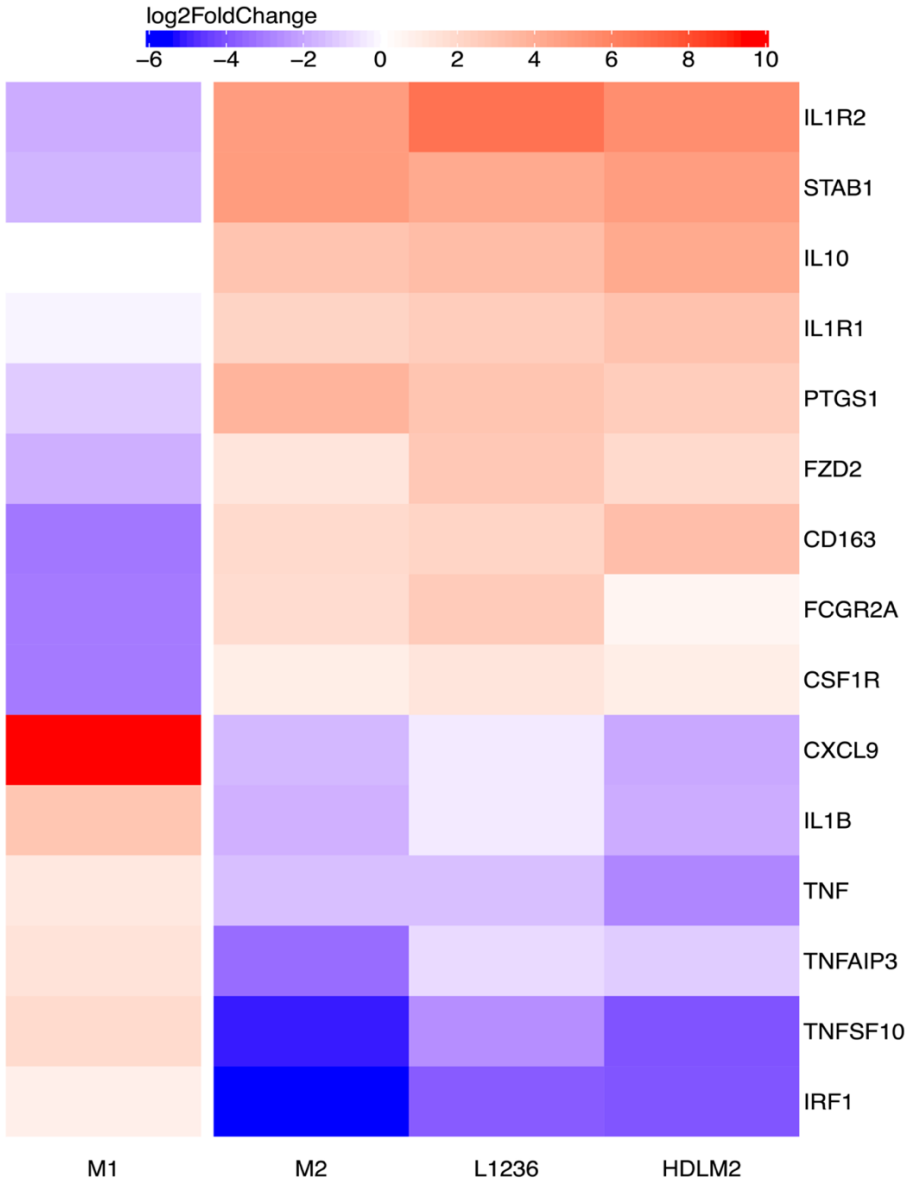

Figure 30. Focused Heatmap of M1 and M2 Marker Genes Highlights M2-Like Profile of Macrophages treated with Hodgkin lymphoma–conditioned media. Heatmap showing the expression of selected classic M1- and M2-associated genes in primary human monocytes (n = 3 donors) differentiated under four conditions: classical M1 polarization (LPS + IFN-γ), alternative M2 polarization (IL-4), and stimulation with conditioned media (CM) from the Hodgkin lymphoma cell lines L1236 or HDLM2. Gene expression is represented as $\log_2$ fold changes relative to unstimulated controls. Macrophages treated with Hodgkin lymphoma–conditioned media exhibited expression profiles similar to M2-polarized macrophages, including increased expression of alternative activation markers (e.g., CD163, IL10, STAB1). Highlighted genes on the right indicate phenotype-specific markers, illustrating the shift toward an M2-like transcriptional state driven by HRS-derived soluble factors.

3.5.3 M2 and CM-treated macrophages upregulate immunosuppressive genes

To further explore the functional implications of the observed M2-like polarization in macrophages treated with conditioned media (CM) from Hodgkin lymphoma cell lines (L1236 and HDLM2), a focused heatmap was generated to assess the expression of immunosuppressive genes across selected macrophage populations (see Figure 31). This analysis included monocytes (unstimulated controls), M2-polarized macrophages (IL-4), and CM-treated macrophages. A selected list of immunoregulatory genes was compiled from the literature based on their established roles in modulating anti-tumor immunity [174,175]. Expression values are shown as transcripts per million (TPM), enabling direct comparison across the four conditions. Monocytes served as the reference baseline. Both M2-polarized and CM-treated macrophages exhibited increased expression of key immunosuppressive genes, including MRC*1*, *IL10*, and *CD274* (PD-L1) [174–176] indicating a shared transcriptional program associated with immune evasion (see Figure 31). In addition, emerging markers such as VSIG4, MMP9, and PDGF were noted [175,176], whose roles in macrophage-mediated suppression remain to be elucidated in cHL. These findings extend previous observations by demonstrating that, beyond phenotypic similarity, CM-treated macrophages may adopt a gene expression profile linked to immunoregulatory functions in the tumor microenvironment.

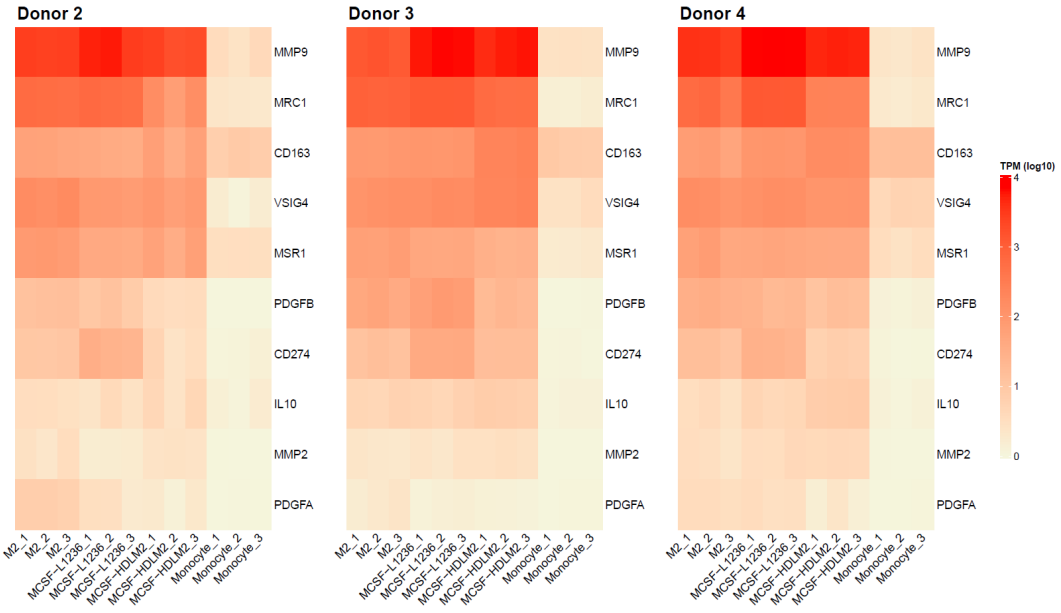

Figure 31. Expression of immunosuppressive genes reveals shared regulatory features between M2-polarized and CM-treated macrophages. Heatmap showing transcript-per-million (TPM) expression values for selected immunosuppressive genes in primary human monocytes (n = 3 biological donors) and macrophages differentiated under three M2-like

conditions: IL-4 stimulation (M2), or treatment with conditioned media (CM) from the Hodgkin lymphoma cell lines L1236 or HDLM2. Unstimulated monocytes (M0) served as baseline controls. Both M2 and CM-treated macrophages exhibited elevated expression of immunosuppressive markers, indicating a shared transcriptional program associated with immune suppression. These results support the notion that soluble factors derived from HRS cells contribute to the induction of an immunosuppressive phenotype in macrophages.

Overall, the transcriptomic data demonstrate that macrophages exposed to conditioned media from HL cell lines adopt a gene expression profile closely resembling IL-4–induced M2 macrophages [170,172,173,175,177]. Principal component analysis and differential gene expression clearly separated pro-inflammatory M1 macrophages from M2 macrophages, with CM-treated macrophages clustering alongside the M2 type. Analysis of established polarization markers and immunosuppressive genes further confirmed that HL-derived factors promote an M2-like, immunosuppressive state in macrophages. This M2-like signature aligns with features commonly attributed to tumor-associated macrophages (TAMs), known to support immune suppression and tumor progression [174–176,178]. These findings indicate that soluble factors released by HRS cells drive macrophage polarization toward a TAM-like state, potentially contributing to immune evasion and remodeling of the tumor microenvironment, consistent with previous reports showing that HL–derived cytokines and chemokines support the development of immunosuppressive macrophage phenotypes [165,169,179–182].

These results provide a transcriptional foundation for HL-driven macrophage reprogramming and lead into the functional studies described in 3.4 section.

3.6 Long-term PD-1 engagement does not alter L1236 proliferation

To assess whether PD-1/PD-L1 interactions promote tumor cell proliferation, co-cultures were established by growing L1236 HRS cells, which endogenously express PD-L1, with HEK293FT cells engineered to express PD-1 or with wild-type HEK293FT cells lacking PD-1 expression (see Figure 32A-B). HEK293FT cells were selected as a controlled system to specifically examine the effect of PD-1/PD-L1 interactions on L1236 proliferation. Because these cells do not endogenously express PD-1, they provided a clean background enabling precise comparison between PD-1–positive and PD-1–negative conditions. By transducing HEK293FT cells to express PD-1, the co-culture system permitted defined engagement of PD-L1 on L1236 cells, isolating the impact of

this checkpoint interaction from other variables typically present in more complex immune cell populations.

Co-cultures were maintained over an extended period in the presence or absence of 15 µg/ml Nivolumab (see Section 2.5.1 for rationale) or cultured in complete RPMI medium alone as a control. This design allowed systematic assessment of L1236 proliferation under conditions permitting PD-1/PD-L1 engagement, lacking such interaction, or including checkpoint blockade.

This setup enabled a focused evaluation of PD-1/PD-L1–mediated regulation of L1236 proliferation, directly addressing the question of whether sustained checkpoint signaling contributes to tumor cell survival in cHL, an aspect not fully explored in previous studies despite short-term evidence for PD-L1–driven pro-survival effects on HRS cells [90].

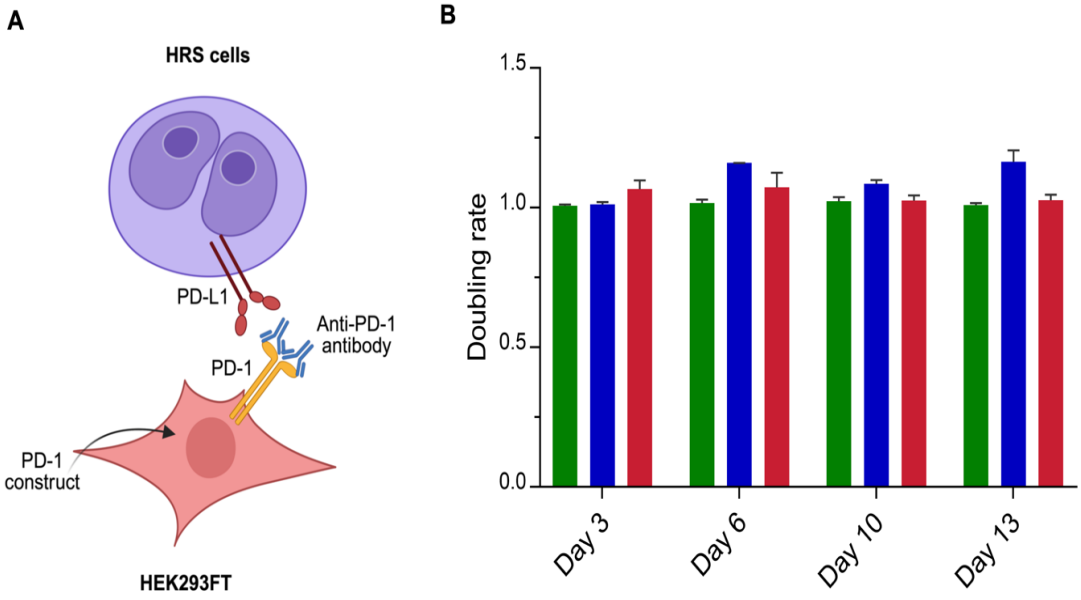

Figure 32. Impact of PD-1 Blockade on L1236 Cell Growth in HEK293FT Co-Culture. **(A)** Schematic of the HEK293FT and L1236 (HRS) cell co-culture assay. L1236 cells expressing PD-L1 were co-cultured with HEK293FT cells transduced to express PD-1. Control HEK293FT cells (lacking PD-1 expression) were also co-cultured with L1236 cells. Cells were cultured either in T cell medium alone (control) or treated with 15 µg/ml Nivolumab. **(B)** L1236 cell proliferation was assessed by measuring cell number every 2–3 days over a 13 days co-culture period (n = 3). Bar colors indicate co-culture conditions: green, HEK293FT (PD-1–negative) + L1236 (control); blue, PD-1$^+$ HEK293FT + L1236 (control); red, PD-1$^+$ HEK293FT + L1236 + Nivolumab (treatment).

L1236 proliferation was not affected by co-culture with PD-1^{+} HEK293FT cells compared to PD-1–negative controls, indicating that PD-L1 engagement by PD-1 had no detectable impact on tumor cell growth in this system (see Figure 32B). Similarly, treatment with Nivolumab to block PD-1 signaling did not alter L1236 proliferation (see Figure 32B). These findings suggest that, within this controlled co-culture model, PD-1/PD-L1 interactions do not directly modulate the proliferation of L1236 cells.

Evaluation of Apoptosis in L1236 Cells Under PD-1/PD-L1 Co-culture Conditions

To further assess whether the observed lack of proliferation changes was associated with apoptotic effects, Caspase-3 activation was measured in L1236 cells following co-culture under the same conditions. Flow cytometry analysis of activated Caspase-3 in L1236 cells after 3 days of co-culture revealed minimal expression across all conditions (see Figure 33). There was no significant difference in Caspase-3 activation between cells cultured with PD-1^{+} HEK293FT or PD-1–negative HEK293FT cells, nor with or without PD-1 blockade. These findings indicate that apoptosis is not differentially induced in L1236 cells under the tested co-culture conditions, consistent with the proliferation data.

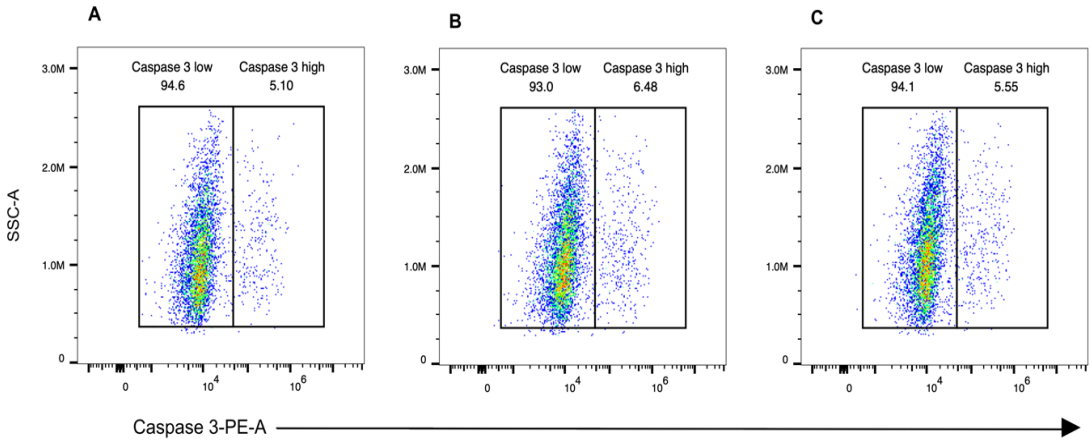

Figure 33. Evaluation of Caspase-3 Activation in L1236 Cells After PD-1 Blockade.L1236 cells expressing PD-L1, were co-cultured for 3 days with HEK293FT cells under three conditions: **(A)** control HEK293FT cells lacking PD-1 expression, **(B)** PD-1^{+} HEK293FT cells without treatment (control), or **(C)** PD-1^{+} HEK293FT cells in the presence of 15 µg/ml Nivolumab (treatment). Apoptosis was assessed by measuring activated Caspase-3 expression in L1236 cells using flow cytometry. Representative plots show minimal Caspase-3–positive populations across conditions. Gates indicate Caspase-3-High and Caspase-3-Low subsets.

Together, these results suggest that, within this controlled co-culture model, PD-1/PD-L1 interactions do not directly modulate L1236 survival or proliferation. Importantly, these findings establish a foundation for subsequent experiments investigating how PD-1/PD-L1 signaling influences immune cell interactions and effector responses in the context of HRS cells.

3.7 $CD8^+$ T cells engage HRS cells and TAMs via PD-1/PD-L1, with TAMs compensating when tumor contact is limited

To investigate whether PD-1/PD-L1 interactions reflect direct engagement between $CD8^+$ T cells and HRS cells in MHC-I–intact contexts, and to determine whether PD-L1–expressing TAMs interact with $CD8^+$ T cells via the same pathway, a sequential staining approach was applied to FFPE cHL tissue sections (see Figure 35). PLA was first performed to detect PD-1/PD-L1 proximity at subcellular resolution, allowing identification of interaction sites before any additional staining. Unlike conventional colocalization-based imaging, PLA detects molecular interactions based on protein proximity rather than spatial overlap of cell markers. Imaging was completed prior to further processing to preserve signal integrity. Following acquisition, PLA products were removed, and multiplex immunofluorescence was performed on the same tissue sections to enable cellular assignment of PLA signal within the tumor microenvironment.

As an initial step to contextualize the cellular environment of PD-1/PD-L1 engagement, CD3 and CD68 were used to broadly assess interactions between T cells and macrophages. CD3 was selected to capture the total T-cell compartment, while CD68 was used as a general macrophage marker. Overlay of mIF staining with PLA signal demonstrated that PD-1/PD-L1 puncta —discrete proximity signals indicating molecular interaction—were frequently located in regions where $CD3^+$ T cells were in close proximity to $CD68^+$ macrophages, indicating that T cell–macrophage interactions contribute to checkpoint engagement in cHL. For clarity, all subsequent references to PLA puncta refer to PD-1/PD-L1 interactions.

To refine this observation and identify the specific immune subsets involved, more selective markers were used in subsequent analyses. CD8 was employed to distinguish cytotoxic T cells within the broader $CD3^+$ population, while CD163 was chosen to define tumor-associated macrophages within the $CD68^+$ compartment. In parallel, CD30 was included to identify HRS cells as another potential interaction partner.

To avoid tissue damage caused by repeated antibody elution during multiplex staining, CD8–CD163 and CD8–CD30 interactions were assessed on sequential sections rather than on the same physical slide, with adjacent cuts from the same tissue block used to approximate matching anatomical regions for comparative analysis.

PLA puncta were consistently detected in regions where $CD3^+$ T cells were located in close proximity to $CD68^+$ macrophages, indicating that PD-1/PD-L1 engagement occurs within T cell–macrophage contacts in the cHL microenvironment (see Figure 34).

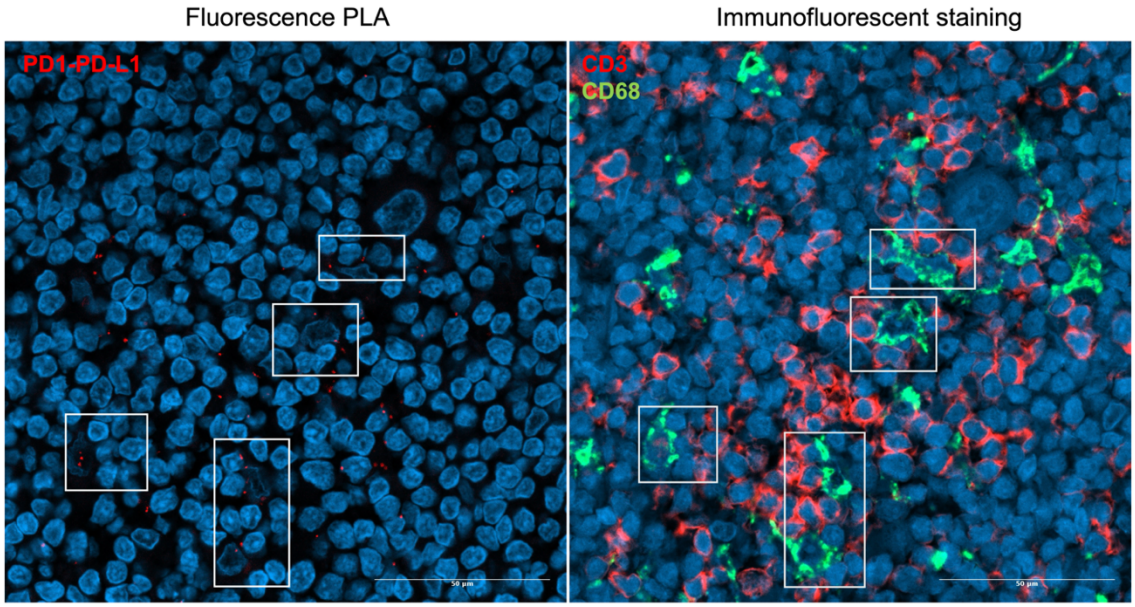

Figure 34. PD-1/PD-L1 interactions are detected between $CD3^+$ T cells and $CD68^+$ macrophages. Side-by-side confocal images (40× magnification) from the same anatomical region illustrate PLA-detected PD-1/PD-L1 interactions and corresponding mIF staining for CD3 and CD68. The left panel shows PLA puncta indicating sites of PD-1/PD-L1 proximity, while the right panel displays the same region stained for $CD3^+$ T cells and $CD68^+$ macrophages. Boxed areas highlight locations where PLA puncta align with zones of T cell–macrophage contact, demonstrating that PD-1/PD-L1 engagement occurs at CD3–CD68 interfaces within the cHL microenvironment. Images were acquired using a Zeiss LSM 800 Confocal Laser Scanning Microscope. 40× magnification. Scale bar = 50 µm.

After refining the analysis to more specific immune subsets, regions with abundant PLA puncta were evaluated on sequential sections stained for CD163 to determine whether tumor-associated macrophages contributed to PD-1/PD-L1 interactions. Regions with abundant PLA puncta were selected because such areas reflect increased PD-1/PD-L1 proximity events and are therefore the most informative locations for identifying which immune cell subsets participate in these interactions. In addition, full-resolution whole-slide imaging was not feasible with the Zeiss LSM 800 confocal

laser scanning microscope, so representative regions within the tumor microenvironment were chosen for detailed evaluation. In these areas, PLA puncta were observed at interfaces between $CD8^+$ and $CD163^+$ cells, supporting the presence of checkpoint interactions between cytotoxic T cells and TAMs (see Figure 35). Similarly, regions showing abundant PLA puncta were subsequently evaluated on sequential sections stained for CD30 to determine whether HRS cells contributed to PD-1/PD-L1 engagement. PLA puncta were detected in regions where $CD8^+$ T cells were located adjacent to $CD30^+$ cells, indicating that HRS cells also contribute to PD-L1–mediated interactions (see Figure 35). Across tissue sections, puncta were not confined to a single compartment but were distributed among both $CD30^+$ tumor cells and $CD163^+$ macrophages, suggesting that PD-1/PD-L1 interactions occur in multiple cellular niches. Negative controls lacking one of the two primary antibodies showed complete absence of puncta, confirming that the detected interactions were specific and not due to background or nonspecific binding (see Figure 19).

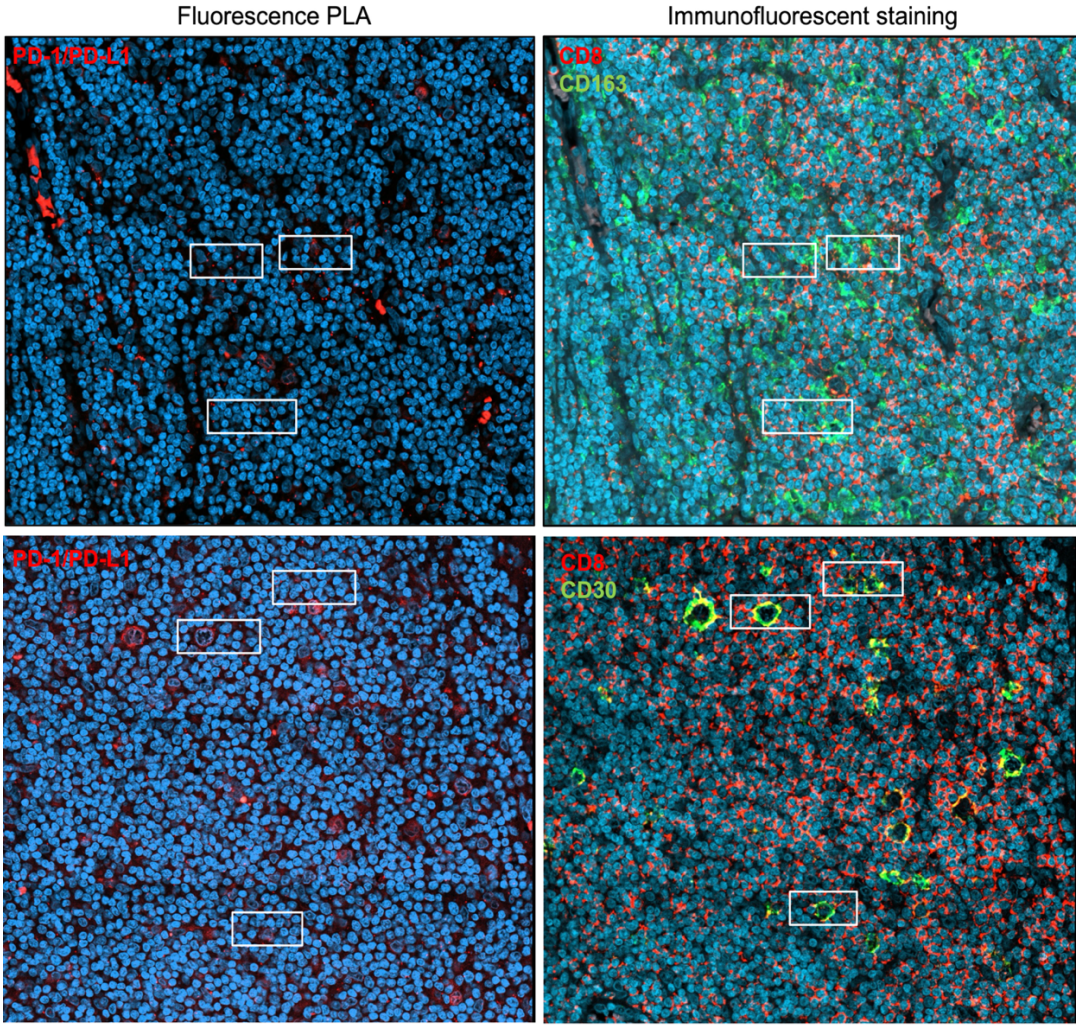

Figure 35. CD8$^+$ T cells engage CD163$^+$ macrophages and CD30$^+$ HRS cells via PD-1/PD-L1 interactions. the upper set of images, the left panel shows PLA puncta indicating sites of PD-1/PD-L1 proximity, while the right panel displays the same region stained for CD8$^+$ T cells and CD163$^+$ macrophages. Boxed areas highlight locations where PLA puncta align with CD8–CD163 interfaces, demonstrating checkpoint engagement between cytotoxic T cells and tumor-associated macrophages. In the lower set of images, the left panel again shows PLA-detected PD-1/PD-L1 interactions, and the right panel displays the corresponding region stained for CD8$^+$ T cells and CD30$^+$ Hodgkin Reed–Sternberg cells. Boxed regions mark sites where PLA signal overlaps with CD8–CD30 contacts, indicating that HRS cells also participate in PD-L1–mediated interactions. Images were acquired using a Zeiss LSM 800 Confocal Laser Scanning Microscope. 40× magnification. Scale bar = 50 μm.

To assess whether PD-1/PD-L1 engagement differs between EBV-positive and EBV-negative cases—where EBV status serves as a biological grouping variable that reflects known differences, including the typically lower MHC-I expression in EBV-negative cHL and higher MHC-I expression in EBV-positive cHL. PLA puncta at CD8–CD30 and CD8–CD163 contacts were quantified separately in EBV-negative and EBV-positive cases. In the first comparison, PD-1/PD-L1 PLA puncta at CD8–CD30 interfaces were quantified and plotted according to EBV status (see Figure 36A). Although the difference did not reach statistical significance, a clear trend toward higher CD8–HRS engagement was observed in EBV-positive cases compared with EBV-negative cases. In a second analysis, PD-1/PD-L1 PLA puncta at CD8–CD163 interfaces were quantified (see Figure 36B) and showed a similar non-significant trend, with EBV-positive cases exhibiting higher engagement than EBV-negative cases. Together, these findings highlight consistent directional trends suggesting that in EBV-positive cHL, both HRS cells and tumor-associated macrophages may more frequently engage CD8$^+$ T cells via PD-1/PD-L1 interactions.

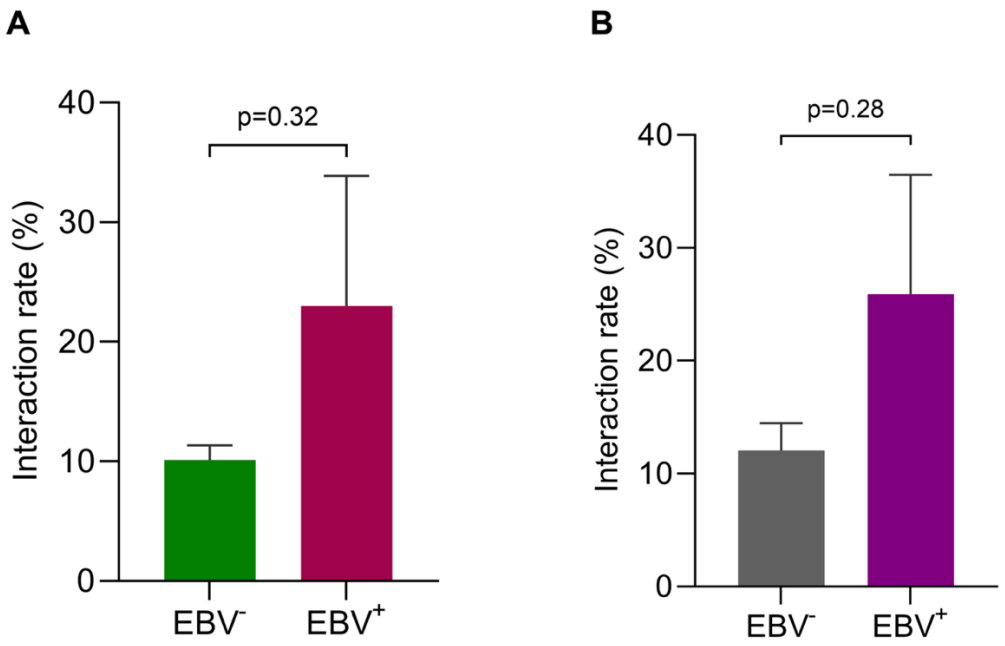

Figure 36. Quantification of PD-1/PD-L1 PLA puncta at CD8–CD30 and CD8–CD163 interfaces in EBV⁻ and EBV⁺ cHL cases. (A) Bar graph showing the interaction rate of PLA puncta at CD8–CD30 interfaces in EBV-negative and EBV-positive samples. Interaction rate between CD8⁺ T cells and CD163⁺ M2 macrophages or CD30⁺ HRS cells, shown as the proportion of partner cells exhibiting PD-1/PD-L1 PLA signal (see section 2.6.7). CD8–HRS engagement via PD-1/PD-L1 was higher in EBV-positive cases than in EBV-negative cases. (B) Quantification of PLA puncta at CD8–CD163 interfaces in the same EBV-negative and EBV-positive samples. Similar to CD30 contacts, CD8–macrophage engagement was more frequent in EBV-positive cases. Sample numbers: EBV⁻ (n = 10), EBV⁺ (n = 4). Data are presented as mean ± SEM. Statistical significance was determined using unpaired Welch's test; p-values are shown on the figure.

In a subset of cases where few or minimal PLA puncta were detected at CD8–CD30 interfaces, the possibility of alternative PD-1/PD-L1 interaction partners was examined independently of EBV status. To address this, individual cases were reassessed to determine whether macrophages might function as the predominant cellular counterparts for CD8⁺ T cells. In these samples, PLA puncta were detected at CD8–CD163 interfaces, even when CD8–HRS engagement was limited. This pattern is most clearly illustrated in sample S1**,** S3, S4 (see Figure 37), and all individual cases are shown in Supplementary Figure S7. Although based on a small number of cases, this pattern suggests that in tumors with reduced direct CD8–HRS interactions, tumor-associated macrophages may provide an alternative route for PD-1/PD-L1 engagement.

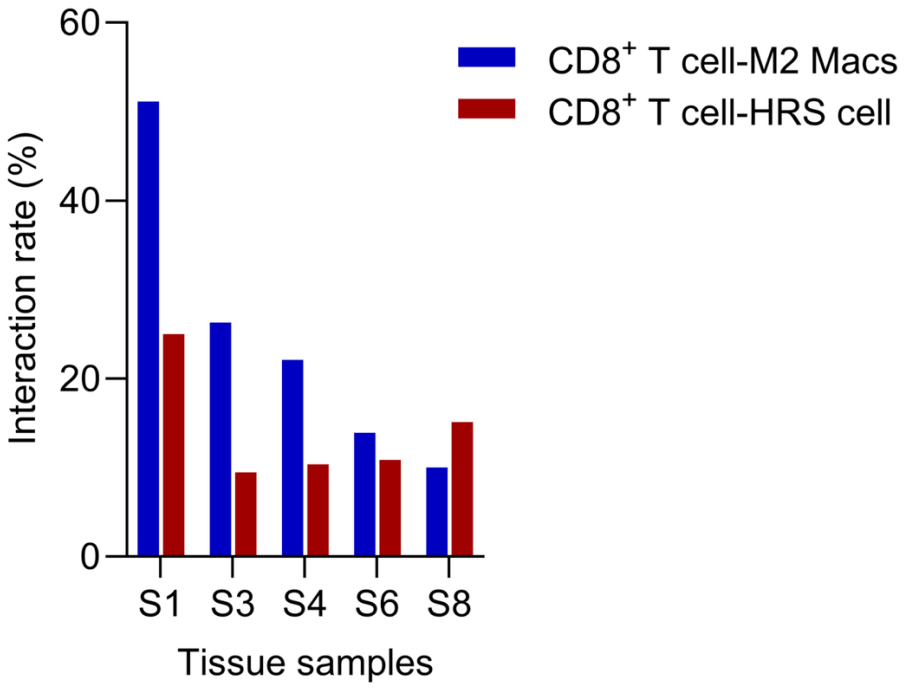

Figure 36. Case-wise analysis of PD-1/PD-L1 PLA puncta at CD8–CD163 and CD8–CD30 interfaces in samples with low CD8–HRS engagement. Bar plots display individual cases ordered by decreasing relative interaction rate at CD8–CD163 interfaces. For each case, the corresponding interaction rate at CD8–CD30 interfaces is shown for comparison. In cases where CD8–HRS interactions were minimal, CD8–CD163 contacts showed higher interaction rates, indicating that tumor-associated macrophages can act as alternative partners for PD-1/PD-L1 engagement when direct interaction with HRS cells is limited. Interaction rate was calculated as described in Section 2.6.7.

4 Discussion

The overarching aim of this thesis was to clarify how the PD-1/PD-L1 axis contributes to immune evasion in cHL, specifically through the suppression of $CD8^+$ T cells**.** To address this question, the work combined tumor-intrinsic and microenvironmental components, examining how HRS cells and tumor-associated macrophages suppress cytotoxic $CD8^+$ T-cell function, whether these inhibitory interactions are reversible by PD-1 blockade, and whether PD-L1 engagement also affects HRS cell survival. Achieving these goals required an experimental framework capable of disentangling antigen-specific T-cell activation from microenvironmental regulation. Therefore, as an essential enabling step, an engineered antigen-specific co-culture model incorporating HRS cells, macrophages, and $CD8^+$ T cells was established and validated. While the co-culture system was not an end in itself, it provided the mechanistic resolution required to dissect the individual contributions of each cell type to PD-1/PD-L1–dependent immune suppression.

More specifically, the study addressed five complementary objectives:

(1) to design and establish an antigen-specific co-culture system that enables precise interrogation of PD-1/PD-L1–mediated immune regulation across defined cellular compartments; (2) to determine how HRS cells suppress $CD8^+$ T cells via PD-1/PD-L1 in cases with intact MHC class I and to evaluate the effect of PD-1 blockade (nivolumab); (3) to characterize TAM-mediated suppression of $CD8^+$ T cells and the extent to which PD-1 blockade can reverse this suppression using functional assays and PLA/IF on FFPE tissue; (4) to assess the long-term consequences of PD-1/PD-L1 reverse signaling for HRS cell proliferation; and (5) to establish whether HRS-derived factors drive TAM polarization toward an M2-like, tumor-supportive phenotype.

The results presented in Chapter 3 provide complementary lines of evidence that PD-1/PD-L1 interactions operate on multiple fronts in cHL. Rather than acting solely as a checkpoint on T cells, the PD-1/PD-L1 axis emerged from this work as a multifunctional hub: HRS cells expressing intact MHC-I suppress antigen-specific $CD8^+$ T-cell activation; PD-L1–expressing TAMs further sustain local $CD8^+$ T-cell suppression; PLA/IF analyses demonstrate direct PD-1/PD-L1 interactions between $CD8^+$ T cells, HRS cells, and TAMs within patient tissues, providing in situ evidence of inhibitory engagement; sustained PD-L1 ligation does not confer proliferative advantages on HRS cells under nutrient-replete conditions;; and soluble factors from HRS cells promote TAM skewing toward an M2-like phenotype, reinforcing an immunosuppressive

microenvironment. Importantly, PD-1 blockade enhanced $CD8^+$ T cell function in functional assays and reduced TAM-mediated suppression, consistent with the mechanistic role of PD-1/PD-L1 interactions in cHL, while highlighting that additional mechanisms within the TME may contribute to persistent immune suppression.

This discussion chapter interprets those findings in the light of the existing literature, critically evaluates methodological strengths and limitations, and positions the results within current understanding of PD-1/PD-L1–mediated immune evasion, tumor–microenvironment interactions, and translational immunotherapy strategies. For clarity, it is organized thematically into three major sections: (1) design and rationale of the antigen-specific co-culture system, highlighting its novelty and methodological significance; (2) PD-1/PD-L1–mediated suppression of $CD8^+$ T cells, integrating evidence for both HRS-driven and TAM-mediated checkpoint engagement; and (3) PD-1/PD-L1–driven modulation of HRS survival and TAM polarization, examining the bidirectional crosstalk between HRS cells and TAMs, in which HRS cells influence TAM polarization and TAMs, in turn, affect HRS-mediated suppression of $CD8^+$ T cells, together reinforcing immune evasion. The chapter concludes by synthesizing these two strands into a unified model, discussing implications for therapy and methodology, and outlining directions for future research.

4.1 Establishment of an antigen-specific co-culture system to dissect PD-1/PD-L1–mediated immune regulation

The first aim of this thesis was to establish a controlled antigen-specific co-culture system, which served as the experimental foundation for dissecting interactions between $CD8^+$ T cells, HRS cells, and macrophages and for evaluating how PD-1/PD-L1 signaling modulates these processes. The development of this system was motivated by the fact that existing PBMC-based co-culture models, while informative, cannot distinguish antigen-dependent activation from background responses of heterogeneous T-cell populations, limiting mechanistic analysis of antigen presentation, T-cell activation, and checkpoint-mediated regulation.

Previous studies have used PBMC–Hodgkin lymphoma co-culture models to examine T-cell interactions with HRS cells, providing important early insight into immune engagement in cHL [183,184]. However, the PBMC-based framework used in these studies presents several methodological constraints that limit mechanistic

interpretation. First, PBMCs contain heterogeneous populations, including $CD4^+$ and $CD8^+$ T cells, NK cells, B cells, and monocytes, making it difficult to assign activation, cytokine secretion, or checkpoint responses to specific T-cell subsets. Second, although HLA matching between PBMC donors and HL cell lines was verified, it is likely that only a very small fraction of endogenous TCRs can recognize HL-associated antigens. Any such antigen-specific responses would therefore be difficult to resolve within the broader PBMC population. Third, cytokines produced by diverse PBMC subsets, such as IL-2, IL-10, or IFN-γ, can secondarily activate other T cells, thereby masking whether observed responses arise from direct TCR–MHC engagement or from cytokine-driven amplification loops. Finally, although genetic manipulation of HL cell lines is technically feasible, PBMC co-cultures do not permit clear interpretation of such perturbations, because the heterogeneous mixture of immune cells makes it impossible to attribute resulting changes to antigen-specific $CD8^+$ T-cell recognition rather than to indirect effects mediated by cytokines, NK cells, or other PBMC subsets. These constraints highlight the need for a controlled, antigen-specific, and cell-type–resolved system capable of probing cytotoxic T-cell recognition and checkpoint-mediated inhibition with greater precision.

To achieve this, $CD8^+$ T cells were engineered to express an NY-ESO-1–reactive TCR restricted to HLA-A*02, while the HRS cell line L1236, which endogenously expresses HLA-A2, was transduced to express the NY-ESO-1 antigen, generating a defined TCR–MHC–peptide axis for interrogation. A key feature of this system is that PD-1 upregulation on $CD8^+$ T cells arises exclusively from productive TCR–MHC engagement rather than from nonspecific stimulation with IL-2, CD28 costimulation, or OKT3. As a result, PD-1 expression directly reflects antigen-driven activation, enabling precise evaluation of how PD-1/PD-L1 signaling modulates cytotoxic T-cell function. Importantly, $CD8^+$ T cells retaining only their endogenous TCRs were included as a specificity control for TCR-dependent signaling. Despite being HLA-A2–matched, these untransduced cells remained non-responsive because their native TCR repertoire did not recognize the NY-ESO-1 peptide, or any endogenous antigens presented by L1236, demonstrating that activation was strictly dependent on NY-ESO-1–restricted TCR–MHC–peptide engagement. The use of 4-1BB, CD107a, and caspase-3 allowed parallel assessment of activation, degranulation, and tumor-cell apoptosis, providing a coherent functional readout of the cytotoxic process. Together, the B2M and PD-L1 knockout controls, along with concordant readouts of activation, degranulation, and

cytotoxicity, provided functional validation of the model's antigen specificity and checkpoint dependence.

This antigen-specific configuration also permitted targeted perturbations of antigen presentation and checkpoint ligand expression. B2M knockout in HRS cells allowed direct testing of MHC-I dependency, confirming that TCR-mediated activation, degranulation, and killing require intact antigen presentation. A macrophage-inclusive variant further expanded the system by incorporating HLA-A2$^+$, NY-ESO-1–expressing macrophages, enabling analysis of antigen-specific T-cell–macrophage interactions and PD-1/PD-L1–dependent suppression in a TAM-like context.

Despite its advantages, this model has limitations. The macrophages used were generated and polarized in vitro and therefore cannot fully reproduce the phenotypic diversity, plasticity, and spatial organization of TAMs in vivo. The system also relies on engineered antigen presentation and a single defined antigen–TCR pair, which offers mechanistic clarity but does not reflect the full diversity of antigen–TCR interactions present in vivo. In addition, the approach is technically demanding, requiring viral engineering, cell sorting, and expansion of primary cells. Finally, reliance on a single HRS cell line limits representation of the broader heterogeneity of cHL. Nevertheless, the modular design of the system allows adaptation to alternative T-cell subsets—such as CD4$^+$ T cells—or to other engineered antigen–TCR pairs in future studies.

Future studies could extend this framework by incorporating additional TCR specificities or by adapting the system to CD4$^+$ T cells to examine helper T-cell–mediated regulation. The model could also be broadened by using patient-derived macrophages or HRS cell lines with distinct genetic backgrounds to increase physiological relevance. Together, the antigen-specific co-culture system developed here provides a mechanistically precise platform for dissecting T-cell regulation in cHL and serves as a complementary approach to patient-derived tissue analyses, enabling controlled evaluation of PD-1/PD-L1–dependent immune evasion across defined cellular compartments.

4.2 HRS cells as mediators of PD-1/PD-L1 dependent CD8$^+$ T cells suppression

The second aim of this thesis was to investigate the direct engagement of HRS cells with CD8$^+$ T cells via the PD-1/PD-L1 axis in MHC-I–intact contexts, to determine how this interaction suppresses T cell activity, and to assess whether blockade of this pathway can

restore cytotoxic responses. Using the antigen-specific co-culture systems established in aim 1, antigen-specific $CD8^+$ T cells effectively recognized and killed MHC-I–positive HRS cells, while B2M-deficient cells lacking MHC-I failed to elicit activation or cytotoxicity. Both pharmacological PD-1 blockade with nivolumab and genetic PD-L1 knockout enhanced $CD8^+$ T cell activity, demonstrating that PD-1/PD-L1 signaling suppresses antigen-specific responses in an MHC-I–dependent manner. Together, the B2M-KO and PD-L1-KO perturbations, combined with parallel readouts of activation (4-1BB), degranulation (CD107a), and apoptosis induction (caspase-3), provided internal validation of the specificity and functional integrity of the co-culture system in this experimental context. Complementary PLA/IF analysis of cHL tissues confirmed PD-1/PD-L1 interactions between $CD8^+$ T cells and HRS cells in situ, supporting the relevance of the checkpoint-mediated inhibitory interactions observed in vitro in the tumor microenvironment.

A prevailing model in classical Hodgkin lymphoma (cHL) posits that immune escape is primarily achieved through genetic inactivation of β2-microglobulin (B2M) and subsequent loss of MHC class I expression, thereby preventing recognition by $CD8^+$ T cells [78]. A recent study found MHC-I loss in more than 79% of evaluable cases, while a subsequent study in relapsed/refractory patients treated with PD-1 blockade reported absent or decreased expression in 93% of tumors, suggesting that antigen presentation is almost universally impaired and that $CD8^+$ T cell surveillance is therefore considered marginal in this disease [79,80]. From this perspective, the clinical efficacy of PD-1 blockade has been interpreted as largely independent of direct $CD8^+$ T cell–HRS interactions, reinforcing a model in which disrupted antigen presentation, rather than PD-1/PD-L1, mediated suppression, is considered the dominant mechanism of $CD8^+$ immune evasion in cHL. In this framework, the therapeutic benefit of PD-1 blockade is thought to arise predominantly through an alternative MHC class II–dependent, $CD4^+$ T-cell–associated mechanism of action, rather than through restoration of classical MHC-I–restricted $CD8^+$ T-cell surveillance.

These findings extend previous models, showing that immune escape in cHL cannot be explained by MHC-I loss alone but also involves checkpoint-mediated suppression in MHC-I–intact contexts. In the $CD8^+$ T-cell compartment, co-culture assays demonstrated that B2M-deficient HRS cells were shown to be invisible to antigen-specific $CD8^+$ T cells, validating loss of MHC-I as a functional escape mechanism (see Figures 22B and 24). Functional assays demonstrated that MHC-I–intact HRS cells

activate $CD8^+$ T cells, but this activity is restrained through PD-1/PD-L1 signaling, as confirmed by cytotoxic markers and apoptosis assays (see Figures 22B and 24). Notably, PD-1/PD-L1 interactions partially limited T cell activation, and treatment with PD-1 blockade or genetic disruption of PD-L1 enhanced this activation (see Figures 22B and 25). Furthermore, our in-situ PLA/IF analyses provided direct evidence that $CD8^+$ T cells engage HRS cells via PD-1/PD-L1 interactions within patient tissues (see Figure 35). Together, these findings establish that immune escape in cHL cannot be explained by MHC-I loss alone and highlight the functional importance of checkpoint-mediated suppression in MHC-I–intact contexts.

Recent studies report lower frequencies of B2M and MHC-I loss (~22–39%) [66–72], indicating that a substantial subset of HRS cells retain antigen-presenting capacity. Our functional data provide a mechanistic underpinning for these observations, showing that such MHC-I–intact HRS cells are not inert but actively engage with $CD8^+$ T cells in a checkpoint-restrained manner. The emerging genomic subtype model of cHL further reinforces this interpretation. Using cfDNA profiling two distinct genetic subtypes was identified: H1 tumors, frequently associated with MHC-I loss, and H2 tumors, which largely retain MHC-I but exhibit higher $CD8^+$ T cell infiltration and PD-L1 amplifications that drive T cell exhaustion [86]. Our results align closely with the H2 phenotype, providing functional evidence that PD-1/PD-L1 interactions are sufficient to suppress $CD8^+$ T cell activity when antigen presentation is intact.

Previous studies have suggested that EBV^+ cases almost uniformly retain intact MHC-I expression on HRS cells, accompanied by increased numbers of $CD8^+$ T cells in the tumor microenvironment [77,185]. More recently, spatially resolved single-cell imaging has provided higher-resolution confirmation of this pattern, showing that EBV-positive cHL nearly universally retains functional MHC-I expression, and that subsets of EBV-negative tumors also harbor MHC-I–positive HRS cells [82]. These MHC-I–expressing cases are consistently associated with immune-enriched microenvironments, including infiltrating $CD8^+$ T cells and $PD\text{-}L1^+$ macrophages. Importantly, our PLA/IF analyses go beyond simply showing close spatial proximity: they directly demonstrate PD-1/PD-L1 interactions occurring between $CD8^+$ T cells and HRS cells in situ. This provides strong mechanistic evidence that checkpoint-mediated suppression is not a theoretical possibility but an active process shaping $CD8^+$ T cell responses within the cHL microenvironment.

These discrepancies in the literature likely reflect differences in methodology (IHC vs. high-resolution multiplex imaging, use of different antibodies), the consideration of EBV status, and the heterogeneity of cHL subtypes, which has been shown to correlate with B2M status [78]. Studies that did not assess EBV status reported high frequencies of MHC-I loss, which may simply have reflected an overrepresentation of EBV^- cases. In contrast, analyses that separated EBV^+ and EBV^- tumors consistently show that EBV^+ cHL almost uniformly retains MHC-I expression. Thresholds for scoring MHC-I positivity may also contribute. Our data provide functional clarity in this debate: while confirming that B2M-deficient HRS cells are invisible to $CD8^+$ T cells, we also demonstrate that MHC-I–intact HRS cells are readily recognized, and that their activity is restrained through PD-1/PD-L1 interactions. These co-culture assays necessarily simplify the T cell–HRS interface—relying on established HRS cell lines, fixed effector-to-target ratios, and excluding other immune and stromal subsets (e.g., Tregs, NK cells, DCs)—so they may not fully capture the spatial and cytokine complexity of cHL microenvironment**.** Notably, our PLA/IF on patient FFPE tissue demonstrates in situ PD-1/PD-L1 engagement between $CD8^+$ T cells and HRS cells**,** but validating this in a larger, EBV-stratified cohort with an expanded multiplex panel (CD8, CD4/FOXP3, CD68/CD163, PD-1/PD-L1, MHC-I/B2M, GZMB, TIM-3/LAG-3) and quantitative interaction metrics would further strengthen and generalize these observations.

Taken together, these data suggest that immune escape in cHL is unlikely to be explained by B2M mutations alone. Instead, they point to a more integrated model in which loss of antigen presentation and checkpoint-mediated suppression represent complementary, context-dependent escape routes. Our functional experiments indicate that $CD8^+$ T cells are capable of recognizing and killing HRS cells when MHC-I is intact, but their activity is attenuated by PD-1/PD-L1 signaling, a suppression that can be effectively reversed by checkpoint blockade.

4.3 MHC class II–restricted $CD4^+$ T-cell regulation through PD-1/PD-L1 interactions in cHL

In addition to the CD8-focused mechanisms described above, several studies indicate that the PD-1/PD-L1 axis in cHL also operates through MHC class II–dependent interactions with $CD4^+$ T cells, providing an additional layer of immune regulation. Although $CD4^+$ T cells were not experimentally examined in this thesis, their potential involvement is

important to consider when interpreting the broader checkpoint landscape in cHL. Earlier studies reported that a substantial proportion of HRS cells exhibit reduced or absent MHC class II expression. However, analyses of relapsed/refractory patients treated with nivolumab demonstrated that nearly all complete responders retained membranous MHC-II expression on their HRS cells, indicating that $CD4^+$ T-cell engagement may contribute to the therapeutic effect of PD-1 blockade in MHC-II–positive tumors.

Spatial profiling studies further support this possibility, demonstrating that PD-1^+ $CD4^+$ T cells frequently localize near PD-$L1^+$ HRS cells, forming microenvironments enriched for inhibitory interactions. In situ analyses confirm direct PD-1/PD-L1 contacts between these cells, suggesting that checkpoint-mediated suppression extends to the $CD4^+$ T-cell compartment and may contribute to the therapeutic activity of PD-1 blockade in tumors that retain MHC-II.

In addition to their interactions with HRS cells, $CD4^+$ T cells may also participate in PD-1/PD-L1–mediated suppression through contacts with PD-$L1^+$ tumor-associated macrophages. Spatial profiling studies demonstrate that PD-1^+ $CD4^+$ T cells are enriched in the vicinity of macrophage-rich niches, where PD-$L1^+$ TAMs form substantial part of the local microenvironment and account for a substantial fraction of PD-L1 expression within the tumor. Although functional assays directly investigating CD4–TAM interactions remain limited, the consistent spatial proximity between these cell types suggests that macrophages may inhibit $CD4^+$ T-cell activity through PD-1/PD-L1 engagement. Such interactions likely contribute to the broader immunoregulatory architecture of cHL, in which TAMs serve as checkpoint partners for multiple T-cell subsets.

Together, these observations indicate that while $CD8^+$ T-cell suppression represents a key mechanism of immune evasion—particularly in MHC-I–intact settings—$CD4^+$ T-cell inhibition may operate in parallel through both HRS cells and PD-$L1^+$ TAMs in tumors that retain MHC-II expression. Although the functional roles of $CD4^+$ T cells were not directly addressed in this thesis, existing studies support a model in which CD4-mediated checkpoint interactions coexist with, rather than replace, CD8-driven mechanisms. In this broader framework, PD-1/PD-L1–dependent immune regulation in cHL is likely shaped by multiple T-cell subsets and multiple antigen-presenting partners, with the relative contribution of each pathway determined by the antigen-presentation profile and cellular composition of the tumor microenvironment.

4.4 TAMs as checkpoint partners in CD8$^+$ T cell suppression

The third aim of this thesis was to investigate whether PD-L1–expressing TAMs suppress antigen-specific CD8$^+$ T cell activity via PD-1/PD-L1 interactions and to determine whether this suppression can be alleviated by PD-1 blockade.

Using co-culture assays, antigen-specific CD8$^+$ T cells were activated when interacting with M2-like macrophages, and this activation was further enhanced by HRS cell–derived soluble factors. In contrast, HRS-derived soluble factors alone failed to activate T cells, indicating that their primary effect was to modulate macrophage function (see Figures 26A–B).

In triple co-cultures incorporating MHC-I–deficient HRS cells, PD-1/PD-L1 signaling partially suppressed CD8$^+$ T cell activation through interactions with TAMs, while treatment with Nivolumab restored T cell responses (see Figure 27). Complementary PLA/IF analyses of cHL tissues directly confirmed PD-1/PD-L1 interactions between CD8$^+$ T cells and TAMs in situ, demonstrating that this checkpoint pathway actively contributes to macrophage-mediated suppression within the tumor microenvironment (see Figure 35).

Previous studies have highlighted the abundance of PD-L1–expressing tumor-associated macrophages (TAMs) within the cHL microenvironment [112]. Topological analyses revealed that a subset of PD-1$^+$ CD8$^+$ T cells is significantly enriched in the vicinity of PD-L1$^+$ TAMs and more frequently in direct contact with them compared with PD-L1$^-$ TAMs [113]. Furthermore, M2-like TAMs are generally associated with immunosuppressive functions and can restrain CD8$^+$ T cell activity [186]. Supporting this notion, multiplexed spatial profiling of HRS cell neighborhoods demonstrated that EBV-positive HRS cells retain antigen presentation pathway proteins (B2M, MHC-I, and MHC-II) and are surrounded by both CD8$^+$ T cells and macrophages, highlighting the close spatial organization conducive to functional interactions [82].

These observations suggest that PD-L1$^+$ TAMs may both present antigens and impose PD-1–dependent suppression on CD8$^+$ T cells, positioning them as potential checkpoint partners for exhausted T cells. However, while spatial proximity supports this possibility, direct functional evidence that TAMs suppress cytotoxic activity via PD-1/PD-L1 interactions remained unresolved, underscoring the need for mechanistic studies.

These findings from the present study extend the understanding of immune regulation in cHL beyond HRS cell–specific mechanisms. Functional assays demonstrate that TAMs restrain antigen-specific $CD8^+$ T cell responses and that this effect is partially reversed by PD-1 blockade. The combination of PLA/IF and co-culture experiments provides direct evidence for checkpoint-mediated interactions between TAMs and T cells, highlighting the microenvironmental context: while HRS cells provide an initiating source of PD-L1, TAMs amplify and sustain suppression, establishing a multilayered barrier to cytotoxic immunity. Although our PLA/IF on FFPE tissues confirms in situ PD-1/PD-L1 engagement between $CD8^+$ T cells and TAMs, the triple co-culture approach necessarily simplifies this interaction, as macrophages were polarized in vitro and may not fully reflect the diversity, plasticity, and spatial organization of TAM subsets in patient tumors. Moreover, technical constraints limited deeper transcriptional profiling: macrophages are particularly fragile during cell sorting (and yield relatively little RNA compared with cell lines), making RNA-seq after co-culture infeasible, and generating sufficient numbers of T cells for post-co-culture RNA-seq would require extremely large-scale expansions of both T cells and macrophages, which was beyond the practical scope of this project. Future studies using patient-derived macrophages, single-cell or spatial transcriptomics to resolve TAM heterogeneity, and optimized approaches for capturing drug-induced transcriptional changes would strengthen and extend these findings, as would functional assays testing additional suppressive mechanisms (e.g., cytokine secretion, metabolic regulation, or co-inhibitory receptors beyond PD-1/PD-L1).

Together, these results suggest that TAMs are unlikely to be bystanders but act as functional checkpoint partners, restraining $CD8^+$ T cell activity via PD-1/PD-L1 engagement. They further indicate that checkpoint blockade can at least partially restore cytotoxic T cell function despite the immunosuppressive microenvironment. While our assays demonstrate checkpoint-mediated suppression, TAMs likely influence $CD8^+$ T cells through additional pathways, such as cytokine secretion or metabolic regulation, which remain to be explored.

4.5 Dual checkpoint engagement and compensatory roles of TAMs

The PLA–mIF approach applied in this study provides direct spatial evidence that PD-1/PD-L1 interactions in cHL occur across multiple cellular compartments, rather than being restricted to a single dominant partner cell. By first performing PLA to detect molecular proximity at subcellular resolution and subsequently re-staining the same sections with multiplex immunofluorescence, it was possible to assign PD-1/PD-L1 interaction to specific cell types with confidence while avoiding the interpretive limitations of colocalization-based imaging. This sequential strategy adds mechanistic resolution to earlier observations of PD-L1 expression on HRS cells and macrophages and PD-1 expression on T cells, moving beyond inference to direct visualization of checkpoint engagement within tissue.

Initial staining with CD3 and CD68 demonstrated that PD-1/PD-L1 interaction commonly arose at T cell–macrophage interfaces, indicating that TAMs are active participants in checkpoint engagement in situ (see Figure 34). Refinement with CD8 and CD163 staining further established that cytotoxic T cells interact with tumor-associated macrophages via PD-1/PD-L1 (see Figure 34), consistent with the functional data showing TAM-mediated suppression of $CD8^+$ T cell activation (see Figures 26-27). These findings align with recent topological studies showing spatial proximity between $PD\text{-}1^+$ T cells and $PD\text{-}L1^+$ macrophages in cHL but crucially extend them by confirming that these proximities reflect direct molecular engagement rather than simple colocalization.

Parallel assessment of CD8–CD30 interfaces demonstrated that HRS cells also contribute to checkpoint engagement. The detection of PLA puncta at CD8–CD30 contacts supports a model in which MHC-I–intact HRS cells can interact directly with cytotoxic T cells through PD-L1, suppressing effector responses (see Figure 34). Importantly, the presence of puncta in both CD8–HRS and CD8–TAM interactions suggests that PD-1/PD-L1 signaling is not monolithic but distributed among compartments, reinforcing the “division of labor” model developed in earlier sections: HRS cells can initiate suppression at the tumor cell level, while TAMs sustain it in the microenvironment.

Grouping cases by EBV status added an additional layer of biological relevance. In this study, PD-1/PD-L1 puncta at CD8–CD30 and CD8–CD163 interfaces (see Figure 35) showed a consistent tendency to be more frequent in EBV-positive compared to EBV-negative cases, suggesting that viral antigenicity may enhances checkpoint engagement

in multiple cellular compartments. This observation is consistent with reports that EBV-positive cHL almost universally retains intact MHC-I expression on HRS cells, increasing the likelihood of direct $CD8^+$ T cell recognition and subsequent PD-1/PD-L1–mediated inhibition [77,82,89]. However, the present study did not stratify either EBV-positive or EBV-negative cases according to their MHC-I status, so it remains unclear whether MHC-I–positive tumors, regardless of EBV status, would exhibit interaction patterns similar to those of EBV-positive disease. In parallel, other studies have shown that PD-L1 is more strongly expressed in EBV-positive cHL, both through 9p24.1 alterations and LMP1-driven signaling, further amplifying the capacity for checkpoint engagement [58,104,110,111]. In addition, EBV-positive tumors have been reported to contain higher densities of $CD163^+$ macrophages, providing a larger pool of PD-L1–expressing myeloid partners capable of sustaining immunoregulatory interactions with $CD8^+$ T cells [58,104]. Together, these findings support the notion that EBV-positive cHL may leverages both tumor-intrinsic and microenvironmental PD-1/PD-L1 pathways to counter heightened immune pressure, using HRS cells and TAMs as complementary suppressive partners.

Another observation was that in some cases with minimal CD8–HRS puncta, CD8–TAMs interactions remained relatively prominent. This provides in situ confirmation of functional data indicating that TAMs can act as alternative or compensatory partners for $CD8^+$ T cells, particularly where MHC-I expression on HRS cells is low or absent. Such a division of labor within the microenvironment may help explain why PD-1 blockade can be effective even in tumors with reduced antigen-presenting capacity: by disrupting macrophage-mediated engagement, the therapy may still relieve suppression even when direct tumor–T cell interactions are infrequent.

Finally, the use of appropriate negative controls and sequential sectioning ensures that the observed puncta reflect true PD-1/PD-L1 engagement rather than nonspecific signal. Compared to previous studies relying on spatial proximity, the current approach offers both molecular specificity and cellular attribution, strengthening conclusions about the cellular architecture of checkpoint engagement in cHL.

Taken together, these findings provide crucial in situ validation of the functional models developed in Aims 2 and 3. They demonstrate that both HRS cells and TAMs engage $CD8^+$ T cells via PD-1/PD-L1 in the native tissue environment, and that the relative contribution of each partner can vary by tumor context, including EBV status. Importantly, in cases where CD8–HRS interactions are limited or absent, such as when MHC-I expression is lost, TAMs still engage $CD8^+$ T cells via PD-1/PD-L1, providing

an alternative or compensatory suppressive mechanism. This spatial and molecular evidence supports a layered model of immune evasion, in which direct tumor–T cell interactions coexist with microenvironmental suppression mediated by TAMs. These data further justify therapeutic strategies that target both compartments, either sequentially or in combination.

4.6 Complementary roles of HRS cells and TAMs in immune evasion

The findings from Aim 2 and Aim 3 collectively reveal a multilayered mechanism of immune suppression in cHL. While HRS cells can directly engage $CD8^+$ T cells via PD-1/PD-L1 interactions, particularly in MHC-I–intact contexts, TAMs provide an additional, complementary layer of regulation. Functional assays and in situ analyses indicate that HRS cells act as initiators of suppression, presenting antigen and expressing PD-L1 to dampen T cell activation. In contrast, M2-like TAMs reinforce and stabilize this suppression, both by directly restraining $CD8^+$ T cell effector function through PD-1/PD-L1 engagement and by shaping the local cytokine milieu to sustain an immunosuppressive microenvironment.

This division of labor, HRS cells initiating and TAMs consolidating immune inhibition, offers a conceptual framework for understanding cHL immune evasion. Clinically, while nivolumab demonstrates high efficacy in cHL, responses are heterogeneous [187–190]: tumors with preserved MHC-I expression on HRS cells and abundant PD-$L1^+$ TAMs may respond differently than tumors with widespread antigen presentation loss or lower TAM density. Recognizing the distinct but complementary roles of HRS cells and TAMs in checkpoint-mediated suppression could inform more precise strategies for immunotherapy, including combination approaches targeting both tumor-intrinsic and microenvironmental mechanisms. A limitation of the current work is that, although our assays show that both HRS cells and TAMs contribute to checkpoint-mediated suppression, TAMs still suppress cytotoxic T cells even when HRS cells have limited interaction with them**.** Future studies integrating quantitative spatial analyses, patient-derived ex vivo models, and systems-level approaches, such as spatial transcriptomics (capturing gene expression in tissue context) and single-cell multiomics (combining RNA with protein or receptor profiling in the same cell), will be needed to clarify these relative contributions and to guide the rational design of therapeutic combinations.

4.7 Regulation of HRS survival via PD-1/PD-L1 signaling

The fourth aim of this thesis was to evaluate whether sustained PD-1/PD-L1 interactions deliver reverse signals to HRS cells that promote survival or proliferation. This question was motivated by prior evidence suggesting that PD-L1 expressed on tumor cells can act not only as a ligand but also as a signaling receptor. Additionally, it is now recognized that immune checkpoint interactions are not strictly unidirectional. While traditionally viewed as signals delivered to receptor-bearing T cells, accumulating evidence shows that several checkpoint ligands, including PD-L1, can also transmit 'reverse signals' into the ligand-expressing cell, often an APC or tumor cell, thereby influencing survival, metabolism, or differentiation pathways [191,192]. Unlike PD-1 signaling in T cells, which requires prior TCR–MHC engagement to be functionally relevant, PD-L1 reverse signaling is independent of antigen presentation and is initiated directly by PD-L1 ligation (e.g., PD-1 binding or antibody crosslinking), with reported links to downstream pathways. Building on this concept, the present work specifically examined whether sustained PD-1/PD-L1 engagement provides such reverse signals in HRS cells under conditions designed to mimic a more physiological environment.

In particular, Jalali et al. employed several experimental systems, including co-cultures of serum-starved L1236 HRS cells with PD-L1 membrane-bound agonistic antibodies, or co-cultures with PD-1–expressing 293T cells, to investigate whether PD-L1 on HRS cells could serve as a ligand for reverse signaling, promoting tumor cell survival and proliferation. Their experiments measured apoptosis (Annexin V/PI) and signaling pathways (p-ERK, p-p38), suggesting that engagement of PD-L1 could enhance HRS cell viability and pro-survival signaling. Notably, they also reported that treatment with Nivolumab could reverse these effects, supporting the potential clinical relevance of disrupting PD-L1 reverse signaling. While these findings provided important mechanistic insights, it is important to recognize that their 293T–L1236 co-culture experiments involved short-term readouts under serum starvation conditions, which may amplify stress-related signaling responses. In this context, the subsequent examination of L1236 proliferation and apoptosis under long-term co-culture conditions with PD-1–expressing 293T cells provides a complementary perspective to assess whether sustained PD-L1 engagement contributes to HRS cell survival in a more physiological setting, forming the basis for the discussion of our own experimental results (see Figure 32).

Using co-culture systems with PD-1–expressing 293T cells and L1236 HRS cells, we assessed whether sustained PD-1/PD-L1 engagement modulates tumor cell proliferation or survival. L1236 cells were maintained under long-term co-culture conditions, with or without Nivolumab treatment, and proliferation and apoptosis were monitored by cell counts and Caspase-3 activation. In contrast to previous short-term, serum-starved studies by Jalali et al., our results demonstrated that prolonged PD-L1 engagement did not alter L1236 proliferation or induce apoptosis (see Figures 32-33). These findings indicate that, under more physiologically relevant culture conditions, PD-1/PD-L1 interactions do not provide detectable pro-survival signals to HRS cells.

Several factors likely explain the apparent discrepancy between these results and the study by Jalali et al. Jalali et al. assessed short-term outcomes (minutes to 48 hours), focusing on acute phosphorylation of ERK/p38 and early apoptotic markers. In contrast, the present work measured sustained changes in proliferation and apoptosis across several days, directly testing the long-term consequences of PD-1/PD-L1 engagement. Moreover, Jalali et al. starved HRS cells prior to stimulation, a condition that may sensitize cells to stress and exaggerate the contribution of survival signals. By contrast, in nutrient-rich conditions, PD-L1 engagement did not produce measurable effects on HRS cell growth. Consistent with this, while Jalali et al. reported that Nivolumab reversed short-term survival effects in serum-starved cells, our long-term co-culture experiments showed that Nivolumab treatment did not alter L1236 proliferation or apoptosis, further supporting the conclusion that sustained PD-L1 engagement does not provide a growth advantage under nutrient-replete conditions (see Figures 32-33). Finally, the readouts differed: while Jalali et al. detected signaling changes and reduced apoptosis, the current study examined whether those signals translate into durable proliferative advantages, finding no evidence to support this.

Taken together, these findings suggest that PD-L1 reverse signaling may occur in HRS cells but that its functional consequences are highly context dependent. Under conditions of cellular stress, transient activation of ERK/p38 pathways may provide a survival advantage, as observed by Jalali et al. However, under steady-state, nutrient-replete conditions, such signaling appears insufficient to sustain proliferation or survival. Importantly, these results do not exclude the possibility of PD-L1 reverse signaling in HRS cells, particularly under stress or acute stimulation. A limitation of this work is that it relied on a single HRS cell line (L1236), and the assays focused only on proliferation and apoptosis, which may not capture broader transcriptional or metabolic consequences

of PD-L1 engagement. While the present long-term assays under nutrient-rich conditions provide a more physiological framework than short-term serum starvation, they still do not reproduce metabolic stresses typical of the cHL microenvironment, such as hypoxia or nutrient competition. Future studies should employ additional HRS models with diverse genetic backgrounds, integrate short-term phospho-signaling assays (e.g., ERK, p38, AKT activation within hours of PD-L1 ligation) with long-term functional readouts (proliferation, apoptosis, metabolic activity), and apply transcriptomic profiling to capture gene-expression changes together with metabolic profiling to detect shifts in nutrient utilization and energy pathways. These approaches under stress conditions will be important to clarify the contexts in which PD-L1 reverse signaling has biological relevance. By extending previous short-term studies to long-term co-culture settings, this work provides evidence that sustained PD-1/PD-L1 engagement does not appear sufficient to promote HRS survival under nutrient-replete condition.

4.8 HRS cells drive macrophage polarization toward an M2-like, immunosuppressive phenotype

The fifth aim of this thesis was to investigate how HRS-derived soluble factors shape macrophage polarization, with a particular focus on whether these tumor-educated macrophages acquire transcriptional programs characteristic of M2-like, immunoregulatory states. While tumor-associated macrophages (TAMs) in cHL have been associated with poor prognosis [61,69], and several studies have explored the influence of HRS cells on macrophages, the precise molecular and functional changes induced by HRS cell–derived factors are still being elucidated. By examining the transcriptomic profiles of macrophages exposed to conditioned media from L1236 and HDLM2 cell lines, this study aims to elucidate the extent to which HRS-derived signals promote an M2-like, immunosuppressive phenotype capable of modulating $CD8^+$ T cell activity.

Primary human monocytes were first differentiated into macrophages and then polarized using conditioned media (CM) from L1236 and HDLM2 HRS cell lines or control stimuli (IL-4 for M2 and LPS + IFN-γ for M1). Principal component analysis of global RNA-seq data revealed a clear separation between M1-polarized macrophages and those stimulated with IL-4 (M2) or tumor-derived CM, with CM-treated macrophages clustering closely with M2 macrophages (see figure 28). Hierarchical clustering further

confirmed that the transcriptional programs induced by HRS cell CM closely resemble those of classical M2 macrophages, indicating that soluble factors secreted by HRS cells are sufficient to drive M2-like polarization (see figure 29). These findings are consistent with previous studies showing that HL-derived CM can promote TAM-like features in vitro, supporting the relevance of this experimental model.

Analysis of canonical polarization markers revealed that CM-treated macrophages exhibited upregulation of M2-associated genes such as CD163, IL10, STAB1, IL1R2, CSF1R, FCGR2A, FZD2, PTGS1, and IL1R1, accompanied by downregulation of M1 markers CXCL9, IL1B, TNF, TNFAIP3, TNFSF10, and IRF1 (see figure 30). These results indicate that HRS-derived CM not only drives a global transcriptional program resembling M2 macrophages but also specifically promotes genes characteristic of alternative activation. Similar findings have been reported, showed that HL-conditioned media induced $CD163^+$ and $MRC1^+$ macrophages with high IL-10 expression, consistent with our RNA-seq data [181,193]. Furthermore, a focused analysis of immunoregulatory genes revealed elevated expression of MRC1 (CD206), CD274 (PD-L1), IL-10, MMP9, MMP2, VSIG4, PDGFB, and PDGFA (see figure 31), suggesting that CM-treated macrophages acquire a transcriptional profile with the potential to suppress $CD8^+$ T cell effector function. VSIG4 is particularly noteworthy, as it has recently been identified as a TAM-associated checkpoint receptor in diffuse large B-cell lymphoma (DLBCL), where its expression correlated with adverse prognosis, though its role in cHL has not been systematically examined [194]. Likewise, PDGFB and PDGFA, while not canonical TAM markers in cHL, are growth factors that macrophages can secrete in tissue remodeling contexts, and their detection here raises the possibility that macrophage-derived PDGF signaling may contribute to the immunoregulatory tumor microenvironment [195]. This extends prior observations identifying GPNMB as an HL-induced immunosuppressive mediator [196], by highlighting soluble factors (e.g., VSIG4, PDGFB, MMP9) that have received less attention in cHL. Several of these markers, such as CD163, MRC1, and IL-10, are well-established TAM markers in cHL [169], underscoring the in vivo relevance of our findings. A limitation of this work is that the conditioned media approach captures only the effects of soluble factors secreted by HRS cells. While this design was intentional to isolate tumor-derived cues, in vivo macrophages are simultaneously exposed to additional inputs from other immune and stromal cells, including cytokines and chemokines that can further shape their phenotype. As such, the macrophages generated here do not fully

recapitulate the transcriptional complexity of patient-derived TAMs. Future studies using more complex co-culture systems or patient-derived material will be important to clarify how HRS-derived signals integrate with additional microenvironmental inputs to drive TAM heterogeneity. It will also be important to test how checkpoint blockade or targeted inhibitors (e.g., against VSIG4, MMP9, or PDGF signaling) reshape these transcriptional and functional states in cHL. These transcriptomic results expand the current view of HRS–macrophage interactions, setting the stage for understanding how TAMs stabilize immune evasion alongside PD-1/PD-L1 pathways characterized in Aim 3.

Together, these findings suggest that HRS cells orchestrate a multilayered immunosuppressive network by polarizing macrophages toward an M2-like phenotype. This polarization complements the direct PD-1/PD-L1–mediated suppression of T cells described in Aim 3, providing a mechanism by which TAMs reinforce and stabilize immune evasion within the tumor microenvironment. By inducing both canonical M2 markers and immunoregulatory genes, HRS-derived CM establishes a microenvironment supportive of tumor survival and resistant to cytotoxic T cell activity. Of note, the upregulation of MMP9 is particularly relevant, as inhibition of this molecule has been shown to restore T cell trafficking and anti-tumor immunity in other cancer models [197], suggesting that MMP9 may represent a critical barrier to effective cytotoxic responses in cHL. In addition, the induction of VSIG4 and PDGF ligands (PDGFB, PDGFA) points to to emerging immunoregulatory axes, with VSIG4 linked to adverse prognosis in DLBCL [194] and PDGF signaling implicated in stromal remodeling and immune suppression in solid tumors [195]. Importantly, dual blockade of PDGFRα/β and PD-1 synergistically suppressed the growth of fibrotic tumors [195], underscoring the therapeutic potential of simultaneously targeting PDGF-driven remodeling and checkpoint pathways. These results highlight not only checkpoint-mediated inhibition but also a broader array of soluble and surface mediators as potential contributors to TAM-driven immunosuppression, underscoring the need for future studies to explore whether targeting VSIG4, MMP9, or PDGF signaling could complement PD-1 blockade in cHL.

By demonstrating that HRS-derived factors polarize macrophages toward an immunosuppressive phenotype, these findings extend the PD-1/PD-L1–centric suppression described in Aim 3, revealing how tumor cells and macrophages cooperate to enforce layered T cell inhibition in cHL. This supports a model in which HRS cells initiate checkpoint-mediated inhibition while simultaneously remodeling macrophages to sustain suppression, creating a cooperative and resilient immunosuppressive network.

4.9 A multilayered model of immune evasion in cHL

This discussion has examined how the PD-1/PD-L1 axis contributes to immune evasion in cHL across four complementary aims. Aim 1 and aim 2 demonstrated that HRS cells directly suppress $CD8^+$ T cell activity in MHC-I–intact contexts via PD-1/PD-L1 interactions, while Aim 3 showed that TAMs act as checkpoint partners that reinforce this suppression within the tumor microenvironment. Aim 4 assessed reverse signaling in HRS cells and found no evidence that sustained PD-L1 engagement promotes survival under physiological conditions, though context-dependent effects remain possible. Finally, aim 5 established that HRS-derived soluble factors polarize macrophages toward an M2-like, immunosuppressive phenotype, underscoring the cooperative role of TAMs in maintaining checkpoint-mediated immune evasion. While these findings are necessarily shaped by the limitations of in vitro systems, together, these findings support a multilayered model in which HRS cells and TAMs act in concert to create a resilient immunosuppressive network, operating through both direct checkpoint engagement and macrophage reprogramming. While much of this work relied on controlled in vitro systems, the in situ PLA/IF analyses provided crucial validation in patient tissue, linking mechanistic insights to native tumor architecture and confirming that these interactions occur in vivo.

The PLA–mIF approach demonstrated that PD-1/PD-L1 interactions are distributed across both tumor-intrinsic and microenvironmental compartments. PLA puncta were detected at CD8–HRS and CD8–TAM interfaces, indicating that checkpoint signaling is not confined to a single cellular partner. In cases with minimal CD8–HRS engagement, prominent CD8–CD163 interactions suggested that TAMs can compensate as alternative partners when direct tumor–T cell contact is limited, such as in MHC-I–deficient contexts. EBV-positive tumors exhibited higher frequencies of puncta at both CD8–CD30 and CD8–CD163 contacts, consistent with reports of intact MHC-I expression on HRS cells, higher PD-L1 levels, and increased $CD163^+$ macrophage density in this subgroup. Altogether, these patterns support a model in which HRS cells initiate checkpoint-mediated suppression while TAMs reinforce and sustain it, creating a layered and adaptable network of immune evasion.

This integrated perspective refines current understanding of immune evasion in cHL and situates the work within the broader field of tumor immunology, where tumor–microenvironment crosstalk is increasingly recognized as a determinant of checkpoint

blockade responses. By linking tumor-intrinsic and microenvironmental mechanisms of PD-1/PD-L1 activity, this thesis provides a conceptual framework that can inform future therapeutic strategies in cHL.

5 Conclusion and Outlook

This thesis dissected the contribution of the PD-1/PD-L1 axis to immune evasion in cHL by functionally examining checkpoint interactions between HRS cells, $CD8^+$ T cells, and TAMs. While immune escape in cHL has often been attributed to loss of MHC class I and the resulting evasion of $CD8^+$ T-cell surveillance, our findings show that when HRS cells retain MHC-I expression, they still engage $CD8^+$ T cells through PD-1/PD-L1 interactions, and this checkpoint signaling can suppress $CD8^+$ T-cell activity despite preserved antigen presentation. Importantly, nivolumab was able to partially restore $CD8^+$ T-cell function under these conditions. Macrophages further strengthen this checkpoint-mediated suppression within the tumor microenvironment. Taken together, the results support a multilayered model in which HRS cells and TAMs cooperate to attenuate cytotoxic immunity through complementary mechanisms rather than a single dominant route.

As a foundation for these mechanistic studies, this thesis established an antigen-specific co-culture system designed to isolate and interrogate TCR-dependent signaling events with high precision. By enforcing defined antigen–TCR pairing, the model enabled controlled analysis of PD-1/PD-L1–mediated suppression and provided a clarity not achievable in PBMC-based systems. Its modular structure also forms a groundwork for extending co-culture platforms to additional immune or stromal cell types and for examining inhibitory pathways beyond PD-1/PD-L1. This system therefore represents an important methodological basis that supported the subsequent dissection of immune regulatory mechanisms in cHL.

In situ PLA/IF analysis further confirmed that PD-1/PD-L1 interactions occur not only between $CD8^+$ T cells and HRS cells, but also between $CD8^+$ T cells and TAMs within intact patient tissue, demonstrating that checkpoint engagement operates through multiple cellular partners in vivo.

A key contribution of this work is the demonstration that HRS cells can suppress antigen-specific $CD8^+$ T-cell activity via PD-1/PD-L1 interactions even when MHC class I expression is preserved. In situ PLA/IF provided direct evidence of checkpoint engagement between HRS cells and $CD8^+$ T cells in patient tissues. Functional assays further showed that $CD8^+$ T cells can recognize and kill MHC-I–intact HRS cells, but that this cytotoxic response is constrained by PD-1/PD-L1 signaling. Both PD-1 blockade and PD-L1 knockout enhanced $CD8^+$ T-cell activity, confirming the functional relevance of

this interaction. These findings challenge models that attribute immune escape in cHL almost exclusively to B2M loss and loss of antigen presentation and instead highlight checkpoint-mediated suppression as a critical barrier in a substantial subset of cases.

Beyond tumor–T-cell interactions, this thesis demonstrates that TAMs act as functional checkpoint partners that reinforce $CD8^+$ T-cell inhibition. In co-culture assays, macrophages expressing PD-L1 suppressed T-cell activity, and this effect was alleviated by PD-1 blockade. PLA/IF analyses confirmed that $CD8^+$ T cells engage TAMs via PD-1/PD-L1 in situ, indicating that macrophages not only surround HRS cells but actively shape the suppressive niche. These findings indicate that TAMs contribute directly to checkpoint-mediated suppression within the tumor microenvironment.

Moreover, PLA/IF revealed that in cases with minimal CD8–HRS engagement, CD8–macrophage interactions remained prominent, supporting the idea that TAMs can compensate as alternative checkpoint partners when direct tumor– $CD8^+$ T-cell contacts are limited.

Having established the contribution of both tumor cells and TAMs to PD-1/PD-L1–mediated suppression, we next asked whether reverse signaling might also play a role. The investigation of PD-L1 reverse signaling in HRS cells showed that sustained PD-1/PD-L1 engagement did not confer a proliferative or survival advantage under nutrient-sufficient, long-term conditions. While earlier studies suggested context-dependent signaling effects under nutrient-restricted conditions or short-term stimulation, the absence of sustained growth benefits in this work indicates that checkpoint-mediated immune evasion in cHL is primarily driven by suppression of T cells rather than direct effects on tumor cell viability or expansion. Nonetheless, the context dependence of reverse signaling remains an open question, particularly under microenvironmental stressors such as hypoxia, glucose restriction, or oxidative stress.

In parallel to these tumor-intrinsic investigations, we also explored how tumor-derived soluble factors shape the immune microenvironment. This thesis demonstrates that HRS-derived soluble factors polarize macrophages toward an M2-like, immunosuppressive phenotype. RNA sequencing revealed that conditioned media from HRS cell lines induced transcriptional programs closely aligned with canonical M2 macrophages, including upregulation of IL-10, CD163, and MRC1. The induction of immunoregulatory mediators such as VSIG4, MMP9, and PDGF family ligands suggests that TAMs contribute to suppression through mechanisms extending beyond PD-1/PD-L1. These

findings provide mechanistic insight into how tumor cells not only engage in checkpoint interactions but also remodel the microenvironment to sustain suppression.

Together, these strands of evidence support a layered model of immune evasion in which HRS cells initiate checkpoint-mediated inhibition of $CD8^+$ T cells in MHC-I–intact contexts, while TAMs consolidate and prolong this suppression. This cooperative framework helps explain both the high efficacy and variability of PD-1 blockade in cHL. Tumors with preserved antigen presentation and abundant PD-$L1^+$ TAMs may derive particular benefit from checkpoint inhibition, whereas cases dominated by antigen loss or alternative suppressive circuits may show incomplete responses.

Notably, PLA/IF spatial mapping demonstrated that both CD8–HRS and CD8–TAM interactions contribute to checkpoint engagement, and that EBV-positive tumors showed higher interaction rate of PD-1/PD-L1 across both interfaces, consistent with their preserved MHC-I expression, higher PD-L1 levels, and increased TAM density.

Although $CD4^+$ T cells were not the main experimental focus of this thesis, prior studies have reported their frequent proximity to PD-L1–expressing HRS cells and TAMs, raising the unresolved question of whether this reflects true MHC-II–restricted engagement or merely localization within PD-L1–rich niches. Proximity alone does not establish functional checkpoint signaling or T-cell suppression. Small populations of cytotoxic $CD4^+$ T cells have been reported in lymphoma and other tumors, suggesting that $CD4^+$ T cells may directly kill MHC-II–positive HRS cells when appropriately activated [198–200]. However, it remains unclear whether helper or cytotoxic $CD4^+$ T-cell functions are actively restrained through PD-1/PD-L1 interactions in cHL.

Future studies should therefore use co-cultures of MHC-II–expressing HRS cells and antigen-specific $CD4^+$ T cells—with and without PD-1/PD-L1 blockade—to test whether checkpoint inhibition restores $CD4^+$ T-cell function. In parallel, macrophage–$CD4^+$ T-cell co-cultures could clarify whether TAMs suppress helper T-cell responses through the same checkpoint axis and whether this indirectly affects $CD8^+$ T-cell priming, effector function, or memory formation. Complementary in situ approaches such as PLA/IF or spatial proteomics will be needed to determine whether $CD4^+$ T cells form bona fide PD-1/PD-L1 interactions with HRS cells or TAMs rather than merely co-localizing. Together, these experiments would clarify whether $CD4^+$ T cells in cHL act as helper cells, acquire cytotoxic activity, or become suppressed through checkpoint engagement—and whether relieving this suppression could indirectly enhance $CD8^+$ T-cell responses.

From a translational standpoint, the data suggest that checkpoint blockade alone may not fully restore cytotoxic immunity in cHL and that rational combination strategies will be needed to overcome microenvironmental resistance. In addition to checkpoint modulation, targeting macrophage-associated mediators offers complementary therapeutic opportunities. VSIG4 can be investigated using Fc-silent blocking antibodies or knockdown systems to assess effects on macrophage polarization and $CD8^+$ T-cell proliferation. MMP9 inhibition, through pharmacologic inhibitors or genetic silencing, can be tested in 3D co-culture models to determine whether reduced matrix remodeling improves T-cell infiltration and cytotoxicity. The role of PDGF signaling can be assessed by blocking PDGF ligands or PDGFR activity in macrophage–stromal co-cultures and examining resulting effects on matrix remodeling and T-cell access. These experiments would show whether blocking macrophage-driven suppression can improve or complement PD-1 therapy in cHL.

Although our data demonstrate that PD-1/PD-L1 interactions occur between $CD8^+$ T cells and TAMs and that nivolumab restores T-cell function by disrupting this interaction, it remains unclear whether the antibody acts solely through T-cell PD-1 blockade or also affects macrophages directly via PD-L1 reverse signaling. To address this, future studies should first determine whether multivalent PD-1 ligation can trigger intracellular signaling in macrophages, using Fc-silent PD-1 reagents to enforce PD-L1 clustering. Validation in primary macrophages and comparison of full-length versus tail-truncated PD-L1 will be essential to confirm receptor dependence. Building on our current T cell–macrophage assays, additional co-cultures will be needed in which $PD\text{-}1^+$ activated T cells engage macrophages under defined conditions, with or without HRS-conditioned media, to test whether macrophage-intrinsic PD-L1 signaling alters T-cell proliferation or macrophage polarization. These refinements go beyond our present system, which captured the suppressive effect of macrophages on $CD8^+$ T cells but did not isolate potential reverse signaling in macrophages themselves. If confirmed, macrophage-intrinsic PD-L1 signaling would expand the current model by suggesting that PD-1 blockade may relieve T-cell suppression and reprogram suppressive myeloid cells simultaneously.

In summary, this thesis advances the understanding of immune evasion in cHL by showing that PD-1/PD-L1 signaling operates through both tumor-intrinsic and microenvironmental mechanisms. It demonstrates that HRS cells and macrophages collaborate to suppress $CD8^+$ T-cell activity and that immune escape reflects more than

antigen loss alone. By integrating functional assays with spatial validation and transcriptional profiling, the work provides a conceptual framework that can guide future mechanistic studies and inform the design of more effective immunotherapies. The outlook emerging from these findings is one in which targeting checkpoint pathways in isolation is unlikely to suffice; instead, dismantling the layered suppressive network formed by HRS cells and TAMs, including potential macrophage-intrinsic PD-L1 signaling, will be key to unlocking durable cytotoxic responses in cHL.

Appendix

Appendix A: Isolation of human peripheral blood mononuclear cells

Peripheral blood mononuclear cells (PBMCs) were isolated from buffy coats by density gradient centrifugation, to generate T cells (Section 2.2.5), macrophages (Section 2.4.1) or feeder cells for T cells REP (Section 2.2.7). PBMCs were prepared freshly for each experiment. Buffy coats (45-50ml) were obtained from the blood bank of the UKGM. Blood was carefully transferred from transfusion bag to T75 cell culture flask. For the T cells, macrophages generation, buffy coats were screened for HLA-A2 expression. To determine which buffy coat expressed HLA-A2, 100 µl of blood was transferred into a 5 ml tube from each donor. 5 µl of anti-human HLA-A2-APC or 20 µl of isotype control antibody (mouse IgG2b-APC) were added to the blood, and the tube was vortexed. The samples were then incubated for 15 min at RT in the dark. During the incubation, a 1x lysing solution was prepared by diluting 10x concentrate lysing solution 1:10 with Millipore H_2O. After incubation, 2 ml of 1x lysing solution was added to the blood-antibody mixture and incubated for 7 min at RT in the dark. The samples were then centrifuged for 10 min at 300 x g. The supernatant was discarded, and the cell pellet was resuspended in 2 ml of FACS buffer and centrifuged for 5 min at 200 x g. The washing step was repeated, and the pellet was resuspended in 200 µl of FACS buffer. Finally, the expression of HLA-A2 was measured using a flow cytometer.

HLA-A2 positive buffy coat was diluted with 1x DPBS Ca^2 and Mg^2 free or RPMI 1640 without any supplement at a ratio of 1:1. Lymphoprep was used as density gradient medium. 12 ml of Lymphoprep were transferred onto the new 50 ml falcon tube, and 25ml diluted blood were gently layered on the top without disturbing the interface between the Lymphoprep and diluted blood. The falcon was centrifuged (800xg, 20 min, 18-20°C, no brake). During centrifugation, difference in density between cells and Lymphoprep cause cells migration and the formation of layers containing different cell types. Granulocytes and erythrocytes have a higher density than mononuclear cells therefore they aggregate through the Lymphoprep at the bottom of the flask. Whereas mononuclear cells with lower density remain and form whitish ring at the interface between plasma and Lymphoprep.

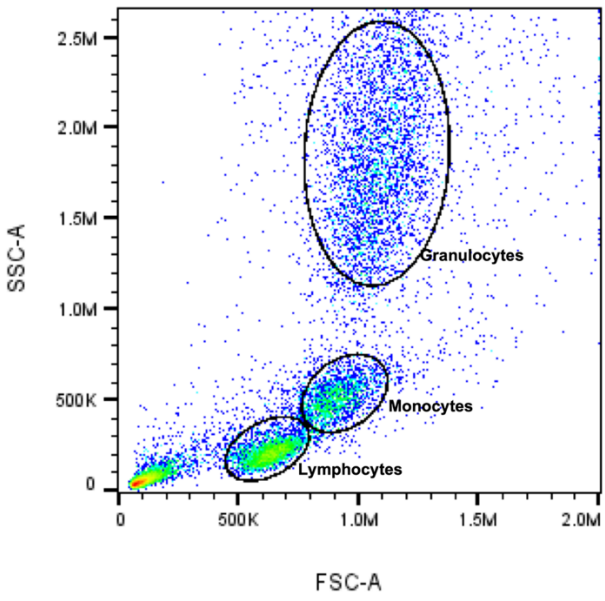

Figure S1. Peripheral blood mononuclear cells (PBMC) isolation. Flow cytometry analysis following PBMC isolation, showing distinct lymphocyte, monocyte, and granulocyte populations, confirming successful isolation of PBMCs.

After centrifugation, mononuclear cells ring was removed by Pasteur pipette and transferred into new Falcon tube. For the T cells generation, PBMCs were washed twice with 50ml PBS or RPMI 1640 without supplements, then centrifuged for 7 min at 500xg. Cell pellet was resuspended and seeded out specifically for T cells generation (Section 2.2.5) or were transferred into T75 cell culture flask containing 40ml complete RPMI medium. After overnight incubation, PBMCs were transferred T25 cell culture flask and irradiated for feeder cell generation (Section 2.2.7). For the monocyte isolation, the following washing steps were performed [201]: mononuclear cells were carefully removed and paced into new tubes (two interfaces per 50-ml tube). Tubes were filled with ice-cold PBS and centrifuged (250xg, 7 min, 4°C, with half brake). After centrifugation, each pellet was resuspended with 5 ml ice-cold PBS, then all cells were pooled into one 50 ml tube containing 40 ml of ice-cold PBS and centrifuged (250 x g, 7 min, 4°C, with full brake). These washing steps were repeated three or four times until the solution was clear, indicating the absence of platelets. Then, monocytes underwent CD14 MACS separation (Section 2.4.1).

Appendix B: Flow cytometry, cell sorting, and gating strategies

This appendix provides detailed protocols for staining, gating, and analysis of flow cytometry and cell sorting experiments.

Cells were harvested and resuspended in FACS staining buffer. To ensure a single-cell suspension, the cell suspension was filtered through a 70 µm cell strainer prior to cell sorting. When the primary goal was to measure only the signal, this step was replaced by thorough pipetting to break up cell clumps.

Surface staining was performed using fluorophore-conjugated antibodies targeting CD271 (LNGFR), CD3, CD56, CD4, CD8, CD137 (4-1BB), CD279 (PD-1), CD274 (PD-L1), HLA-A, B, C (B2M), CD80, CD86, and CD14, depending on the cell type and experimental aim. Cells were incubated with the respective antibodies for 30 min at 4°C in the dark. Staining procedures for HLA-A2, activated Caspase 3, and CD107a were performed as described in Appendix A1 and Sections 2.5.2-2.5.3, respectively.

Intracellular staining for NY-ESO-1 was performed as follows:

Cells were harvested and centrifuged at 500 × g for 5 min at RT. The supernatant was aspirated, and the cell pellet was washed with 1 ml of FACS staining buffer, followed by centrifugation at 500 × g for 5 min at RT. The pellet was then resuspended in 100 µl of 4% paraformaldehyde (PFA) per 1 million cells and mixed thoroughly to dissociate the pellet and prevent cross-linking of individual cells. Cells were incubated for 15 min at RT to allow proper fixation. Following incubation, 1,000 µl of FACS staining buffer was added, and the cells were centrifuged at 500×g for 5 min at RT. The supernatant was aspirated, and the pellet was resuspended in 100 µl of ice-cold PBS. Cells were permeabilized by adding 900 µl of 100% methanol, followed by incubation on ice for 30 min. The cells were then centrifuged at 500 × g for 5 min at RT. Cell pellet was often not visible due to the methanol incubation step. The supernatant was aspirated, and the pellet was resuspended in 1 ml of FACS staining buffer.

The cell suspension was then divided equally into two Eppendorf tubes: one for the isotype control and the other for NY-ESO-1 staining. Cells were centrifuged at 500 × g for 5 min at RT, and the pellets were resuspended in 50 µl of the respective antibody solution. Cells were incubated with the antibodies for 1 h at 4°C in the dark. After incubation 1ml FACS staining buffer was added and centrifuged at 500xg for 5 min at RT. The supernatant was aspirated, and the pellet was resuspended in 200 µl of FACS

staining buffer. The cell suspension was transferred into a 96-well FACS plate for measurement using a flow cytometer.

For the measurement of cell surface or intracellular markers, signal detection was performed using a CytoFLEX Flow Cytometer equipped with four lasers: 405 nm (Violet laser), 488 nm (Blue laser), 561 nm (Yellow-green laser), and 638 nm (Red laser), operating in a 13-color configuration with a 4-2-4-3 laser setup.

For cell sorting, stained cells were sorted using a BD FACSMelody Cell Sorter equipped with three lasers: 488 nm (blue diode laser, 20 mW), 561 nm (yellow-green semiconductor laser, 50 mW), and 640 nm (red diode laser, 40 mW). The instrument operated in an 8-color configuration with a 2-2-4 laser setup. Sorted cells were collected into tubes containing culture medium (e.g., RPMI with 10% FBS) to ensure viability. Post-sorting purity was assessed by reanalyzing a fraction of the sorted cells and was consistently >95%.

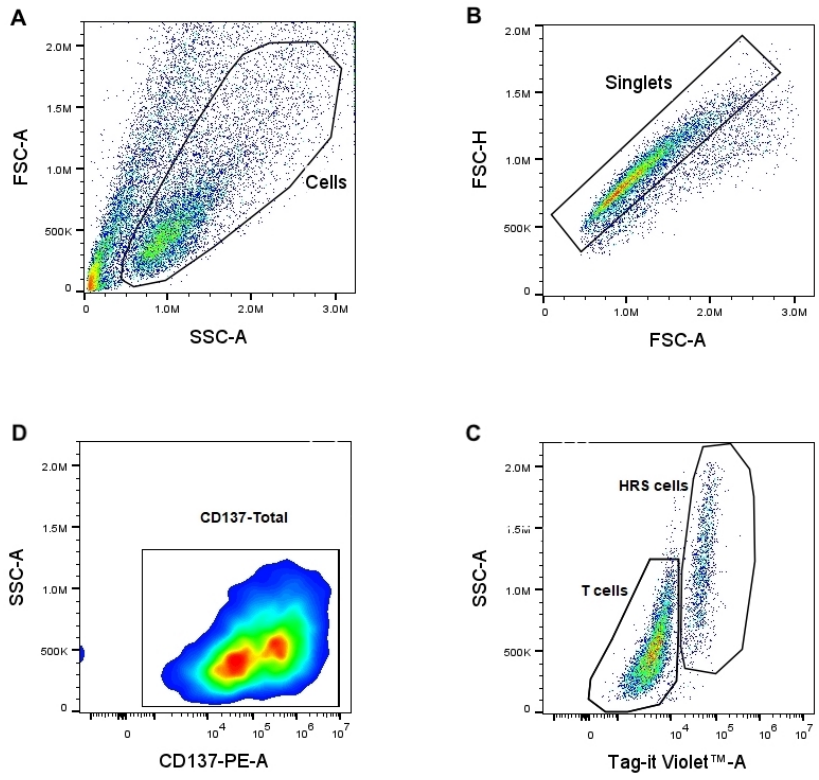

Figure S2. Gating strategy for identification of CD8$^+$CD137$^+$ T cells after co-culture with target HRS cells. Representative gating steps performed in FlowJo v10.10 are shown. (A) Debris was excluded based on forward and side scatter (FSC vs. SSC), and (B) doublets were removed using FSC-A vs. FSC-H. (C) CD8$^+$ T cells were selected, (D) followed by gating on CD137 (4-1BB)–positive cells to assess activation. This strategy was applied to T cells following 24 h co-culture with antigen-expressing HRS cells. MFI was used to assess the expression level of the marker in the gated population.

Target cell populations were identified using sequential gating strategies in FlowJo v10.10 software, including debris exclusion using forward and side scatter (FSC vs. SSC), doublet discrimination (FSC-H vs. FSC-A), viability gating, and fluorophore-based marker expression. A representative gating hierarchy used to identify $CD8^+CD137^+$ T cells following co-culture experiments is shown in Figure S2.

Appendix C: PD-1 blockade fails to activate endogenous $CD8^+$ T cells

To assess whether PD-1 blockade enhances activation of endogenous (non–TCR-transduced) $CD8^+$ T cells in the presence of HRS cells, primary human $CD8^+$ T cells were co-cultured with NY-ESO-1^+ L1236 cells with or without 15 µg/ml Nivolumab. As shown in the representative flow cytometry plots (Figure S3A–B), co-culture with wild-type L1236 cells led to a reduction in 4-1BB expression compared to baseline, and Nivolumab treatment did not restore activation. A similar pattern was observed when endogenous $CD8^+$ T cells were co-cultured with B2M-deficient L1236 cells (Figure S3C–D), with no increase in 4-1BB expression following PD-1 blockade. These findings indicate that, in the absence of antigen-specific TCR recognition, endogenous $CD8^+$ T cells do not become activated by HRS cells and fail to respond to PD-1 blockade.

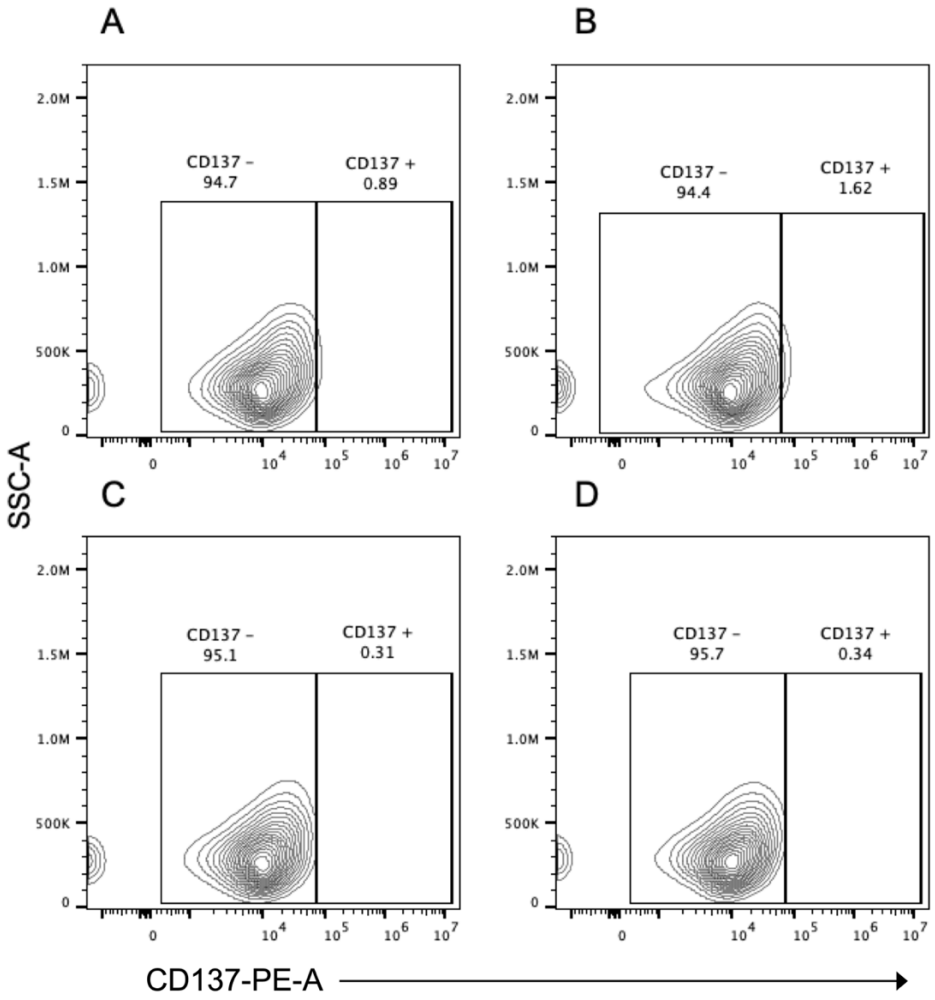

Figure S3. Representative flow cytometry analysis of T cell activation following co-culture with L1236 cells. Primary human endogenous TCR CD8$^+$ T were co-cultured for 24 h with NY-ESO-1$^+$ L1236 cells, either (A) untreated (control) or (B) treated with 15 µg/ml Nivolumab. Or (C) endogenous TCR CD8$^+$ T cells were cultured with the L1236 B2M KO cells, either (C) untreated (control) or (D) treated with 15 µg/ml Nivolumab. CD8$^+$ T cells were gated and analyzed for 4-1BB expression as a marker of activation. The plots show representative results from one experiment, illustrating downregulation of 4-1BB upon co-culture and no enhancement by Nivolumab treatment.

Supplementary Material

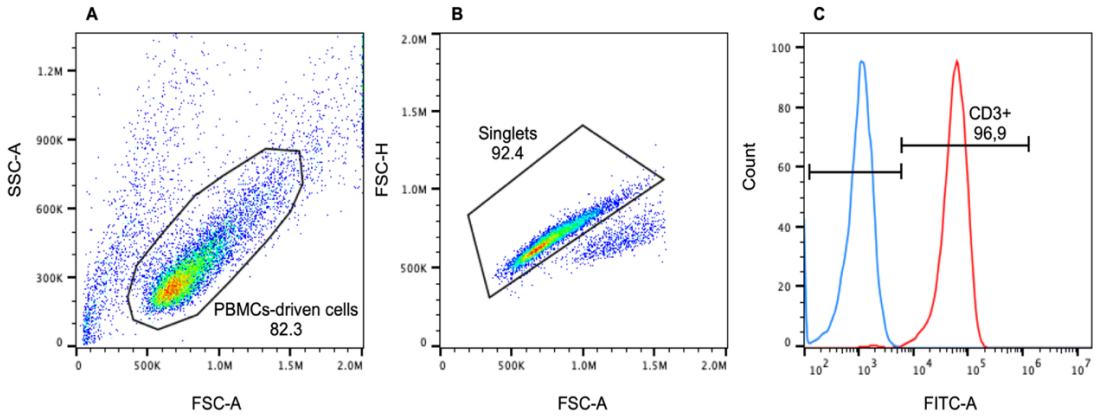

Figure S4. Enrichment of CD3⁺ T cells after OKT3/IL-2 activation of PBMCs

Flow cytometry analysis showing predominant CD3⁺ T-cell population following OKT3/IL-2 activation of PBMCs prior to magnetic enrichment. Representative gating strategy performed in FlowJo v10.10 is shown. (A) Debris was excluded using forward and side scatter (FSC vs. SSC). (B) Doublets were removed based on FSC-A vs. FSC-H. (C) CD3⁺ T cells (red histogram) were identified using anti-CD3 staining and compared against the corresponding isotype control (blue histogram).

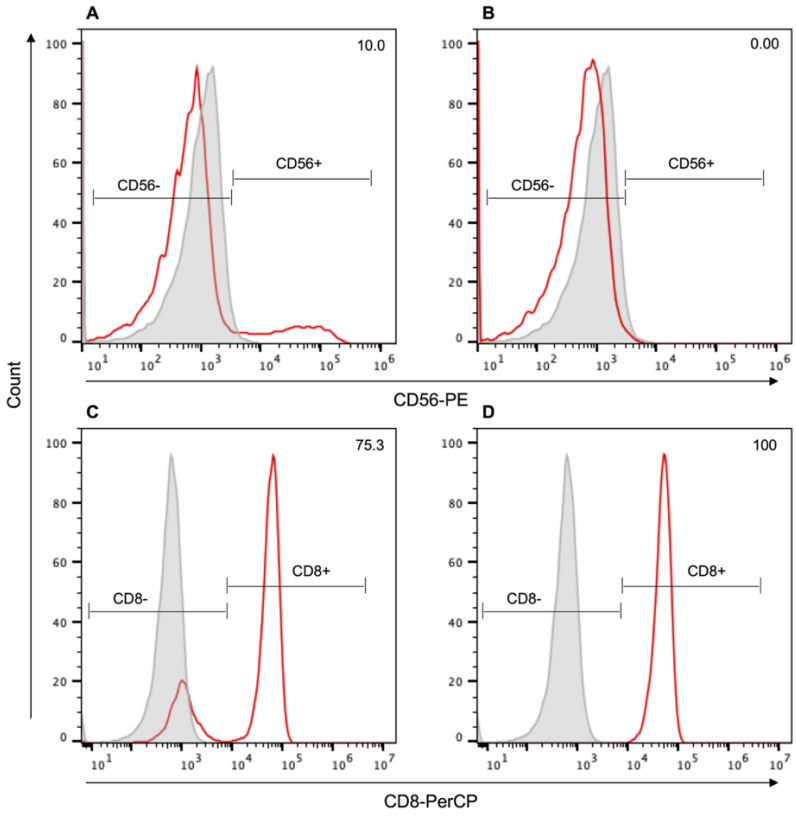

Figure S5. Validation of CD56 depletion and CD8⁺ T-cell enrichment during generation of endogenous TCR CD8⁺ T cells.

(A–B) Following OKT3/IL-2 activation of PBMCs, CD56⁺ cells were depleted to remove NK cells and CD56⁺ T-cell subsets**.** Panel A shows the population before CD56 MACS depletion, and Panel B shows the population after depletion**.** In panel B, overlaid histograms demonstrate complete loss of CD56⁺ cells (red) compared with the isotype control (filled gray), confirming highly efficient depletion. (C–D) CD56-depleted T cells were subsequently subjected to CD8⁺ MACS enrichment to obtain a purified CD8⁺ T-cell fraction—an essential step for the downstream isolation of untransduced CD8⁺ NGFR⁻ T cells. Panel C shows the population before CD8 MACS enrichment, and Panel D shows the population after enrichment. Overlaid histograms depict the CD8⁺ population (red) relative to the isotype control (filled gray), demonstrating the successful generation of a highly pure CD8⁺ T-cell subset. Percentages of marker-positive cells are indicated; histograms normalized to mode.

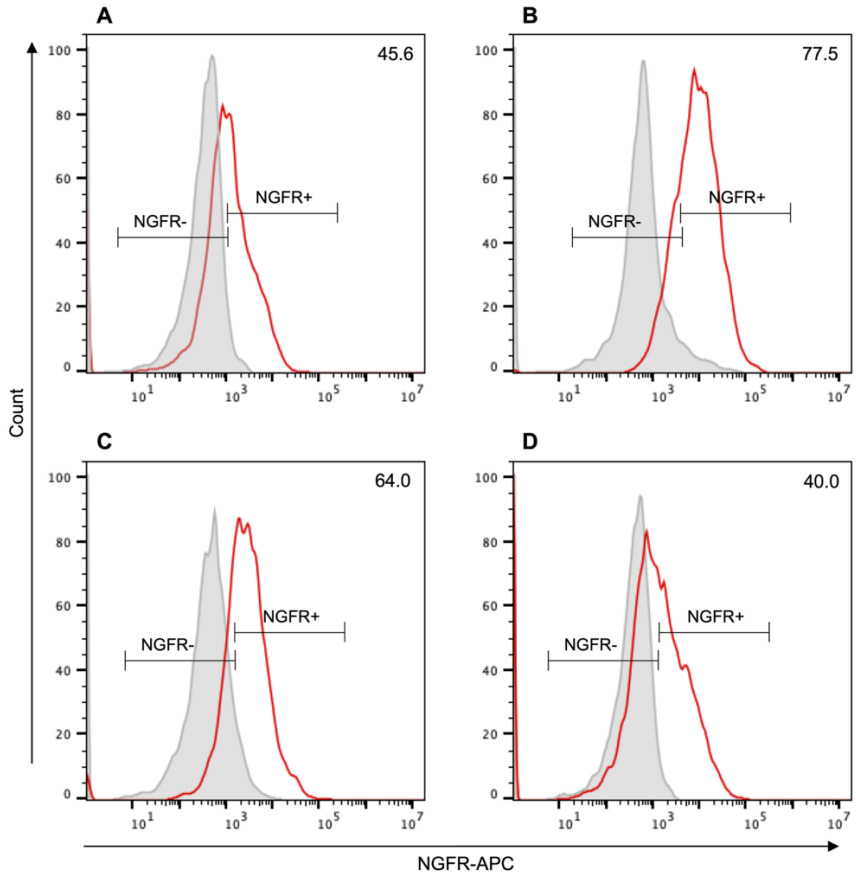

Figure S6. Functional validation of viral infectivity from monoclonal PG13 producer lines.

(A–D) Following generation of monoclonal PG13 producer lines, supernatants containing retroviral particles were tested for transduction efficiency across multiple B-cell lymphoma lines to confirm functional infectivity. Transduction was assessed in (A) BL41, (B) Jijoye, (C) Karpas 1106, and (D) U2940 cells, using NGFR expression as a marker of successful viral integration. Overlaid histograms show the NGFR⁺ population (red) compared with the isotype control (filled gray), demonstrating robust transduction of each target cell line and confirming the functional infectivity of virus produced by PG13 cells. Percentages of marker-positive cells are indicated; histograms normalized to mode.

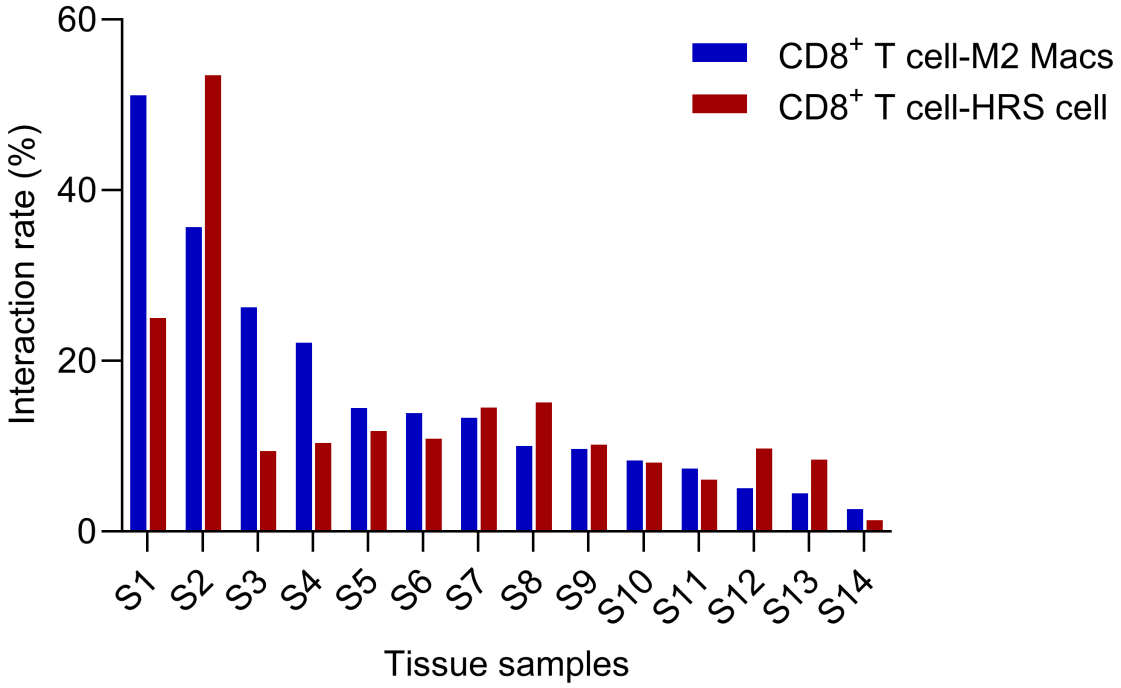

Figure S7. Case-wise analysis of PD-1/PD-L1 PLA puncta at CD8–CD163 and CD8–CD30 interfaces.

Bar plots display individual cases ordered by decreasing relative interaction rate at CD8–CD163 interfaces. For each case, the corresponding interaction rate at CD8–CD30 interfaces is shown for comparison. In cases where CD8–HRS interactions were minimal, CD8–CD163 contacts showed higher interaction rates, indicating that tumor-associated macrophages can act as alternative partners for PD-1/PD-L1 engagement when direct interaction with HRS cells is limited. Interaction rate was calculated as described in Section 2.6.7.

Reference

1. Hodgkin. On some Morbid Appearances of the Absorbent Glands and Spleen. Med Chir Trans. 1832;17:68–114.

2. Jaffe NLHES, Harald Stein JWV. Pathology and Genetics of Tumours of Haematopoietic and Lymphoid Tissues - World Health Organization. IARC Press; 2001.

3. Huang J, Pang WS, Lok V, Zhang L, Lucero-Prisno DE, Xu W, et al. Incidence, mortality, risk factors, and trends for Hodgkin lymphoma: a global data analysis. J Hematol Oncol [Internet]. 2022 Dec [cited 2025 July 26];15(1). Available from: https://jhoonline.biomedcentral.com/articles/10.1186/s13045-022-01281-9

4. Punnett A, Tsang RW, Hodgson DC. Hodgkin Lymphoma Across the Age Spectrum: Epidemiology, Therapy, and Late Effects. Seminars in Radiation Oncology. 2010 Jan;20(1):30–44.

5. Diehl V, editor. Hodgkin's disease. London: Baillière Tindall; 1996. 401 p. (Baillières' clinical haematology).

6. Borchmann P, Eichenauer DA, Engert A. State of the art in the treatment of Hodgkin lymphoma. Nat Rev Clin Oncol. 2012 Aug;9(8):450–9.

7. Lakhtakia R, Burney I. A Historical Tale of Two Lymphomas. Hodgkin lymphoma.

8. PUSEY WA. CASES OF SARCOMA AND OF HODGKIN'S DISEASE TREATED BY EXPOSURES TO X-RAYS—A PRELIMINARY REPORT. Journal of the American Medical Association. 1902 Jan 18;XXXVIII(3):166–9.

9. DeVita Jr VT. A selective history of the therapy of Hodgkin's disease. British Journal of Haematology. 2003;122(5):718–27.

10. Devita VT, Serpick AA, Carbone PP. Combination Chemotherapy in the Treatment of Advanced Hodgkin's Disease. Ann Intern Med. 1970 Dec 1;73(6):881–95.

11. Devita VT, Simon RM, Hubbard SM, Young RC, Berard CW, Moxley JH, et al. Curability of Advanced Hodgkin's Disease with Chemotherapy: Long-Term Follow-up of MOPP-Treated Patients at the National Cancer Institute. Ann Intern Med. 1980 May 1;92(5):587–95.

12. Bonadonna G, Zucali R, Monfardini S, De Lena M, Uslenghi C. Combination chemotherapy of Hodgkin's disease with adriamycin, bleomycin, vinblastine, and imidazole carboxamide versus MOPP. Cancer. 1975 July;36(1):252–9.

13. Santoro A, Bonadonna G, Valagussa P, Zucali R, Viviani S, Villani F, et al. Long-term results of combined chemotherapy-radiotherapy approach in Hodgkin's disease: superiority of ABVD plus radiotherapy versus MOPP plus radiotherapy. JCO. 1987 Jan;5(1):27–37.

14. Rathore B, Kadin ME. Hodgkin's lymphoma therapy: past, present, and future. Expert Opinion on Pharmacotherapy. 2010 Dec;11(17):2891–906.

15. Diehl V, Sieber M, Rüffer U, Lathan B, Hasenclever D, Pfreundschuh M, et al. BEACOPP: An intensified chemotherapy regimen in advanced Hodgkin's disease. Annals of Oncology. 1997 Feb;8(2):143–8.

16. Hutchings M, Loft A, Hansen M, Pedersen LM, Buhl T, Jurlander J, et al. FDG-PET after two cycles of chemotherapy predicts treatment failure and progression-free survival in Hodgkin lymphoma. Blood. 2006 Jan 1;107(1):52–9.

17. van Leeuwen FE, Ng AK. Long-term risk of second malignancy and cardiovascular disease after Hodgkin lymphoma treatment. Hematology Am Soc Hematol Educ Program. 2016 Dec 2;2016(1):323–30.

18. Younes A, Ansell SM. Novel agents in the treatment of Hodgkin lymphoma: Biological basis and clinical results. Seminars in Hematology. 2016 July;53(3):186–9.

19. Cai Q, Xia Y, Liu P, Zhang Y, Zou Q, Cai J. Real-World Study Evaluating the Efficacy of Frontline Brentuximab Vedotin Plus Chemotherapy in Newly Diagnosed Patients with Hodgkin Lymphoma: A Retrospective Analysis. Blood. 2022 Nov 15;140(Supplement 1):12035–6.

20. Chen R, Zinzani PL, Fanale MA, Armand P, Johnson NA, Brice P, et al. Phase II Study of the Efficacy and Safety of Pembrolizumab for Relapsed/Refractory Classic Hodgkin Lymphoma. Journal of Clinical Oncology [Internet]. 2017 July 1 [cited 2025 July 28]; Available from: https://ascopubs.org/doi/10.1200/JCO.2016.72.1316

21. Ansell SM, Lesokhin AM, Borrello I, Halwani A, Scott EC, Gutierrez M, et al. PD-1 Blockade with Nivolumab in Relapsed or Refractory Hodgkin's Lymphoma. N Engl J Med. 2015 Jan 22;372(4):311–9.

22. Younes A, Santoro A, Shipp M, Zinzani PL, Timmerman JM, Ansell S, et al. Nivolumab for classical Hodgkin's lymphoma after failure of both autologous stem-cell transplantation and brentuximab vedotin: a multicentre, multicohort, single-arm phase 2 trial. The Lancet Oncology. 2016 Sept;17(9):1283–94.

23. Armand P, Shipp MA, Ribrag V, Michot JM, Zinzani PL, Kuruvilla J, et al. Programmed Death-1 Blockade With Pembrolizumab in Patients With Classical Hodgkin Lymphoma After Brentuximab Vedotin Failure. Journal of Clinical Oncology [Internet]. 2016 Nov 1 [cited 2025 July 28]; Available from: https://ascopubs.org/doi/10.1200/JCO.2016.67.3467

24. Alaggio R, Amador C, Anagnostopoulos I, Attygalle AD, Araujo IB de O, Berti E, et al. The 5th edition of the World Health Organization Classification of Haematolymphoid Tumours: Lymphoid Neoplasms. Leukemia. 2022 July;36(7):1720–48.

25. Wang HW, Balakrishna JP, Pittaluga S, Jaffe ES. Diagnosis of Hodgkin Lymphoma in the Modern Era. Br J Haematol. 2019 Jan;184(1):45–59.

26. Shanbhag S, Ambinder R. Hodgkin Lymphoma: a review and update on recent progress. CA Cancer J Clin. 2018 Mar;68(2):116–32.

27. Mani H, Jaffe ES. HODGKIN LYMPHOMA: AN UPDATE ON ITS BIOLOGY WITH NEWER INSIGHTS INTO CLASSIFICATION. Clin Lymphoma Myeloma. 2009 June;9(3):206–16.

28. Schmitz R, Stanelle J, Hansmann ML, Küppers R. Pathogenesis of Classical and Lymphocyte-Predominant Hodgkin Lymphoma. Annu Rev Pathol Mech Dis. 2009 Feb 1;4(1):151–74.

29. Kosydar S, Ansell SM. The biology of classical Hodgkin lymphoma. Seminars in Hematology. 2024 Aug;61(4):212–20.

30. Weniger MA, Küppers R. Molecular biology of Hodgkin lymphoma. Leukemia. 2021 Apr;35(4):968–81.

31. Oudejans JJ, Kummer JA, Jiwa M, van der Valk P, Ossenkoppele GJ, Kluin PM, et al. Granzyme B expression in Reed-Sternberg cells of Hodgkin's disease. Am J Pathol. 1996 Jan;148(1):233–40.

32. Venkataraman G, Song JY, Tzankov A, Dirnhofer S, Heinze G, Kohl M, et al. Aberrant T-cell antigen expression in classical Hodgkin lymphoma is associated with decreased event-free survival and overall survival. Blood. 2013 Mar 7;121(10):1795–804.

33. Müschen M, Rajewsky K, Bräuninger A, Baur AS, Oudejans JJ, Roers A, et al. Rare Occurrence of Classical Hodgkin's Disease as a T Cell Lymphoma. The Journal of Experimental Medicine. 2000 Jan 17;191(2):387–94.

34. Seitz V, Hummel M, Marafioti T, Anagnostopoulos I, Assaf C, Stein H. Detection of clonal T-cell receptor gamma-chain gene rearrangements in Reed-Sternberg cells of classic Hodgkin disease.

35. Tzankov A, Bourgau C, Kaiser A, Zimpfer A, Maurer R, Pileri SA, et al. Rare expression of T-cell markers in classical Hodgkin's lymphoma. Modern Pathology. 2005 Dec;18(12):1542–9.

36. Rengstl B, Newrzela S, Heinrich T, Weiser C, Thalheimer FB, Schmid F, et al. Incomplete cytokinesis and re-fusion of small mononucleated Hodgkin cells lead to giant multinucleated Reed–Sternberg cells. Proc Natl Acad Sci U S A. 2013 Dec 17;110(51):20729–34.

37. Connors JM, Cozen W, Steidl C, Carbone A, Hoppe RT, Flechtner HH, et al. Hodgkin lymphoma. Nat Rev Dis Primers. 2020 July 23;6(1):61.

38. Hu Y. JAK/STAT Pathway in Classical Hodgkin Lymphoma: From Pathogenic Mechanisms to Therapies. 2025;153.

39. Xue C, Yao Q, Gu X, Shi Q, Yuan X, Chu Q, et al. Evolving cognition of the JAK-STAT signaling pathway: autoimmune disorders and cancer. Sig Transduct Target Ther. 2023 May 19;8(1):204.

40. Gunawardana J, Chan FC, Telenius A, Woolcock B, Kridel R, Tan KL, et al. Recurrent somatic mutations of PTPN1 in primary mediastinal B cell lymphoma and Hodgkin lymphoma. Nat Genet. 2014 Apr;46(4):329–35.

41. Lamprecht B, Kreher S, Anagnostopoulos I, Jöhrens K, Monteleone G, Jundt F, et al. Aberrant expression of the Th2 cytokine IL-21 in Hodgkin lymphoma cells regulates STAT3 signaling and attracts Treg cells via regulation of MIP-3α. Blood. 2008 Oct 15;112(8):3339–47.

42. Barth TFE, Martin-Subero JI, Joos S, Menz CK, Hasel C, Mechtersheimer G, et al. Gains of 2p involving the REL locus correlate with nuclear c-Rel protein accumulation in neoplastic cells of classical Hodgkin lymphoma. Blood. 2003 May 1;101(9):3681–6.

43. Steidl C, Connors JM, Gascoyne RD. Molecular Pathogenesis of Hodgkin's Lymphoma: Increasing Evidence of the Importance of the Microenvironment. JCO. 2011 May 10;29(14):1812–26.

44. Swerdlow SH, Campo E, Pileri SA, Harris NL, Stein H, Siebert R, et al. The 2016 revision of the World Health Organization classification of lymphoid neoplasms. Blood. 2016 May 19;127(20):2375–90.

45. Masel R, Roche ME, Martinez-Outschoorn U. Hodgkin Lymphoma: A disease shaped by the tumor micro- and macroenvironment. Best Practice & Research Clinical Haematology. 2023 Dec;36(4):101514.

46. Bertuzzi C, Sabattini E, Agostinelli C. Immune Microenvironment Features and Dynamics in Hodgkin Lymphoma. Cancers. 2021 July 20;13(14):3634.

47. Carbone A, Gloghini A, Carlo Stella C. Tumor microenvironment contribution to checkpoint blockade therapy. Lessons learned from Hodgkin lymphoma. Blood. 2023 Mar 10;blood.2022016590.

48. Aldinucci D, Celegato M, Casagrande N. Microenvironmental interactions in classical Hodgkin lymphoma and their role in promoting tumor growth, immune escape and drug resistance. Cancer Letters. 2016 Sept;380(1):243–52.

49. Aldinucci D, Borghese C, Casagrande N. Formation of the Immunosuppressive Microenvironment of Classic Hodgkin Lymphoma and Therapeutic Approaches to Counter It. IJMS. 2019 May 15;20(10):2416.

50. Aldinucci D, Pinto A, Gloghini A, Carbone A. Chemokine receptors as therapeutic tools in Hodgkin lymphoma: CCR4 and beyond. Blood. 2010 Jan 21;115(3):746–7.

51. Marshall NA, Christie LE, Munro LR, Culligan DJ, Johnston PW, Barker RN, et al. Immunosuppressive regulatory T cells are abundant in the reactive lymphocytes of Hodgkin lymphoma. Blood. 2004 Mar 1;103(5):1755–62.

52. Weniger MA, Küppers R. Molecular biology of Hodgkin lymphoma. Leukemia. 2021 Apr;35(4):968–81.

53. Hartmann S, Jakobus C, Rengstl B, Döring C, Newrzela S, Brodt HR, et al. Spindle-shaped CD163+ rosetting macrophages replace CD4+ T-cells in HIV-related classical Hodgkin lymphoma. Modern Pathology. 2013 May;26(5):648–57.

54. Pantanowitz L, Carbone A, Dolcetti R. Microenvironment and HIV-related lymphomagenesis. Seminars in Cancer Biology. 2015 Oct;34:52–7.

55. Skinnider BF, Mak TW. The role of cytokines in classical Hodgkin lymphoma. Blood. 2002 June 15;99(12):4283–97.

56. Carbone A, Gloghini A, Caruso A, De Paoli P, Dolcetti R. The impact of EBV and HIV infection on the microenvironmental niche underlying Hodgkin lymphoma pathogenesis: The impact of EBV and HIV on CHL pathogenesis. Int J Cancer. 2017 Mar 15;140(6):1233–45.

57. Kapatai G, Murray P. Contribution of the Epstein–Barr virus to the molecular pathogenesis of Hodgkin lymphoma. J Clin Pathol. 2007 Dec;60(12):1342–9.

58. Green MR, Rodig S, Juszczynski P, Ouyang J, Sinha P, O'Donnell E, et al. Constitutive AP-1 Activity and EBV Infection Induce PD-L1 in Hodgkin Lymphomas and Posttransplant Lymphoproliferative Disorders: Implications for Targeted Therapy. Clinical Cancer Research. 2012 Mar 15;18(6):1611–8.

59. Kanakry JA, Li H, Gellert LL, Lemas MV, Hsieh W son, Hong F, et al. Plasma Epstein-Barr virus DNA predicts outcome in advanced Hodgkin lymphoma: correlative analysis from a large North American cooperative group trial. Blood. 2013 May 2;121(18):3547–53.

60. Mantovani A, Marchesi F, Malesci A, Laghi L, Allavena P. Tumour-associated macrophages as treatment targets in oncology. Nat Rev Clin Oncol. 2017 July;14(7):399–416.

61. Steidl C, Lee T, Shah SP, Farinha P, Han G, Nayar T, et al. Tumor-Associated Macrophages and Survival in Classic Hodgkin's Lymphoma. N Engl J Med. 2010 Mar 11;362(10):875–85.

62. Boutilier AJ, Elsawa SF. Macrophage Polarization States in the Tumor Microenvironment. IJMS. 2021 June 29;22(13):6995.

63. Sica A, Mantovani A. Macrophage plasticity and polarization: in vivo veritas. J Clin Invest. 2012 Mar 1;122(3):787–95.

64. Orecchioni M, Ghosheh Y, Pramod AB, Ley K. Macrophage Polarization: Different Gene Signatures in M1(LPS+) vs. Classically and M2(LPS–) vs. Alternatively Activated Macrophages. Front Immunol. 2019 May 24;10:1084.

65. Noy R, Pollard JW. Tumor-Associated Macrophages: From Mechanisms to Therapy. Immunity. 2014 July;41(1):49–61.

66. Komohara Y, Jinushi M, Takeya M. Clinical significance of macrophage heterogeneity in human malignant tumors. Cancer Science. 2014 Jan;105(1):1–8.

67. Tan KL, Scott DW, Hong F, Kahl BS, Fisher RI, Bartlett NL, et al. Tumor-associated macrophages predict inferior outcomes in classic Hodgkin lymphoma: a correlative study from the E2496 Intergroup trial. Blood. 2012 Oct 18;120(16):3280–7.

68. Harris JA, Jain S, Ren Q, Zarineh A, Liu C, Ibrahim S. CD163 versus CD68 in tumor associated macrophages of classical hodgkin lymphoma. Diagn Pathol. 2012 Dec;7(1):12.

69. Guo B, Cen H, Tan X, Ke Q. Meta-analysis of the prognostic and clinical value of tumor-associated macrophages in adult classical Hodgkin lymphoma. BMC Med. 2016 Dec;14(1):159.

70. Chen DS, Mellman I. Oncology Meets Immunology: The Cancer-Immunity Cycle. Immunity. 2013 July;39(1):1–10.

71. Goodnow CC, Sprent J, De St Groth BF, Vinuesa CG. Cellular and genetic mechanisms of self tolerance and autoimmunity. Nature. 2005 June 2;435(7042):590–7.

72. Heath WR, Carbone FR. Cross-presentation in viral immunity and self-tolerance. Nat Rev Immunol. 2001 Nov 1;1(2):126–34.

73. Szeto C, Lobos CA, Nguyen AT, Gras S. TCR Recognition of Peptide–MHC-I: Rule Makers and Breakers. IJMS. 2020 Dec 23;22(1):68.

74. Garcia-Lora A, Algarra I, Garrido F. MHC class I antigens, immune surveillance, and tumor immune escape. Journal Cellular Physiology. 2003 June;195(3):346–55.

75. Patel SS, Weirather JL, Lipschitz M, Lako A, Chen PH, Griffin GK, et al. The microenvironmental niche in classic Hodgkin lymphoma is enriched for CTLA-4-positive T-cells that are PD-1-negative. Blood. 2019 Oct 10;blood.2019002206.

76. Steidl C, Shah SP, Woolcock BW, Rui L, Kawahara M, Farinha P, et al. MHC class II transactivator CIITA is a recurrent gene fusion partner in lymphoid cancers. Nature. 2011 Mar;471(7338):377–81.

77. Oudejans J, Jiwa N, Kummer J, Horstman A, Vos W, Baak J, et al. Analysis of major histocompatibility complex class I expression on Reed- Sternberg cells in relation to the cytotoxic T-cell response in Epstein- Barr virus-positive and -negative Hodgkin's disease. Blood. 1996 May 1;87(9):3844–51.

78. Reichel J, Chadburn A, Rubinstein PG, Giulino-Roth L, Tam W, Liu Y, et al. Flow sorting and exome sequencing reveal the oncogenome of primary Hodgkin and Reed-Sternberg cells. Blood. 2015 Feb 12;125(7):1061–72.

79. Roemer MGM, Advani RH, Redd RA, Pinkus GS, Natkunam Y, Ligon AH, et al. Classical Hodgkin Lymphoma with Reduced β2M/MHC Class I Expression Is Associated with Inferior Outcome Independent of 9p24.1 Status. Cancer Immunology Research. 2016 Nov 1;4(11):910–6.

80. Roemer MGM, Redd RA, Cader FZ, Pak CJ, Abdelrahman S, Ouyang J, et al. Major Histocompatibility Complex Class II and Programmed Death Ligand 1 Expression Predict Outcome After Programmed Death 1 Blockade in Classic Hodgkin Lymphoma. JCO. 2018 Apr 1;36(10):942–50.

81. Sobesky S, Mammadova L, Cirillo M, Drees EEE, Mattlener J, Dörr H, et al. In-depth cell-free DNA sequencing reveals genomic landscape of Hodgkin's lymphoma and facilitates ultrasensitive residual disease detection. Med. 2021 Oct;2(10):1171-1193.e11.

82. Pourmaleki M, Jones CJ, Mellinghoff SD, Greenstein BD, Kumar P, Foronda M, et al. Multiplexed Spatial Profiling of Hodgkin Reed–Sternberg Cell Neighborhoods in Classic Hodgkin Lymphoma. Clinical Cancer Research. 2024 Sept 3;30(17):3881–93.

83. Liang WS, Vergilio JA, Salhia B, Huang HJ, Oki Y, Garrido-Laguna I, et al. Comprehensive Genomic Profiling of Hodgkin Lymphoma Reveals Recurrently Mutated Genes and Increased Mutation Burden. The Oncologist. 2019 Feb 1;24(2):219–28.

84. Spina V, Bruscaggin A, Cuccaro A, Martini M, Di Trani M, Forestieri G, et al. Circulating tumor DNA reveals genetics, clonal evolution, and residual disease in classical Hodgkin lymphoma. Blood. 2018 May 31;131(22):2413–25.

85. Tiacci E, Ladewig E, Schiavoni G, Penson A, Fortini E, Pettirossi V, et al. Pervasive mutations of JAK-STAT pathway genes in classical Hodgkin lymphoma. Blood. 2018 May 31;131(22):2454–65.

86. Alig SK, Shahrokh Esfahani M, Garofalo A, Li MY, Rossi C, Flerlage T, et al. Distinct Hodgkin lymphoma subtypes defined by noninvasive genomic profiling. Nature. 2024 Jan 25;625(7996):778–87.

87. Maura F, Ziccheddu B, Xiang JZ, Bhinder B, Rosiene J, Abascal F, et al. Molecular Evolution of Classic Hodgkin Lymphoma Revealed Through Whole-Genome Sequencing of Hodgkin and Reed Sternberg Cells. Blood Cancer Discovery. 2023 May 1;4(3):208–27.

88. Desch AK, Hartung K, Botzen A, Brobeil A, Rummel M, Kurch L, et al. Genotyping circulating tumor DNA of pediatric Hodgkin lymphoma. Leukemia. 2020 Jan;34(1):151–66.

89. Nijland M, Veenstra RN, Visser L, Xu C, Kushekhar K, Van Imhoff GW, et al. HLA dependent immune escape mechanisms in B-cell lymphomas: Implications for immune checkpoint inhibitor therapy? OncoImmunology. 2017 Apr 3;6(4):e1295202.

90. Shah K, Al-Haidari A, Sun J, Kazi JU. T cell receptor (TCR) signaling in health and disease. Sig Transduct Target Ther. 2021 Dec 13;6(1):412.

91. Beier KC, Kallinich T, Hamelmann E. Master switches of T-cell activation and differentiation. Eur Respir J. 2007 Apr;29(4):804–12.

92. Smith R, Shen R. Complexities in comparing the impact of costimulatory domains on approved CD19 CAR functionality. J Transl Med. 2023 July 30;21(1):515.

93. Singh R, Kim YH, Lee SJ, Eom HS, Choi BK. 4-1BB immunotherapy: advances and hurdles. Exp Mol Med. 2024 Jan 4;56(1):32–9.

94. Rausch L, Kallies A. Molecular Mechanisms Governing CD8 T Cell Differentiation and Checkpoint Inhibitor Response in Cancer.

95. Croft M. Co-stimulatory members of the TNFR family: keys to effective T-cell immunity? Nat Rev Immunol. 2003 Aug;3(8):609–20.

96. Watts TH, Yeung KKM, Yu T, Lee S, Eshraghisamani R. TNF/TNFR Superfamily Members in Costimulation of T Cell Responses—Revisited. Annual Review of Immunology. 2025 Apr 25;43(1):113–42.

97. Otano I, Azpilikueta A, Glez-Vaz J, Alvarez M, Medina-Echeverz J, Cortés-Domínguez I, et al. CD137 (4-1BB) costimulation of CD8+ T cells is more potent when provided in cis than in trans with respect to CD3-TCR stimulation. Nat Commun. 2021 Dec 15;12(1):7296.

98. Etxeberria I, Glez-Vaz J, Teijeira Á, Melero I. New emerging targets in cancer immunotherapy: CD137/4-1BB costimulatory axis. ESMO Open. 2019;4:e000733.

99. Salmaninejad A, Valilou SF, Shabgah AG, Aslani S, Alimardani M, Pasdar A, et al. PD-1/PD-L1 pathway: Basic biology and role in cancer immunotherapy. Journal Cellular Physiology. 2019 Oct;234(10):16824–37.

100. He J, Hu Y, Hu M, Li B. Development of PD-1/PD-L1 Pathway in Tumor Immune Microenvironment and Treatment for Non-Small Cell Lung Cancer. Sci Rep. 2015 Aug 17;5(1):13110.

101. Han Y, Liu D, Li L. PD-1/PD-L1 pathway: current researches in cancer.

102. Keir ME, Butte MJ, Freeman GJ, Sharpe AH. PD-1 and Its Ligands in Tolerance and Immunity. Annu Rev Immunol. 2008 Apr 1;26(1):677–704.

103. Lin X, Kang K, Chen P, Zeng Z, Li G, Xiong W, et al. Regulatory mechanisms of PD-1/PD-L1 in cancers. Mol Cancer. 2024 May 18;23(1):108.

104. De Charette M, Houot R. Hide or defend, the two strategies of lymphoma immune evasion: potential implications for immunotherapy. Haematologica. 2018 Aug;103(8):1256–68.

105. Chen BJ, Chapuy B, Ouyang J, Sun HH, Roemer MGM, Xu ML, et al. PD-L1 Expression Is Characteristic of a Subset of Aggressive B-cell Lymphomas and Virus-Associated Malignancies. Clinical Cancer Research. 2013 July 1;19(13):3462–73.

106. Calabretta E, d'Amore F, Carlo-Stella C. Immune and Inflammatory Cells of the Tumor Microenvironment Represent Novel Therapeutic Targets in Classical Hodgkin Lymphoma. IJMS. 2019 Nov 5;20(21):5503.

107. Vari F, Arpon D, Keane C, Hertzberg MS, Talaulikar D, Jain S, et al. Immune evasion via PD-1/PD-L1 on NK cells and monocyte/macrophages is more prominent in Hodgkin lymphoma than DLBCL. Blood. 2018 Apr 19;131(16):1809–19.

108. Nagasaki J, Togashi Y, Sugawara T, Itami M, Yamauchi N, Yuda J, et al. The critical role of CD4+ T cells in PD-1 blockade against MHC-II–expressing tumors such as classic Hodgkin lymphoma. Blood Advances. 2020 Sept 8;4(17):4069–82.

109. Zhulai G, Oleinik E. Targeting regulatory T cells in anti-PD-1/PD-L1 cancer immunotherapy. Scand J Immunol. 2022 Mar;95(3):e13129.

110. Green MR, Monti S, Rodig SJ, Juszczynski P, Currie T, O'Donnell E, et al. Integrative analysis reveals selective 9p24.1 amplification, increased PD-1 ligand expression, and further induction via JAK2 in nodular sclerosing Hodgkin lymphoma and primary mediastinal large B-cell lymphoma. Blood. 2010 Oct 28;116(17):3268–77.

111. Roemer MGM, Advani RH, Ligon AH, Natkunam Y, Redd RA, Homer H, et al. *PD-L1* and *PD-L2* Genetic Alterations Define Classical Hodgkin Lymphoma and Predict Outcome. JCO. 2016 Aug 10;34(23):2690–7.

112. Chen BJ, Chapuy B, Ouyang J, Sun HH, Roemer MGM, Xu ML, et al. PD-L1 Expression Is Characteristic of a Subset of Aggressive B-cell Lymphomas and Virus-Associated Malignancies. Clinical Cancer Research. 2013 July 1;19(13):3462–73.

113. Carey CD, Gusenleitner D, Lipschitz M, Roemer MGM, Stack EC, Gjini E, et al. Topological analysis reveals a PD-L1-associated microenvironmental niche for Reed-Sternberg cells in Hodgkin lymphoma. Blood. 2017 Nov 30;130(22):2420–30.

114. Kawashima M, Carreras J, Higuchi H, Kotaki R, Hoshina T, Okuyama K, et al. PD-L1/L2 protein levels rapidly increase on monocytes via trogocytosis from tumor cells in classical Hodgkin lymphoma. Leukemia. 2020 Sept;34(9):2405–17.

115. El Halabi L, Adam J, Gravelle P, Marty V, Danu A, Lazarovici J, et al. Expression of the Immune Checkpoint Regulators LAG-3 and TIM-3 in Classical Hodgkin Lymphoma. Clinical Lymphoma Myeloma and Leukemia. 2021 Apr;21(4):257-266.e3.

116. Takata K, Aoki T, Chong LC, Milne K, Miyata-Takata T, Singh K, et al. Identification of LAG3+ T Cell Populations in the Tumor Microenvironment of Classical Hodgkin Lymphoma and B-Cell Non-Hodgkin Lymphoma. Blood. 2020 Nov 5;136(Supplement 1):19–19.

117. Annibali O, Bianchi A, Grifoni A, Tomarchio V, Tafuri M, Verri M, et al. A novel scoring system for TIGIT expression in classic Hodgkin lymphoma. Sci Rep. 2021 Mar 29;11(1):7059.

118. Robbins PF, Kassim SH, Tran TLN, Crystal JS, Morgan RA, Feldman SA, et al. A Pilot Trial Using Lymphocytes Genetically Engineered with an NY-ESO-1–Reactive T-cell Receptor: Long-term Follow-up and Correlates with Response. Clinical Cancer Research. 2015 Mar 1;21(5):1019–27.

119. Swift S, Lorens J, Achacoso P, Nolan GP. Rapid Production of Retroviruses for Efficient Gene Delivery to Mammalian Cells Using 293 T Cell–Based Systems. CP in Immunology [Internet]. 1999 June [cited 2025 Nov 2];31(1). Available from: https://currentprotocols.onlinelibrary.wiley.com/doi/10.1002/0471142735.im1017cs31

120. Loew R, Meyer Y, Kuehlcke K, Gama-Norton L, Wirth D, Hauser H, et al. A new PG13-based packaging cell line for stable production of clinical-grade self-inactivating γ-retroviral vectors using targeted integration. Gene Ther. 2010 Feb;17(2):272–80.

121. Miller AD, Garcia JV, Von Suhr N, Lynch CM, Wilson C, Eiden MV. Construction and properties of retrovirus packaging cells based on gibbon ape leukemia virus. J Virol. 1991 May;65(5):2220–4.

122. Feldman SA, Xu H, Black MA, Park TS, Robbins PF, Kochenderfer JN, et al. Use of the *piggyBac* Transposon to Create Stable Packaging Cell Lines for the Production of Clinical-Grade Self-Inactivating γ-Retroviral Vectors. Human Gene Therapy Methods. 2014 Aug;25(4):253–60.

123. Mirus Bio. TransIT-293 Transfection Reagent Protocol [Internet]. Mirus Bio LLC; [cited 2025 Feb 18]. Available from: https://www.mirusbio.com/product/transit-293-transfection-reagent-0-4-ml/

124. Zhang L, Feldman SA, Zheng Z, Chinnasamy N, Xu H, Nahvi AV, et al. Evaluation of γ-Retroviral Vectors That Mediate the Inducible Expression of IL-12 for Clinical Application. Journal of Immunotherapy. 2012 June;35(5):430–9.

125. Feldman SA, Goff SL, Xu H, Black MA, Kochenderfer JN, Johnson LA, et al. Rapid Production of Clinical-Grade Gammaretroviral Vectors in Expanded Surface Roller Bottles Using a “Modified” Step-Filtration Process for Clearance of Packaging Cells. Human Gene Therapy. 2011 Jan;22(1):107–15.

126. Steven A. Rosenberg JNK. Construction and Pre-clinical Evaluation of an Anti-CD19 Chimeric Antigen Receptor. In: Definitions [Internet]. Qeios; 2020 [cited 2025 Feb 18]. Available from: https://www.qeios.com/read/definition/17918

127. Takara Bio Inc. RetroNectin Recombinant Human Fibronectin Fragment Protocol [Internet]. Takara Bio Inc; [cited 2025 Feb 18]. Available from: https://www.takarabio.com/products/cell-therapy/gmp-grade-reagents/retronectin-recombinant-human-fibronectin-fragment

128. Patel SJ, Sanjana NE, Kishton RJ, Eidizadeh A, Vodnala SK, Cam M, et al. Identification of essential genes for cancer immunotherapy. Nature. 2017 Aug;548(7669):537–42.

129. Dersh D, Phelan JD, Gumina ME, Wang B, Arbuckle JH, Holly J, et al. Genome-wide Screens Identify Lineage- and Tumor-Specific Genes Modulating MHC-I- and MHC-II-Restricted Immunosurveillance of Human Lymphomas. Immunity. 2021 Jan;54(1):116-131.e10.

130. Miltenyi Biotec. CD56 MicroBeads, human [Internet]. Miltenyi Biotec; Available from: https://static.miltenyibiotec.com/asset/150655405641/document_8b37lamp493d94ojk6nl6fk219?content-disposition=inline

131. Miltenyi Biotec. REAlease* CD8 MicroBead Kit, human [Internet]. Miltenyi Biotec; Available from: https://static.miltenyibiotec.com/asset/150655405641/document_7ccub473dt157bs7dd74moq13j?content-disposition=inline

132. Miltenyi Biotec. MACSelect LNGFR MicroBeads [Internet]. Miltenyi Biotec; Available from: https://static.miltenyibiotec.com/asset/150655405641/document_i6cnaeg72t6mjcklvi3b5qul21?content-disposition=inline

133. Jin J, Sabatino M, Somerville R, Wilson JR, Dudley ME, Stroncek DF, et al. Simplified Method of the Growth of Human Tumor Infiltrating Lymphocytes in Gas-permeable Flasks to Numbers Needed for Patient Treatment. Journal of Immunotherapy. 2012 Apr;35(3):283–92.

134. Somerville RP, Devillier L, Parkhurst MR, Rosenberg SA, Dudley ME. Clinical scale rapid expansion of lymphocytes for adoptive cell transfer therapy in the WAVE® bioreactor. J Transl Med. 2012 Dec;10(1):69.

135. Wickström S, Lövgren T. Expansion of Tumor-Infiltrating Lymphocytes from Melanoma Tumors. In: Pico De Coaña Y, editor. Immune Checkpoint Blockade [Internet]. New York, NY: Springer New York; 2019 [cited 2025 Feb 25]. p. 105–18. (Methods in Molecular Biology; vol. 1913). Available from: http://link.springer.com/10.1007/978-1-4939-8979-9_7

136. Dudley ME, Wunderlich JR, Shelton TE, Even J, Rosenberg SA. Generation of Tumor-Infiltrating Lymphocyte Cultures for Use in Adoptive Transfer Therapy for Melanoma Patients: Journal of Immunotherapy. 2003 July;26(4):332–42.

137. Miltenyi Biotec. CD14 MicroBeads, human [Internet]. Miltenyi Biotec; Available from: https://www.miltenyibiotec.com/DE-en/products/cd14-microbeads-human.html#130-050-201

138. Jalali S, Price-Troska T, Bothun C, Villasboas J, Kim HJ, Yang ZZ, et al. Reverse signaling via PD-L1 supports malignant cell growth and survival in classical Hodgkin lymphoma. Blood Cancer Journal. 2019 Feb 19;9(3):22.

139. Wieleba I, Wojas-Krawczyk K, Chmielewska I, Wójcik-Superczyńska M, Krawczyk P, Milanowski J. In vitro preliminary study on different anti-PD-1 antibody concentrations on T cells activation. Sci Rep. 2022 May 19;12(1):8370.

140. Vetrei C, Passariello M, Froechlich G, Rapuano Lembo R, Zambrano N, De Lorenzo C. Immunomodulatory mAbs as Tools to Investigate on Cis-Interaction of PD-1/PD-L1 on Tumor Cells and to Set Up Methods for Early Screening of Safe and Potent Combinatorial Treatments. Cancers. 2021 June 8;13(12):2858.

141. Lamoreaux L, Roederer M, Koup R. Intracellular cytokine optimization and standard operating procedure. Nat Protoc. 2006 Aug;1(3):1507–16.

142. García-Piñeres AJ, Hildesheim A, Williams M, Trivett M, Strobl S, Pinto LA. DNAse treatment following thawing of Cryopreserved PBMC is a procedure suitable for lymphocyte functional studies. Journal of Immunological Methods. 2006 June;313(1–2):209–13.

143. Wölfl M, Greenberg PD. Antigen-specific activation and cytokine-facilitated expansion of naive, human CD8+ T cells. Nat Protoc. 2014 Apr;9(4):950–66.

144. Lorenzo-Herrero S, Sordo-Bahamonde C, Gonzalez S, López-Soto A. CD107a Degranulation Assay to Evaluate Immune Cell Antitumor Activity. In: López-Soto A, Folgueras AR, editors. Cancer Immunosurveillance [Internet]. New York, NY: Springer New York; 2019 [cited 2024 Nov 14]. p. 119–30. (Methods in Molecular Biology; vol. 1884). Available from: http://link.springer.com/10.1007/978-1-4939-8885-3_7

145. Miller RT. TECHNICAL IMMUNOHISTOCHEMISTRY: Achieving Reliability and Reproducibility of. :57.

146. Buchvalov IB, Böcker W. Immunohistochemistry: basics and methods. Heidelberg: Springer; 2010. 153 p.

147. Zhang W, Hubbard A, Jones T, Racolta A, Bhaumik S, Cummins N, et al. Fully automated 5-plex fluorescent immunohistochemistry with tyramide signal amplification and same species antibodies. Laboratory Investigation. 2017 July;97(7):873–85.

148. Lim JCT, Yeong JPS, Lim CJ, Ong CCH, Wong SC, Chew VSP, et al. An automated staining protocol for seven-colour immunofluorescence of human tissue sections for diagnostic and prognostic use. Pathology. 2018 Apr;50(3):333–41.

149. Ali MM, Li F, Zhang Z, Zhang K, Kang DK, Ankrum JA, et al. Rolling circle amplification: a versatile tool for chemical biology, materials science and medicine. Chem Soc Rev. 2014;43(10):3324.

150. Detter JC, Nelson JR, Richardson PM. Phi29 DNA polymerase based rolling circle amplification of templates for DNA sequencing. 2004 [cited 2020 Feb 7]; Available from: https://escholarship.org/uc/item/6ks6s7r4

151. Söderberg O, Gullberg M, Jarvius M, Ridderstråle K, Leuchowius KJ, Jarvius J, et al. Direct observation of individual endogenous protein complexes in situ by proximity ligation. Nat Methods. 2006 Dec;3(12):995–1000.

152. Wang Y, Li J, Li F, Li S, Zhong R. <i>In Situ</i> Detection of the p53-E6 and pRb-E7 Complex Formation in EC109 Cell by Proximity Ligation Assay. JCT. 2019;10(04):336–44.

153. Bagchi S, Fredriksson R, Wallén-Mackenzie Å. In Situ Proximity Ligation Assay (PLA). In: Hnasko R, editor. ELISA [Internet]. New York, NY: Springer New York; 2015 [cited 2024 Oct 18]. p. 149–59. (Methods in Molecular Biology; vol. 1318). Available from: https://link.springer.com/10.1007/978-1-4939-2742-5_15

154. Leuchowius KJ, Clausson CM, Grannas K, Erbilgin Y, Botling J, Zieba A, et al. Parallel Visualization of Multiple Protein Complexes in Individual Cells in Tumor Tissue. Molecular & Cellular Proteomics. 2013 June 1;12(6):1563–71.

155. Duolink In Situ - Fluorescence.

156. Buchwalow I, Samoilova V, Boecker W, Tiemann M. Multiple immunolabeling with antibodies from the same host species in combination with tyramide signal amplification. Acta Histochemica. 2018 July;120(5):405–11.

157. Stack EC, Wang C, Roman KA, Hoyt CC. Multiplexed immunohistochemistry, imaging, and quantitation: A review, with an assessment of Tyramide signal amplification, multispectral imaging and multiplex analysis. Methods. 2014 Nov;70(1):46–58.

158. Parra ER, Uraoka N, Jiang M, Cook P, Gibbons D, Forget MA, et al. Validation of multiplex immunofluorescence panels using multispectral microscopy for immune-profiling of formalin-fixed and paraffin-embedded human tumor tissues. Sci Rep. 2017 Oct 17;7(1):13380.

159. Giaretta I, Madeo D, Bonaguro R, Cappellari A, Rodeghiero F, Palù G. A comparative evaluation of gene transfer into blood cells using the same retroviral backbone for independent expression of the EGFP and ΔLNGFR marker genes. 2000;85.

160. Vogel DYS, Glim JE, Stavenuiter AWD, Breur M, Heijnen P, Amor S, et al. Human macrophage polarization in vitro: Maturation and activation methods compared. Immunobiology. 2014 Sept;219(9):695–703.

161. McWhorter FY, Wang T, Nguyen P, Chung T, Liu WF. Modulation of macrophage phenotype by cell shape. Proc Natl Acad Sci USA. 2013 Oct 22;110(43):17253–8.

162. Huang PW, Chang JWC. Immune checkpoint inhibitors win the 2018 Nobel Prize. Biomedical Journal. 2019 Oct;42(5):299–306.

163. Zaki MAA, Wada N, Ikeda J, Shibayama H, Hashimoto K, Yamagami T, et al. Prognostic implication of types of tumor-associated macrophages in Hodgkin lymphoma. Virchows Arch. 2011 Oct;459(4):361–6.

164. Kamper P, Bendix K, Hamilton-Dutoit S, Honore B, Nyengaard JR, d'Amore F. Tumor-infiltrating macrophages correlate with adverse prognosis and Epstein-Barr virus status in classical Hodgkin's lymphoma. Haematologica. 2011 Feb 1;96(2):269–76.

165. Szydlowski M, Pawlak M, Garbicz F, Górniak P, Żurańska J, Król M, et al. Hodgkin Lymphoma Reed-Sternberg Cells Induce Immunosuppressive and Pro-Angiogenic Phenotype of Tumor-Associated Macrophages in a Paracrine Manner. Blood. 2020 Nov 5;136(Supplement 1):30–30.

166. Kerneur C, Cano CE, Olive D. Major pathways involved in macrophage polarization in cancer. Front Immunol. 2022 Oct 17;13:1026954.

167. Menéndez V, Solórzano JL, Fernández S, Montalbán C, García JF. The Hodgkin Lymphoma Immune Microenvironment: Turning Bad News into Good. Cancers. 2022 Mar 7;14(5):1360.

168. Tudor CS, Bruns H, Daniel C, Distel LV, Hartmann A, Gerbitz A, et al. Macrophages and Dendritic Cells as Actors in the Immune Reaction of Classical Hodgkin Lymphoma. Dolcetti R, editor. PLoS ONE. 2014 Dec 3;9(12):e114345.

169. Arlt A, Von Bonin F, Rehberg T, Perez-Rubio P, Engelmann JC, Limm K, et al. High CD206 levels in Hodgkin lymphoma-educated macrophages are linked to matrix-remodeling and lymphoma dissemination. Molecular Oncology. 2020 Mar;14(3):571–89.

170. Rakina M, Larionova I, Kzhyshkowska J. Macrophage diversity in human cancers: New insight provided by single-cell resolution and spatial context. Heliyon. 2024 Apr;10(7):e28332.

171. Hirose K, Iwabuchi K, Shimada K, Kiyanagi T, Iwahara C, Nakayama H, et al. Different responses to oxidized low-density lipoproteins in human polarized macrophages. Lipids Health Dis. 2011 Dec;10(1):1.

172. Cencini E, Fabbri A, Sicuranza A, Gozzetti A, Bocchia M. The Role of Tumor-Associated Macrophages in Hematologic Malignancies. Cancers. 2021 July 18;13(14):3597.

173. Ley K. Macrophage Polarization: Different Gene Signatures in M1(LPS+) vs. Classically and M2(LPS–) vs. Alternatively Activated Macrophages.

174. Ahmad A. Epigenetic regulation of immunosuppressive tumor-associated macrophages through dysregulated microRNAs. Seminars in Cell & Developmental Biology. 2022 Apr;124:26–33.

175. Sezginer O, Unver N. Dissection of pro-tumoral macrophage subtypes and immunosuppressive cells participating in M2 polarization. Inflamm Res. 2024 Sept;73(9):1411–23.

176. Rakina M, Larionova I, Kzhyshkowska J. Macrophage diversity in human cancers: New insight provided by single-cell resolution and spatial context. Heliyon. 2024 Apr;10(7):e28332.

177. Malheiro V, Elbs-Glatz Y, Obarzanek-Fojt M, Maniura-Weber K, Bruinink A. Harvesting pre-polarized macrophages using thermo-responsive substrates. Sci Rep. 2017 Feb 14;7(1):42495.

178. Yang Y, Li S, To KKW, Zhu S, Wang F, Fu L. Tumor-associated macrophages remodel the suppressive tumor immune microenvironment and targeted therapy for immunotherapy. J Exp Clin Cancer Res. 2025 May 16;44(1):145.

179. Locatelli SL, Careddu G, Serio S, Consonni FM, Maeda A, Viswanadha S, et al. Targeting Cancer Cells and Tumor Microenvironment in Preclinical and Clinical Models of Hodgkin Lymphoma Using the Dual PI3Kδ/γ Inhibitor RP6530. Clinical Cancer Research. 2019 Feb 1;25(3):1098–112.

180. Casagrande N, Borghese C, Visser L, Mongiat M, Colombatti A, Aldinucci D. CCR5 antagonism by maraviroc inhibits Hodgkin lymphoma microenvironment interactions and xenograft growth. Haematologica. 2019 Mar;104(3):564–75.

181. Ruella M, Klichinsky M, Kenderian SS, Shestova O, Ziober A, Kraft DO, et al. Overcoming the Immunosuppressive Tumor Microenvironment of Hodgkin Lymphoma Using Chimeric Antigen Receptor T Cells. Cancer Discovery. 2017 Oct 1;7(10):1154–67.

182. Bahlmann LC, Xue C, Chin AA, Skirzynska A, Lu J, Thériault B, et al. Targeting tumour-associated macrophages in hodgkin lymphoma using engineered extracellular matrix-mimicking cryogels. Biomaterials. 2023 June;297:122121.

183. Veldman J, Visser L, Huberts-Kregel M, Muller N, Hepkema B, Van Den Berg A, et al. Rosetting T cells in Hodgkin lymphoma are activated by immunological synapse components HLA class II and CD58. Blood. 2020 Nov 19;136(21):2437–41.

184. Martinez Alcala R, Lei Y, Visser L, Diepstra A, Veldman J. Programmed cell death-1 inhibition activates CD4 T cells in a novel in vitro model of Hodgkin lymphoma. Br J Haematol. 2025 Oct;207(4):1643–7.

185. Lee SP, Constandinou CM, Thomas WA, Croom-Carter D, Blake NW, Murray PG, et al. Antigen Presenting Phenotype of Hodgkin Reed-Sternberg Cells: Analysis of the HLA Class I Processing Pathway and the Effects of Interleukin-10 on Epstein-Barr Virus-Specific Cytotoxic T-Cell Recognition.

186. Yang Y, Li S, To KKW, Zhu S, Wang F, Fu L. Tumor-associated macrophages remodel the suppressive tumor immune microenvironment and targeted therapy for immunotherapy. J Exp Clin Cancer Res. 2025 May 16;44(1):145.

187. Amraee A, Evazi MR, Shakeri M, Roozbeh N, Ghazanfarpour M, Ghorbani M, et al. Efficacy of nivolumab as checkpoint inhibitor drug on survival rate of patients with relapsed/refractory classical Hodgkin lymphoma: a meta-analysis of prospective clinical study. Clin Transl Oncol. 2019 Aug 12;21(8):1093–103.

188. Burlile JF, Frechette KM, Breen WG, Hwang SR, Higgins AS, Nedved AN, et al. Patterns of progression after immune checkpoint inhibitors for Hodgkin

lymphoma: implications for radiation therapy. Blood Advances. 2024 Mar 12;8(5):1250–7.

189. Kline J, Godfrey J, Ansell SM. The immune landscape and response to immune checkpoint blockade therapy in lymphoma. Blood. 2020 Feb 20;135(8):523–33.

190. Harker-Murray P, Mauz-Körholz C, Leblanc TM, Mascarin M, Michel G, Cooper S, et al. Nivolumab, Brentuximab Vedotin, +/- Bendamustine For R/R Hodgkin Lymphoma in Children, Adolescents, and Young Adults. Blood. 2022 Dec 23;blood.2022017118.

191. Lecis D, Sangaletti S, Colombo MP, Chiodoni C. Immune Checkpoint Ligand Reverse Signaling: Looking Back to Go Forward in Cancer Therapy. Cancers. 2019 May 4;11(5):624.

192. Hudson K, Cross N, Jordan-Mahy N, Leyland R. The Extrinsic and Intrinsic Roles of PD-L1 and Its Receptor PD-1: Implications for Immunotherapy Treatment. Front Immunol. 2020 Oct 21;11:568931.

193. Tudor CS, Bruns H, Daniel C, Distel LV, Hartmann A, Gerbitz A, et al. Macrophages and Dendritic Cells as Actors in the Immune Reaction of Classical Hodgkin Lymphoma. Dolcetti R, editor. PLoS ONE. 2014 Dec 3;9(12):e114345.

194. Ma D, Wang Y, Shen Q, Liu X, Lu W, Li S, et al. VSIG4 as a tumor-associated macrophage marker predicting adverse prognosis in diffuse large B-cell lymphoma. Front Immunol. 2025 June 5;16:1567035.

195. Akiyama T, Yasuda T, Uchihara T, Yasuda-Yoshihara N, Tan BJY, Yonemura A, et al. Stromal Reprogramming through Dual PDGFRα/β Blockade Boosts the Efficacy of Anti–PD-1 Immunotherapy in Fibrotic Tumors. Cancer Research. 2023 Mar 2;83(5):753–70.

196. Masand N, Perry TA, Pugh M, Fennell E, Hennessy A, Wei W, et al. Hodgkin/Reed-Sternberg cells induce GPNMB expression and release from macrophages to suppress T-cell responses to the Epstein-Barr virus-encoded LMP2A protein. haematol [Internet]. 2024 Aug 22 [cited 2025 Sept 26]; Available from: https://haematologica.org/article/view/haematol.2024.285319

197. Juric V, O'Sullivan C, Stefanutti E, Kovalenko M, Greenstein A, Barry-Hamilton V, et al. MMP-9 inhibition promotes anti-tumor immunity through disruption of biochemical and physical barriers to T-cell trafficking to tumors. St-Pierre Y, editor. PLoS ONE. 2018 Nov 30;13(11):e0207255.

198. Takeuchi A, Saito T. CD4 CTL, a Cytotoxic Subset of CD4+ T Cells, Their Differentiation and Function. Front Immunol [Internet]. 2017 Feb 23 [cited 2025 Oct 8];8. Available from: http://journal.frontiersin.org/article/10.3389/fimmu.2017.00194/full

199. Oh DY, Fong L. Cytotoxic CD4+ T cells in cancer: Expanding the immune effector toolbox. Immunity. 2021 Dec;54(12):2701–11.

200. Cenerenti M, Saillard M, Romero P, Jandus C. The Era of Cytotoxic CD4 T Cells. Front Immunol. 2022 Apr 27;13:867189.

201. Rios FJ, Touyz RM, Montezano AC. Isolation and Differentiation of Human Macrophages. In: Touyz RM, Schiffrin EL, editors. Hypertension [Internet]. New York, NY: Springer New York; 2017 [cited 2024 Nov 12]. p. 311–20. (Methods in Molecular Biology; vol. 1527). Available from: http://link.springer.com/10.1007/978-1-4939-6625-7_24

Acknowledgements

First and foremost, I would like to express my sincere gratitude to Prof. Dr. Roland Schmitz for supervising the research presented in this thesis. His scientific guidance, constructive feedback, and insightful discussions have contributed to shaping the direction of this work. I also appreciate his careful reading of the thesis and the valuable comments he provided. I am grateful for the opportunity to have learned much from his expertise throughout the course of this project. I am also sincerely grateful to Prof. Dr. Undraga Schagdarsurengin for her formal supervision and for the continuous support she offered throughout my doctoral journey. Her generous availability during seminars, her thoughtful advice, and her attentive reading of the thesis greatly strengthened both the scientific content and the clarity of the final manuscript. I also wish to thank Prof. Dr. Stefan Gattenlöhner for his early supervision of my doctoral project and for the valuable methodological support he provided. I am thankful for the provision of cHL tissue samples and for his expert assessment of the immunohistochemical stainings, which helped validate key aspects of the experimental work. I would also like to express my gratitude to Dr. Mehmet Kemal Tur, who kindly welcomed me as a scholarship holder in his former group. His support at that stage played an important role in enabling me to continue my doctoral work. Finally, I would like to express my appreciation to Prof. Dr. Christoph Rummel and Prof. Dr. Andreas Krueger for agreeing to take part in my thesis examination committee and for the time and care they dedicated to evaluating this work.

Furthermore, I would like to express my gratitude to Jutta Schieferstein, Jasmin Habicht, Sibylle Pscherer, Laura Köhler, Nikolai Fuhr, Frank Dönges, Claudia Keller and Gabriela Michel for their technical assistance. Their contributions to sample preparation, laboratory procedures, and experimental workflows were invaluable to this project. I would also like to thank Dr. José Alberto Rodríguez Castillo for the support in configuring the specialized microscopy settings and for developing the custom Fiji script that facilitated key image-analysis steps in this study. In addition, I am grateful to Martin Speckmann for the expert assistance with cell sorting and for the helpful support provided during the analysis of selected datasets. I am sincerely grateful to Tessa Engelstädter for the careful quantification of the PLA dots, which contributed to the analyses presented in this thesis. I am further grateful to Becker Stephanie for performing the bioinformatic processing and analysis of the RNA-seq dataset, which substantially strengthened the transcriptomic component of this study. I would also like to thank Dr. Frederike Hagedorn

for providing the cHL cases and for evaluating the expression patterns observed in the tissue stainings.

I would like to express my appreciation to Dr. Sergej Sereda for the support with the slide scanner and for the valuable advice that helped me navigate several challenging moments during the PhD. Finally, I would like to sincerely thank everyone in the Medical Physics Department at UKGM Giessen for their time, and constant support throughout this work. I would like to thank my group members for making my time in the group truly enjoyable. I appreciated the friendly conversations, and the pleasant lunch breaks we shared. I would also like to thank my friends Zahra Saboori and Edita Islami from neighboring labs for their support and for creating a positive and encouraging atmosphere on our floor. Their presence made this period considerably more pleasant.

I would also like to thank my family and friends for their love, support, and encouragement throughout these years. I am especially grateful to Dr. Gayane Plass for guiding me toward the scholarship opportunity and for the personal support she provided during that time. This thesis would not have been possible without my best friend, Tatevik Vardanyan, who has been a constant source of strength, providing unwavering emotional support during challenging moments and the motivation to keep moving forward. Her belief in me, even when I doubted myself, helped me remain focused and determined.

Eidesstattliche Erklärung

„Ich erkläre: Ich habe die vorgelegte Dissertation selbstständig und ohne unerlaubte fremde Hilfe und nur mit den Hilfen angefertigt, die ich in der Dissertation angegeben habe. Alle Textstellen, die wörtlich oder sinngemäß aus veröffentlichten Schriften entnommen sind, und alle Angaben, die auf mündlichen Auskünften beruhen, sind als solche kenntlich gemacht. Ich stimme einer evtl. Überprüfung meiner Dissertation durch eine Antiplagiat-Software zu. Bei den von mir durchgeführten und in der Dissertation erwähnten Untersuchungen habe ich die Grundsätze guter wissenschaftlicher Praxis, wie sie in der „Satzung der Justus-Liebig-Universität Gießen zur Sicherung guter wissenschaftlicher Praxis“ niedergelegt sind, eingehalten.“

Angaben zu auf künstlicher Intelligenz (KI) basierender Hilfen wie ChatGPT oder SchulKI von OpenAI oder Gemini von Google zur Erstellung meiner Dissertation (Zutreffendes angekreuzt):

☐ Ich habe bei der Erstellung dieses Textes kein KI-Tool verwendet.

☒ Ich habe ein KI-Tool in den folgenden Bereichen eingesetzt (Mehrfachnennungen möglich):

- ☐ Ideen finden, meine Kreativität anregen
- ☐ Verstehen von Konzepten, Recherche von Fakten und Definitionen
- ☒ Optimierung eines von mir verfassten Textes
- ☐ Erstellen ganzer Textpassagen nach meinen Vorgaben

Folgende KI-Tools habe ich verwendet, damit aufgeführte Teile meines Textes von dem Tool wie folgt profitiert haben:
ChatGPT (OpenAI): zur sprachlichen Glättung und stilistischen Verbesserung einzelner von mir verfasster Textpassagen. Inhaltliche Aussagen wurden nicht verändert oder erzeugt.

Datum: 25.11.2025 Unterschrift: Hasmik Yegoryan